

# PE&RS

March 2022

Volume 88, Number 3

PHOTOGRAMMETRIC ENGINEERING & REMOTE SENSING The official journal for imaging and geospatial information science and technology



# ASPRS 2022 Annual Conference — Virtual

## March 21-25, 2022

<https://my.asprs.org/2022Conference>

### ASPRS 2022 Annual Conference—Virtual Technical Program

#### March 21 – 25, 2022

**Missing the In-Person event at Geo Week this year! You can still...**

**SUBMIT** a proposal to present a 15-minute oral presentation, 5-minute Ignite-style talk, or a poster for our online Poster Gallery! <https://my.asprs.org/2022Conference/Call-for-Abstracts>

**ATTEND** ASPRS workshops as live webinars and access as on-demand recordings through our online learning platform, ProLearn!

**ATTEND** oral presentations made by researchers, professionals, and students from around the world highlighting applications of photogrammetry and remote sensing in areas such as:

- Sustainability
- Urban planning and modeling
- Hydrologic modeling
- Food production and crop management
- Disaster response
- Wildfire management and response
- ...

**HEAR** and see industry leaders and policy makers discuss the roadmap forward in areas such as:

- new guidelines and specifications for UAS mapping that will become a reference for many contracting agencies at the federal, state, and local level
- revisions to positional accuracy standards that will accommodate very high resolution lidar and imagery collected from UAS
- transition to the NGS modernized gravity-based National Spatial Reference System (NSRS)
- standards for mapping to support autonomous vehicle operation on intelligent road networks
- ....

**EARN** Professional Development Hours based on Zoom attendance at virtual technical sessions and workshops.

**Last year, over 350 participants from 16 countries joined in the week of virtual presentations! Don't miss it this year!**

**REGISTER NOW!**

<https://my.asprs.org/2022Conference>



## ANNOUNCEMENTS

Teledyne Geospatial announced the sale of its next generation bathymetric CZMIL SuperNova to leading professional services firm **Dewberry**. Dewberry is the first private North American company to purchase the CZMIL SuperNova, adding this unique capability in support of state and federal coastal zone mapping programs, surveying of wetlands, lacustrine and riverine systems, submerged habitat detection and offshore mapping for renewable energy governance.

The CZMIL SuperNova's ability to deliver Quality Level 1 (QL1) data from altitudes greater than 1,200 feet and its Secchi depth penetration range (down to 70 meters in optimal conditions) will allow Dewberry to deliver the quality data required for their projects. Leveraging advanced artificial intelligence and machine learning (AI/ML) techniques for automated land/water discrimination and noise classification, the CZMIL SuperNova bathymetric solution also sets a new standard in processing workflow efficiency through automation in the CARIS software suite without compromising quality.



USGS Landsat 9 Collection 2 Level-1 and Level-2 data will be made available for download from EarthExplorer, Machine to Machine (M2M), and LandsatLook. Initially, USGS will provide only full-bundle downloads. USGS will provide single band downloads and browse images, and Landsat 9 Collection 2 U.S. Analysis Ready Data shortly thereafter. Commercial cloud data distribution will take 3-5 days to reach full capacity.

The recently deployed Landsat 9 satellite passed its post-launch assessment review and is now operational. This milestone marks the beginning of the satellite's mission to extend Landsat's unparalleled, 50-year record of imaging Earth's land surfaces, surface waters, and coastal regions from space. Landsat 9 launched September 27, 2021, from Vandenberg Space Force Base in California. The satellite carries two science instruments, the Operational Land Imager 2 (OLI-2) and the Thermal Infrared Sensor 2 (TIRS-2). The OLI-2 captures observations of the Earth's surface in visible, near-infrared, and shortwave-infrared bands, and TIRS-2 measures thermal infrared radiation, or heat, emitted from the Earth's surface.

Landsat 9 improvements include higher radiometric resolution for OLI-2 (14-bit quantization increased from 12-bits for Landsat 8), enabling sensors to detect more subtle differences, especially over darker areas such as water or dense forests. With this higher radiometric resolution, Landsat 9 can

differentiate 16,384 shades of a given wavelength. In comparison, Landsat 8 provides 12-bit data and 4,096 shades, and Landsat 7 detects only 256 shades with its 8-bit resolution. In addition to the OLI-2 improvement, TIRS-2 has significantly reduced stray light compared to the Landsat 8 TIRS, which enables improved atmospheric correction and more accurate surface temperature measurements.

All commissioning and calibration activities show Landsat 9 performing just as well, if not better, than Landsat 8. In addition to routine calibration methods (i.e., on-board calibration sources, lunar observations, pseudo invariant calibration sites (PICS), and direct field in situ measurements), an underfly of Landsat 9 with Landsat 8 in mid-November 2021 provided cross-calibration between the two satellites' onboard instruments, ensuring data consistency across the Landsat Collection 2 archive.

Working in tandem with Landsat 8, Landsat 9 will provide major improvements to the nation's land imaging, sustainable resource management, and climate science capabilities. Landsat's imagery provides a landscape-level view of the land surface, surface waters (inland lakes and rivers) and coastal zones, and the changes that occur from both natural processes and human-induced activity.

"Landsat 9 is distinctive among Earth observation missions because it carries the honor to extend the 50-year Landsat observational record into the next 50 years," said Chris Crawford, USGS Landsat 9 Project Scientist. Partnered in orbit with Landsat 8, Landsat 9 will ensure continued eight-day global land and near-shore revisit."

Since October 31, 2021, Landsat 9 has collected over 57,000 images of the planet and will collect approximately 750 images of Earth each day. These images will be processed, archived, and distributed from the USGS Earth Resources Observation and Science (EROS) Center in Sioux Falls, South Dakota. Since 2008, the USGS Landsat Archive has provided more than 100 million images to data users around the world, free of charge.

Landsat 9 is a joint mission between the USGS and NASA and is the latest in the Landsat series of remote sensing satellites. The Landsat Program has been providing global coverage of landscape change since 1972. Landsat's unique long-term data record provides the basis for a critical understanding of environmental and climate changes occurring in the United States and around the world.

## TECHNOLOGY

Applanix, a Trimble Company announced the Trimble® AP+ Land GNSS-inertial OEM solution for accurate and robust position and orientation for georeferencing sensors and position-

ing vehicles in land mobile mapping applications. This enables users to accurately and efficiently track and monitor fleets, produce high-definition (HD) maps and 3D models, or act as a ref-



erence solution for advanced driver-assistance systems (ADAS) testing, even in the most challenging GNSS environments.

The Trimble AP+ Land is a comprehensive solution for land vehicle applications that is small enough to easily integrate into the most compact mobile mapping systems. It is also compatible with virtually any type of mapping sensor, including single or multi-lidar systems, video cameras, photogrammetric and panoramic cameras and other similar sensors.

Configurable to meet the mapping, positioning and direct georeferencing (DG) accuracy demands of mapping and positioning applications in challenging GNSS signal environments.

The Trimble AP+ Land OEM solution is fully supported by the industry-leading Applanix POSPac MMS post-processing software, which features Trimble CenterPoint RTX post-processing for centimeter-level positioning globally without the need for base stations. These capabilities make it an ideal solution for integrators to produce a highly efficient land mobile mapping system.

For lidar integrators, the Trimble AP+ Land OEM is compatible with the POSPac MMS LiDAR QC tools. SLAM technology computes the IMU to lidar boresight misalignment angles and also adjusts the trajectory to achieve the highest level of georeferencing accuracy in the generated point cloud.

The Trimble AP+ Land OEM solution and POSPac MMS are available through Applanix sales channels. For more information visit: [mobilemapping.applanix.com](http://mobilemapping.applanix.com).



Phase One, a leading developer of digital imaging technologies, announced the iXM-GS120 aerial camera built to meet

the demanding needs of national security and geo-intelligence gathering projects. Designed for use on unmanned aerial vehicles (UAVs), fixed-wing aircraft, and helicopters, the iXM-GS120 is the first wide-area, 120MP resolution camera designed around advanced global shutter sensor technology.

The iXM-GS120 underscores the Phase One commitment to pioneering development of reliable and innovative aerial imaging solutions. The single-sensor design combined with 120MP resolution guarantees fast collection of detailed information over a wide area of interest in every frame, reducing flight times and enhancing effectiveness. With regards to processing, this design also eliminates the time-consuming stitching together of image scenes from multi-sensor camera systems.

The new camera is the most productive airborne system ever developed by Phase One. Integrating a CMOS global shutter sensor, the iXM-GS120 boasts a remarkable seven frame-per-second capture rate and broad dynamic range. The high-sensitivity, low-noise technology gives the camera an ability to collect data in low-light conditions, thereby expanding its operating window by several hours per day.

Available in RGB color and monochrome versions, the iXM-GS120's range of applications is further broadened by an expansive selection of Fields of View for operation at numerous different aircraft altitudes and speeds. Compatible fields of view include a range of lenses from 35mm to 300mm.

Weighing just 630 grams, the compact camera body mounts easily on a wide range of platforms, including Group 3 tactical unmanned aircraft for long endurance operation.

Learn more at: [https://phaseone.ws/security\\_and\\_space](https://phaseone.ws/security_and_space).

## EVENTS

The 22<sup>nd</sup> William T. Pecora Memorial Remote Sensing Symposium (Pecora 22) will convene in Denver, Colorado, USA from October 23 – 28, 2022, and will focus on all aspects of Earth observation, spanning scientific discoveries to operational applications, and from sensors to decisions. Continuous monitoring of the Earth involves the integration and analysis of both historical and contemporary remotely sensed imagery. It occurs across spatial and temporal scales, measurement objectives, and embraces a broad range of remote sensing and analytical methodologies.

The Pecora 22 conference will also celebrate the 50th anniversary of the launch of the first Landsat satellite and the accomplishments that followed. The conference theme, Opening the Aperture to Innovation: Expanding Our Collective Understanding of a Changing Earth, embraces both the innovations and

discoveries that resulted from 50 years of Landsat Earth observations, and also current and future innovations in science and technology that are contributing to our ability to improve our understanding and better manage the Earth's environment.

We are currently accepting proposals for conference sessions and abstracts.

**The deadline for both is now March 15, 2022.**

For more information see the conference website at <http://pecora22.org>

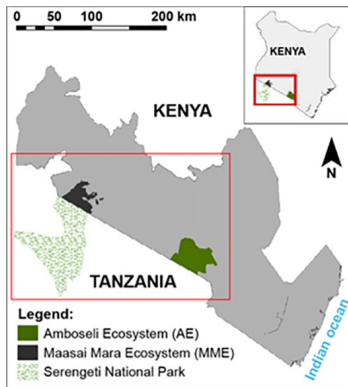
Questions? Contact the Pecora 22 Technical Program Committee at [pecora@usgs.gov](mailto:pecora@usgs.gov).



## CALENDAR

- 3-6 October, **GIS-PRO 2022**, Boise, Idaho. For more information, visit <https://www.urisa.org/gis-pro>.
- 23-27 October, **Pecora 22**, Denver, Colorado. For more information, visit <https://pecora22.org/>.





# 147

## SectorInsights.org—RCMRD/SERVIR Eastern & Southern Africa Collaborate with Kenya Wildlife Conservancy Association (KWCA) to Train Conservancy Managers in the use of GIS and Satellite Data for Conservation

By Edward Ouko and Robinson Mugo

## COLUMNS

**145** GIS Tips & Tricks—You May Not Be The Only One Confused About Python Formatting

**149** Grids and Datums Update  
This month we look at the Ukraine

## ANNOUNCEMENTS

**150** ASPRS Certifications

**152** Signatures  
The Column of the Student Advisory Council

**153** Headquarters News

**153** New ASPRS Members  
Join us in welcoming our newest members to ASPRS.

### Call for *PE&RS* Special Issue Submissions

- 154** Multimodal Remote Sensing Data Processing and Analysis for Earth Observation
- 164** Modelling, Representation, and Visualization of the Remote Sensing Data for Forestry Management
- 180** Monitoring Earth Hazard with Remote Sensing Techniques
- 198** AI-Based Environmental Monitoring with UAV Systems

## DEPARTMENTS

- 141** Industry News
- 142** Calendar
- 206** In-Press *PE&RS* Articles
- 207** Who's Who in ASPRS
- 208** ASPRS Sustaining Members

### 155 Potential of Open Source Remote Sensing Data for Improved Spatiotemporal Monitoring of Inland Water Quality in India: Case Study of Gujarat

Neetu Singh, Shivanand Mallikarjun Nalgire, Meeta Gupta, and Pennan Chinnasamy

Unison of in situ data with satellite remote sensing data has been widely used for water body quality monitoring; however, the developed synergized model is unique and thus needs to be recalibrated and revalidated before applying to other water bodies. In some Indian locations, water quality monitoring is conducted only once a year due to associated costs and time. To aid such instances, in this article, stepwise linear regression models were developed using in situ (annual) and Landsat 7 (biweekly) remote sensing data and validated for two inland water bodies (Sursagar and Nalsarovar lakes) in Gujarat state for dissolved oxygen, biochemical oxygen demand, electrical conductivity, pH, and nitrate.

### 165 Automated 3D Reconstruction of LoD2 and LoD1 Models for All 10 Million Buildings of the Netherlands

Ravi Peters, Balázs Dukai, Stelios Vitalis, Jordi van Liempt, and Jantien Stoter

In this article, we present our workflow to automatically reconstruct three-dimensional (3D) building models based on two-dimensional building polygons and a lidar point cloud.

### 171 Dynamic Linkage Between Urbanization, Electrical Power Consumption, and Suitability Analysis Using Remote Sensing and GIS Techniques

Muhammad Nasar Ahmad, Qimin Cheng, and Fang Luo

This article proposes an estimation method for assessing urban sprawl using multispectral remote sensing data: SNPP-VIIRS, DMSP/OLS, Landsat 5-TM, and Landsat 8-OLI. This study focuses on the impacts of human activities, in terms of increased electrical-power consumption (EPC) due to urbanization.

### 181 An Optimal GeoAI Workflow for Pan-Arctic Permafrost Feature Detection from High-Resolution Satellite Imagery

Mahendra R. Udawalpola, Amit Hasan, Anna Liljedahl, Aiman Soliman, Jeffrey Terstriep, and Chandni Witharana

High-spatial-resolution satellite imagery enables transformational opportunities to observe, map, and document the micro-topographic transitions occurring in Arctic polygonal tundra at multiple spatial and temporal frequencies. Knowledge discovery through artificial intelligence, big imagery, and high-performance computing (HPC) resources is just starting to be realized in Arctic permafrost science. We have developed a novel high-performance image-analysis frame-work—Mapping Application for Arctic Permafrost Land Environment (MAPLE)—that enables the integration of operational-scale GeoAI capabilities into Arctic permafrost modeling. Interoperability across heterogeneous HPC systems and optimal usage of computational resources are key design goals of MAPLE.

### 189 Assessing the Impact of Land Use Changes on Net Primary Productivity in Wuhan, China

Yan Gu, Zhenfeng Shao, Xiao Huang, Yuanhao Fu, Jiyuan Gao, and Yewen Fan

Since 2000, major changes have taken place in Wuhan city. Land use and land cover (LULC) has changed significantly, characterized by increased construction land, reducing farmland, grassland, and forest land due to the rapid urbanization process. Taking advantage of LULC data and Moderate Resolution Imaging Spectroradiometer Net Primary Production (MODIS NPP) data from 2000 to 2020, we analyze the impact of LULC type transformation on NPP, reveal the relationship between LULC type and NPP, and quantify the impact of urban expansion on NPP by taking Wuhan, China as a study case.

### 199 Information Extraction from High-Resolution Remote Sensing Images Based on Multi-Scale Segmentation and Case-Based Reasoning

Jun Xu, Jiansong Li, Hao Peng, Yanjun He, and Bin Wu

In object-oriented information extraction from high-resolution remote sensing images, the segmentation and classification of images involves considerable manual participation, which limits the development of automation and intelligence for these purposes. Based on the multi-scale segmentation strategy and case-based reasoning, a new method for extracting high-resolution remote sensing image information by fully using the image and nonimage features of the case object is proposed.

**See the Cover Description on Page 144**



# COVER DESCRIPTION



While Inuit people have lived in the Foxe Basin for thousands of years, English mariner William Baffin was among the first Europeans to explore this shallow, icy basin north of Hudson Bay. Among the details he noted in his 1615 log: the tan color of the sea ice.

More than 400 years later, the phenomenon continues to stand out, even in satellite imagery. The Operational Land Imager (OLI) on Landsat 8 captured this image of beige ice drifting south of Prince Charles Island on June 22, 2016. The color is likely due to staining from silt and sediment—particles of eroded rock and soil that accumulate on the ocean floor.

Land surrounds most of the Foxe Basin, so sediment sources are never far away. Since the basin is shallow, winds and waves often stir up sediment from the ocean floor. Particles circulate throughout the water column, sometimes reaching the surface and becoming embedded directly within sea ice. Over time, these sediments can become concentrated in ice at the surface because of sublimation and the melting of the ice. In some areas, the water is shallow enough that sea ice rubs directly against the ocean floor and picks up sediment that way.

Some of the color could also be caused by algae, which can grow under the ice and wash up onto the surface during storms.

For more information, visit <https://landsat.visibleearth.nasa.gov/view.php?id=149283>

NASA Earth Observatory image by Joshua Stevens, using Landsat data from the U.S. Geological Survey. Story by Adam Voiland.



## PHOTOGRAMMETRIC ENGINEERING & REMOTE SENSING

### JOURNAL STAFF

Publisher ASPRS  
Editor-In-Chief Alper Yilmaz  
Assistant Director — Publications Rae Kelley  
Electronic Publications Manager/Graphic Artist Matthew Austin

*Photogrammetric Engineering & Remote Sensing* is the official journal of the American Society for Photogrammetry and Remote Sensing. It is devoted to the exchange of ideas and information about the applications of photogrammetry, remote sensing, and geographic information systems. The technical activities of the Society are conducted through the following Technical Divisions: Geographic Information Systems, Photogrammetric Applications, Lidar, Primary Data Acquisition, Professional Practice, Remote Sensing Applications, and Unmanned Autonomous Systems Division. Additional information on the functioning of the Technical Divisions and the Society can be found in the Yearbook issue of *PE&RS*.

Correspondence relating to all business and editorial matters pertaining to this and other Society publications should be directed to the American Society for Photogrammetry and Remote Sensing, 8550 United Plaza Boulevard, Suite 1001, Baton Rouge, LA 70809, including inquiries, memberships, subscriptions, changes in address, manuscripts for publication, advertising, back issues, and publications. The telephone number of the Society Headquarters is 301-493-0290; the fax number is 225-408-4422; web address is [www.asprs.org](http://www.asprs.org).

**PE&RS.** *PE&RS* (ISSN0099-1112) is published monthly by the American Society for Photogrammetry and Remote Sensing, 425 Barlow Place, Suite 210, Bethesda, Maryland 20814-2144. Periodicals postage paid at Bethesda, Maryland and at additional mailing offices.

**SUBSCRIPTION.** For the 2022 subscription year, ASPRS is offering two options to our *PE&RS* subscribers — an e-Subscription and the print edition. e-Subscribers can add printed copies to their subscriptions for a small additional charge. Print and Electronic subscriptions are on a calendar-year basis that runs from January through December. We recommend that customers who choose print and e-Subscription with print renew on a calendar-year basis.

The rate for a Print subscription for the USA is \$1105.00 USD, for Canadian\* is \$1164.00 USD, and for Non-USA is \$1235.00 USD.

The rate for e-Subscription (digital) Site License for the USA and Non-USA is \$1040.00 USD and for Canadian\* is \$1089.00 USD.

The rate for e-Subscription (digital) plus Print for the USA is \$1405.00 USD, for Canadian\* is \$1464.00 USD, and for Non-USA is \$1435.00 USD.

\*Note: e-Subscription, Print subscription, and e-Subscription plus Print for Canada includes 5% of the total amount for Canada's Goods and Services Tax (GST #135123065). **PLEASE NOTE: All Subscription Agencies receive a 20.00 USD discount.**

**POSTMASTER.** Send address changes to *PE&RS*, ASPRS Headquarters, 8550 United Plaza Boulevard, Suite 1001, Baton Rouge, LA 70809. CDN CPM # (40020812).

**MEMBERSHIP.** Membership is open to any person actively engaged in the practice of photogrammetry, photointerpretation, remote sensing and geographic information systems; or who by means of education or profession is interested in the application or development of these arts and sciences. Membership is for one year, with renewal based on the anniversary date of the month joined. Membership Dues include a 12-month electronic subscription to *PE&RS*. To receive a print copy of *PE&RS* there is an additional postage fee of \$60.00 USD for U.S. shipping; \$65.00 USD for Canadian shipping; or \$75.00 USD for international shipping per year. Annual Individual Member dues for members residing in the U.S. and Other Foreign Members are \$150.00 USD and \$158.00 USD for Canadians. Annual Student Member dues for members residing in the U.S. are \$50.00 USD; \$53.00 USD for Canadian; and \$60.00 USD for Other Foreign Members. A tax of 5% for Canada's Goods and Service Tax (GST #135123065) is applied to all members residing in Canada.

**COPYRIGHT 2022.** Copyright by the American Society for Photogrammetry and Remote Sensing. Reproduction of this issue or any part thereof (except short quotations for use in preparing technical and scientific papers) may be made only after obtaining the specific approval of the Managing Editor. The Society is not responsible for any statements made or opinions expressed in technical papers, advertisements, or other portions of this publication. Printed in the United States of America.

### Be a part of ASPRS Social Media:



[facebook.com/ASPRS.org](https://facebook.com/ASPRS.org)



[linkedin.com/groups/2745128/profile](https://linkedin.com/groups/2745128/profile)



[twitter.com/ASPRsorg](https://twitter.com/ASPRsorg)



[youtube.com/user/ASPRS](https://youtube.com/user/ASPRS)



## You May Not Be The Only One Confused About Python Formatting

One of the continuing theses of this column is that with GIS software, there are always multiple ways to accomplish the same end goal. With Python scripting, it is even more true, but with a twist. When scripting there are 101 additional things to think about. Does the function have the right inheritance hierarchy? Are there too many comments? Was that fourth IF- statement indented properly? And then there is an entire additional list of items when geographic information system (GIS) software is thrown into the mix. What worked perfectly fine in the code editor you are using for your development environment suddenly doesn't cooperate when bringing it into another GIS interface. Then, a major factor to keep in mind when developing scripts is identifying what version of Python your software is using and what format a script needs to be written in for the software to understand a particular command. For this month's Tip & Trick, we will focus on formatting strings with the F-String function.

In Python, there are three methods of formatted strings (f-strings) that can be used to format syntax and change display expressions. Each method was developed as new versions of Python were released; the intent was to make formatting simpler, but of course, with different versions, new issues and confusion can arise.

### FOR PYTHON VERSION 1.0

In Python 1.0, the f-string method involves using %formatting. The percent (%) operator acts as a placeholder in a statement while the variable being formatted is then added after the % (Example 1). If there is more than one variable needed in a statement, then the variables are included after the % operator using parenthesis and commas to separate each variable (Example 2).

**Example 1.** Basic use of %formatting where variable "baker" is being incorporated into a print statement.

```
baker = "cleo"
print ("Welcome to %s's bakery"%baker)
Result: Welcome to Cleo's bakery
```

**Example 2.** Formatting with more than one variable.

```
food = "donuts"
num = 73
baker = "Cleo"
print ("Welcome to %s's bakery!. There are %s %s in stock."%(baker, num, food))
Result: Welcome to Cleo's bakery! There are 73 donuts in stock.
```

### FOR PYTHON VERSION 2.0

In Python 2.0, the f-string method involves using the string format; where curly brackets "{}" are used to contain a string variable (otherwise known as "str.format()"). The {} act as a placeholder for the variable "while .format()" follows after; the variable is contained within the parenthesis (Example 3). As many variables as needed can be added within the parenthesis, where even variables in a dictionary (Example 4) can be called and formatted in a statement.

**Example 3.** Basic use of string format where baker, number, and food variables are applied to the print statement.

```
Food = "donuts"
Num = 73
Baker = "Cleo"
Print ("Welcome to {}'s bakery! There are {} {} in stock."format(baker, num, food))
Result: Welcome to Cleo's bakery! There are 73 donuts in stock.
```

**Example 4.** Accessing a dictionary with string format for the print statement.

```
bakery = {"baker": "Daniel", "food": "danishes"}
print ("Welcome to {baker}'s bakery! We sell {food}."format (**bakery))
Result: Welcome to Daniel's bakery! We sell danishes.
```

### FOR PYTHON VERSION 3.0

In Python version 3.0, the f-string method is similar to str.format() but now it is written out as f "{}". By using lowercase f or uppercase F in the beginning of the statement, the curly brackets containing the variable can be placed more easily (Example 5). This method makes editing syntax more efficient and easier to follow.

**Example 5.** Basic use of f"{}" where variables are placed throughout the print statement.

```
baker = "Cleo"
rival = "Daniel"
b1 = "donuts"
b2 = "danishes"
print (f'{rival}'s bakery is {baker}'s rival. But their {b2} can't compare to our {b1}!')
Result: Daniel's bakery is Cleo's rival. But their danishes can't compare to our donuts!
```

Photogrammetric Engineering & Remote Sensing  
Vol. 88, No. 3, March 2022, pp. 145-146.  
0099-1112/22/145-146

© 2022 American Society for Photogrammetry  
and Remote Sensing  
doi: 10.14358/PERS.88.3.145



Table 1. Comparison of several popular GIS software programs and compatible Python versions.

GIS Software	Version	Python Version Used	Recommended F-string to use
ArcGIS Desktop	10.0-10.8.1	Python 2.6.5 - Python 2.7.18	<ul style="list-style-type: none"> <li>% formatting</li> <li>str.format()</li> </ul>
ArcGIS Enterprise	10.0 - 10.2.1, 10.5, 10.5.1, 10.6, 10.6.1, 10.7, 10.8, 10.9	Python 2.6.5 - Python 2.7.18	<ul style="list-style-type: none"> <li>% formatting</li> <li>str.format()</li> </ul>
ArcGIS Enterprise cont.	10.4 - 10.9 *(note: versions may include upgraded set of python libraries)	Python 3.4.1 - 3.7.9	<ul style="list-style-type: none"> <li>f "{}" formatting</li> </ul>
ArcGIS Notebook	10.7 - 10.9 *(note: versions may include upgraded set of python libraries)	Python 3	<ul style="list-style-type: none"> <li>f "{}" formatting</li> </ul>
ArcGIS Pro	1.0 - 1.2	Python installation required	<ul style="list-style-type: none"> <li>% formatting</li> <li>str.format()</li> <li>f "{}" formatting</li> </ul>
ArcGIS Pro cont.	1.3 - 2.8.3	Python 3	<ul style="list-style-type: none"> <li>f "{}" formatting</li> </ul>
Global Mapper	v22.0 - v23.0	Python 3.9	<ul style="list-style-type: none"> <li>f "{}" formatting</li> </ul>
QGIS	v3.16 - v3.22	Python 3	<ul style="list-style-type: none"> <li>f "{}" formatting</li> </ul>
QGRASS GIS	7.4.4 - 7.8.6	Python 2.7 - Python 3	<ul style="list-style-type: none"> <li>% formatting</li> <li>str.format()</li> <li>f "{}" formatting</li> </ul>
Microsoft Azure Maps	2.0	Python 2.7 - Python 3.8	<ul style="list-style-type: none"> <li>% formatting</li> <li>str.format()</li> <li>f "{}" formatting</li> </ul>

Understanding the different methods of f-strings is not only useful for formatting scripts, but also significant to formatting tools for different GIS software systems. Not all GIS systems may have Python incorporated into their back-end code; while some GIS software may use older versions of Python. The trick to formatting lines of code with f-strings is knowing what version of Python the software uses.

Every update to a piece of software is going to come with its own positives and negatives. One update may solve developing needs and make work much easier. On the other hand, an update may have the most up to date version of Python, but may take away a feature the last version had that was needed for a special kind of analysis or cartographic work. Table 1 summarizes popular GIS software and Python versions, there are a variety of packages that come in certain software versions.

Knowing how to adapt code for frameworks is part of an application and script's life cycle. Not every project requires legacy code to function, but having a basis of what formatting is required makes the adaptation and troubleshooting process run smoother.

It is important to note that there is no wrong way to write scripts and tools; there is always more than one way to accomplish the end-goal. Rather, it is a matter of how clear they are to users and developers that determines their usability. If a project is dependent on features of one system version over another, developing code that's understandable for that specific system is essential. But where there are limits, there also lies creative bounds. Once a system's syntax limits are understood, it becomes easier to adapt code for the best use of a project or task.

Below are some additional sources for help with Python scripting.

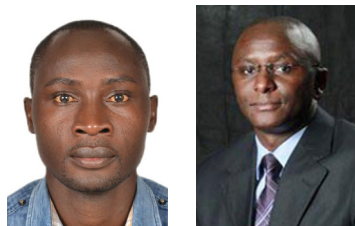
## SOURCES

- "Arcgis Notebook Server." *Available Python Libraries-ArcGIS Notebook Server | Documentation for ArcGIS Enterprise*, <https://enterprise.arcgis.com/en/notebook/latest/python/windows/available-python-libraries.htm>.
- FAQ: What Version of Python Is Used in Arcgis?, <https://support.esri.com/en/technical-article/000013224>.
- Real Python. "Python 3's F-Strings: An Improved String Formatting Syntax (Guide)." *Real Python*, Real Python, 19 Mar. 2021, <https://realpython.com/python-f-strings/>.
- Jablonski, J. "Python 3's F-Strings: An Improved String Formatting Syntax (Guide)." *Real Python*, Real Python, 19 Mar. 2021, <https://realpython.com/python-f-strings/>.
- "Microsoft Azure SDK for Python." *Microsoft Docs*, <https://docs.microsoft.com/en-us/python/api/overview/azure/mgmt-maps-readme?view=azure-python>.
- "Python in Global Mapper." *Python Scripting*, <https://www.bluemarblegeo.com/knowledgebase/global-mapper-23/Python.htm>.
- QGIS Documentation, <https://qgis.org/en/docs/index.html>.
- Requirements to Compile Grass GIS 7, <https://grass.osgeo.org/grass74/source/REQUIREMENTS.html>.

Send your questions, comments, and tips to [GISTT@ASPRS.org](mailto:GISTT@ASPRS.org).

*YoLani Martin is a Geospatial Analyst with Dewberry's Fairfax, VA office. She is a resource for open source tools and Python scripting. Al Karlin, Ph.D., CMS-L, GISP is with Dewberry's Geospatial and Technology Services group in Tampa, FL. As a senior geospatial scientist, Al works with all aspects of Lidar, remote sensing, photogrammetry, and GIS-related projects.*





Edward Ouko and Robinson Mugo

## RCMRD/SERVIR Eastern & Southern Africa Collaborate with Kenya Wildlife Conservancy Association (KWCA) to Train Conservancy Managers in the use of GIS and Satellite Data for Conservation

The Maasai Mara Wildlife Conservation Association (MMWCA)<sup>1</sup> and Amboseli Ecosystem Trust (AET)<sup>2</sup> are two key biodiversity hotspots in Kenya, and whose wildlife corridors extend into neighbouring Tanzania. The two ecosystems constitute habitats for very important wildlife species (keystone species such as Elephants). The Mara ecosystem accounts for 25% of Kenya's wildlife (Figure 1) and nearly three quarters of

The Mara and Amboseli ecosystems are valuable national and community assets, whose conservation and sustainability will greatly enhance the wealth and resilience of the local communities to climate change and economic shocks. Unfortunately, the impact of environmental degradation due to human activities and the effects of climate change are apparent in both ecosystems, which calls for prudent and data driven conservation efforts. However, given the vast areas, and a myriad of threats to natural ecosystems and wildlife, conservation managers must improve their skills in data collection, analysis and synthesis for prompt decision making. As a result, conservation managers, policymakers and others are increasingly relying on geospatial information and analysis to monitor and assess pressures on habitats, understand species status, vulnerability and distribution patterns. Geographic information science (GIS) is therefore critical in monitoring external threats, planning of conservation actions and response.

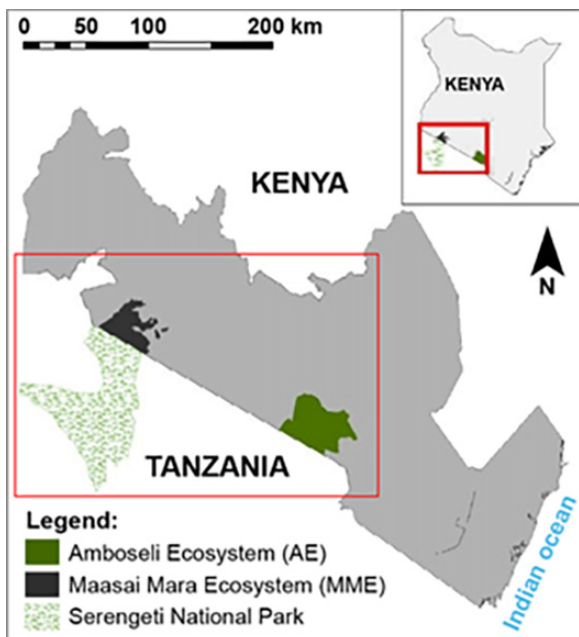


Figure 1. The location of Maasai Mara and Amboseli ecosystems in Kenya.

the protected area population. On the other hand, the Amboseli ecosystem is one of Kenya's premier parks both in terms of biodiversity conservation and tourist visitation. The MMWCA manages 15 conservancies covering an area of 347,011 acres (about 1400 square kilometres), supporting 14,528 land-owners and 280 community rangers, while the AET has current membership of 20 conservancies covering approximately 394,834 acres (about 1597 square kilometres) supporting 65,881 households and close to 500 community rangers.

The SERVIR Eastern and Southern Africa (E&SA) project<sup>3</sup> is a joint initiative of the National Aeronautics and Space Administration (NASA), the United States Agency for International Development (USAID), and the Regional Centre for Mapping of Resources for Development (RCMRD)<sup>4</sup>. SERVIR partners with countries and organizations in eastern and southern Africa to address critical challenges in climate change, food security, water and related disasters, land use, and air quality. Using satellite data and geospatial technology, SERVIR co-develops innovative solutions through a network of regional hubs to improve resilience and sustainable resource management at local, national and regional scales. In Kenya, SERVIR is collaborating with KWCA to build a GIS portal for managing conservation data, and also training conservancy managers in the use of GIS and satellite imagery derived from NASA and Copernicus hubs to improve decisions in conservation. Recently, SERVIR E&SA and

<sup>1</sup> <https://maraconservancies.org/>

<sup>2</sup> <https://amboseliecosystem.org/>

<sup>3</sup> <https://servirglobal.net/Regions/ESAFfrica>

<sup>4</sup> <https://www.nasa.gov/>



KWCA brought together 30 conservancy managers from the MMWCA and AET for training in the application of geospatial tools in conservation management and monitoring. The managers were taken through the use of GPS devices, open-source GIS and remote sensing software (QGIS), data use and manipulation in a GIS environment and map creation of key natural resources. The training models were built on open-source tools to facilitate access to and manipulation of GIS and remote sensing (satellite) data and products within the conservation networks.

The collaboration between the RCMRD and KWCA fulfils SERVIR's strategic goal to empower regional and national actors in the use of Earth observation information for development decision making. KWCA works with landowners and communities through 167 conservancies in Kenya to sustainably conserve and manage wildlife and their habitat outside formal protected areas for the benefit of the people of Kenya. At the same time RCMRD and SERVIR bridge the skills gap in use of geospatial tools for better decision making. The partnership is built around a Memorandum of Understanding covering collaboration in the areas of data, tools co-development and capacity enhancement in the application of geospatial tools in conservation management. The SERVIR project believes improved capacity in the use of geospatial tools and technologies among the conservation practitioners will be important in strengthening conservation efforts on the ground and enhance citizen science led data collection among the conservation community. This would enable the various conservation actors like KWCA and communities to play key roles in defining future spatial data and products which serve local conservation and ecological needs. On the gender lens, KWCA did a remarkable job of identifying a number of women to participate in the training, making up approximately 25% of the participants Figure 2.



Figure 2: Ms. Faria shows a map of grazing zones she developed during the training, for her practical exercises.

Following the successful training, the conservancy managers expressed confidence that the skills acquired during the engagement will be vital in their daily conservation monitoring activities. According to Daniel Kaaka, the Amboseli Ecosystem Coordinator, "The remote sensing and GIS training was a hands-on opportunity for Amboseli Ecosystem conservancy managers to interrogate and inform decision making by the click of a button." Sarah Omusala, of Gamewatchers Safaris Conservation and Porini Camps, observed that "the training empowered the conservancy managers in collecting data on flora and fauna, thus adding to their skills and tools for managing protected areas, and also monitoring habitat health, identifying the wild animals and livestock movements, illegal activities, and grazing areas based on land use and landcover types".

## References

<https://www.rcmr.org/about-us/about-rcmr>

<https://kwcakenya.com/>

<https://www.servirglobal.net/>

## Authors

**Edward Ouko** is a Thematic Lead for the Ecosystem and Modelling Service Area of the SERVIR Eastern & Southern Africa Project at the Regional Centre for Mapping of Resources for Development (RCMRD) in Nairobi, Kenya. He holds a double Master of Science in GIS and Remote Sensing with bias to Global Environment Modelling from Lund University, Sweden and University of Twente, in the Netherlands. His research interests include ecosystem modelling, biostatistics, species distribution modelling, forestry, and system modelling. He is passionate about application of remote sensing (Optical and SAR) to monitor ecosystems and landscapes across the globe.

**Robinson Mugo** is the Project Manager of the SERVIR Eastern & Southern Africa Project at the Regional Centre for Mapping of Resources for Development (RCMRD) in Nairobi, Kenya. SERVIR is a partnership with USAID and NASA which fosters the use of Earth observation (EO) data and geospatial tools for development decision making in various societal benefit areas. He also serves as a board member of the Kenya Education Network Trust (KENET), the National Research and Education Network (NREN) of Kenya. He holds a PhD in Satellite Oceanography and GIS from Hokkaido University, Japan, with research interests in ecological informatics, species distribution modeling using machine learning models, and water quality monitoring using EO data.



# & GRIDS DATUMS

BY Clifford J. Mugnier, CP, CMS, FASPRS

## THE UKRAINE

The Grids & Datums column has completed an exploration of every country on the Earth. For those who did not get to enjoy this world tour the first time, *PE&RS* is reprinting prior articles from the column. This month's article on the Ukraine was originally printed in 2004 but contains updates to their coordinate system since then.

**P**aleolithic remains have been found in the region, but the oldest dwelling in Kiev is from the 25<sup>th</sup> century B.C., about 4,500 years ago. "Ukraine was the center of the first Slavic state, Kievan Rus, which during the 10<sup>th</sup> and 11<sup>th</sup> centuries was the largest and most powerful state in Europe. Weakened by internecine quarrels and Mongol invasions, Kievan Rus was incorporated into the Grand Duchy of Lithuania and eventually into the Polish-Lithuanian Commonwealth. The cultural and religious legacy of Kievan Rus laid the foundation for Ukrainian nationalism through subsequent centuries. A new Ukrainian state, the Cossack Hetmanate, was established during the mid-17<sup>th</sup> century after an uprising against the Poles. Despite continuous Muscovite pressure, the Hetmanate managed to remain autonomous for well over 100 years. During the latter part of the 18<sup>th</sup> century, most Ukrainian ethnographic territory was absorbed by the Russian Empire. Following the collapse of czarist Russia in 1917, Ukraine was able to bring about a short-lived period of independence (1917-1920) but was reconquered and forced to endure a brutal Soviet rule that engineered two artificial famines (1921-22 and 1932-33) in which over 8 million died. In World War II, German and Soviet armies were responsible for some 7 to 8 million more deaths." (*World Factbook*, 2004). The republic achieved independence in 1991.

Ukraine is slightly smaller than Texas and borders Belarus (891 km), Hungary (103 km), Moldova (939 km), Poland (526



km), România (169 km), Russia (1,576 km), and Slovakia (97 km). The coastline is 2,782 km along the Black Sea and the Sea of Azov. The climate is temperate continental, and most of Ukraine is steppes and plateaus, with the Carpathian Mountains in the west and the southeastern coast of the Crimea from Sevastopol through Yalta and north to Feodosiya. The lowest point is the Black Sea (0 m), and the highest point is Hora Hoverla (2,061 m). The capital is Kiev, and according to legend, the city was founded in 482 A.D. by a royal family of three brothers and one sister.

The czarist Russians performed surveys and topographic mapping of Ukraine in the 19<sup>th</sup> and early 20<sup>th</sup> centuries, but these works were for military purposes only. They did nothing with respect to individual land ownership registration, and they preferred the sazhen for their unit of measurement. (Paraphrased from Poland, *PE&RS*, September 2000). The existing classical triangulation net is a dense mesh to the west along the border with Poland, Hungary, România, and Moldova, primarily in the mountainous region and extending as far east as Rivne, Ternopil', and Chernivtsi. A southern chain of figures reaches from the western city of

Photogrammetric Engineering & Remote Sensing  
Vol. 88, No. 3, March 2022, pp. 149-151.  
0099-1112/22/149-151

© 2022 American Society for Photogrammetry  
and Remote Sensing  
doi: 10.14358/PERS.88.3.149



Izmayil, through Odessa and Kherson to the Crimea where it includes Feodosiya and Kerch. There are seven other meridional arcs that are connected by three more-or-less continuous east-west chains. Although some first-order work is evident around Kiev, there is a very dense network about Yalta in the Crimea. There are a number of high-order local surveys evident in Ukraine, and I suspect that some of these locations may be coincident with now-empty underground silos; a once-favorite area for ICBM sites when the USSR had control of Ukraine.

The observations for the Horizontal State Geodetic Network (HSGN) of Ukraine began in 1923-25, but it took over 30 years to complete both horizontal and vertical leveling

work. Completed in 1970, the first-order network has been maintained while densification has continued for third and fourth-order control. The HSGN consists of 19,538 points that include 547 first-order and 5,386 second-order points. The HSGN is on the "System 42" datum established (in 1942) by the USSR where the origin point is at Pulkovo Observatory where:  $\Phi_0 = 59^\circ 46' 18.55''$  North,  $\Lambda_0 = 30^\circ 19' 42.09''$  East of Greenwich. The defining azimuth at the point of origin to Signal A is  $\alpha_0 = 317^\circ 02' 50.62''$ . System 42 is referenced to the Krassovsky 1940 ellipsoid where  $a = 6,378,245.0$  meters, and  $1/f = 298.3$ . The previously mentioned dense and continuous western network is entirely first-order in quality. The remainder of the first-order network of the Ukraine

## STAND OUT FROM THE REST

### EARN ASPRS CERTIFICATION

ASPRS congratulates these recently Certified and Re-certified individuals:

#### RECERTIFIED PHOTOGRAMMETRIST

##### **Kirk Spell, Certification #R1498CP**

Effective July 13, 2021, expires July 13, 2026

##### **Colby Forke, Certification #R1598CP**

Effective August 3, 2021, expires August 3, 2026

##### **Samuel Vessel, Certification #R1605CP**

Effective September 12, 2021, expires September 12, 2026

##### **Robert Hertwig, Certification #R1606CP**

Effective November 30, 2021, expires November 30, 2026

##### **Glenn D. Logan, Certification #R1039CP**

Effective February 7, 2019, expires February 7, 2024

##### **Tian Wu, Certification #R1516CP**

Effective November 21, 2021, expires November 21, 2026

##### **Michael Martin, Certification #R1608CP**

Effective December 3, 2021, expires December 3, 2026

##### **Michael B. Joos, Certification #R1101CP**

Effective November 13, 2021, expires November 13, 2026

##### **Mark DiLeo, Certification #R892CP**

Effective July 26, 2021, expires July 26, 2026

##### **Adam Smith, Certification #R1521CP**

Effective December 12, 2021, expires, December 22, 2026

##### **Dusanka Urosevic, Certification #R1280CP**

Effective December 13, 2020, expires, December 13, 2025

##### **Lorraine B. Amenda, Certification #R1517CP**

Effective December 12, 2021, expires, December 12, 2026

##### **Todd Schmidt, Certification #R1609CP**

Effective December 3, 2021, expires, December 3, 2026

##### **Raymond D. Joslyn, Certification #R1509CP**

Effective October 21, 2021, expires, October 21, 2026

#### RECERTIFIED GIS/LIS TECHNOLOGIST

##### **Evan E. Echlin, Certification #R293GST**

Effective October 19, 2020, expires October 19, 2025

ASPRS Certification validates your professional practice and experience. It differentiates you from others in the profession. For more information on the ASPRS Certification program: contact [certification@asprs.org](mailto:certification@asprs.org), visit <https://www.asprs.org/general/asprs-certification-program.html>.



is comprised of polygons: the lengths of each section being less than 200-250 km. There are 250 LaPlace (astronomic) stations in the HSGN which are located at each end of the first-order triangulation polygons and in the middle of each section. In continuous first-order chains, the LaPlace stations are spaced every 10 triangles, and the accuracy of the azimuths is  $\pm 1.2''$ . In second-order chains, LaPlace stations are located at baseline terminals. The accuracy of baseline distance measurements is not less than  $4 \times 10^{-6}$ . In general, a single Ukraine map sheet at a scale of 1:1,000,000 will contain about 35-70 LaPlace station points and about 20-30 baselines. The average density of HSGN points is 1 point in  $30 \text{ km}^2$ , but this varies in different regions. For instance, in the industrial region around Donbass, the density goes up to 1 point in  $5\text{-}10 \text{ km}^2$ , while in the rural region around Polissia the density goes down to about 1 point in  $40\text{-}50 \text{ km}^2$ . The grid system associated with the Ukraine HSGN is the same as with all former countries of the Soviet Union – the Russia Belts which are identical to the UTM grid except that the scale factor at origin ( $m_0$ ) = unity. For large-scale mapping, the width of the belts reduces to  $3^\circ$  rather than the standard  $6^\circ$  belt.

The Vertical State Geodetic Network (VSGN) consists of almost 11,000 km of first-order leveling, plus 12,600 km of second-order leveling, 6,000 km of third-order leveling, and about 300,000 km of ordinary leveling. The average distance from any site in Ukraine to a first- or second-order level line does not exceed 40 km. The first-order VSGN is tied to the vertical networks of Poland, Slovakia, România, Hungary, Russia, and Belarus. The vertical datum is referenced to the Kronstadt tide gauge located at the Baltic Sea, near St. Petersburg (Russia). Benchmark spacing in Ukraine is not in my files. The State Gravimetric Network is comprised of 80 first-order points and 20 second-order points with the fundamental point located in Poltava.

The NGA does not list datum transformation parameters from System 42 to WGS84 for Ukraine. My guess is that the parameters are pretty close to what they are for Moscow since the strategic importance of the country was so enormous to the USSR. Ukraine has now passed legislation that denotes WGS84 as the national datum of the republic.

Years ago, I sat in a hotel room in South America and watched “The Wall” being torn down. I was working on a U.S. A.I.D. project for land titlelization in which I designed the geodetic and photogrammetric aspects of the project for a canton in Ecuador. That process is a major project now in Ukraine, and GPS technology is an integral component of the social transformation. Those that read my columns are aware that I often grouse on “La Ley” – “The Law” as it exists in much of Latin America in which a branch of the federal government is given the exclusive monopoly for geodetic surveying and topographic mapping of a country. That is a custom derived from the European way of doing things

back in the 19<sup>th</sup> century. I don’t care for the concept because it frustrates private commercial mapping in favor of some federal groups, usually the military. Such an idea seems to be the current state of affairs in Ukraine, and their federal government appears to have passed a similar 19th-century era-type law. This may be a result of sociological/economic phenomena more than anything else, but it’s disappointing to see such developments in new republics striving for excellence in a worldwide capitalistic environment. I wish them success in their endeavors to provide farmers with a title to the soil their forefathers have tilled for so many centuries; the geodetic and photogrammetric sciences will allow the technical aspects to flow smoothly.

I have to thank Dr. Momchil Minchev of Sofia, Bulgaria for his generous assistance in locating geodetic publications in English on the Ukraine for me. The reports of Dr. Michael Cheremshynsky of the Ukraine Main Administration of Geodesy, Cartography, and Cadastre of Ukraine in Kiev have made the technical details of the geodetic history possible for this article. Once again, Dr. Minchev has helped me unravel an enigma.

## Ukraine Update

“2020 can be considered as the year of geospatial data in Ukraine with the Ukrainian geospatial community facing a historic moment of digitalization. We have introduced a ‘single window’ for natural resource management, which will help to save budget funds and develop territories, strengthen public control over the activities of state bodies and increase public confidence in the government.

“In April 2020, Ukraine’s law on the National Spatial Data Infrastructure (NSDI) was finally adopted by the Ukrainian Parliament after more than 10 years and 4 attempts. Although Ukraine is not an EU Member State, the law is fully in line with INSPIRE and also reflects the main principles of EU open data policy” (*State Service of Ukraine for Geodesy, Cartography and Cadastre (StateGeoCadastre) 2022*).

The Ukrainian government’s geodetic website ([https://dgm.gki.com.ua/pererahunok-po-gelmertu-\(po-kljuchu\)-na-ploschini](https://dgm.gki.com.ua/pererahunok-po-gelmertu-(po-kljuchu)-na-ploschini)) offers a Helmert-style datum conversion tool and appears to have a completely open access portal to the nation’s geodetic network, as typical for a free republic. The website pages are in Ukrainian and in English.

The contents of this column reflect the views of the author, who is responsible for the facts and accuracy of the data presented herein. The contents do not necessarily reflect the official views or policies of the American Society for Photogrammetry and Remote Sensing and/or the Louisiana State University Center for GeoInformatics (C<sup>4</sup>G).

This column was previously published in *PE&RS*.



## ASPRS SAC GIS DAY CELEBRATIONS

### To celebrate GIS Day, the ASPRS Student Advisory Council (SAC) hosted an online Map Cartography Contest!

Maps were welcomed in any format including hand-drawn. Entries were limited to one map per ASPRS member. The submission deadline was November 17, 2021 and online voting was held on November 18th. There were a variety of entries, all beautiful in their own form. Submissions can be viewed online at <https://sites.google.com/pdx.edu/asprs-sac-map-contest>.

“It is difficult to pick only 5. All of them are amazing!” voiced numerous voters. This was something we were ecstatic to hear.

Originally 5 prizes were decided but we extended the prizes to six participants when voting resulted in a tie. The prizes included a free one year “ArcGIS for Personal Use license” and the opportunity to have their map displayed in the Poster Gallery at the ASPRS Annual Conference at Geo Week this past February. Winners were also offered a position as a Student Volunteer at the Annual Conference.

The winners, a short biography, and their corresponding maps are mentioned below.

***“It is difficult to pick only 5. All of them are amazing!”***



Andy Egogo-Stanley

#### **Street Guide of a Section of Ado-Ekiti, Ekiti State, Nigeria**

Andy Egogo-Stanley is a recent graduate in Surveying and Geoinformatics with interest in spatial data science and machine learning, from the University of Lagos, Nigeria. He served as the General Secretary of the Nigerian Institution of Surveying and Geoinformatics Students (NISGS), 2019 – 2020.



Akinnusi Samuel

#### **Deforestation of the Amazon Rainforest in Rondônia, Brazil**

Akinnusi Samuel completed his BSc in Surveying and Geoinformatics from the University of Lagos. His BSc research was on air pollution and its relationship with land cover change in Nigeria. He is also a member of several geospatial organizations and through volunteering is working towards achievement of the SDGs.



Gbiri Joshua

#### **Dzaleka Refugee Camp Watershed**

Gbiri Joshua is an undergraduate student of Surveying and Geoinformatics at the University of Lagos, Nigeria with research interest in machine learning and GIS. He is a member of several geospatial communities and holds a Remote Pilot license from AUVSI. In addition, he loves teaching, playing guitar, and debating.



Marty Marquis

#### **Rocky Mountain Way: Best Markets for Live Music in the Rockies**

Marty Marquis is a graduate student of GIS at Portland State University. He also spent over a decade studying “applied geography,” touring and performing in a band. His interests include architecture, analog synthesis, and American football. Marty lives in Scappoose, Oregon with his wife and children.



Rabia Munsaf Khan

#### **A GIS Based Drastic Model for Assessing Groundwater Vulnerability**

Rabia Munsaf Khan is a Fulbright PhD scholar at SUNY ESF with research interest in water quality monitoring using machine learning techniques. She is also serving as Communications Councilor at ASPRS SAC. As a quintessential altruist she has moderated over 100 students in the past years on multiple platforms.



Peter Samson

#### **Glacial Lake Kalapuya**

Peter Samson is a lifelong cartophile, now retired, whose career took him through geology; science education; project and event management; and consulting to nonprofits on strategic planning, finance, grant-writing, and fundraising. He also enjoys outdoor activities, pie baking, and volunteering.

### If you are interested in participating in SAC activities:

- Join us every other Thursday from 10-11 am PST!
- Join us via this zoom link, <https://tinyurl.com/SACASPRSMeting>

#### ASPRS STUDENT ADVISORY COUNCIL

LAUREN MCKINNEY-WISE  
COUNCIL CHAIR  
OSCAR DURAN  
DEPUTY COUNCIL CHAIR  
CHUKWUMA JOHN OKOLIE  
COMMUNICATIONS COUNCIL MEMBER

TBD  
EDUCATION & PROFESSIONAL NETWORKING CHAIR  
ALI ALRUZUQ  
DEPUTY EDUCATION & PROFESSIONAL NETWORKING CHAIR  
TESINI PRECIOUS DOMBO  
COMMUNICATIONS COUNCIL MEMBER

RABIA MUNSAF KHAN  
COMMUNICATIONS COUNCIL CHAIR  
KENNETH EKPETERE  
CHAPTERS COMMITTEE CHAIR  
FREDA ELIKEM DORBU  
COMMUNICATIONS COUNCIL MEMBER

## JOURNAL STAFF

### Editor-In-Chief

Alper Yilmaz, Ph.D., [PERSEditor@asprs.org](mailto:PERSEditor@asprs.org)

### Associate Editors

Rongjun Qin, Ph.D., [qin.324@osu.edu](mailto:qin.324@osu.edu)

Michael Yang, Ph.D., [michael.yang@utwente.nl](mailto:michael.yang@utwente.nl)

Petra Helmholz, Ph.D., [Petra.Helmholz@curtin.edu.au](mailto:Petra.Helmholz@curtin.edu.au)

Bo Wu, Ph.D., [bo.wu@polyu.edu.hk](mailto:bo.wu@polyu.edu.hk)

Clement Mallet, Ph.D., [clmallet@gmail.com](mailto:clmallet@gmail.com)

Prasad Thenkabail, Ph.D., [pthenkabail@usgs.gov](mailto:pthenkabail@usgs.gov)

Ruisheng Wang, Ph.D., [ruiswang@ucalgary.ca](mailto:ruiswang@ucalgary.ca)

Desheng Liu, Ph.D., [liu.738@osu.edu](mailto:liu.738@osu.edu)

Valérie Gouet-Brunet, Ph.D., [valerie.gouet@ign.fr](mailto:valerie.gouet@ign.fr)

Dorota Iwaszczuk, Ph.D., [dorota.iwaszczuk@tum.de](mailto:dorota.iwaszczuk@tum.de)

Qunming Wang, Ph.D., [wqm11111@126.com](mailto:wqm11111@126.com)

Filiz Sunar, Ph.D., [fsunar@itu.edu.tr](mailto:fsunar@itu.edu.tr)

Norbert Pfeifer, np@ipf.tuwien.ac.at

Jan Dirk Wegner, [jan.wegner@geod.baug.ethz.ch](mailto:jan.wegner@geod.baug.ethz.ch)

Hongyan Zhang, [zhanghongyan@whu.edu.cn](mailto:zhanghongyan@whu.edu.cn)

Dongdong Wang, Ph.D., [ddwang@umd.edu](mailto:ddwang@umd.edu)

Zhenfeng Shao, Ph.D., [shaozhenfeng@whu.edu.cn](mailto:shaozhenfeng@whu.edu.cn)

Ribana Roscher, Ph.D., [ribana.roscher@uni-bonn.de](mailto:ribana.roscher@uni-bonn.de)

Sidike Paheding, Ph.D., [spahedin@mtu.edu](mailto:spahedin@mtu.edu)

### Contributing Editors

#### Highlight Editor

Jie Shan, Ph.D., [jshan@ecn.purdue.edu](mailto:jshan@ecn.purdue.edu)

#### Feature Articles

Michael Joos, CP, GISP, [featureeditor@asprs.org](mailto:featureeditor@asprs.org)

#### Grids & Datums Column

Clifford J. Mugnier, C.P., C.M.S., [cjmce@lsu.edu](mailto:cjmce@lsu.edu)

#### Book Reviews

Sagar Deshpande, Ph.D., [bookreview@asprs.org](mailto:bookreview@asprs.org)

#### Mapping Matters Column

Qassim Abdullah, Ph.D., [Mapping\\_Matters@asprs.org](mailto:Mapping_Matters@asprs.org)

#### Sector Insight

Lucia Lovison-Golob, Ph.D., [lucia.lovison@sat-drones.com](mailto:lucia.lovison@sat-drones.com)

Bob Ryerson, Ph.D., FASPRS, [bryerson@kingeomatics.com](mailto:bryerson@kingeomatics.com)

#### GIS Tips & Tricks

Alvan Karlin, Ph.D., CMS-L, GISP [akarlin@Dewberry.com](mailto:akarlin@Dewberry.com)

### ASPRS Staff

#### Assistant Director — Publications

Rae Kelley, [rkelley@asprs.org](mailto:rkelley@asprs.org)

#### Electronic Publications Manager/Graphic Artist

Matthew Austin, [maustin@asprs.org](mailto:maustin@asprs.org)

#### Advertising Sales Representative

Bill Spilman, [bill@innovativemediasolutions.com](mailto:bill@innovativemediasolutions.com)

## CONGRATULATIONS TO ASPRS'S NEWLY ELECTED BOARD MEMBERS!

We are extremely fortunate to have such a strong group of dedicated professionals express their desire to help lead the future direction of ASPRS. I am very excited to see what Jin, Matt, Hank and Bahram will do to craft the future of their respective Divisions. As I close out my tenure, I know that the future of ASPRS is in good hands with the election of Dr. Kar as well. I look forward to watching the Society benefit from her leadership."

-ASPRS President, Jason Stoker

ASPRS Vice President – Bandana Kar

GIS Assistant Division Director – Jin Lee

Lidar Assistant Division Director – Mat Bethel

PAD Assistant Division Director – Hank Theiss

UAS Assistant Division Director – Bahram Salehi

## ASPRS ANNOUNCES THE 2022 GEOBYTE SERIES

Visit <https://www.asprs.org/geobytes.html> for more information and to register.

## NEW ASPRS MEMBERS

ASPRS would like to welcome the following new members!

Trent Adams	Adama Mochenwa
Benjamin Ifedjeji Ajisafe	David C. Newkirk
Abena Boatemaa Asare-Ansah	James Rego Nicolau, IV
Quest Besing	Ismaila Abiola Olaniyi
Jon Blickwede, Sr.	Constantine Papadakis
Rachael Brady	Mark Paulson, PLS
Benjamin Bush	Maya Price
David Cakalic	Charles Robison
Dave J. Cook	Brian Scott
Stuart Gibson	Johnathan Paul Smeh
Rupert Dujon Green	Timothy Tallmadge
Tim Haynie	Ewoud Van Der Cruyssen
Jon Loder	Kara Leigh Wayman
Alex Martin	Kevin R. Winslow
Joseph McNichols	Tristan Wirkus
Katherine Milla, PhD	Shane Zentner, GISP

FOR MORE INFORMATION ON ASPRS MEMBERSHIP, VISIT  
[HTTP://WWW.ASPRS.ORG/JOIN-NOW](http://WWW.ASPRS.ORG/JOIN-NOW)



# Call for *PE&RS* Special Issue Submissions

## Multimodal Remote Sensing Data Processing and Analysis for Earth Observation

Earth observation, by providing critical information on natural resources, hazardous areas, and climate change, among others, is a powerful tool in all aspects of life. The observations come primarily from space-based sensors such as satellites, but they highly depend on ground-based remote sensing devices. Multimodal remote sensing systems integrate optical and passive microwave radiometers to improve the quality of observations. The versatility of multimodal RS offers enormous potential to monitor diverse target phenomena in all climate system components with high spatial, temporal, or spectral resolution. It provides innovative methods for processing multispectral, hyperspectral, and polarimetric remote sensing data for different vegetation, geophysical, and atmospheric applications to understand the earth better. However, there are still challenges to achieving maximum exploitation of multimodal data. At the same time, the combination of multimodal remote sensing technologies is a powerful approach that can yield significant advantages compared to traditional single-modal sensors.

The techniques such as image processing is typically used to adjust and refine data derived from remote sensing. Its capabilities are also useful for merging data sources. Image processing techniques, such as filtering and feature extraction, are well suited for dealing with the high-dimensionality of spatially distributed systems. The input data may come from different sensors, each with a different spatial resolution and measurement scale ('multimodal'). It provides approaches for the extraction of relevant non-topographic information from remote sensing data, such as demographic indicators from satellite images of urban areas, which could assist in future spatial modelling of these areas. It helps to analyze shape, topography, and texture phenomena for soil and vegetation data and various methods for image fusion and analysis of the optical, radar, and gravity data. It covers a wide range of geospatial applications, including land and water resources management, urban planning, environmental monitoring, natural hazards and climate change, oceanography, engineering design, and national security and intelligence. It processes multi-spectral, thematic-mapping, thermal-infrared (TIR), hyperspectral data acquired from optical, SAR or lidar platforms with advanced techniques in the areas of scene characterization and feature extraction.

This special issue is intended for remote sensing scientists, engineers, and researchers involved in its application for earth observation. Innovative techniques dealing with climate monitoring; environmental monitoring, including pollution monitoring and deforestation detection; geographical information system (GIS) applications; maps generation, land cover classification and change detection; mineral exploration industries; hydrology and

water resources management; based on multimodal remote sensing data are most invited for submission.

List of Topics (include, but not limited to the following):

- Deep learning and computer vision for earth observation and multimodal remote sensing
- Semantic and instance segmentation of the multimodal remote sensing data for earth observation and analysis
- Multimodal remote sensing data fusion, interpretation and analysis for earth observation
- Hyperspectral remote sensing and image processing for earth observation
- Light weight deep neural network algorithms for earth surveillance
- Earth object classification and recognition using multimodal remote sensing approaches
- Multi-resolution and multi-modal remote sensing for enhancing the earth observation processes
- Novel applications of multi-modal remote sensing in earth monitoring and surveillance processes
- Spatio-temporal data analysis for efficient earth observation
- Multimodal data reconstruction and restoration for efficient classification process
- Benchmarking multimodal datasets for earth observation
- New algorithms and frameworks for efficient analysis of multimodal remote sensing data

**Deadline for Manuscript Submission**  
**August 1, 2022**

**Submit your Manuscript to**  
**<http://asprs-pers.edmgr.com>**

### Guest Editors

**Dr. Ahmed A. Abd El-Latif**, [alatif@science.menofia.edu.eg](mailto:alatif@science.menofia.edu.eg), Associate Professor, *Department of Mathematics and Computer Science, Faculty of Science, Menoufia University*, Egypt.

**Dr. Edmond Shu-lim Ho**, [e.ho@northumbria.ac.uk](mailto:e.ho@northumbria.ac.uk), Senior Lecturer, *Department of Computer and Information Sciences, Northumbria University, Newcastle upon Tyne*, United Kingdom.

**Dr. Jialiang Peng**, [jialiangpeng@hlju.edu.cn](mailto:jialiangpeng@hlju.edu.cn), Associate Professor, *School of Data Science and Technology, Heilongjiang University*, China.

# Potential of Open Source Remote Sensing Data for Improved Spatiotemporal Monitoring of Inland Water Quality in India: Case Study of Gujarat

Neetu Singh, Shivanand Mallikarjun Nalgire, Meeta Gupta, and Pennan Chinnasamy

## Abstract

*Unison of in situ data with satellite remote sensing data has been widely used for water body quality monitoring; however, the developed synergized model is unique and thus needs to be recalibrated and revalidated before applying to other water bodies. In some Indian locations, water quality monitoring is conducted only once a year due to associated costs and time. To aid such instances, in this study, stepwise linear regression models were developed using in situ (annual) and Landsat 7 (biweekly) remote sensing data and validated for two inland water bodies (Sursagar and Nalsarovar lakes) in Gujarat state for dissolved oxygen, biochemical oxygen demand, electrical conductivity, pH, and nitrate. Results indicated that all models showed good to excellent performance metrics based on an  $r$  value ( $p < 0.01$ ) ranging from 0.86 to 0.98 and 0.72 to 0.99 for Sursagar and Nalsarovar lakes, respectively. All models had root mean square errors less than 0.5, and residual predictive deviations greater than 2, which depicted good predictability. The models were able to increase the water quality assessment from annual resolution to biweekly resolution and provided insights on the dynamics of water quality parameters, improved understanding on key drivers for the change, and identified peak pollution leading to unfit conditions for domestic or agricultural consumption.*

## Introduction

Access to clean water has become a critical issue worldwide due to growing population, industrialization and increasing pollutant loads due to climate and land-use changes into freshwater ecosystems (Chinnasamy *et al.* 2021, Sagan *et al.* 2020). Over the past ten decades, half of the natural wetlands and a significant number of freshwater bodies have vanished due to water pollution and growing economic activities (UN Water 2020). In India, river and lake pollution has been a crucial problem over the past few decades (Kumar *et al.* 2017). It is estimated that around 70% of the surface water bodies in India are polluted by biological, toxic, organic, and inorganic pollutants (Sengupta 2018). Every day, rivers and other water bodies receive around 40 million liters of wastewater, with a negligible fraction adequately treated (Hirani and Dimble 2019). Traditionally, surface water bodies have been a significant source of water supply for drinking and domestic purposes. However, with widespread urbanization and industrialization becoming predominant, these water sources have been contaminated severely and are considered unfit for human consumption and other activities, such as irrigation and recreation (Kumar *et al.* 2017). Also, polluted water supplies increase the cost of water treatment and minimize water oxygenation by limiting sunlight transfer.

Neetu Singh and Meeta Gupta are with IITB-Monash Research Academy, India, and Center for Technology Alternatives for Rural Areas (CTARA), Indian Institute of Technology, Bombay (IITB), India.

Shivanand Mallikarjun Nalgire and Pennan Chinnasamy are with Center for Technology Alternatives for Rural Areas (CTARA), Indian Institute of Technology, Bombay (IITB), India (p.chinnasamy@iitb.ac.in).

Contributed by Zhenfeng Shao, July 15, 2021 (sent for review September 9, 2021; reviewed by Md. Enamul Huq, Hongping Zhang).

The surface water quality (SWQ) is estimated based on different physical, chemical, and biological parameters (Sagan *et al.* 2020). The conventional methods adopted to determine the water quality involve *in situ* and in-field measurements or collecting water samples from the field and performing analysis in the nearest laboratories. Although the *in situ* measurement delivers accurate results, the entire exercise is time consuming, labor intensive, and costly (Al-Shaibah *et al.* 2021). In addition, due to the low spatial and temporal resolution, the existing sampling methods adopted do not capture either the spatial or the temporal extent required for the accurate assessment and management of the water bodies (Mushtaq and Nee Lala 2017). Therefore, there is a constant need to update and upgrade methods for inland water quality assessments and frequent monitoring.

With the advancement and growing role of remote sensing (Chinnasamy and Parikh 2021) and geographic information systems (GIS), new techniques have emerged for assessing water quality using satellite data to reduce time and cost and increase accuracy (Al-Shaibah *et al.* 2021). The widely used approach to estimate SWQ parameter concentration using remote sensing data involves fitting a linear regression between spectral bands/band combinations and temporally coincident *in situ* SWQ observations, called empirical modeling (González-Márquez *et al.* 2018). This approach has a limitation of nongeneralizability across large spatial and temporal scales, though it can be outweighed by its capability to provide model transparency, cost-effectiveness, simplicity, and minimal computational requirements (Topp *et al.* 2020). On this note, satellite images have been widely used to develop synergized models with *in situ* data to assess the quality of water bodies globally. For example, El Din and Zhang (2017) developed linear regression models using Landsat 8 data to estimate optical parameters, such as turbidity, total suspended solids (TSS), and concentration of nonoptical parameters, such as chemical oxygen demand (COD), biochemical oxygen demand (BOD), and dissolved oxygen (DO), in Saint John River, Canada. In another study, González-Márquez *et al.* (2018) used Landsat 8 data to assess spatial and temporal variation of phosphates ( $\text{PO}_4$ ), electrical conductivity (EC), TSS, turbidity, and pH in Playa Colorado Bay. The developed water quality models had coefficients of determination ( $R^2$ ) in the range of 0.637–0.955. Zhang *et al.* (2017) used Landsat images along with the linear stepwise regression method to estimate total nitrogen (TN), total phosphorus (TP), permanganate index ( $\text{CODMn}$ ), and 5-day biochemical oxygen demand (BOD5) in Danjiangkou Reservoir, China, which indicated a water quality deterioration trend between May 2006 and May 2014. The application of multitemporal Landsat images in the aforementioned studies has established their potential to estimate the spatial and temporal variation of SWQ parameters. Such an application is needed for Indian inland waters, as some water bodies are monitored only once a year for water quality parameters. This low monitoring frequency impedes the understanding of water quality changes and the insights on what causes these changes.

Photogrammetric Engineering & Remote Sensing  
Vol. 88, No. 3, March 2022, pp. 155–163.  
0099-1112/22/155–163

© 2022 American Society for Photogrammetry  
and Remote Sensing  
doi: 10.14358/PERS.21-00044R2



Gujarat, located on the western coast of India, is the most industrialized and urbanized state of India. The increasing population pressure and development changes have exerted staggering pressure on water resources concerning quantity and quality. The state ranks fourth in the top five states with highly polluted rivers and lakes in India (Langa 2021). Many cities in Gujarat have to deal with huge quantity untreated sewage from the industries being discharged in rivers and lakes, which has reduced the biodiversity and the regenerative capacity of the water bodies, leaving them unfit for human consumption (Gujarat Ecology Commission [GEC] 2017). Especially the lakes located in the Central and South Gujarat regions, accounting for 83% of the total surface water resources of the state, have been witnessing this phenomenon for a long time (GEC 2017). Amongst the many lakes, Nalsarovar and Sursagar lakes have been severely impacted. Nalsarovar lake is a site of international and ecological importance, and the Sursagar Lake holds historical importance for the state; however, access to clean water remains a major challenge for the water users, water managers, and the authorities. Thus, to restore the health of these water bodies, it is imperative to carry out long-term water quality monitoring and assessment. There has been some effort undertaken to study the water quality of Nalsarovar and Sursagar lakes using field measurements for specific periods and locations. However, the absence of long-term SWQ data has restricted the extent of the water quality analysis of these lakes, which is the need of the hour for better management.

For Nalsarovar and Sursagar lakes, SWQ monitoring using remote sensing images has not been done previously, and long-term monitoring is absent. Thus, the empirical models built in this study to predict SWQ parameter concentration using remote sensing images can bring a paradigm shift in the SWQ monitoring of these lakes. The trends and anomalies in the concentration of SWQ parameters can efficiently predict future water quality outbreaks. The proposed methodology can be further utilized to derive long-term SWQ data of other lakes with similar geologic and environmental settings.

This research aimed to develop empirical water quality models to demonstrate the feasibility of satellite remote sensing in the characterization of lakes of Gujarat. The developed empirical models were used to retrieve DO, pH, EC, BOD, and nitrate concentrations of the lakes. Additionally, water quality parameter concentrations of previous years were estimated using the established models.

## Study Area

### Sursagar Lake

Sursagar Lake, formerly known as Chandan Talav, is located at  $22^{\circ}18'02.96''\text{N}$  latitude and  $73^{\circ}12'14.09''\text{E}$  longitude, in the center of Vadodra city (in Gujarat, a northeastern state in India), at an elevation of 35 m above mean sea level (AMSL) (Figure 1). Built in the 18th century, this perennial lake measures 327 m in length and 213 m in width and has an average depth of 3.7 m. The lake has several underwater gates that are opened in case of flooding, and the excess water pours into the Vishwamitri River. The city experiences a subtropical type climate with moderate humidity, with rainfall received mainly from the southwest monsoon during June–September. The average annual rainfall is 903 mm, and the average annual temperature is  $34^{\circ}\text{C}$  during the period 1989–2018 (Guhathakurta *et al.* 2020).

Before 1990, Sursagar Lake was a major source of drinking water in the city; however, due to rapid industrialization with simultaneous urbanization in the city, water quantity and quality have been adversely impacted (Gujarat Environment Management Institute [GEMI] 2020). Currently, the lake is surrounded by commercial complexes, temples, and residential buildings. Additionally, many chemicals, pharmaceutical, and textile industries thrive in the city. The untreated sewage from these industries and complexes is often released into the storm water drains and ends up entering the lake's inlet channels due to an inadequate drainage network, thereby contaminating the lake water (Brahmbhatt and Shah 2018). Over the years, the lake has become one of the most polluted lakes among the municipal corporations in the entire state (The Times of India 2017).

In an attempt to beautify the lake and use it for recreational purposes, construction activities within and around the lake have further led to an increase in waste generation (GEMI 2020). Another activity leading to pollution in the lake is the immersion of idols during the 10-day Ganesh Chaturthi festival. A huge quantity of china clay used in the idols and decoration materials, such as clothes, paints, and plastic garlands, have deteriorated the water quality by blocking the inlet channels (Patel and Shah 2016; GEMI 2020).

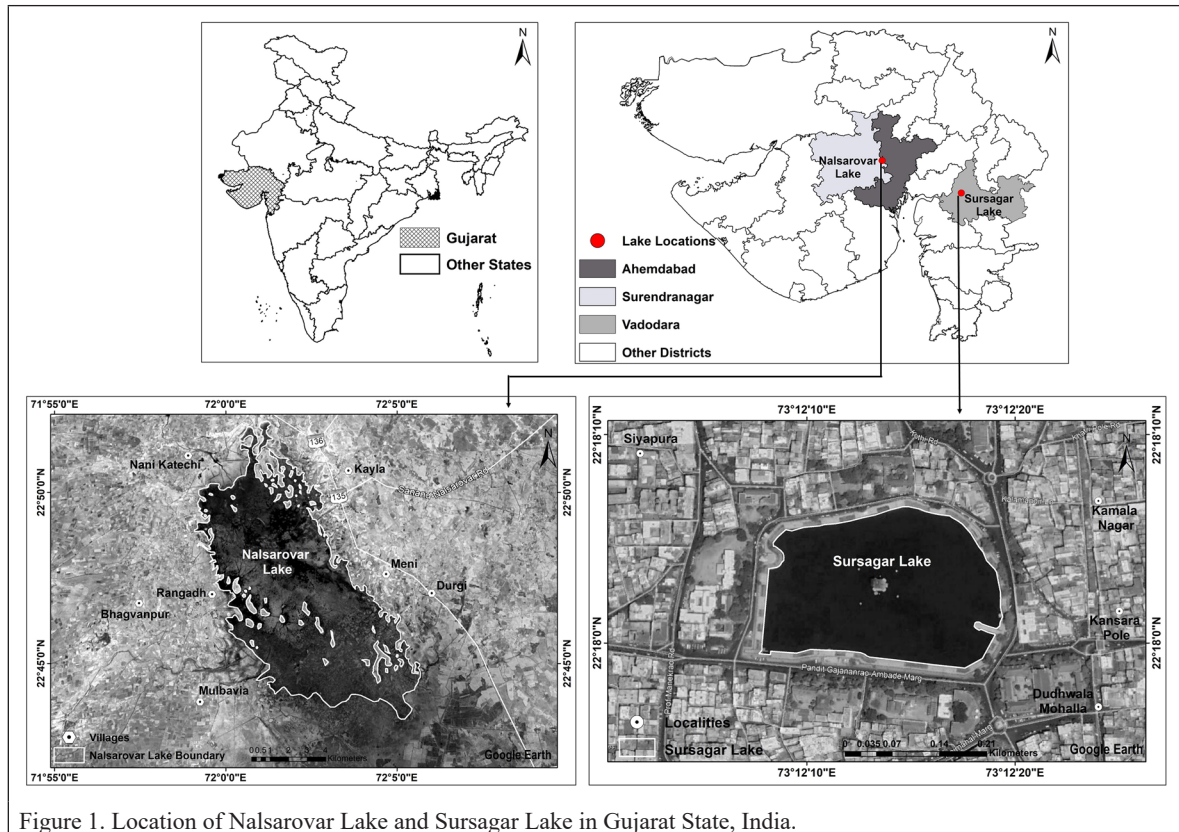


Figure 1. Location of Nalsarovar Lake and Sursagar Lake in Gujarat State, India.

## Nalsarovar Lake

Nalsarovar Lake is the largest natural freshwater inland wetland in the Thar Desert biogeographic region. The lake is located at 22°46'33.03"N latitude and 72°02'21.00"E longitude along the western border of the Ahmedabad district and the southern border of the Surendranagar district (Figure 1) at an elevation of 7.92 m AMSL. Nalsarovar Lake is spread in an area of 120 km<sup>2</sup> and is the largest wetland bird sanctuary in India. Because of the rich biodiversity and socio-economic importance, the lake was declared a Ramsar Site in 2012.

Nalsarovar is a shallow lake with muddy lagoons and has its genesis by the elevation of land between the present-day Gulf of Khambhat and Gulf of Kachchh during the late quaternary period (Rathod and Parasharya 2018). The lake has over 300 islets or bays, of which 36 are relatively large and located mainly on its western boundary (Chauhan *et al.* 2021). The entire area receives an average rainfall of about 500–600 mm, and the average temperature reaches up to a maximum of 35°C during May and falls below 10°C during December (Biswas and Pandey 2019).

The lake receives water mainly from two rivers, the Brahmini and the Bhogavo, and from the surrounding catchment in the north, west, and east in a diffused manner (Vankar *et al.* 2018). The lake gets inundated during the southwest monsoon (June–September), while it dries up almost entirely in the summer. This lake has also been a principal source of livelihood for the local dependent communities of the peripheral 12 villages for many years. They carry out fishing, wheat cultivation, and tourism-based activities to generate income (Biswas and Pandey 2019). The primary source of pollution in the lake is the household sewage and agricultural runoff from the villages that are located in at northwestern boundary, while the state development authorities ensure that no industrial effluent enters the lake. Additionally, land reclamation and new developmental activities, along with illegal bird poaching, pose threats to the water quality of the lake (Japan International Cooperation Agency and Nippon Koei India Pvt Ltd India 2020).

## Data and Methodology

### *In Situ* SWQ Data

The *in situ* SWQ data for the two lakes have been collected from the Gujarat Pollution Control Board (GPCB), which is the nodal agency at the state level to implement environmental laws and rules within Gujarat for the protection of the environment. Under the National Water Quality Programme, GPCB collaborates with the Central Pollution Control Board (CPCB) to monitor and assess the water quality and facilitate the prevention and control of pollution. Lake water sampling and parameter monitoring are done as per the Guidelines on Water Quality Monitoring 2017, issued by the Ministry of Environment, Forest, and Climate Change. Water samples are analyzed for 25 physicochemical and biological parameters using the analytical techniques as prescribed by the American Public Health Association and the Bureau of Indian Standards. The analyzed water quality parameters are then compared with the “designated best use” water quality criteria recommended by the CPCB.

For this study, the water quality data for both the lakes, Nalsarovar and Sursagar, have been collected for a 13-year period from 2006 to 2019. For the assessment of these two lakes, five major parameters (i.e., DO, pH, EC, BOD, and nitrate) have been considered. The significance of the selected parameters, along with the factors influencing their concentration and affecting the water quality, are discussed next. The pH, with a range value of 0–14, is a very important parameter that defines the acidic (0–6), neutral (7), or basic nature (8–14) of the water. A high or low pH can affect the solubility and biological availability of the chemicals and heavy metals in the water. Additionally, aquatic life can be stressed or die when exposed to extreme pH levels or when pH changes rapidly, as the majority prefers a pH range of 6.5–9.0 (CPCB 2019). The pH of a lake can be affected by photosynthetic and respiration activities, which depend on the carbonate–bicarbonate–carbon dioxide equilibrium (Kumari *et al.* 2019; Pant *et al.* 2019; Sudarshan *et al.* 2019). Anthropogenic activities like dumping industrial sewage

in the streams and acidic runoff from mining areas can have immediate and intense effects on the pH levels.

An indirect estimate of the amount dissolved salts present in water is provided by the EC value. Low values of EC (<1000 µs/cm) indicate pristine to normal status of a lake and its surroundings (CPCB 2019). The EC of a lake is affected primarily by the catchment geology. For example, lakes surrounded by clayey soil tend to show high EC because of the presence of minerals that ionize when washed with water (Borowiak *et al.* 2020). Additionally, high EC can arise by various other factors, such as wastewater from sewage treatment plants, agricultural runoff loaded with chloride, nitrate and phosphate from fertilizers, high evaporation rates leading to concentration of dissolved salts in the remaining water, and a larger catchment surface area relative to the lake area, which increases the contact with the soil and washes up more ions (Kumari *et al.* 2019; Borowiak *et al.* 2020).

The DO is considered one of the most important parameters to assess the health of the surface water body. The higher the DO concentration in a water body, the better the water quality and the ability to support aquatic life. Low levels of DO (<4 mg/L) can occur due to algal blooms, driven by high levels of nitrogen and phosphorus found in fertilizers (CPCB 2019; Pant *et al.* 2019). As these algae die and decompose, DO in the water is consumed, resulting in insufficient amounts available for other aquatic life. DO is inversely related to BOD. BOD measures the amount of dissolved oxygen consumed by microorganisms to decompose the organic matter present in the water (Sudarshan *et al.* 2019). Higher values of BOD can arise due to the untreated sewage from industries and residential areas entering into the lake inlets, leading to more consumption of dissolved oxygen (Vasistha and Ganguly 2020).

Nitrates are essential for aquatic plant growth; however, the overabundance can cause several adverse health and ecological impacts. Nitrates are introduced into the water bodies through the discharge of sewage and industrial wastes and runoff from agricultural fields containing nitrogen-rich chemical fertilizers (Pant *et al.* 2019; Sudarshan *et al.* 2019). Excessive nitrate concentration can lead to algal growth, which can degrade the water quality by depleting the oxygen levels (Vasistha and Ganguly 2020).

### Remote Sensing Satellite Data

Landsat imagery is widely applied for water quality assessments, as it features global coverage, free access, high resolution, and multispectral data with an unprecedented 43-year record of observations of the global land surface, land conditions, and dynamics (Mushtaq and Nee Lala 2017). Using the Google Earth Engine (GEE) cloud computing platform, a Landsat 7 data set was obtained and processed ranging from the period between 1999 and 2020 for the study lakes in Gujarat. The Landsat 7 surface reflectance (SR) data of the pixels coincident with the location of the water body were acquired from GEE, which were then processed to remove the atmospheric, radiometric, and geometric influences.

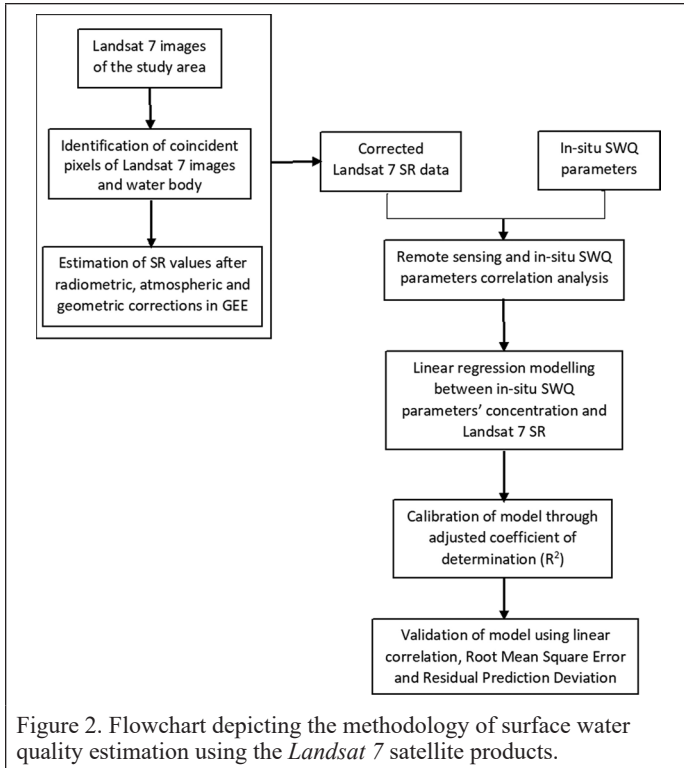
### Methodology

The overall methodology of this study is represented in Figure 2, wherein the remote sensing data are used to generate the empirical models of SWQ parameter concentrations for water bodies of Gujarat state. The processed SR data were used to build the empirical models of SWQ parameters through a linear regression algorithm. The models were calibrated using 75% of *in situ* SWQ observations and then validated using the remaining 25% of *in situ* SWQ observations.

### Remote Sensing Data Preprocessing

The remote sensing data process begins with the acquisition of data hosted on the GEE cloud, which is atmospherically corrected using the Landsat Ecosystem Disturbance Adaptive Processing System and includes a cloud, shadow, water, and snow mask produced using CFMask as well as a per-pixel saturation mask. CFMask is a multi-pass algorithm that uses an artificial intelligence model (decision trees) to prospectively label pixels in the scene; it then validates or discards those labels according to scene-wide statistics. It also creates a cloud shadow mask by iteratively estimating cloud heights and projecting them onto the ground (Zhu *et al.* 2015). Cloud filtering and masking were performed using the provided pixel quality assurance bands to select only pixels containing cloud-free images.





### Correlation Analysis

Correlation analysis of *in situ* SWQ parameters and *Landsat* 7 SR data was conducted using Pearson correlation coefficient ( $r$ ), which can have a value between  $-1$  and  $+1$ . Coefficient values close to  $-1$  indicate a strong inverse relationship among the variables. In contrast, correlation values close to  $+1$  indicate a strong positive relationship, and values close to zero indicate no relationship among the variables (Pearson 1909).

The correlation analysis of *in situ* SWQ parameters (DO, pH, EC, BOD, and nitrate) with each other was conducted to ascertain their relationship. The strong correlation between two or more parameters depicts that one parameter can be used as a representative of other correlated parameters for water quality analysis. Also, their models may show resemblance and thus can improve the model calibration (El Din and Zhang 2017).

The correlation analysis of *in situ* SWQ parameters and their logarithms with addition, subtraction, ratio, exponent, natural log, and individual value of *Landsat* 7 SR data was conducted. The strength of correlation between the SWQ parameter and SR or SR combination can facilitate the elimination of the weakly correlated variables for the calibration of the regression model (González-Márquez *et al.* 2018)

### Model Calibration and Validation

It is noted that logarithms of dependent variables can improve the distribution of the data and thus may provide a better correlation with the independent variables (Swain and Sahoo 2017). In this study, empirical models were built using SR or SR combination values as independent variables and temporally coincident *in situ* SWQ parameters and their logarithms as dependent variables. The empirical modeling technique provides transparency and lesser computational requirements (González-Márquez *et al.* 2018; Topp *et al.* 2020). The empirical models are built using a linear regression algorithm that assumes that the relationship between the independent and dependent variables is linear and additive (Sagan *et al.* 2020).

The dependent variables were divided into two data sets for calibration (75% of all SWQ observations) and validation of the model (25% of all SWQ observations). For calibration, the stepwise linear regression (SLR) variable selection method was used to choose the best subset of independent variables. The SLR method starts with a null model, then the independent variable that produces the maximum rise in the adjusted  $R^2$  value is added to the model at each subsequent step. This process is repeated until the adjusted  $R^2$  stops maximizing (Kabe 1963). The OLSRR package of R software was used for calibration in this study,

as it can perform the SLR algorithm to produce the final optimal set of independent variables that contained most of the information and build the significant fit model (Hebbali 2017). The performance of the developed model was evaluated using scatter plots between *in situ* SWQ observations and modeled data and adjusted coefficient of determination ( $R^2$ ) (Helland 1987).

For the validation of models, linear correlation, root mean square error (RMSE), and residual predictive deviation (RPD) were computed using the predicted variables and corresponding *in situ* SWQ observations. Linear correlation of predicted variables and associated *in situ* SWQ observations (25% of all SWQ observations) was tested using Pearson's correlation coefficient ( $r$ ). The ideal prediction model exhibits the lowest RMSE, calculated as the square root of the mean of the squared difference between predicted and *in situ* SWQ observed values (Equation (1)) (Aptula *et al.* 2005). The RPD values of the models were calculated using Equation (2) to account for the model's reliability, with excellent models having  $RPD > 2$ , fair models having  $1.4 < RPD < 2$ , and nonreliable models having  $RPD < 1.4$  (Ncama *et al.* 2017):

$$RMSE = \sqrt{\sum (y_{pred} - y_{obs})^2 / n} \quad (1)$$

$$RPD = \frac{RMSE}{SD} \quad (2)$$

Here,  $n$  is the number of SWQ observations,  $y_{obs}$  is the *in situ* SWQ observed values,  $y_{pred}$  is the model predicted value of SWQ parameters, and  $SD$  is the standard deviation of reference data values.

### Statistical Analysis of Predicted Data

The developed models were used to predict the SWQ parameter concentration from 1999 to 2020. The trend in the predicted data was estimated using the nonparametric Mann-Kendall (MK) test and the nonparametric Pettitt change point test (Singh and Chinnasamy 2021). Before using the trend test, the autocorrelation test was conducted to detect the temporal correlation of SWQ data to avoid false trend detection.

The MK test was employed to detect monotonic trends in SWQ data (Mann 1945). The MK test statistic for a time series is expressed by

$$S = \sum_{k=1}^{n-1} \sum_{j=k+1}^n \text{sgn}(x_j - x_k) \quad (3)$$

where  $\text{sgn}$  is the signum function,  $x$  is the variable,  $n$  denotes the number of data, and  $i, j, k$  are indices.

The Pettitt test is a nonparametric change point detection test that detects change points based on the abrupt change in the mean of the data (Pettitt 1979). The Pettitt test is based on the Mann-Whitney two-sample test (Mann and Whitney 1947). The Mann-Whitney test statistic is given by

$$D_{ij} = \text{sgn}(x_i - x_j) = \begin{cases} -1 & (x_i - x_j) < 0 \\ 0 & (x_i - x_j) = 0 \\ +1 & (x_i - x_j) > 0 \end{cases} \quad (4)$$

where  $x_i$  and  $x_j$  are random variables of the data set, with  $x_i$  following  $x_j$  in time, the test statistic is defined as  $U_{i,T}$ , as shown in

$$U_{i,T} = \sum_{t=1}^i \sum_{j=t+1}^T D_{ij} \quad (5)$$

The test statistic  $U_{i,T}$  is calculated for all random variables from 1 to  $T$ , where the largest value of  $|U_{i,T}|$  is taken as the change point. Thus, for the condition given by

$$K_i = \max_{1 \leq i \leq T} |U_{i,T}| \quad (6)$$

The test statistic  $K_i$ , if found significantly different from zero, is considered as a change point.

## Results and Discussion

### Descriptive Statistics of SWQ in Study Area

The descriptive statistics for the SWQ of Sursagar and Nalsarovar lakes are given in Tables 1 and 2, respectively.

As per CPCB (2019) standards, DO should be above 4 mg/L for propagation of wildlife, fisheries, and drinking water with conventional treatment, while it should be above 6 mg/L to be used for drinking water without conventional treatment, thus indicating that the DO quality in both study areas was not directly fit for human consumption and was close to support fish and wildlife. The CPCB had set a pH range of 6.5–8.5 for wildlife, fisheries, and domestic uses, as it is more neutral, and both study areas had satisfied this criterion. As per CPCB, the EC should not go beyond 2250  $\mu\text{mhos/cm}$ , and Tables 1 and 2 indicate that threshold was breached; however the average was below this limit, so the lake water was suitable for irrigation and industrial use. The BOD level is recommended by CPCB to be below 3 mg/L for all uses; however, statistics show that both study sites had elevated BOD levels above the limit. It was also noted that the nitrate levels in both study areas were well below the maximum limit of 20 mg/L as prescribed by CPCB for all uses.

### Correlation Analysis

The Pearson correlation analysis ( $p < 0.01$ ) for Sursagar lake showed that only EC and DO have significant correlation ( $-0.61$ ) with each other, while for all other SWQ parameters, the  $r$  value was close to 0. Thus, for the water quality analysis of Sursagar Lake, all the SWQ parameters need to be considered.

For Nalsarovar Lake, the Pearson correlation analysis ( $p < 0.01$ ) showed a strong correlation between BOD and pH (0.67) along with BOD and DO ( $-0.73$ ), while for other SWQ parameters, the  $r$  value was close to 0. Thus, the BOD of Nalsarovar Lake can be expressed using the pH and DO of the water body. However, as all other parameters are not correlated, all the parameters will be analyzed to comprehend the SWQ of Nalsarovar Lake.

The  $r$  values of SWQ parameters and their logarithms with individual SR and SR combinations were found to be weak to moderate (0.4–0.6). However, they were used as an initial step to create subsets of independent variables for the empirical modeling of SWQ parameters.

### Calibration and Validation of the SWQ Models

The empirical modeling through the SLR method showed that the Landsat 7 SR of bands blue (B1), green (B2), red (B3), near infrared (B4), shortwave infrared 1 (B5), thermal (B6), and shortwave infrared 2 (B7) have significantly contributed to the development of accurate models for estimating concentrations of SWQ parameters for Sursagar and Nalsarovar lakes. Furthermore, SR ratios effectively estimated SWQ parameter concentrations, as SR ratios can augment spectral contrast between discrete targets and remove most of the effect of brightness in the analysis of spectral differences (El Din and Zhang 2017).

The models developed by the SLR method to estimate DO, pH, EC, BOD, and nitrate concentration of Sursagar and Nalsarovar lakes with their adjusted  $R^2$  values are summarized in Tables 3 and 4, respectively. The SLR method resulted in significant models ( $p < 0.05$ ) to estimate SWQ parameters of Sursagar Lake with the adjusted  $R^2$  value  $>0.74$  and for Nalsarovar Lake with the adjusted  $R^2$  value  $>0.84$ .

To validate the accuracy of the SLR models, the derived SWQ parameter concentrations were compared with the *in situ* SWQ observations (2016–2019) of Sursagar and Nalsarovar lakes. The derived and observed values were compared using the  $r$ , RMSE, and RPD values, which are sufficient to validate the proposed models (Al-Shaibah *et al.* 2021; Ambrose-Igho *et al.* 2021) as explained in the section “Model Calibration and Validation.” The  $r$ , RMSE, and RPD values obtained by validating the developed models for Sursagar and Nalsarovar lakes are summarized in Tables 5 and 6, respectively. All models showed good to excellent performance based on the  $r$  value ( $p < 0.01$ ) ranging from 0.86 to 0.98 for Sursagar Lake and from 0.72 to 0.99 for Nalsarovar Lake. It is to be noted that the RMSE values of all models were less than 0.5 and that the RPD values were more than 2, which depicts good predictability of all the models. The model built to predict the nitrate concentration of Nalsarovar Lake has shown the best performance with  $r = 0.93$ , RMSE = 0.05 mg/L, and RPD = 10.21.

Table 1. Descriptive statistics of surface water quality parameters for Sursagar Lake for the period 2006–2019 (source: Gujarat Pollution Control Board).

Parameters	Mean	Standard Deviation	Standard Error	Minimum	Maximum
DO (mg/L)	3.45	2.15	0.61	1.2	8.1
pH	7.98	0.39	0.11	7.4	8.5
EC ( $\mu\text{mhos/cm}$ )	2017.08	730.97	202.74	775	2970.00
BOD (mg/L)	8.48	4.66	1.29	1.5	18
Nitrate (mg/L)	0.96	1.43	0.4	0.03	5.55

BOD = biochemical oxygen demand; DO = dissolved oxygen; EC = electrical conductivity; pH = potential of hydrogen.

Table 2. Descriptive statistics of surface water quality for the Nalsarovar Lake for the period 2006–2019 (source: Gujarat Pollution Control Board).

Parameters	Mean	Standard Deviation	Standard Error	Minimum	Maximum
DO (mg/L)	5.27	2.12	0.61	0	8.2
pH	7.63	0.26	0.07	7.3	8.2
EC ( $\mu\text{mhos/cm}$ )	1084.08	922	266.16	298	2806
BOD (mg/L)	3.66	3.5	1.01	1.5	14
Nitrate (mg/L)	0.63	1.62	0.47	0	5.71

BOD = biochemical oxygen demand; DO = dissolved oxygen; EC = electrical conductivity; pH = potential of hydrogen.

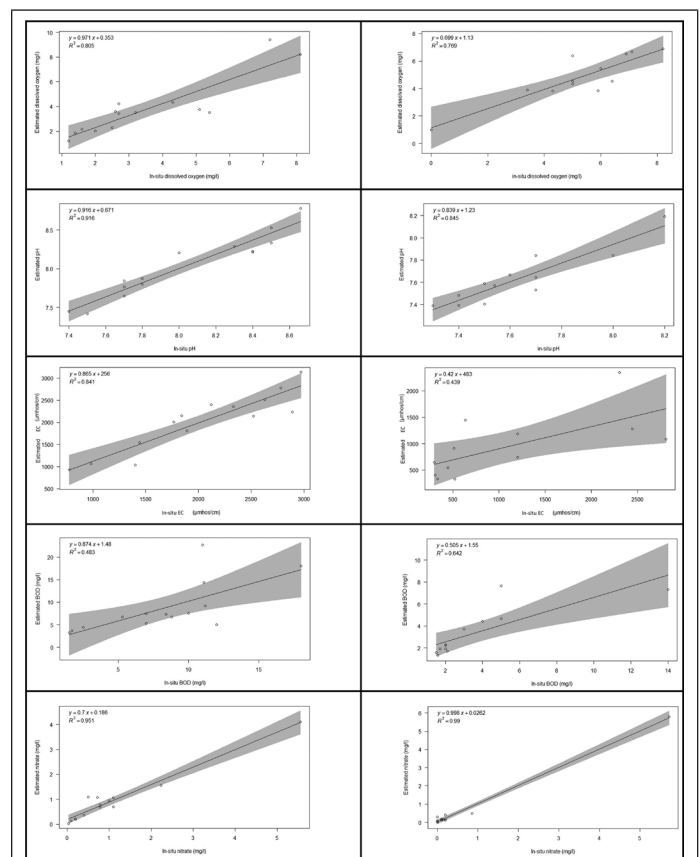


Figure 3. Scatter plots between the observed (*in situ*) and estimated surface water quality parameters of Sursagar Lake (left) and Nalsarovar Lake (right).

The performance of the models was further verified using the scatter plot between *in situ* SWQ parameter concentrations and corresponding estimated SWQ parameter concentrations, as shown in Figure 3. The



Table 3. Comparison of model performances for estimating surface water quality parameters of Sursagar Lake.

Linear Regression Model	Adjusted $R^2$
$\log_e(DO) = -20.02 + 852.2 \times B3(1 - 1.68 \times B3) + 0.38 \times \frac{B6}{B2} \left( 2.24 \times 10^{-4} \times \frac{B6}{B2} - 1 \right) + 0.29 \times \frac{B6}{B3} \left( 1 - 2.23 \times 10^{-4} \times \frac{B6}{B3} \right)$	0.78
$pH = 103.51 + 624.26 \times \frac{B5}{B1} \times \left( 0.42 \times \frac{B5}{B1} - 1 \right) + 447.91 \times \frac{B7}{B1} \times \left( 1 - 0.51 \times \frac{B7}{B1} \right) + 98.27 \times \frac{B4}{B5} \times \left( 1 - 0.42 \times \frac{B4}{B5} \right)$	0.84
$\log_e(EC) = -1.52 + 2591.4 \times B7(3.14 \times B7 - 1) + 79.60 \times B4(0.76 \times B4 - 1) + 2310.26 \times B5 \times (1 - 2.53 \times B5)$	0.74
$\log_e(BOD) = 374.2 + 0.11 \times \frac{B6}{B2} \left( 1 - 2.1 \times 10^{-4} \times \frac{B6}{B2} \right) + 18.73 \times \frac{B4}{B5} \left( 1 - 0.42 \times \frac{B4}{B5} \right) - 197.1 \times e^{B1}$	0.82
$\log_e(Nitrate) = -47.60 + 110.24 \times \frac{B7}{B1} \times \left( 1 - 0.43 \times \frac{B7}{B1} \right) + 5384.87 \times (B5 - B7) \times (1 - 13.14 \times (B5 - B7)) + 1378.54 \times B7(1 - 2.92 \times B7)$	0.86

BOD = biochemical oxygen demand; DO = dissolved oxygen; EC = electrical conductivity; pH = potential of hydrogen.

Table 4. Comparison of model performances for estimating surface water quality parameters of Nalsarovar Lake.

Linear Regression Model	Adjusted $R^2$
$\log_e(DO) = 732.6 + 4.90 \times B6(0.002 \times B6 - 1) + 422.7 \times (B2 - B7) \times (7.1 \times (B2 - B7) - 1) + 6.41 \times 10^{-3} \times \left( \frac{B6}{B4} \right) \times \left( 1 - 2 \times 10^{-4} \times \left( \frac{B6}{B4} \right) \right)$	0.86
$pH = 9.39 - 4.92 \times 10^{-130} \times e^{B6} \left( 2.24 \times 10^{-131} - 1 \right) + 3.80 \times \frac{B2}{B7} \times \left( 1 - 0.09 \times \frac{B2}{B7} \right) + 4.89 \times \frac{B4}{B7} \times \left( 0.1 \times \frac{B4}{B7} - 1 \right)$	0.90
$\log_e(EC) = -4.53 + 2.44 \times 10^5 \times \frac{B1}{B6} \left( 1 - 801 \times \frac{B1}{B6} \right) + 846.3 \times B2 \times (1 + 2.74 \times B2) + 157.9 \times B7$	0.84
$\log_e(BOD) = -141.94 + 6.13 \times (B2 + B5) \times (1 + 4.08 \times (B2 + B5)) + 238.88 \times \frac{B2}{B3} \times \left( 1 - 0.39 \times \frac{B2}{B3} \right) - 5.85 \times \frac{B3}{B5}$	0.95
$Nitrate = 16.74 + 506.8 \times B1(3.82 \times B1 - 1) + 531.3 \times B2(1 - 4 \times B2) - 5.31 \times 10^{-2} \times B6$	0.98

BOD = biochemical oxygen demand; DO = dissolved oxygen; EC = electrical conductivity; pH = potential of hydrogen.

Table 5. Validation results of linear regression models of surface water quality (SWQ) parameters of Sursagar Lake.

SWQ Parameter	Pearson Correlation Coefficient ( $r$ )	Root Mean Square Error	Residual Predictive Deviation
DO (mg/L)	0.98	0.29	2.1
pH	0.88	0.14	2.43
EC ( $\mu$ mhos/cm)	0.94	0.18	3.37
BOD (mg/L)	0.86	0.47	2
Nitrate (mg/L)	0.97	0.23	3.47

BOD = biochemical oxygen demand; DO = dissolved oxygen; EC = electrical conductivity; pH = potential of hydrogen.

linear regression line between the *in situ* and estimated SWQ parameter concentrations of Sursagar and Nalsarovar lakes was found satisfactory for all models with  $R^2$  value ranging from 0.44 to 0.99.

The  $r$ , RMSE, RPD, and  $R^2$  of the scatter plot of the models depict that the SLR models are capable of retrieving and predicting the SWQ parameter concentrations in Sursagar and Nalsarovar lakes for the same parameters in different months and years, which is a significant contribution of this study. The results of model calibration and validation suggest that water quality can be successfully derived through remote sensing and GIS data. Moreover, the capability of remote sensing to capture direct and indirect measurements provides critical data for water resources management and planning (Kamruzzaman *et al.* 2020; Shao *et al.* 2020).

The SLR analysis showed that for Sursagar Lake, pH, EC, and nitrate are dependent on SR of B1, B4, B5, B7, and their combinations, while DO is sensitive to SR of B2, B3, B6, and their ratios, and BOD is dependent on SR of B1, B2, B4, B5, B6, and their ratios. For Nalsarovar

Table 6. Validation results of linear regression models of surface water quality (SWQ) parameters of Nalsarovar Lake.

SWQ Parameter	Pearson Correlation Coefficient ( $r$ )	Root Mean Square Error	Residual Predictive Deviation
DO (mg/L)	0.99	0.11	2
pH	0.72	0.14	2.65
EC ( $\mu$ mhos/cm)	0.93	0.44	2.56
BOD (mg/L)	0.94	0.26	2.42
Nitrate (mg/L)	0.93	0.05	10.21

BOD = biochemical oxygen demand; DO = dissolved oxygen; EC = electrical conductivity; pH = potential of hydrogen.

Lake, DO and pH are dependent on SR of B2, B4, B6, B7, and their combinations, while EC and nitrate are dependent on SR of B1, B2, B6, B7, and their combinations, and BOD is sensitive to SR of B2, B3, B5, and their combinations. The seven bands of *Landsat 7* contributed to the generation of water quality models. However, the models developed in this study differ from reported models in the literature (El Din and Zhang 2017; González-Márquez *et al.* 2018; Zhang *et al.* 2017), showing the need for exclusive parameterization and calibration for individual water bodies.

The application of remote sensing and GIS is a suitable approach for monitoring time-varying phenomena, thus providing opportunities to retrieve and predict the data to achieve a robust understanding of the ecosystem.

#### Prediction of Past and Missing SWQ Data for Detailed Analysis

Compared to the conventional SWQ measurement techniques, one of the benefits of empirical modeling using remote sensing data is that we can use them to generate the SWQ data for any required period (as per the availability of the remote sensing data) for detailed water quality

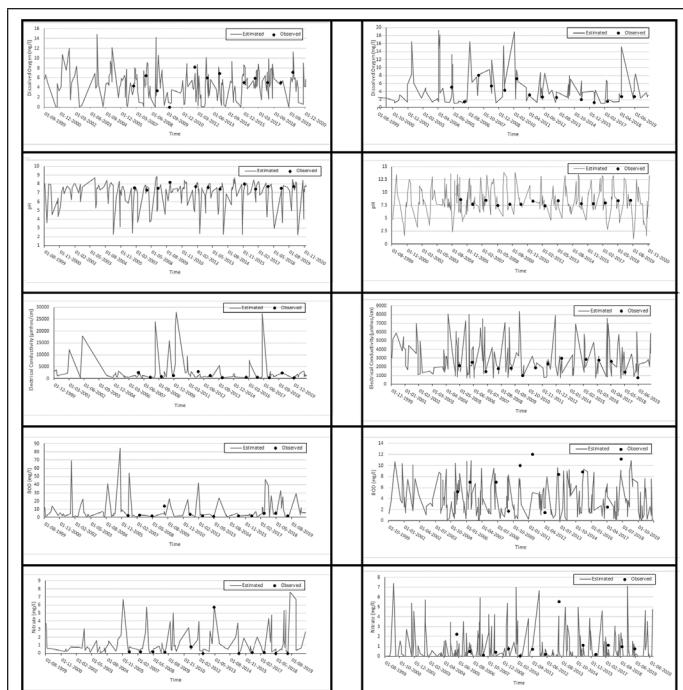


Figure 4. Observed (in situ) and estimated surface water quality parameters of Sursagar Lake (left) and Nalsarovar Lake (right) from 1999 to 2020.

analysis. Accordingly, the *Landsat 7* SR from 1999 to 2020 were used to obtain the corresponding SWQ parameter concentrations of Sursagar and Nalsarovar lakes (Figure 4) using the developed and validated models (Tables 3 and 4).

The DO of Sursagar Lake from 1999 to 2020 was found to be varying from 1.01 mg/L to 19.24 mg/L. The minimum DO level was observed during the winter season with an average value of 2.65 mg/L, and the maximum level was observed during the monsoon season with an average value of 8.85 mg/L. As the main cause of pollution in Sursagar Lake is industrial effluent and sewage, it is plausible that dilution of pollutants during the monsoon season led to a rise in DO level, while the BOD level was found to be low during the monsoon season with an average value of 0.44 mg/L. The high DO level during the monsoon season explains the corresponding low BOD levels in Sursagar Lake (Kumari and Sharma 2019). The nitrate level of Sursagar Lake was found to vary from  $6 \times 10^{-4}$  mg/L to 7.39 mg/L, and the minimum nitrate level was observed during the monsoon season with an average value of 0.31 mg/L, which can be explained by the dilution of pollutants due to heavy rainfall (Roy and Majumder 2019). The dilution during the monsoon season also explains the low EC level of Sursagar Lake. The pH of Sursagar Lake was found to be at a minimum during the monsoon season with an average value of 4.4 and maximum during the winter season with an average value of 11.23.

For Nalsarovar Lake, the DO (1999–2020) was found to vary from  $6 \times 10^{-4}$  mg/L to 14.87 mg/L, and the minimum DO level was observed during the monsoon season with an average value of 0.01 mg/L from 1999 to 2020, and the maximum DO level was observed during the winter season with an average value of 6.61 mg/L. As per Atulkumar (2020), the agricultural runoff received by the lake during the monsoon season will increase the nutrient loading and subsequently reduce the DO level, which was also noted in this study. The BOD level was found to be maximum during the monsoon season with an average value of 46.50 mg/L. The high BOD level is usually associated with low DO levels (Kumari and Sharma 2019), which justifies the high BOD level during the monsoon season in Nalsarovar Lake. The nitrate level of Nalsarovar Lake was found to vary from  $3 \times 10^{-3}$  mg/L to 7.61 mg/L, and the maximum level was observed during the monsoon season with an average value of 3.75 mg/L. Low DO, high BOD, and high nitrate concentration

indicate the eutrophic status of the lake (Kumari and Sharma 2019). The rise in agricultural runoff associated with sediment load during the monsoon season indicates the rise in the EC level of Nalsarovar Lake during the monsoon season (Vankar *et al.* 2018). The pH of the lake was found to vary from 2.2 to 8.8. The average pH during the summer season was 5.90, and during the winter season, it was 7.30, which is in close proximity of the observations of Vankar *et al.* (2018).

The coherence between the predicted SWQ parameter concentrations from 1999 to 2020 (Figure 4) and lake characteristics depicts the efficacy of the proposed models in this study to capture the lake water quality and its seasonal variations. The peaks and troughs observed in Figure 4 depict the SWQ parameter changes with seasons and climate variability, which can aid in better management.

Results indicated that the SWQ parameters of Sursagar and Nalsarovar lakes have diverse seasonal patterns. SLR models built using *Landsat 7* images could include these variations and effectively predict the parameter concentrations (Figure 4). Thus, remote sensing and GIS capabilities can provide time-stamped and geo-tagged data that can depict trends and anomalies in the concentration of key indicators of SWQ to predict future water quality outbreaks efficiently when *in situ* data are limited.

Change points and trends of predicted SWQ parameters were estimated to analyze the annual variations. The MK test and the Pettitt change point test were used to determine the trends of the SWQ distribution and the possible locations of the change points. The MK test results ( $p < 0.05$ ) and the Pettitt change point test results ( $p < 0.05$ ) of SWQ distribution (1999–2020) are summarized in Table 7 for Sursagar and Nalsarovar lakes.

Table 7. Trends and change points of annual surface water quality (SWQ) distribution of Sursagar Lake and Nalsarovar Lake.

SWQ Parameter	Sursagar Lake		Nalsarovar Lake	
	Trend (Mann-Kendall Test)	Change Point (Pettitt Test)	Trend (Mann-Kendall Test)	Change Point (Pettitt Test)
DO	Upward	2001	Upward	2015
pH	Downward	2002	Upward	2000
EC	Downward	2001	Downward	2011
BOD	Downward	2014	Upward	2016
Nitrate	Upward	2006	Upward	2008

BOD = biochemical oxygen demand; DO = dissolved oxygen; EC = electrical conductivity; pH = potential of hydrogen.

The MK test showed that the DO and nitrate concentrations of Sursagar Lake rose from 1999 to 2020, while pH, EC, and BOD concentration presented a falling trend. For Nalsarovar Lake, except for EC, all other parameters showed a rising trend. The Pettitt test for Sursagar Lake showed that DO and EC have a common change point (2001), close to that of pH (2002). The change point of BOD was 2014, and for nitrate, it was 2006. For Nalsarovar Lake, the change points of DO and BOD were located close to each other, at 2015 and 2016, respectively, while the change points for pH, EC, and nitrate were 2000, 2011, and 2008.

The derived change points (Table 7) have divided the SWQ parameter concentrations time series into two sections. The linear regression was employed to analyze two sections (before change point and after change point) of the time series, as shown in Figure 4. For Sursagar Lake, the overall trend of DO is upward, but the regression line of the section after the change point (2001) has a downward trend with a slope of 0.144 mg/L/yr; thus, after 2001, the DO level has been reduced in the Sursagar Lake. The overall trend of pH level in Sursagar Lake was downward, and a similar trend was found in the two sections; also, the slope of the regression line in the second section (after change point) is higher than in the first section (before change point). The overall trend of EC level in Sursagar Lake is downward; however, the two sections show an upward trend, so we can say that the EC level has increased from 2002 to 2020, but the extent is lesser than that of the



first section (1999–2001). The overall trend of BOD is downward, and a similar trend was observed in the first section of distribution, but in the second section, a slight rise (0.013 mg/L/yr) has been observed. The overall trend of nitrate in Sursagar Lake is upward. However, both sections depict a downward trend. Thus, we can say that the nitrate level has increased from 1999 to 2020, but from 2006 to 2020, it is decreasing. Thus, we can say that the quality of Sursagar Lake is recovering, except that DO all other parameters depict improvement in the water quality of the lake.

For Nalsarovar Lake, the overall DO trend was upward, but the two sections show a downward trend. Thus, the DO level has increased from 1999 to 2020; however, it is decreasing from 2016 to 2020 with a slight amount of 0.04 mg/L/yr. Likewise, the overall trend of pH and BOD level in Nalsarovar Lake was upward, and the two sections show a downward trend, which depicts that the pH and BOD levels are dropping in the second section. The overall trend of EC level in Nalsarovar Lake is downward, but the two sections show an upward trend, so the EC level has increased from 2013 to 2020, but the extent is lesser than that of the first section (1999–2012). The overall trend of nitrate in Nalsarovar Lake is upward, and a similar trend was found after the change point (2008), and the nitrate level is rising in Nalsarovar Lake. Thus, we can say that the quality of Nalsarovar Lake is recovering; however, nitrate concentration needs to be managed. The higher concentration of nitrate observed in Nalsarovar Lake is due to the agricultural runoff from surrounding villages (Vankar *et al.* 2018). Sursagar and Nalsarovar lakes hold ecological and agricultural significance, and long-term water quality analysis of these lakes is needed for their conservation. Thus, this study has put forward a methodology to estimate the past and real-time SWQ parameter concentration values using the site-specific empirical models.

## Conclusions

Inland water quality is an important factor and needs to be monitored periodically for better management and to support domestic and agricultural consumption. Since depending only on *in situ* measurements can be costly and time consuming, this study used *in situ* data and remote sensing data-driven SLR models to predict water quality parameters (DO, pH, EC, BOD and nitrate) for two lakes in Gujarat—Sursagar and Nalsarovar—from 1999 to 2020. The models developed using the SLR method have shown good to excellent performance in predicting SWQ parameter concentrations based on the *r* value ( $p < 0.01$ ) ranging from 0.86 to 0.98 for Sursagar Lake and from 0.72 to 0.99 for Nalsarovar Lake. The RMSE values of all models were less than 0.5, and the RPD values were more than 2, which depicts good predictability of all the models. Results indicated that the SLR models had good potential for predicting the water quality parameters and improve the temporal resolution from annual (*in situ* based) to biweekly. The availability of such an improved spatiotemporal resolution will aid in a better understanding of inter- and intraseasonal variability and in documenting potential drivers for such variability. Policymakers and stakeholders should incorporate such synergized models with ongoing field monitoring activities to better protect and manage the precious inland waters of India.

## Acknowledgments

The authors are thankful to the Gujarat Pollution Control Board and the Central Pollution Control Board for providing the SWQ data of Nalsarovar and Sursagar lakes. This work was partially supported by the Programmatic Cooperation between the Directorate-General for International Cooperation (DGIS) of the Dutch Ministry of Foreign Affairs and IHE Delft in the period 2016–2023, also called DUPC2 [DUPC2]; and by the United Nations Educational, Scientific and Cultural Organization – Institute for Water Education (IHE Delft) [2019/089/108483/EWH (GRACERS project)].

## References

- Al-Shaibah, B., X. Liu, J. Zhang, Z. Tong, M. Zhang, A. El-Zeiny, C. Faichia, M. Hussain, and M. Tayyab. 2021. Modeling water quality parameters using landsat multispectral images: A case study of Erlong Lake, northeast China. *Remote Sensing* 13(9):1603.
- Ambrose-Igho, G., W. M. Seyoum, W. L. Perry, and C. M. O'Reilly. 2021. Spatiotemporal analysis of water quality indicators in small lakes using Sentinel-2 satellite data: Lake Bloomington and Evergreen Lake, central Illinois, USA. *Environmental Processes* 8(2):637–660.
- Aptula, A. O., N. G. Jeliaskova, T. W. Schultz, and M. T. Cronin. 2005. The better predictive model: High  $q^2$  for the training set or low root mean square error of prediction for the test set? *QSAR and Combinatorial Science* 24(3):385–396.
- Atulkumar, T. M. 2020. *Assessment of Nutrient Dynamics and Physico-Chemical Status of Freshwater Reservoirs of Vadodara District, Gujarat, India*. Doctoral dissertation, Maharaja Sayajirao University of Baroda.
- Biswas, C. and C. N. Pandey. 2019. Assessing climate change vulnerability: A case study of Nalsarovar Lake, Gujarat. *International Journal of Disaster Recovery and Business Continuity* 10:1–12.
- Borowiak, M., D. Borowiak, and K. Nowinski. 2020. Spatial differentiation and multiannual dynamics of water conductivity in lakes of the Suwałki Landscape Park. *Water* 12(5):1277.
- Brahmbhatt, R. J. and G. Shah. 2018. critical study of infrastructure facilities in walled city area for smart city Vadodara. *Journal of Emerging Technologies and Innovative Research* 5:395–400.
- Central Pollution Control Board (CPCB). 2019. Water Quality Criteria. <<https://cpcb.nic.in/water-quality-criteria>> Accessed 13 June 2021.
- Chauhan, K., J. Patel, S. H. Shukla, and M. H. Kalubarme. 2021. Monitoring water spread and aquatic vegetation using spectral indices in Nalsarovar, Gujarat State-India. *International Journal of Environment and Geoinformatics* 8(1):49–56.
- Chinnasamy, P., Maske, A.B., Honap, V., Chaudhary, S. and Agoramoorthy, G., 2021, May. Sustainable development of water resources in marginalised semi-arid regions of India: Case study of Dahod in Gujarat, India. *Natural Resources Forum* 45(2): 105–119
- Chinnasamy, P. and Parikh, A., 2021. Remote sensing-based assessment of Coastal Regulation Zones in India: a case study of Mumbai, India. *Environment, Development and Sustainability* 23(5) : 7931–7950.
- Doña, C., J. M. Sánchez, V. Caselles, J. A. Domínguez, and A. Camacho. 2014. Empirical relationships for monitoring water quality of lakes and reservoirs through multispectral images. *IEEE Journal of Selected Topics in Applied Earth Observations and Remote Sensing* 7(5):1632–1641.
- El Din, E. S. and Y. Zhang. 2017. Estimation of both optical and nonoptical surface water quality parameters using Landsat 8 OLI imagery and statistical techniques. *Journal of Applied Remote Sensing* 11(4):046008.
- Gholizadeh, M. H., A. M. Melesse, and L. Reddi. 2016. A comprehensive review on water quality parameters estimation using remote sensing techniques. *Sensors* 16(8):1298.
- Goel, P. K. 2006. *Water Pollution: Causes, Effects and Control*. New Delhi: New Age International.
- González-Márquez, L. C., F. M. Torres-Bejarano, C. Rodríguez-Cuevas, A. C. Torregroza-Espinosa, and J. A. Sandoval-Romero. 2018. Estimation of water quality parameters using Landsat 8 images: Application to Playa Colorada Bay, Sinaloa, Mexico. *Applied Geomatics* 10(2):147–158.
- Guhathakurta, P., N. Kulkarni, P. Menon, A. K. Prasad, S. T. Sable, and S. C. Advani. 2020. *Observed Rainfall Variability and Changes over Gujarat State (ESSO/IMD/HS/Rainfall Variability/08(2020)/32)*. New Delhi: Climate Research Division, India Meteorological Department.
- Gujarat Ecology Commission (GEC). 2017. State of Environment Report Gujarat 2017. <<http://gujenvs.nic.in/PDF/soer-2017.pdf>> Accessed 15 June 2021.
- Gujarat Environment Management Institute (GEMI). 2020. *A Report on Environmental Monitoring for major lakes of Gujarat. Forests & Environment Department*. Gandhinagar: Government of Gujarat. <<https://gemi.gujarat.gov.in/uploads/Assets/career/serbadvotismen02192020010830295.pdf>> Accessed 15 June 2021.
- Hebbali, A. 2017. Tools for building OLS regression models [R] package OLSRRolsrr version 0.5. 1]. *Comprehensive R Archive Network (CRAN)*.
- Helland, I. S. 1987. On the interpretation and use of  $R^2$  in regression analysis. *Biometrics*: 61–69.

- Hirani, P. and Dimble, V. 2019. Water Pollution Is Killing Millions of Indians. Here's How Technology and Reliable Data Can Change That.
- Huq, M. E., S. Fahad, Z. Shao, M. S. Sarven, I. A. Khan, M. Alam, M. Saeed, H. Ullah, M. Adnan, S. Saud, and Q. Cheng. 2020. Arsenic in a groundwater environment in Bangladesh: Occurrence and mobilization. *Journal of Environmental Management* 262:110318.
- Japan International Cooperation Agency and Nippon Koei India Pvt Ltd. 2020. *The Preparatory Survey on Project for Ecosystem Restoration in Gujarat in India*. Gandhinagar: Gujarat Forest Department. <<https://openjicareport.jica.go.jp/pdf/1000042362.pdf>> Accessed 11 June 2021.
- Kabe, D. G. 1963. Stepwise multivariate linear regression. *Journal of the American Statistical Association* 58(303):770–773.
- Kamruzzaman, M. M., S. A. Alanazi, M. Alruwaili, N. Alshammari, M. H. Siddiqi, and M. E. Huq. 2020. Water resource evaluation and identifying groundwater potential zones in arid area using remote sensing and geographic information system. *Journal of Computer Science* 16(3):266–279.
- Khattab, M. F. and B. J. Merkel. 2014. Application of Landsat 5 and Landsat 7 images data for water quality mapping in Mosul Dam Lake, northern Iraq. *Arabian Journal of Geosciences* 7(9):3557–3573.
- Kumar, S. H., M. Meena, and K. Verma. 2017. Water pollution in India: Its impact on the human health: Causes and remedies. *International Journal of Applied Environmental Sciences* 12(2):275–279.
- Kumari, R. and R. C. Sharma. 2019. Assessment of water quality index and multivariate analysis of high altitude sacred Lake Prashar, Himachal Pradesh, India. *International Journal of Environmental Science and Technology* 16(10):6125–6134.
- Kumari, S., J. A. Khan, and M. S. Lal Thakur. 2019. Study of physicochemical characteristics of water and soil in relations to fish production in Motia Lake Reservoir. *Journal of Atmospheric Earth Sciences* 2:006.
- Langa, M. 2021. Gujarat Rivers Remain Highly Polluted Despite Norms. <<https://www.thehindu.com/news/national/other-states/gujarat-rivers-remain-highly-polluted-despite-norms/article33589234.ece>> Accessed 15 June 2021.
- Loveland, T. R. and J. L. Dwyer. 2012. Landsat: Building a strong future. *Remote Sensing of Environment* 122:22–29.
- Mann, H. B. 1945. Nonparametric tests against trend. *Econometrica* XX:245–259.
- Mann, H. B. and D. R. Whitney. 1947. On a test of whether one of two random variables is stochastically larger than the other. *Annals of Mathematical Statistics* XX:50–60.
- Mushtaq, F. and M. G. Nee Lala. 2017. Remote estimation of water quality parameters of Himalayan lake (Kashmir) using Landsat 8 OLI imagery. *Geocarto International* 32(3):274–285.
- Ncama, K., U. L. Opara, S. Z. Tesfay, O. A. Fawole, and L. S. Magwaza. 2017. Application of Vis/NIR spectroscopy for predicting sweetness and flavour parameters of “Valencia” orange (*Citrus sinensis*) and “Star Ruby” grapefruit (*Citrus x paradisi* Macfad). *Journal of Food Engineering* 193:86–94.
- Pant, R. R., K. B. Pal, N. L. Adhikari, S. Adhikari, and A. D. Mishra. 2019. Water quality assessment of Begnas and Rupa Lakes, Lesser Himalaya Pokhara, Nepal. *Journal of the Institute of Engineering* 15(2):113–122.
- Patel, K. P. and M. Shah. 2016. Experimental study on the water quality of Sursagar Lake. *International Journal of Advance Research in Science and Engineering* 5:188–193.
- Pearson, K. 1909. Determination of the coefficient of correlation. *Science* 30(757):23–25.
- Pettitt, A. N. 1979. A non-parametric approach to the change-point problem. *Journal of the Royal Statistical Society: Series C (Applied Statistics)* 28(2):126–135.
- Rathod, D. M. and B. M. Parasharya. 2018. Odonate diversity of Nalsarovar Bird Sanctuary—A Ramsar site in Gujarat, India. *Journal of Threatened Taxa* 10(8):12117–12122.
- Roy, R. and M. Majumder. 2019. Assessment of water quality trends in Loktak Lake, Manipur, India. *Environmental Earth Sciences* 78(13):1–12.
- Sagan, V., K. T. Peterson, M. Maimaitijiang, P. Sidike, J. Sloan, B. A. Greeling, S. Maalouf, and C. Adams. 2020. Monitoring inland water quality using remote sensing: Potential and limitations of spectral indices, bio-optical simulations, machine learning, and cloud computing. *Earth-Science Reviews* 205:103187.
- Sengupta, S. 2018. Polluted Surface and Groundwater Could Cause a Cape Town-Like Situation. <<https://www.downtoearth.org.in/news/water/polluted-surface-and-groundwater-could-cause-a-cape-town-like-situation-62365>> Accessed 15 June 2021.
- Shao, Z., M. E. Huq, B. Cai, O. Altan, and Y. Li. 2020. Integrated remote sensing and GIS approach using Fuzzy-AHP to delineate and identify groundwater potential zones in semi-arid Shanxi Province, China. *Environmental Modelling and Software* 134:104868.
- Singh, N. and Chinnasamy, P., 2021. Non-stationary flood frequency analysis and attribution of streamflow series: a case study of Periyar River, India. *Hydrological Sciences Journal* 66(13): 1866-1881.
- Sudarshan, P., M. K. Mahesh, and T. V. Ramachandra. 2019. Assessment of seasonal variation in water quality and water quality index (WQI) of Hebbal Lake, Bangalore, India. *Environment and Ecology* 37(1B):309–317.
- Swain, R. and B. Sahoo. 2017. Improving river water quality monitoring using satellite data products and a genetic algorithm processing approach. *Sustainability of Water Quality and Ecology* 9:88–114.
- The Times of India. 2017. VMC Adopts New Tech to Clean Up Sursagar Lake. <<https://timesofindia.indiatimes.com/city/vadodara/vmc-adopts-new-tech-to-clean-up-sursagar-lake/articleshow/58743314.cms>> Accessed 13 June 2021.
- Topp, S. N., T. M. Pavelsky, D. Jensen, M. Simard, and M. R. Ross. 2020. Research trends in the use of remote sensing for inland water quality science: Moving towards multidisciplinary applications. *Water* 12(1):169.
- UN Water. 2020. *World Water Development Report: Water and Climate Change*. Paris: UNESCO World Water Assessment Programme.
- Vankar, J., K. Tatu, R. D. Kamboj, L. Christian, and R. Gupta. 2018. Assessment of surface water quality in different habitats of Nal Sarovar Bird Sanctuary Ramsar site, Gujarat, India. *Research and Reviews: Journals of Ecology* 7:29–40.
- Vasistha, P., and R. Ganguly. 2020. Water quality assessment of natural lakes and its importance: An overview. *Materials Today: Proceedings* 32:544–552.
- Zhang, Y., X. Huang, W. Yin, and D. Zhu. 2017. Multitemporal landsat image based water quality analyses of Danjiangkou Reservoir. *Photogrammetric Engineering and Remote Sensing* 83(9):643–652.
- Zhu, Z., S. Wang, and C. E. Woodcock. 2015. Improvement and expansion of the Fmask algorithm: Cloud, cloud shadow, and snow detection for Landsats 4–7, 8, and Sentinel 2 images. *Remote Sensing of Environment* 159:269–277.



## Modelling, Representation, and Visualization of the Remote Sensing Data for Forestry Management

Remote sensing data includes aerial photography, videography data, multispectral scanner (MSS), Radar, and laser to map and understand various forest cover types and features. An accurate digital model of a selected forest type is developed using forest inventory data in educational and experimental forestry and extensive databases. It includes the formalization and compilation of methods for integrating forest inventory databases and remote sensing data with three-dimensional models for a dynamic display of forest changes.

Big data technology employs vast amounts of forestry data for forestry applications that require real-time inquiry and calculation. The techniques and strategies of forestry data analysis are integrated into the big data forestry framework, enabling interfaces that other Programmes may call. Virtual Reality addresses constraints in forest management such as temporal dependence, irreversibility of decisions, spatial-quantitative change of characteristics, and numerous objectives. Virtual representations integrate various computer graphics systems with display and interface devices to create a spatial presence in an interactive 3 D environment. Visualization of plant species' growth patterns, changes in species and their composition, and other morphological properties of forests are enhanced using machine learning and regression analysis methods as part of a digital model. In modelling, deep learning (DL) replicates expert observations on hundreds or thousands of hectares of trees.

Remote sensing is being used to map the distribution of forest resources, global changes in flora with the seasonal variations, and the 3D structure of forests. Graphic Information System (GIS) based visualizations depict dynamics through animations and 3D geo model visualizations and allow advanced spatial analytics and modelling in geographical phenomena for forest management. Digital forest modelling includes integrating forest inventory data, forest inventory database formation, graphics objects of forest inventory allocations with a digital forest model, and technology for visualizing forest inventory data. It helps forecast changes and visualizes situational phenomena occurring in forests using data and models involving spatial-temporal linkages.

Standard aerial shots capture images that view unseen components to the naked eye, such as the Earth's surface's physical structure and chemical composition. The challenges in remote sensing models include insufficient Remote Sensing (RS), spatial, spectral, and temporal resolution to detect degradation accurately. High costs of RS, the gap between operational and scientific uses, and lack of information sharing are some of the challenges of RS for forest management. The list of topics of interest include but are not limited to the following:

- Advancement of forest surveillance through Geographical Information Systems
- State of the art and perspectives of modelling and visualization framework for Forest type mapping and assessment of distribution
- Futuristic Satellite data analysis for stock maps and forest inventory analysis
- Big data-enabled GIS framework for forest management information
- AI-based Space Remote Sensing For Forest Ecosystem Assessment
- Enhanced visualization through deep learning for forest management solutions
- Novel approaches of multi-temporal satellite data using digital image analysis for forest management
- Advance representation of discrete objects and continuous fields in virtual environments through VR framework
- Database framework for regional and plot-based forest allotment data for model representation and visualization
- Development of scalable models for area-based metrics from Light Detection and Ranging (lidar) devices and photographic structure-for-motion (SFM)

**Deadline for Manuscript Submission—June 7, 2022**

**Submit your Manuscript to <http://asprs-pers.edmgr.com>**

### Guest Editors

**Dr. Gai-Ge Wang**, [gai-gewang@outlook.com](mailto:gai-gewang@outlook.com) and [wgg@ouc.edu.cn](mailto:wgg@ouc.edu.cn), *Department of Computer Science and Technology, Ocean University of China, China*

**Dr. Xiao-Zhi Gao**, [xiao.z.gao@gmail.com](mailto:xiao.z.gao@gmail.com) and [xiao-zhi.gao@uef.fi](mailto:xiao-zhi.gao@uef.fi), *Machine Vision and Pattern Recognition Laboratory, School of Engineering Science, Lappeenranta University of Technology, Finland.*

**Dr. Yan Pei**, [peiyan@u-aizu.ac.jp](mailto:peiyan@u-aizu.ac.jp), *Computer Science Division, The University of Aizu, Japan.*

# Automated 3D Reconstruction of LoD2 and LoD1 Models for All 10 Million Buildings of the Netherlands

Ravi Peters, Balázs Dukai, Stelios Vitalis, Jordi van Liempt, and Jantien Stoter

## Abstract

*In this paper, we present our workflow to automatically reconstruct three-dimensional (3D) building models based on two-dimensional building polygons and a lidar point cloud. The workflow generates models at different levels of detail (LoDs) to support data requirements of different applications from one consistent source. Specific attention has been paid to make the workflow robust to quickly run a new iteration in case of improvements in an algorithm or in case new input data become available. The quality of the reconstructed data highly depends on the quality of the input data and is monitored in several steps of the process. A 3D viewer has been developed to view and download the openly available 3D data at different LoDs in different formats. The workflow has been applied to all 10 million buildings of the Netherlands. The 3D service will be updated after new input data becomes available.*

## Introduction

Three-dimensional (3D) city models are widely used in urban applications. The outcomes of such applications serve as input for planning and decision-making processes that aim at making cities cooler, sustainable, more accessible, greener, carbon dioxide-neutral, etc. (Biljecki *et al.* 2016; Deren *et al.* 2021). Models of buildings are prominent objects in these models. The building models can be generated at different levels of detail (LoDs). Taking the terminology of CityGML, a building can be modeled at four main levels of detail for the outer shell of the building, i.e., LoD0, LoD1, LoD2, and LoD3, and at LoD4 for the interior of the building (OGC 2012; Kutzner *et al.* 2020). Each of these four CityGML LoDs can be further refined (Biljecki *et al.* 2016; Sun *et al.* 2019).

A higher level of detail is often preferred over a lower one, since building models at higher LoDs look closer to reality. However, higher levels of detail are more complicated (and therefore more expensive) to acquire because it is harder to reconstruct them in an automated manner from available source data. In addition, using models at higher levels of detail in spatial analysis does not automatically lead to better results (Biljecki *et al.* 2018), while at the same time too much detail may have a negative impact on performance. Therefore, for some applications it is better to avoid too much irrelevant detail.

The LoD of a 3D city model is therefore driven by the specific data requirements of the urban application for which it is built (see also the section “LoD in Relation to Urban Applications”). However, the highest achievable LoD is also restricted by the available source data and the reconstruction method used (see also the section “LoD in Relation to Reconstruction Method”).

While many 3D city models exist for various parts of the Netherlands, they are often generated for relatively small areas, are using different reconstruction methods, and are based on different source

data. Furthermore, the update cycles are different, and the level of detail is also different because it is collected for different applications.

This can result in inconsistencies between 3D city models of the same area. There may be discrepancies between the geometries of building models like the geometry or height of the footprint. Also, the reference heights for the same building might differ over data sets since the heights may represent different references (e.g., gutter, ridge, maximum) or the reference heights are based on different statistical calculations. In addition, buildings (or building parts) available in one data set might be missing in another data set. There may also be temporal differences because the input data sets that were used for the reconstruction come from another date. Typically, there is no plan to maintain and update the once generated 3D data. This may be another source for indiscrepancies.

All these differences have profound influences in practice, such as affecting the applications for which an existing 3D model can be used, the processing that is necessary to use it, and the likely errors that will be present in the end result.

In this research, we demonstrate how to create a consistent country-wide 3D city model in LoD1.2, LoD1.3, and LoD2.2. In order to achieve this, we look at three main aspects.

First, to ensure consistency between 3D city models of the same area and different LoDs, to improve efficiency, and serve the 3D data needs of different urban applications, we investigate how to reconstruct building models for large areas at different LoDs in one reconstruction process, based on the same reconstruction principles and based on the same source data. For the block models, we provide the user with several reference heights, so that the user can select the appropriate reference height to extrude building blocks for the specific application.

Second, our objective is to develop a fully automated reconstruction method. Our focus is on 3D city models covering large areas to support countrywide urban applications. This requires a fully automated reconstruction method. Automated reconstruction also enables standardization of the output data resulting in consistent geometries, semantics, and temporal aspects of the data. This consistency is also ensured when new models are reconstructed in the future with the same automated procedure based on updated source data.

Third, we investigate how to monitor and assess the quality of the building models that are automatically generated on such a large scale. This is essential for users to assess if models are fit for a specific use.

Finally, we also investigate the visualization and dissemination of such a big data set so that the city model is accessible and usable in an efficient manner.

## Structure of this Paper

In this paper, we present our methodology to reconstruct LoD1.2, LoD1.3, and LoD2.2 models of all buildings in the Netherlands in one process. The section “Scope of the Research and Previous

---

3D Geoinformation group, Delft University of Technology, Faculty of Architecture and the Built Environment, Department of Urbanism, Julianalaan 134, Delft 2628BL, The Netherlands (j.e.stoter@tudelft.nl).

Contributed by Zhenfeng Shao, June 7, 2021 (sent for review September 9, 2021; reviewed by Nan Yang, Hongping Zhang).

---

Photogrammetric Engineering & Remote Sensing  
Vol. 88, No. 3, March 2022, pp. 165–170.  
0099-1112/22/165–170

© 2022 American Society for Photogrammetry  
and Remote Sensing  
doi: 10.14358/PERS.21-00032R2



Work” further outlines the scope of this research by elaborating on the different LoDs of 3D city models and related work. We present our reconstruction methodology in the section “Methodology for Automated 3D Reconstruction” and the implementation in the section “Implementation”. We close with conclusions in the last section.

## Scope of the Research and Previous Work

In this section, we first explain how the reconstructed level of detail of 3D building models depends on the one hand on the data requirements for which the data is collected (section “LoD in Relation to Urban Applications”) and on the other hand on the reconstruction method (section “LoD in Relation to Reconstruction Method”). We then describe the motivation for the LoDs that we reconstruct in our research in the section “The LoDs in Our Research”. Finally, the section “3D City Models of Large Areas” presents other work on the reconstruction of 3D data for large areas.

### LoD in Relation to Urban Applications

As in two dimensions (2D), a one-fits-all approach does not exist for a 3D city model. Instead, specific applications require specific 3D data as is analyzed in Biljecki *et al.* (2015). For example, block models (LoD1) are sufficient for shadow-, wind-, and noise-simulations. Roof structures (LoD2) with information on the roof materials are needed for solar potential estimation or in accurate energy demand estimation. Although LoD2 models are often also preferred in visualizations since they provide a realistic experience, realistic looking LoD2 models could still be ambiguous (Biljecki *et al.* 2018).

### LoD in Relation to Reconstruction Method

LoD1 models for every building can be automatically generated rather easily from point clouds and 2D building polygons, i.e., footprints (Ledoux *et al.* 2021). Therefore, LoD1 models are frequently generated by various organizations, as such source data are increasingly available as open data. However, automatically generated LoD1 models for the same area can still differ in, for example, their reference heights (e.g., the rooftop, the gutter height, one third of the roof-height) and the underlying statistical calculations. Many users are not aware of those multiple options to reconstruct a 3D block model, while these options do influence the outcome of analyses for which the LoD1 models are used (Biljecki *et al.* 2018).

With respect to LoD2 models, many roof shapes can be generated fully automatically, although LoD2 reconstruction is still a current topic of research, as both the quality of available surveyed data and new 3D reconstruction algorithms still steadily improve (Rottensteiner *et al.* 2014; Lafarge 2015; Pärvi *et al.* 2018).

The additional elements for LoD3 models are hard to reconstruct in an automated manner. Therefore, they are generated manually or are the result of converted Industry Foundation Classes (IFC) models from the BIM domain (Donkers *et al.* 2016; Colucci *et al.* 2020).

### The LoDs in Our Research

In our research, we focus on the reconstruction of LoD1.2, LoD1.3, and LoD2.2 building models using the terminology of the refined LoD framework of Biljecki *et al.* (2016). We distinguish between two types of LoD1 models: LoD1 models that are a result of extruding a complete building footprint to one height, i.e., LoD1.2 models in Biljecki *et al.* (2016) and models that are extruded to one or more heights in case significant height jumps occur within the footprint, like a church with a tower or a house with a shed attached, i.e., LoD1.3 models. Both models are relatively simple and are therefore appropriate for applications that need simplified models. But LoD1.3 models enable more realistic visualizations. In addition, LoD1.3 models are also more accurate data for simulations that take block-shaped models of buildings as input, such as noise simulation where buildings act as noise barriers. This is why the automated reconstruction of LoD1.3 models is included in our research. LoD1.3 models are more difficult to automatically generate than LoD1.2 because it requires the detection of height discontinuities within the building footprint.

The LoD1.0/LoD2.0 and LoD1.1/LoD2.1 models are based on generalized footprints and therefore outside the scope of our research. The LoD3 representations are outside our scope since they require manual work.

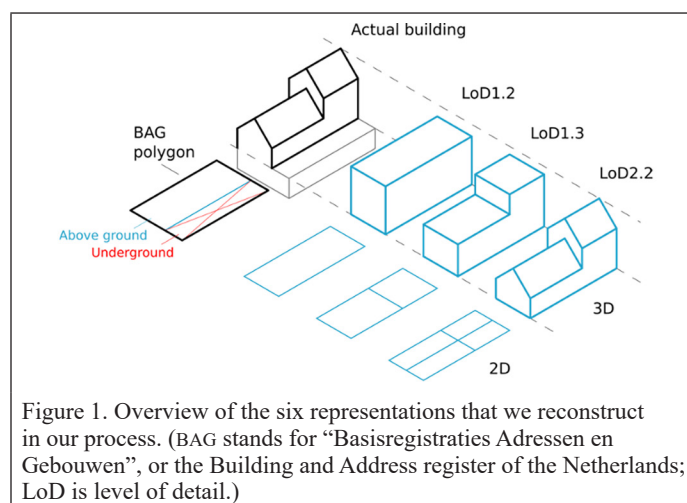
### 3D City Models of Large Areas

There are many other examples of data sets containing building models of large cities or even nations as shown by an inventory by Santhanavanich (2020). Examples are the whole United States, containing 125 million building models at LoD1, the city of New York (with 100 LoD2 models of iconic buildings), as well as the LoD2 models of Montreal, Helsinki, Singapore, cities in North Rhine-Westphalia State (in LoD 1 and LoD2), and many other cities in Germany. An example of an LoD2 building data set covering a whole nation is the swissBUILDINGS3D 2.0 data set (Swisstopo, 2021). It is a vector-based data set which describes (among other topographic objects) buildings as 3D models with roof geometries and roof overhangs. The building models were extracted in a semi-automated manner from aerial images using a photogrammetric method of digital image (stereo) correlation, enhanced with additional information as attributes. Other building elements (footprint, facades, roof overhangs) are created with automated procedures.

Several of these initiatives highlight a problem of existing 3D models: often they are the result of a one-time capture, with a few mostly manual updating exceptions. Updates and extensions may be considered in the future but were not foreseen at the moment they were captured. In addition, existing models resulting from the same workflow (and thus consistent) are limited to one or at the most to two different levels of detail for the same area and therefore the 3D data are limited to specific applications. More often, different LoDs of the same area are a result of different workflows and are therefore nonconsistent with respect to geometry, temporal aspects, and semantics. Finally, detailed metadata about how the buildings were reconstructed, including quality information, are often not generated and thus missing.

## Methodology for Automated 3D Reconstruction

In this section, we describe the reconstruction methodology of LoD1.2, LoD1.3, and LoD2.2 that we have developed and implemented for large areas, which we deliver as both 3D models and 2D+heights data (see Figure 1).



First, we describe the input data that we use in the reconstruction. Then, we describe the process itself. Since the LoD2.2 reconstruction generates information that is used in the reconstructions of the other LoDs (e.g., distinguishing between points that fall on walls and on roofs; generating a planar partition of the original footprint based on the identified roof planes), we start with the LoD2.2 reconstruction.

## Input Data

For our reconstruction process we use building polygons (“Basisregistraties Adressen en Gebouwen”, or the Building and Address register of the Netherlands (BAG)) and lidar point data (“Actueel Hoogtebestand Nederland”, the national height model of the Netherlands (AHN)) as input.

**BAG:** The polygons come from the Building and Address register of the Netherlands (BAG). This data set contains all buildings and addresses in the Netherlands. The geometry of addresses is collected as points and those of buildings as polygons (i.e., outline as seen from above). Municipalities are responsible for collecting the BAG data and keeping the data up-to-date.

The geometry for BAG buildings is acquired from aerial photos and terrestrial measurements and the data positional data accuracy is 30 cm. The data is provided via the national geo-portal PDOK (2021) both in a viewer and as download service. BAG also contains the history of buildings, i.e., buildings that are planned and buildings that have existed in the past but now have been removed.

For our reconstruction, we make a selection of the BAG buildings that have been realized and have not (yet) been demolished, i.e., the input building polygon data set represents the current situation.

**AHN:** The national height model of the Netherlands (AHN, 2019) is a point cloud acquired by airborne lidar. The first version of AHN (with a density of at least one point per 16 square meters, and in forests one point per 36 square meters) was completed in 2003. In the period of 2009 to 2012, the second version of the data set was acquired with an average point density of 10 points per square meter. The third version was collected between 2014 and 2019. The resolution of AHN3 that we use for our reconstruction process is similar to the one of AHN2. In addition, it contains a classification of the point cloud. For the AHN2 and AHN3 point clouds, it is specified that an object of  $2 \times 2$  m can be mapped with an accuracy of at least 50 cm. The height accuracy is 10 cm. We use the classes “building” and “ground points” to determine building heights respectively heights at ground level. The fourth version of AHN will become available in the next two years. AHN4 will have a point density of about 10–14 points per square meter, and in some locations even higher.

## LoD2.2

Our reconstruction method improves upon our earlier research as described in Dukai, Ledoux, and Stoter (2019) Dukai *et al.* (2020), and Stoter *et al.* (2020). The main improvement in this work is the addition of LoD2.2 output.

Our method uses footprints and height points that are well aligned as input and consists of two steps. In the first part the input footprint is partitioned into roof parts. And in the second part this 2D roof partition is extruded into a 3D model.

## Footprint Partitioning

In this first step, the input footprint is partitioned by breaklines detected in roof planes (see Figure 2).

These roof planes are detected if sufficient points can be found for that plane using a region-growing algorithm (see Figure 2.2). For the AHN that we use, with a point density of  $\sim 8$  points/m<sup>2</sup>, we set the minimum number of points to 15, which is equal to a roof element of about 2 square meters. Points that are on a wall plane (facade), or not part of any plane are removed.

We derive two types of lines from the planes: boundary lines and intersection lines (see Figure 2.3). The boundary lines of roof planes are detected using the  $\alpha$ -shape of each detected roof plane. The intersection lines are generated at the location where adjacent planes intersect, e.g., on top of a gable roof.

Before the boundary and intersection lines are used to subdivide the footprint, they are regularized and duplicate lines are removed. For example, the line on top of the gable roof in Figure 2.3 is detected three times: once as an intersection line and twice as a boundary line, i.e., once for each incident roof plane.

The remaining lines are used to subdivide the footprint into an initial planar partition (Figure 2.4). This is referred to as the initial roof partition. The initial roof partition may still have a high complexity, i.e., it may contain many small faces. To further reduce the complexity of the roof-partition, an optimization step is performed using a

graph-cut optimization (Zebedin, 2008). In this step, a roof plane is assigned to each face in the roof-partition (see Figure 2.5). This is done in such a way that the total error with the input point cloud is minimized and the total length of the edges between faces of a different roof plane is minimized. The latter assures a minimum number of edges and vertices, i.e., a low model complexity. After this step, the edges for which the two incident faces are assigned to the same roof plane are removed from the partition. The faces in the resulting final roof partition are referred to as roof parts.

## Extrusion

In the LoD2.2 reconstruction, the identified roof parts are extruded from ground level to a 3D mesh (Figure 2.6). The mesh consists of three types of surfaces: the ground plane, the roof surfaces, and the wall surfaces. The height of the ground plane is based on the lowest point around the building and is calculated as the fifth percentile of all ground points that are within a 4 m buffer of the building. An intersection curve of the terrain could also be used for this. The construction is done in such a way that no internal walls are created and the mesh is topologically correct.

## LoD1.3

The LoD1.3 reconstruction uses the same footprint partitioning as is generated for the LoD2.2 reconstruction. But for LoD1.3, the footprint partitions are further simplified by merging neighboring parts that have no significant height difference. We use 3 m as a threshold in this process, which is more or less equal to a floor-height, no matter the area. As the height reference we use the 70th percentile height for each roof part. The merging starts with merging from small to large height gaps and is an iterative process, i.e., if merging two roof parts leads to an elevation difference of  $< 3$  m with another part, they are merged again. The iteration stops when there are no more height differences smaller than 3 m between adjacent roof parts.

In the next step, reference heights are calculated for each remaining part and used to extrude the part.

As explained in the section “LoD in Relation to Reconstruction Method”, these reference heights can represent different extrusion heights for one building, i.e., the roof edge, the ridge height, or the maximum height (like a chimney). Furthermore, the underlying statistical calculations used to calculate the extrusion height can differ, e.g., average, median, or maximum.

To standardize possible extrusion variations and to let the user choose which one to use, our method calculates four different reference heights from the points that fall on a roof part (excluding the points on walls) and assigns these to the 2D roof parts, i.e., minimum, maximum, 50th percentile, and 70th percentile.

The LoD1.3 models are provided in two representations: as 2D roof-parts with the different reference heights as attributes, and as reconstructed (i.e., extruded) 3D models based on the 70th percentile of the roof points the specific part contains. The 2D roof parts also

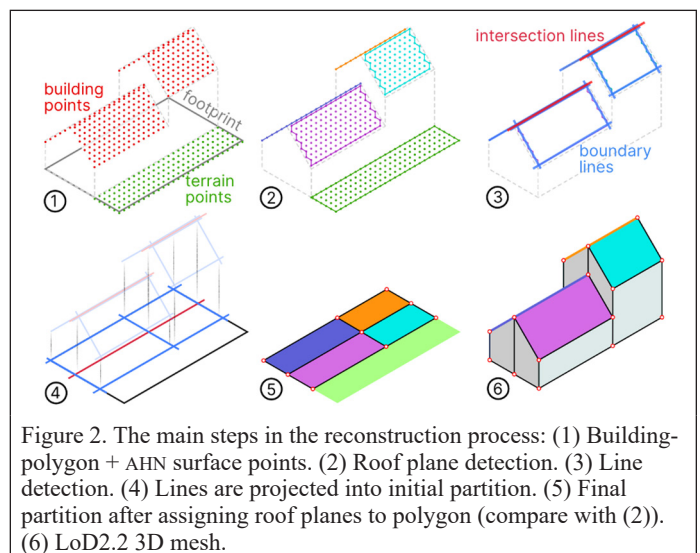


Figure 2. The main steps in the reconstruction process: (1) Building-polygon + AHN surface points. (2) Roof plane detection. (3) Line detection. (4) Lines are projected into initial partition. (5) Final partition after assigning roof planes to polygon (compare with (2)). (6) LoD2.2 3D mesh.



contain the identification of the original building to link the individual roof parts to the original building. The 3D models are reconstructed in such a way that there are no inner walls.

The reconstructed 3D models are represented as solids since rules for solids are stricter than for MultiSurfaces, e.g., using the solid geometry enforces a 2-manifold (i.e., watertight) 3D object.

For the ground surface, the same height is used as for the LoD2.2 models, i.e., fifth percentile of all surface points that fall within 4 m radius of footprint.

### LoD1.2

For the LoD1.2 models, we calculate the same four reference heights for the extrusion as we do for LoD1.3 and assign these to the original footprints. Also for LoD1.2, our method both reconstructs the 3D block models (based on the 70th percentile of height points that fall on all roof parts of the building) and assigns the four reference heights to the original 2D footprints. The same surface height is used as for the other LoDs.

## Implementation

### Implementation of the Reconstruction Process

The implementation of the whole process as described above is visualized in Figure 3. The input data is tiled to make the reconstruction and dissemination of the data more manageable. After reconstruction, the building models are stored in a PostgreSQL database from which the data is exported or directly consumed in various formats.

There are two considerations for optimally tiling the building footprints. First, the objective is to limit the number of buildings in each tile so that the workload is as balanced as possible between the processes. Second, the buildings should be spatially clustered so that the corresponding point cloud can be read efficiently. To meet both conditions, we use a quadtree with a maximum cell size of 3500 for subdividing the buildings (see Figure 4).

Thus, the building tiles are the leaves of the quadtree, where each tile contains a maximum of 3500 buildings. This assures that the reconstruction-time per tile is more or less the same and that the tiles available for download are similar in file size. The reconstruction of all ten million buildings in the Netherlands takes about 40 hours, with 30 concurrent processes on a single machine (two Xeon E5-2650 Central Processing Units, 128 GB RAM). The computation cost scales linearly with the number of buildings, since each building is processed independently. The reconstruction process is highly automated, which allows us to quickly run a new iteration in case of improvements in an algorithm or in case new input data becomes available. Figure 5 shows an example of reconstructed 3D models at different LoDs for one building.

### Visualization and Dissemination

To view and query as well as to download the reconstructed building models, we built a website with a 3D viewer (Figure 6). The 3D viewer was developed with two main goals: network performance (i.e., fast fetching of the data) and client performance, i.e., to minimize the resource needed on the device being used (including mobile devices). We developed our own solution since we could not find a suitable off-the-shelf solution.

To satisfy the network and client performance, we use a web graphics-friendly format with minimal size requirements, i.e., 3D Tiles<sup>1</sup>. This is based on the glTF format<sup>2</sup>. We export the data set to 3D Tiles using the same tiling scheme as for the reconstruction of the buildings, which ensures that tiles have a relatively equal distribution of objects. We use 3DTilesRendererJS<sup>3</sup> to render these tiles in the viewer. Our solution to make the user interface easy for users and mobile friendly uses VueJS<sup>4</sup> for the website's logic and Bulma<sup>5</sup> for the styling of the user interface elements.

The viewer provides several functionalities that enable users to investigate the whole data set, as well as share it with others. A user lands at an initial point and can move around the country. A simple flat terrain using Web Map Tile Service (WMTS)<sup>6</sup> is used to provide proper orientation context to the user. Each location in the viewer corresponds to a unique address so that the user can bookmark or share the current

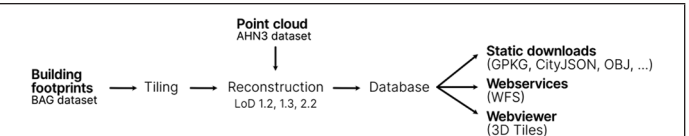


Figure 3. Overview of the multiple levels of detail (LoDs) reconstruction process. (BAG is Building and Address register of the Netherlands; AHN is the national height model of the Netherlands; GPKG is GeoPackage; CityJSON is a JSON-based encoding for a subset of the CityGML data model; OBJ is the Wavefront object file; WFS is Web Feature Service.)

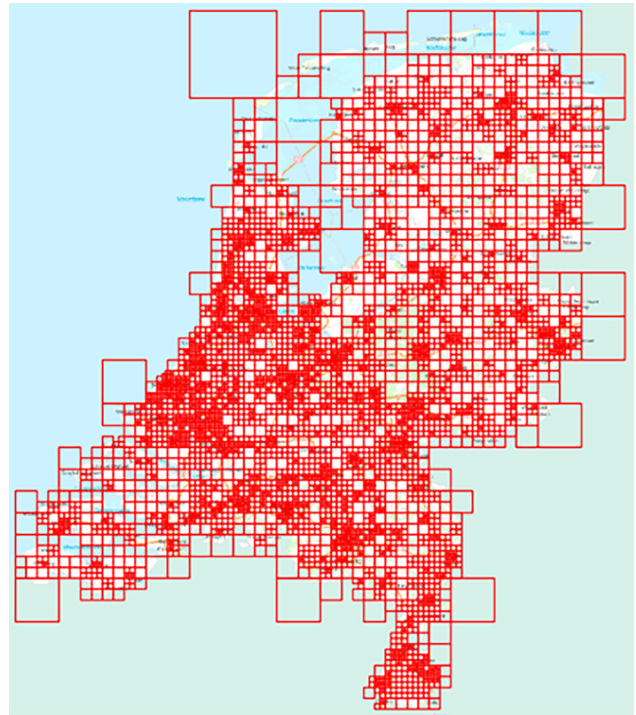


Figure 4. Quadtree-based tiling scheme for data processing and dissemination.

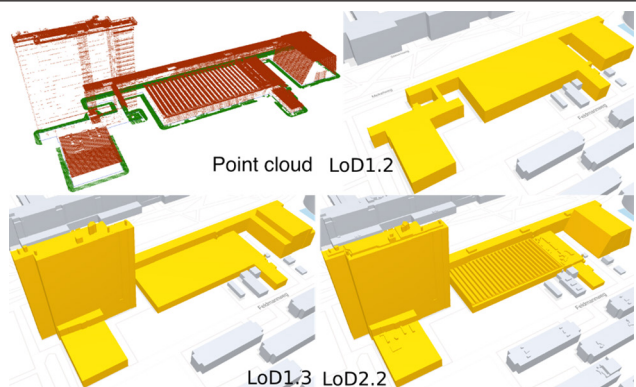


Figure 5. Faculty building of Electrical Engineering, Mathematics and Computer Science at Delft University of Technology (TU Delft) campus. AHN3 point cloud and reconstructions at LoD1.2, LoD1.3, and LoD2.2. At LoD1.3, only height jumps >3 m are kept, and therefore it contains fewer roof structures than LoD2.2.

1. <https://github.com/CesiumGS/3d-tiles>

2. <https://www.khronos.org/glTF/>

3. <https://github.com/NASA-AMMOS/3DTilesRendererJS/>

4. <https://vuejs.org/>

5. <https://bulma.io/>

6. <http://opengeospatial.github.io/e-learning/wmts/text/index.html>



view with others. Finally, the user can click on a building and get its information, as well as some derived properties: the height of the building at the specified point, and the slope of the surface that the user clicked on.

Through the website [www.3DBAG.nl](http://www.3DBAG.nl), the data is downloadable in different formats: GeoPackage, PostGIS backup, Wavefront OBJ, and CityJSON. The viewer also contains a function to report errors by users to help us improve our process, which can concern any part of the process, i.e., from preprocessing input data to reconstruction, viewing, and use.

### Quality Information

Quality information regarding the resulting models is needed to identify a badly reconstructed model or an exceptional situation for which the 3D reconstruction process had not yet accounted for. With this information, the reconstruction process can be improved. In addition, it provides the user with information on how good a specific model is so that the user can act upon this.

We calculate two types of quality parameters and assign these as attributes to the individual models. First, we calculate parameters that assess the quality of the source data for the specific building. For example, the number of points that were available for the 3D reconstruction, the no-data area, and the timeliness of the source data. Second, we calculate parameters that measure the success of the automatic reconstruction, e.g., the root-mean-square error (RMSE) between the reconstructed model and the input points, the maximum error between reconstructed mesh and the point clouds and eventual invalidity codes both in 2D (which means the input data contained an error) and in 3D (which means that the reconstruction failed). For the LoD2.2 building models of the Netherlands, the RMSE is less than 31 cm for 95% of the models and less than 9 cm for 75% of the models (see Figure 7). A more extensive evaluation is in progress. This evaluation is based on the quality parameters that we calculate in order to identify opportunities to further improve our workflow (Dukai *et al.* 2021).

### Conclusions

In this paper, we describe the process that we have developed to automatically reconstruct LoD1.2, LoD1.3, and LoD2.2 building models (supporting differing reference heights for the block models) for large areas in one reconstruction process and based on the same source data. This provides the user with consistent 3D data of the same area meeting the data-needs of different applications. We monitor quality information throughout the entire process in order to continuously improve the process from input data, preprocessing, and 3D reconstruction to download and use the data in urban applications. In addition, the user can use the quality information to decide on the fit-for-purpose of the data for their own application.

The 3D data that we generate has been a good source to experiment and test all kinds of urban applications that need 3D data, and it is being used in, for example, noise simulations (Stoter *et al.* 2020), wind flow simulations (García-Sánchez *et al.* 2021), and energy consumption calculations (Wang *et al.* 2020; León-Sánchez *et al.* 2021).

Based on experiences and users' feedback, we will improve the process and optimize for different users and applications. These improvements may be generic such as filling the no\_data areas in the point cloud with artificial intelligence; better alignment to specific data needs of urban applications, like optimizing the level of detail for specific applications (in relation to processing time); and enriching the data with relevant information, for example distinguish between external and internal walls and their areas for energy-related applications or the estimation of the number of floors per building. In addition, the availability of the next version of AHN (to be expected next year) will provide more reconstruction possibilities, as can be seen in Figure 8. In future research, we will also study more fundamental issues, i.e., how to maintain and manage different temporal and geometric versions of the 3D data and how to better align the different parts in the process to obtain even better results.

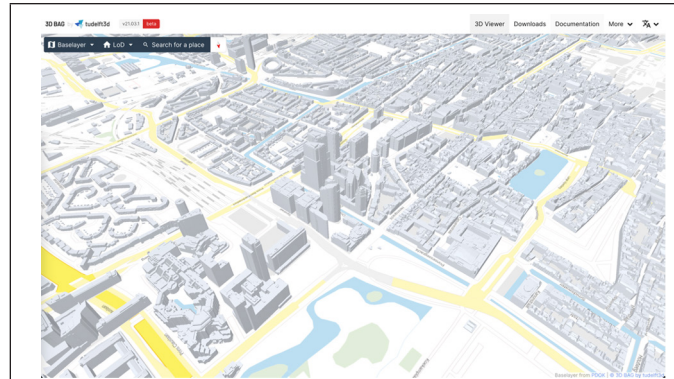


Figure 6. Screenshot of the developed 3D viewer available at [www.3dbag.nl](http://www.3dbag.nl).

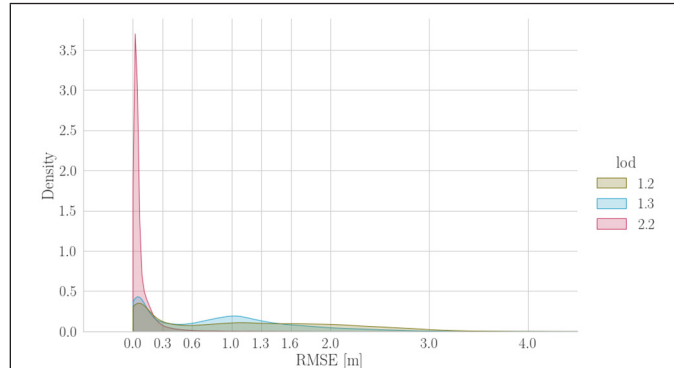


Figure 7. The root-mean-square error (RMSE) between the input point cloud and the LoD2 reconstruction result (Dukai *et al.* 2021).

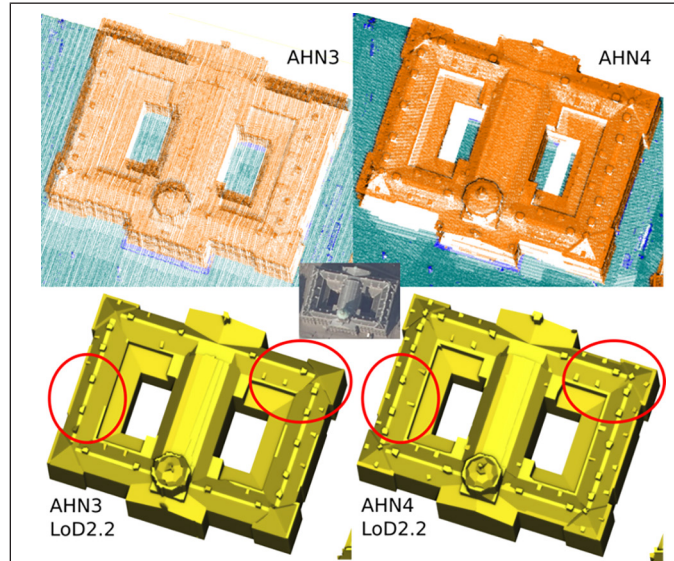


Figure 8. The palace in Amsterdam. AHN3 and AHN4 point clouds and the resulting LoD2.2 reconstruction. More details are reconstructed from the AHN4 point cloud because it has a higher resolution.

### Acknowledgments

This project received funding from the European Research Council (ERC) under the European Union's Horizon2020 Research & Innovation Programme (grant agreement no. 677312 UMN-D: Urban modelling in higher dimensions). Part of the research was done within the VOLTA project funded from the European Union's Horizon 2020 research and innovation programme under the Marie Skłodowska-Curie (grant agreement No 734687).

## References

- Biljecki, F., G.B.M. Heuvelink, H. Ledoux and J. Stoter. 2018. The effect of acquisition error and level of detail on the accuracy of spatial analyses. *Cartography and Geographic Information Science* 45(2):156–176.
- Biljecki, F., H. Ledoux and J. Stoter. 2016. An improved LOD specification for 3D building models. *Computers, Environment and Urban Systems* 59:25–37.
- Biljecki, F., J. Stoter, H. Ledoux, S. Zlatanova and A. Çöltekin. 2015. Applications of 3D city models: State of the art review. *ISPRS International Journal of Geo-Information* 4(4):2842–2889.
- Colucci, E., V. De Ruvo, A. Lingua, F. Matrone and G. Rizzo. 2020. HBIM-GIS integration: From IFC to CityGML standard for damaged cultural heritage in a multiscale 3D GIS. *Applied Sciences* 10:1356. <https://doi.org/10.3390/app10041356>.
- Deren, L., Y. Wenbo and S. Zhenfeng. 2021. Smart city based on digital twins. *Computational Urban Science* 1(4). <https://doi.org/10.1007/s43762-021-00005-y>.
- Donkers, S., H. Ledoux, J. Zhao and J. Stoter. 2016. Automatic conversion of IFC datasets to geometrically and semantically correct CityGML LOD3 buildings. *Transactions in GIS* 20(4):547–569.
- Dukai, B., H. Ledoux and J. Stoter. 2019. A multi-height LoD1 model of all buildings in the Netherlands. *ISPRS Annals of the Photogrammetry, Remote Sensing and Spatial Information Sciences* IV-4/W8:51–57.
- Dukai, B., R. Peters, J. Van Liempt, S. Vitalis and J. Stoter. 2021. Quality assessment of a large dataset containing automatically reconstructed 3D building models. *The International Archives of the Photogrammetry, Remote Sensing and Spatial Information Sciences* XLVI-4/W4-2021:17–24. <https://doi.org/10.5194/isprs-archives-XLVI-4-W4-2021-17-2021>.
- Dukai, B., R. Peters, T. Wu, T. Commandeur, H. Ledoux, T. Baving, M. Post, V. van Altena, W. van Hinsbergh and J. Stoter. 2020. Generating, storing, updating and disseminating a countrywide 3D model. Pages 27–32 in *Proceedings ISPRS 15th 3D GeoInfo Conference*, held in London, U.K., 7–11 September 2020.
- García-Sánchez, C., S. Vitalis, I. Pađen and J. Stoter. 2021. The impact of level of detail in 3D city models for CFD-based wind flow simulations. *The International Archives of the Photogrammetry, Remote Sensing and Spatial Information Sciences* XLVI-4/W4-2021:67–72. <https://doi.org/10.5194/isprs-archives-XLVI-4-W4-2021-67-2021>.
- Kutzner, T., K. Chaturvedi and T. H. Kolbe. 2020. CityGML 3.0: New functions open up new applications. *Journal of Photogrammetry, Remote Sensing and Geoinformation Science* 88:43–61.
- Lafarge, F. 2015. Some new research directions to explore in urban reconstruction. *Joint Urban Remote Sensing Event (JURSE)*:1–4. <https://doi.org/10.1109/JURSE.2015.7120488>.
- Ledoux, H., K. Arroyo Ohori, K. Kumar, B. Dukai, A. Labetski and S. Vitalis. 2019. CityJSON: A compact and easy-to-use encoding of the CityGML data model. *Hugo Open Geospatial Data, Software and Standards* 4(4). <https://doi.org/10.1186/s40965-019-0064-0>.
- Ledoux, H., F. Biljecki, B. Dukai, K. Kumar, R. Peters, J. Stoter and T. Commandeur. 2021. 3drier: Automatic reconstruction of 3D city models. *Journal of Open Source Software* 6(57):2866.
- Ledoux, H., T. Commandeur, C. Nagel, S. Trometer and S. Vager. 2016. Automatic reconstruction of simulation-ready 3D city models. <https://3d.bk.tudelft.nl/projects/simwind/simwind-final-report.pdf>.
- León-Sánchez, C., D. Giannelli, G. Agugiaro and J. Stoter. 2021. Testing the new 3D bag dataset for energy demand estimation of residential buildings. *The International Archives of the Photogrammetry, Remote Sensing and Spatial Information Sciences* XLVI-4/W1-2021:69–76. <https://doi.org/10.5194/isprs-archives-XLVI-4-W1-2021-69-2021>, 2021.
- Open Geospatial Consortium (OGC). 2012. *OGC City Geography Markup Language (CityGML) Encoding Standard 2.0.0 (Document No. 12019)*. Wayland, Mass.: Open Geospatial Consortium.
- Pärvi, I. M., F. Remondino and E. Ozdemir. 2018. LOD2 building generation experiences and comparisons. *Journal of Applied Engineering Sciences* 8(2):59–64. <https://doi.org/10.2478/jaes-2018-0019>.
- Public Services on the Map (PDOK). 2021. National Geo-Portal. <<https://www.pdok.nl>> Last accessed December 2021.
- Rottensteiner, F., G. Sohn, M. Gerke, J. D. Wegner, U. Breitkopf and J. Jung. 2014. Results of the ISPRS benchmark on urban object detection and 3D building reconstruction. *ISPRS Journal of Photogrammetry and Remote Sensing* 93:256–271.
- Santhanavanich, J. 2020. Open-Source CityGML 3D Semantical Building Models in 2020. <<https://towardsdatascience.com/open-source-3d-semantical-building-models-in-2020-f47c91f6cd97>> Accessed DATE.
- Stoter, J., R. Peters, T. Commandeur, B. Dukai, K. Kumar and H. Ledoux. 2020. Automated reconstruction of 3D input data for noise simulation. *Computers, Environment and Urban Systems* 80:101424.
- Sun, J., P. Olsson, H. Eriksson and L. Harrie. 2019. Evaluating the geometric aspects of integrating BIM data into city models evaluating the geometric aspects of integrating BIM data into city models. *Spatial Science*. 65(2):235–255. <https://doi.org/10.1080/14498596.2019.1636722>.
- Swisstopo. 2021. <<https://www.swisstopo.admin.ch/en/knowledge-facts/topographic-landscape-model.html>> Last accessed 17 December 2021.
- Wang, C., S. Tindemans, C. Miller, G. Agugiaro and J. Stoter. 2020. Bayesian calibration at the urban scale: A case study on a large residential heating demand application in Amsterdam. *Journal of Building Performance Simulation* 13(3):347–361.
- Zebedin, L., J. Bauer, K. Karner and H. Bischof. 2008. Fusion of feature- and area-based information for urban buildings modeling from aerial imagery. Pages 873–886 in *Computer Vision–ECCV 2008*. Edited by D. Forsyth, P. Torr and A. Zisserman. Lecture Notes in Computer Science vol. 5305. Berlin: Springer. [https://doi.org/10.1007/978-3-540-88693-8\\_64](https://doi.org/10.1007/978-3-540-88693-8_64).

# Dynamic Linkage Between Urbanization, Electrical Power Consumption, and Suitability Analysis Using Remote Sensing and GIS Techniques

Muhammad Nasar Ahmad, Qimin Cheng, and Fang Luo

## Abstract

*This article proposes an estimation method for assessing urban sprawl using multispectral remote sensing data: SNPP-VIIRS, DMSP/OLS, Landsat 5-TM, and Landsat 8-OLI. This study focuses on the impacts of human activities, in terms of increased electrical-power consumption (EPC) due to urbanization. For this purpose, night-time light data are used to measure the EPC growth from 2000 to 2020. We also perform a suitability analysis using geographic information-systems techniques to propose a new urban town in Lahore to mitigate urbanization and EPC increase. We found an overall increase of 33% in urban area and an EPC increase of 21.6% in the last two decades. We also find that the best proposed site for the new urban town is in the northwest of Lahore..*

## Introduction

Urbanization is an emerging problem worldwide. It mainly affects socioeconomic factors and the demographic composition of locations, leading to many environmental and ecological problems such as urban heat islands and waterlogging. These complications are increasing as time goes on, due to rapid urbanization all over the world.

According to Q. Zhang and Seto (2011), a United States survey stated that by 2050 the global population will increase by 2.7 billion. For the most part, people readily move from rural to urban zones to seek better living and work opportunities and to enhance their earnings, which leads to an increase in population density and urbanization. Ding *et al.* (2016) concluded that most agricultural farmland is converted into urban areas, which will have negative effects on regional climate change. Imhoff *et al.* (1997) note that when analyzing urban sprawl and its dynamics, it is necessary to identify factors and the effects of urbanization on society and the environment.

Urban expansion is a reflection of urban growth patterns, which can be either scattered or fragmented. An abrupt increase in urbanization also results in the loss of vegetation, biological diversity, freshwater resources, and energy production sources. Dowall and Ellis (2009) explain that most of the growth in urban sprawl occurred in Asia over the past few decades. According to Sutton (1997), urbanization has negative impacts that are typically observed in underdeveloped countries. There is a need to control the outcomes of urbanization. The health of

the environment and food security in densely populated regions are the main reasons for monitoring urban settings, because they address public health issues as well as fiscal concerns.

Globally, the main factor is people who migrate to enhance their livelihoods and earnings and secure their future. In the past, statistical data and conventional methods were used to analyze changes in urbanization. But these methods are slightly complicated and require considerable time for data collection and surveying. Taubenböck *et al.* (2012) described limitations of these conventional methods. Researchers are now using remote sensing technology to speed up analysis and identify changes in land cover/land use.

Remote sensing is a dynamic tool that is used to acquire accurate, prompt, and up-to-date spatial information on urban growth patterns across the globe. However, mapping of urban clusters is quite difficult, because of mixed land use, which includes buildup, rivers, vegetation, and barren land. Many satellite products are available which incorporate different sensors and image characteristics, for mapping built-up areas and urban clusters. However, this also depends on the available spectral and spatial resolution of the satellite imagery.

In past, multiple satellite images were used, such as MODIS, Spot, and Ikonos, but these satellite products were acquired only during daytime (Zhao *et al.* 2018). But nighttime light (NTL) data have a particular characteristic that allows a sensor to acquire data in the absence of sunlight. Because light-source detection is strongly correlated with urban activities at any given location at night, researchers in the past considered emission of light as an indicator of electrical-power consumption, human activities, population expansion, and urban sprawl (Yi *et al.* 2014; Zhou *et al.* 2014).

Thus, the use of NTL data is quite practical for analyzing the distribution of urban expansion using image-processing techniques combined with multi-source data. Small *et al.* (2005) determined that electrical-power consumption is a major factor for countries in terms of energy production. As discussed by Letu *et al.* (2010) and Mellander *et al.* (2015), NTL data can also be used to predict future economic growth and reliability, with respect to available energy resources. According to Kiran Chand *et al.* (2009), mostly solar power, wind power, and coal are used to produce electricity on a global scale.

Nighttime light data typically capture artificial light emitted from the earth's surface at night. NTL products including DMSP/OLS and NPP-Visible Infrared Imaging Radiometer Suite (VIIRS) data can be used to assess large areas, because they have a resolution of 750 m to 1 km. Nighttime light data (NTLD) are also convenient for determining time-series change over the globe, because there are many freely available products. According to Huang *et al.* (2014), NTLD have been used more since the launch of version 4 and VIIRS products.

Muhammad Nasar Ahmad is with the State Key Laboratory of Information Engineering in Surveying, Mapping and Remote Sensing, Wuhan University, Wuhan, China (mnasarahmad@whu.edu.cn).

Qimin Cheng is with the School of Electronics Information and Communications, Huazhong University of Science and Technology, Wuhan, China.

Fang Luo is with the Department of Computer Science and Technology, Wuhan University of Technology, Wuhan, China.

Contributed by Zhenfeng Shao, May 11, 2021 (sent for review October 8, 2021; reviewed by Nana Yaw Danquah Twumasi, Hongping Zhang).

Photogrammetric Engineering & Remote Sensing  
Vol. 88, No. 3, March 2022, pp. 171–179.  
0099-1112/22/171–179

© 2022 American Society for Photogrammetry  
and Remote Sensing  
doi: 10.14358/PERS.21-00026R3



Lahore, Pakistan, is facing the worst electricity shortfall in the past two decades, and lots of research work is required in this domain. This shortfall is basically due to rapid urbanization, because the available supply is lower than the demand for electricity. As population has increased by 2.28 million, from 10.36 million in 2015 to 12.64 million in 2020, electrical-power consumption (EPC) per capita in Lahore has increased by an estimate of 12.10 kW h due to the increase in population and urbanization.

This article aimed to identify overall growth in EPC from 2000 to 2020 using NTL and Landsat data. Therefore, population increase and EPC were also correlated with urban area extracted from NTL data. Historically, in Lahore most of the urbanization has been observed in a horizontal direction. The selected study area is the second-largest city of Pakistan, and the tendency of people to migrate to this city has been very high in the last 30 years. Now there is no more space for the city to grow in a horizontal direction. Thus, in response to this uncontrollable urbanization there must be a new urban town, which would consist of vertical infrastructure development. For this purpose, the CommunityViz Scenario 360 module was used to identify the best site for a new urban town that would consist of skyscrapers and vertical development.

This research work is significant as it contributes to the identification of increased electrical-power consumption, urban population, and urbanization in Lahore over the past two decades. It also provides a solution in the form of a proposed location of a new urban town to control rapid urbanization and reduce electricity consumption. The originality of our work is that no previous research work has been done on increased electrical-power consumption in this study area using NTL data products and remote sensing, and no one has used CommunityViz Scenario 360 to identify the location of a new urban core in Lahore.

## Study Area and Data

### Study Area

Lahore is the capital city of Punjab Province, in Pakistan, and is located in the northeastern part of the province. According to a recent census, it has a population of 12 642 000, making it is the second-largest

city by population in Pakistan. It has an area of 1772 km<sup>2</sup> and a geographical position of 31°34'55.3620" N and 74°19'45.7536" E. The location of the study area is shown in Figure 1.

### Data-Set Overview

#### DMSP/OLS Nighttime Light Data

In terms of technical specifications, NTL has two spectral bands: visible and thermal infrared. Cloud-free composite images for the years 2000 and 2010 were downloaded from the National Oceanic and Atmospheric Administration (NOAA) website and further preprocessed. Defense Meteorological Satellite Program (DMSP) OLS data were only available until 2013, so another composite of NTL data was used for the year 2020. Pandey *et al.* (2013) and Shi *et al.* (2014) believe that 0.56 km is comparatively high spatial resolution for NTL data products. However, spatial resolution can fluctuate with respect to different locations and distance from the Equator (Amaral *et al.* 2005; Yin *et al.* 2020). The acquisition time and sensor information can be found in Table 1, which has an overall spatial resolution of 1 km.

#### SNPP-VIIRS

The *Suomi National Polar-Orbiting Partnership* (SNPP) satellite launched in October 2011 and was designed to acquire high-resolution radiometric data on a daily basis for both daytime and nighttime. It is operated in collaboration with NASA and NOAA. The primary sensor on SNPP is a VIIRS. The source data are produced in Hierarchical Data Format-5, and are available through NOAA's Comprehensive Large Array-data Stewardship System archive. The National Geophysical Data Center developed a service to geo-locate VIIRS images to improve usability, meet data needs, and reduce data volume. For research purposes, a daily mosaic of daytime VIIRS with I-bands and nighttime day/night band data is available worldwide. Table 1 provides the overall details of the data set used in this study.

#### Landsat Data Set

Landsat imagery is acquired under the NASA/USGS program, which provides the longest and most continuous space-based satellite imagery worldwide (Deng and Wu 2013). Landsat images have been available

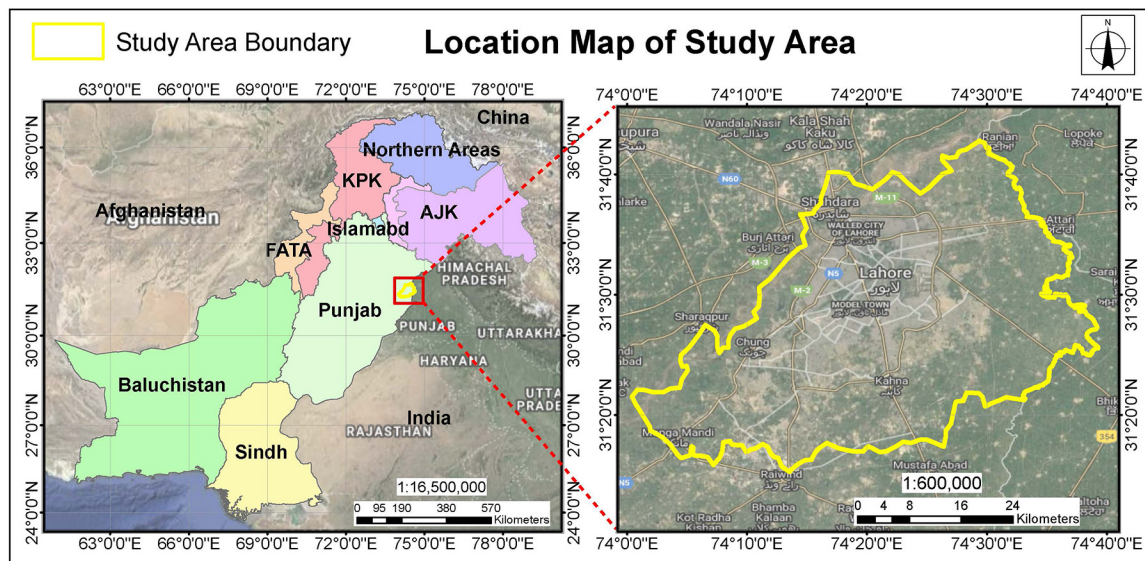


Figure 1. Location of the study area.

Table 1. Satellite imagery used in this study.

Satellite	Sensor Type	Acquisition Date	Spatial Resolution	Source
DMSP/OLS	OLS	March 2000–2010	1 km	<a href="https://ngdc.noaa.gov/eog/dmsp">https://ngdc.noaa.gov/eog/dmsp</a>
NPP-VIIRS	SNPP	March 2020	750 m	<a href="https://ngdc.noaa.gov/eog/viirs.html">https://ngdc.noaa.gov/eog/viirs.html</a>
Landsat 5	TM	March 2000/2010	30 m	<a href="https://earthexplorer.usgs.gov">https://earthexplorer.usgs.gov</a>
Landsat 8	OLI	March 2020	30 m	<a href="https://earthexplorer.usgs.gov">https://earthexplorer.usgs.gov</a>

since 1972. This study was carried out using two Landsat products—Thematic Mapper (TM) and Operational Land Imager (OLI)/Thermal Infrared Sensor (TIRS) sensors—and the data were downloaded from the USGS website. Satellite imagery was acquired at 10-y intervals, within the first quarter of each year to avoid variations due to climate. The Landsat data used to carry out this study are listed in Table 2.

#### Punjab Population Data

The government of Pakistan updated census data records in 2017, with the collaboration of the military, and changes were made in national databases of sectors involved. For this study, Lahore population data were collected from the Pakistan Bureau of Statistics and cross-checked with the United Nations Population Prospects 2019 (Table 3). Population data are available through 2035, but they are projected on the basis of 2015–2020 data values by the relevant department.

#### Electrical-Power Consumption (EPC) data

EPC data were acquired from the Lahore Electric Supply Company, a department of the local government, which maintained these data with the collaboration of the National Transmission and Despatch Company. The data were acquired in kilowatt-hours per capita and used to generate further computations and comparisons of EPC with total night light area. Details of electricity consumed per capita from 2000 to 2020 are presented in Table 4.

#### Lahore Vector Shape-File Data

The shape file of union council boundaries was acquired from the Lahore Development Authority's website. The rest of the spatial data were digitized and projected using Google Earth satellite imagery for suitability analysis: union Council boundaries, airports, walled city boundaries, railway stations, highways, and the Ravi River.

## Methods and Processing

Multi-source satellite data can be combined to provide temporal observations or more information for environmental applications, such as monitoring land cover/land use management and conditions. This study hypothesizes that a methodology can be developed to assess urban expansion in the Lahore jurisdiction by using multi-source satellite data. These observations can be used to highlight changes in EPC, specifically increases due to the impacts of human socioeconomic activity, using NTL.

For this purpose, NTL, population density, and EPC can be correlated to determine the impacts of urban-area expansion on population and EPC. A flowchart depicting the general methodology of data flow, integration, and analysis is shown in Figure 2.

Numerous methods have previously been used by researchers to carry out the EPC calculations and to compare population densities with nighttime light data, including linear correlation, log-to-log, and second-order regression models. However, according to Y. Liu *et al.* (2015), more accurate results were attained in most studies by using simple linear regression and correlation models. Shi *et al.* (2014) also explained that linear correlation is a resilient technique to compare NTL area with economic indicators. Therefore, we constructed a linear correlation model in this study,

$$G = wL + c \quad (1)$$

where  $G$  denotes the statistical data (such as population density or EPC for a specified location) and  $L$  is the total amount of light at night (Ma *et al.* 2015; Xu *et al.* 2020). The buildup area was extracted from DMSP/OLS and SNPP-VIIRS imagery through the summation of all the pixels depicting an urban area in the study area, where  $w$  is the coefficient and  $c$  denotes the intercept. Lo (2002) determined that population density can be calculated by simple division of total population by the total area for a specific location. So the number of people per unit of area (square kilometer) was determined by

$$P_D = T_p / T_A \quad (2)$$

where  $P_D$  = population density,  $T_p$  = total population, and  $T_A$  = total area.

Table 2. Details of Landsat imagery.

Sensor ID	Sensor Type	Acquisition Date	Row/Path	Spatial Resolution
LT051490382000031101T1	TM	11 March 2000	149/038	30 m
LT051490382010030601T1	TM	07 March 2010	149/038	30 m
LC081490382020021501RT	OLI_TIRS	15 February 2020	149/038	30 m

Source: NASA/USGS-Earth Explorer.

Table 3. Population statistics for Lahore from 2000 through 2035.

Year	Population	Growth Rate
2000	5 576 372	3.69
2005	6 856 969	4.31
2010	8 432 132	4.22
2015	10 369 137	4.22
2020	12 642 423	4.04
2025	14 825 828	3.24
2030	16 883 085	2.63
2035	19 116 605	2.52

Source: Bureau of Statistics, Pakistan

Table 4. EPC data per capita (kW h) for Pakistan and Lahore.

Year	Pakistan	Lahore
2000	362.4048	12.456 958
2010	442.1800	20.160 709 1
2020	532.5123	32.265 440 4

Source: Lahore Electric Supply Company

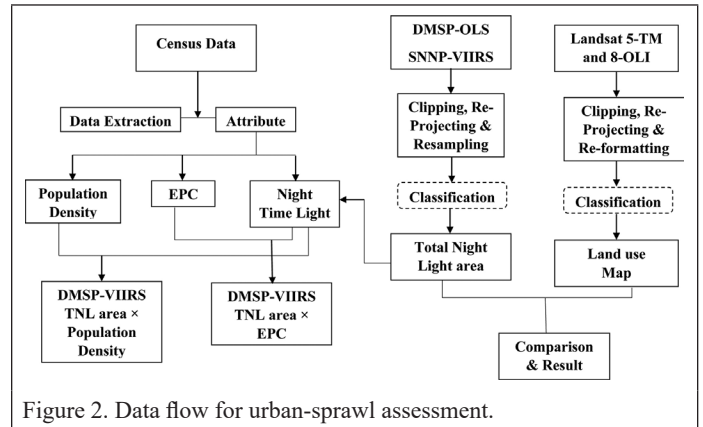


Figure 2. Data flow for urban-sprawl assessment.

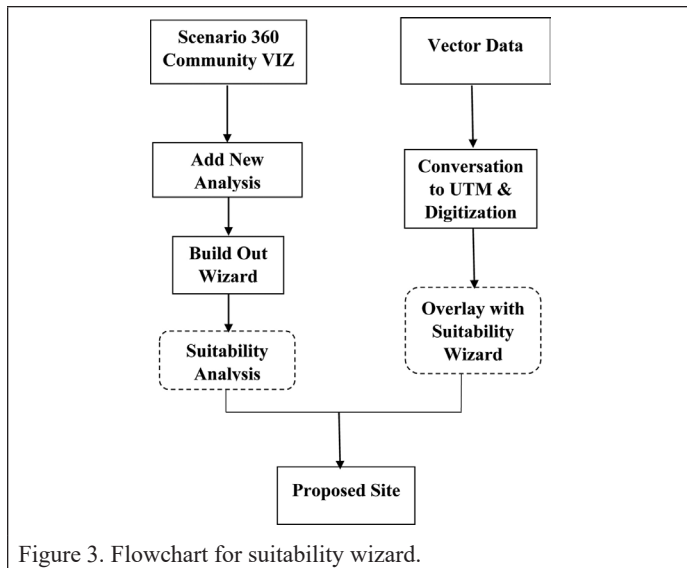
The area was also calculated for each type of land use, such as areas that were built up, from a classified image, which was then used to analyze the changes in urban area. J. Zhang *et al.* (2014) described how area can be calculated by multiplying the number of pixels and total pixel area. These calculations (yielding values in square kilometers per square meter) have been done using

$$\text{Area} = \text{NP} \times \text{PA} \times 10^{-5} \quad (3)$$

where NP designates the number of pixels for each class and PA is the pixel area, which is always 900 m<sup>2</sup> for Landsat because it has a resolution of 30 m.

Furthermore, Figure 3 shows the data flow for the suitability analysis for the proposed site of a new urban town in Lahore.

CommunityViz Scenario 360 is a spatial decision support system—that is, an interactive, computer-based system designed to support users in achieving higher effectiveness in decision making while solving a spatial problem (Tao 2013). It is designed to assist spatial planners in



the software used to conduct image processing included ERDAS Imagine, ENVI, and ArcGIS. Similarly, statistical software was used to analyze and to compute the linear correlation between NTL area, population density, and electrical-power consumption.

### Classification Methods and Details

For all three satellites images from 2000 to 2020, NTL data were classified using a maximum hood classifier in ERDAS Imagine. NTL is already a classified form provided by the Defense Meteorological Satellite Program, but we converted it to a projected coordinate system and classified it so that we could compute the overall change in EPC for each year.

A support vector machine classifier was used to classify the Landsat imagery into three classes for all three successive years. For nighttime light data, no specific classifier was required, because it only contained two day/night values; it can be classified according to analysis requirements. But in this study, the purpose of classification was only to extract urban areas from satellite imagery. However, for Landsat classification there are distinct land use types with discrete reflectances, and therefore the support vector machine was used to classify data. Because the support vector machine is very supportive for spectral detection and dynamic supervised classification (Amaral *et al.* 2006; Z. Liu *et al.* 2012). The description of the classes is as follows: urban area (built-up areas and any infrastructure), nonurban area (barren land, open land), vegetation (both farmland and vegetation), and water (all waterbodies, rivers, lakes, and canals). Moreover, for NTLD the nonurban area class includes all land uses excluding built-up area, because it focuses on urban area emitting light during nighttime.

For instance, there are only two classes for DMSP/OLS and SNPP/VIIIRS: urban and nonurban, where nonurban refers to all other land use types, including farmland, barren land, waterbodies, and open land. But for Landsat data there are three classes: urban area, vegetation, and waterbodies. Table 6 provides details on the classification methods, names of classes, and number of signatures made for each category.

### Calculating Population Density for Each Year

Population data for Lahore were acquired from the Pakistan Bureau of Statistics, which was responsible for acquiring and updating the relevant population data on a yearly basis. City population data records were available, and so we filtered Lahore from the overall database. Population data are shown in Table 3, and the formula used to process the population data further and calculate population density (Equation 2) has already been discussed.

## Results

We found that during the past two decades, urban sprawl and EPC have increased unevenly. Dynamic changes in urban sprawl, and its impacts on EPC, were found increase each year. Most of the urban developments were observed in the southeastern and western parts of the city. The results are further explained for each data set.

### DMSP/OLS and SNPP-VIIRS

Images were processed and classified using ERDAS Imagine software. In addition, we constructed a confusion matrix to assess the overall accuracy of classification. The average accuracy from 2000 to 2020 was determined to be 90.65%, with a  $\kappa$  coefficient of 83.24% (Table 7). The maps in Figure 4a show the overall increase in urban sprawl. These results were obtained using NTLD for Lahore from 2000 to 2020. Notice the significant growth in urban area for 2020 as compared to 2000. Moreover, Figure 4b compares three zones in 2000 and 2020 using NTLD results. It shows rapid change in urban area within two decades in all three zones.

making land use plans and decisions. It helps analysts view, analyze, and understand land use alternatives and their impacts. CommunityViz Scenario 360 is a spatial decision support system processed on ArcMap using CommunityViz. A proposed site for a new urban town is constructed on the basis of the criteria shown in Table 5, which also provides details of the targeted layer and score result.

Table 5. Defining criteria and spatial layers.

Criterion	Target Layer	Formula Type	Score Result
Far from airport	Airport	Proximity	Lower
Near Lahore walled city	Existing plazas	Proximity	Higher
Near railway station/network	Railway station	Proximity	Higher
Near highways	Roads	Proximity	Higher
Easy access to nearby cities	Cities	Proximity	Higher
Near freshwater resource	River	Proximity	Higher

Moreover, all the alternatives were projected on the basis of availability of land, entry/exit from/to Lahore city, and the criteria defined for the identification of a suitable location for the new urban town. The available alternatives were Kot Begum, Ravi Town, to the north; Shahpur, Iqbal Town, to the south; Bhangali, Aziz Bhatti Town, to the east; and Gajju Matta, Nishtar Town, to the west.

### Imagery Resampling and Reprojection

The data set used in this study came with a geographical reference system, which had a resolution of 1 km for DMSP/OLS and 750 m (Cao *et al.* 2009) for the SNPP-VIIRS data. To rationalize, make the analysis smooth, and obtain more consistent results, we resampled the data to a 500-m spatial resolution. For this reason, both data sets were reprojected to the WGS 1984 UTM Zone 43N, where Lahore lies. After that, both satellite images were resampled with a spatial resolution of 500 m using the available data-management and raster-processing resampling tool in ArcMap.

Furthermore, all three images—DMSP/OLS, SNPP-VIIRS, and Landsat 5-TM/8-OLI—were clipped using the vector boundary of the study area. To calculate the area, the NTL data were also reprojected to WGS 1984 UTM Zone 43N, and the projected coordinate system was converted into ENVI HDF format for further processing. For this purpose,

Table 6. Defining classification methods and satellite data used.

Satellite Data	Classifier	Number of classes	Names of Classes	Training Samples per Class
DMSP/OLS	Maximum likelihood	2	Urban area, nonurban area	>1000
SNPP/VIIRS	Maximum likelihood	2	Urban area, nonurban area	>1000
Landsat 5-TM, 8-OLI	SVM	3	Urban area, vegetation, waterbodies	>6000

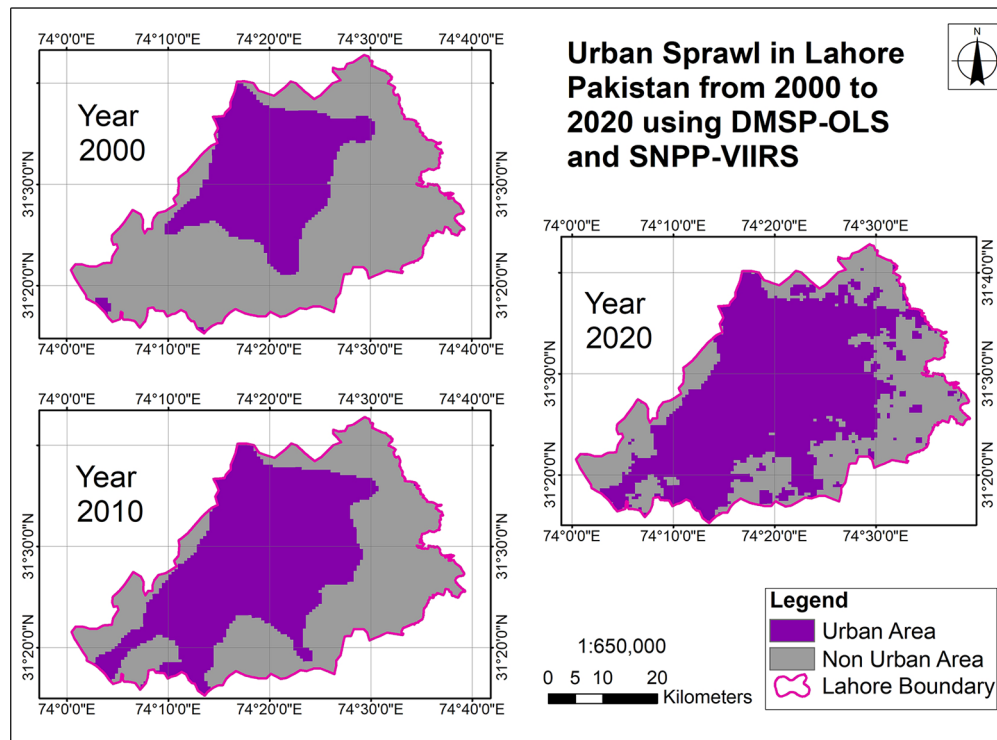


Table 7. Overall accuracy and  $\kappa$  coefficients using DMSP-VIIRS nighttime light data.

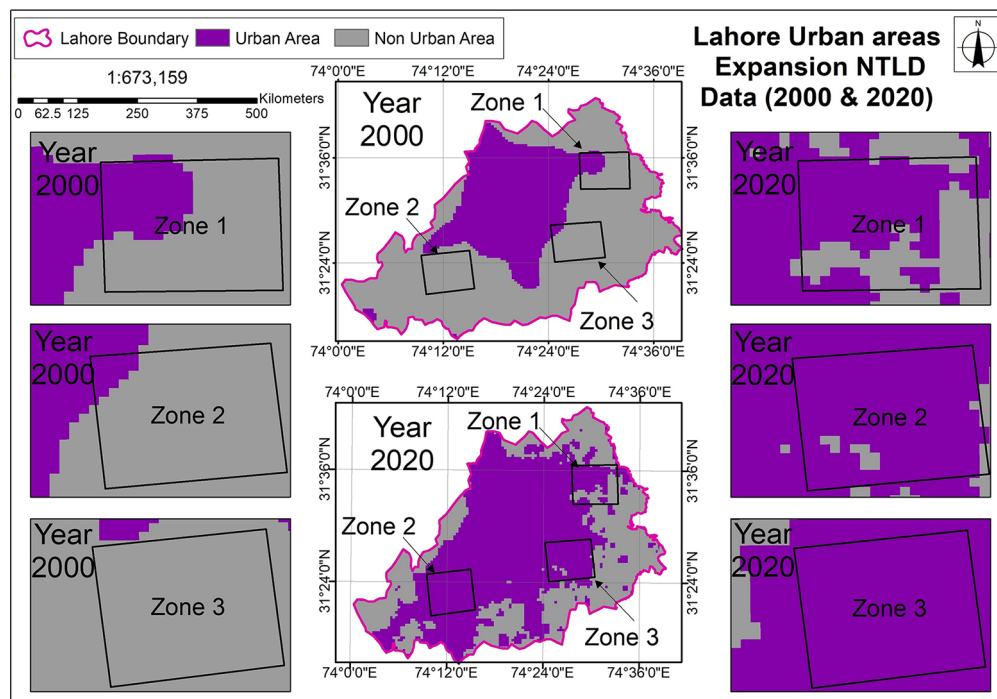
	Year		
	2000	2010	2020
Overall Accuracy	86.05	89.2	91.71
$\kappa$ Coefficient	78.8	81.53	85.4

To validate the classification results, we performed accuracy assessments using a postclassification tool on ENVI software, as shown in Table 7.

Basically, a confusion matrix cross-validates classification results and determines whether or not a classifier has been applied correctly. It is available in all image-classification software to determine classification accuracy. The back-end algorithm gives an estimation of the values assigned to a class, and if they were accurately classified uses a comparison signature that was made on the same image by the user.



(a)



(b)

Figure 4. (a) Classification map obtained using nighttime light data. (b) Comparison map obtained using nighttime light data.

Landsat 5-TM and 8-OLI

We also found an abrupt change in the urban area observable in Figure 5a, which depicts the Landsat classification results from the support vector machine classifier from 2000 to 2020. On the other hand, overall degradation can also be observed for total vegetation cover. Most of the urban area was converted from farmland to built-up area during the last 20 years. Furthermore, Figure 5b shows the comparison of three zones for both 2000 and 2020 using Landsat classification results. It can be seen there is an enormous change in urban area in all three zones.

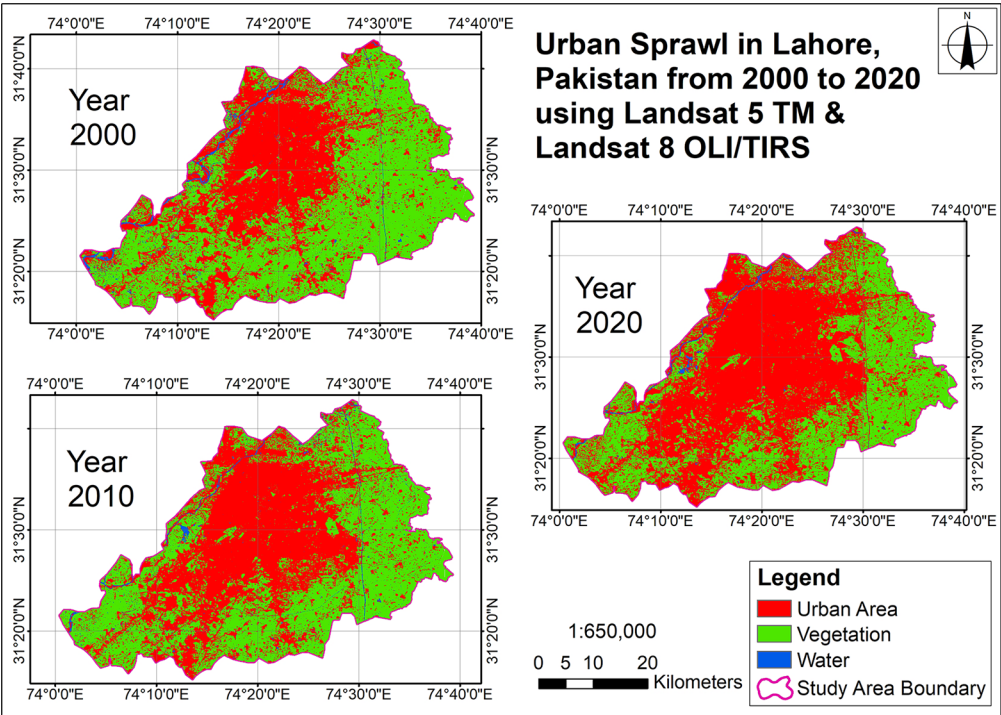
Table 8 shows the accuracy assessment calculations for Landsat imagery from 2000 to 2020.

Table 8. Overall accuracy and  $\kappa$  coefficients obtained using Landsat data sets.

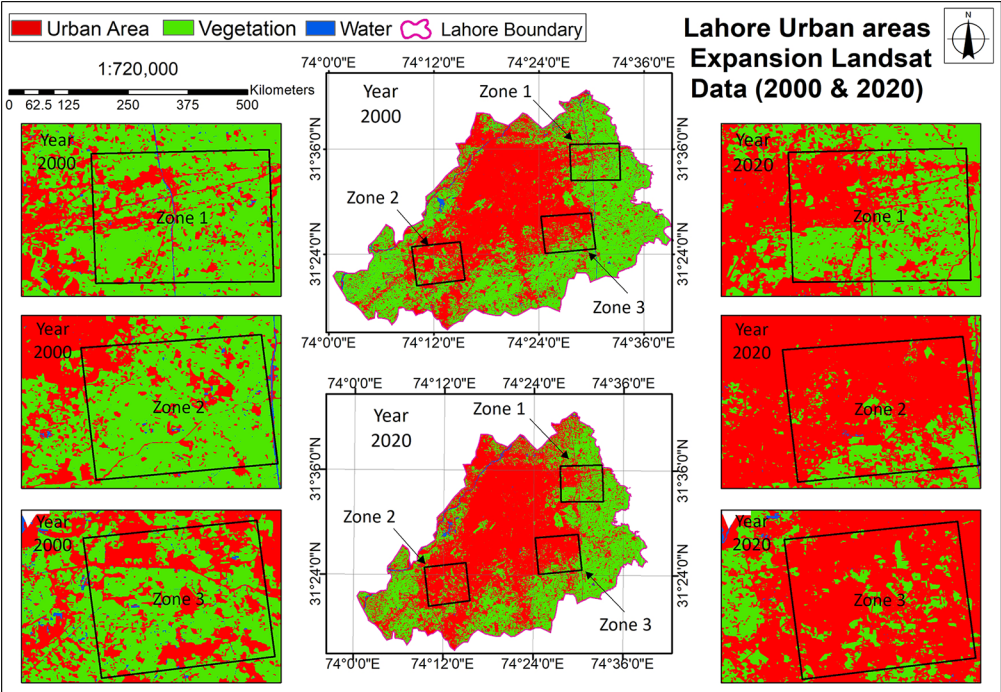
	Year		
	2000	2010	2020
Overall Accuracy	87.2	89.5	91.7
$\kappa$ Coefficient	71.5	80.3	83.03

EPC and Population-Density Increase

We have further sorted out World Bank data to determine the overall growth in EPC and population density. Figures 6 and 7 show an overall increase in both indicators, and Table 9 shows overall population increase.



(a)



(b)

Figure 5. (a) Land use classification map using Landsat data. (b) Comparison map using Landsat data.

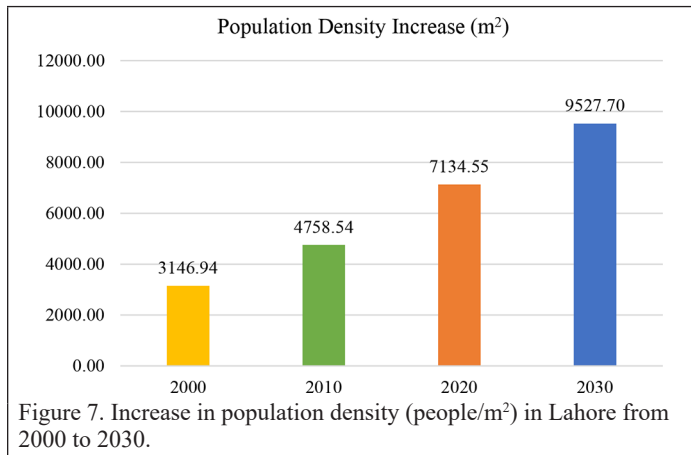
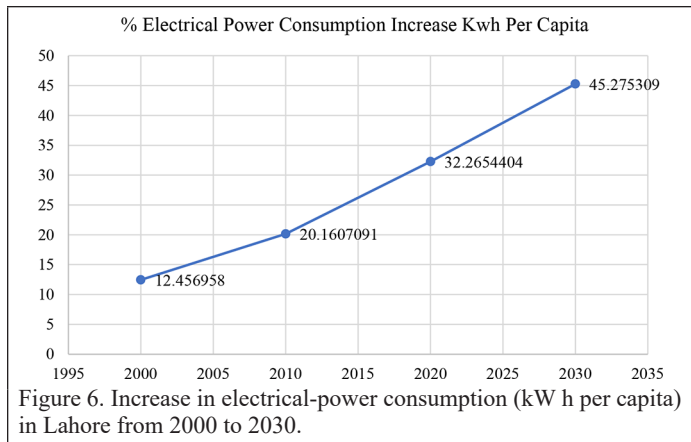


Table 9. Population-density increases.

Year	% Increase
2000	12.80
2010	19.36
2020	29.04
2030	38.78

### Vegetation Loss

Classification results were also used to identify the extent of vegetation loss from conversion of vegetation to urban area. The raster-analyst tool in ArcMap was used to subtract classified images for each year to find out the vegetation loss (Figure 8).

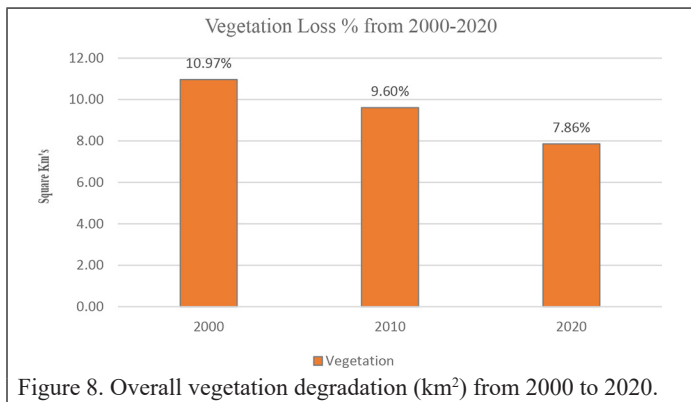


Table 10. Urban-area increase and vegetation loss.

Time Span	Urban Sprawl (%)	Vegetation Loss (%)
2000–2010	61.07	31.50
2010–2020	69.38	26.47
Overall		28.43

An overall loss of 28.43% in vegetation was observed from 2000 to 2020, as shown in Table 10.

### EPC and Population Density Correlated With NTL Data

To measure changes in the urban population, the DMSP nighttime light area data were correlated with EPC data. An increase in EPC was estimated by linear correlation between the total night light area, which was extracted from the nighttime light data set, and the EPC obtained from statistical data. Calculations were performed as previously stated, and we found high positive correlations for both indicators and NTLD (Figures 9 and 10), with gradual increases from 2000 to 2020.

### Proposed Location for a New Urban Town in Lahore

We constructed a spatial decision support system on ArcMap using the CommunityViz Scenario 360 tool. Figure 11 shows the weighting assumptions used for suitability analysis for each spatial layer and criterion automatically generated in CommunityViz.

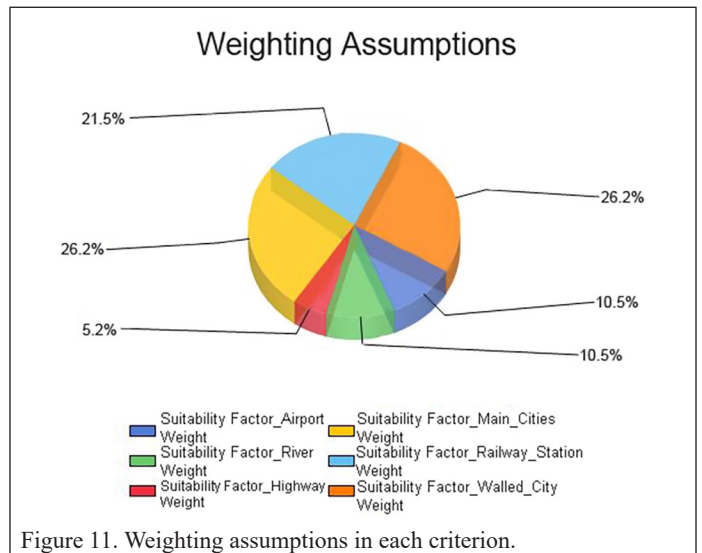
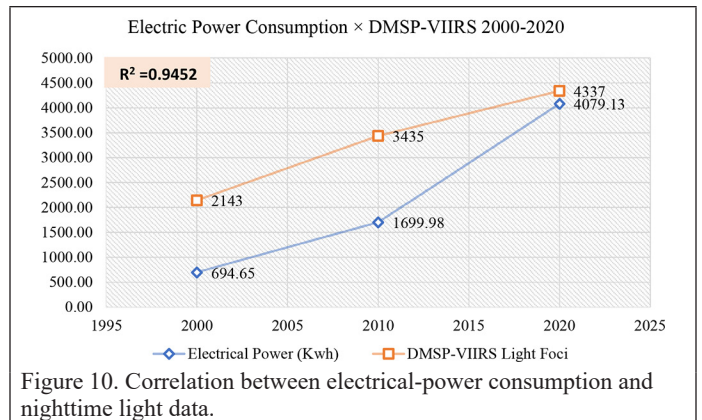
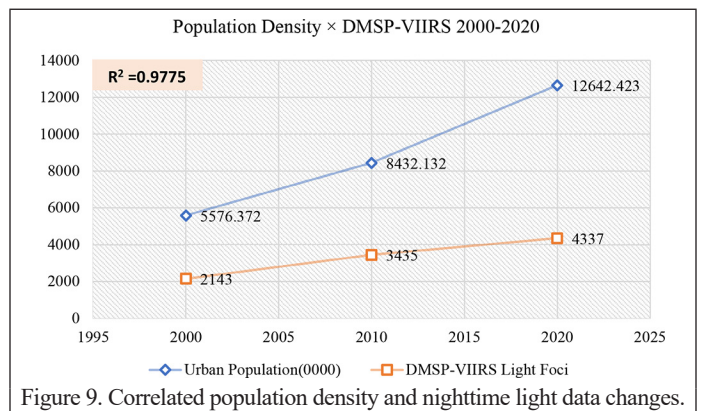




Figure 12 shows that Kot Begum in Ravi Town, in the northwest of the study area, is the best proposed location for the new urban town. This allows for social and environmental problems to be solved with geospatial techniques like remote sensing and encourages policy makers to pay more attention to and invest more in geospatial infrastructure as a means of solving most environmental problems.

## Discussion

We found that useful results can be obtained by using statistical data and DMSP/OLS and SNPP-VIIRS nighttime light data in terms of correlating economic indicators with urban populations and EPC. DMSP/OLS data and NPP-VIIRS data are the most common sources for mapping urban sprawl and determining economic indicators (Xia *et al.* 2019). During the rapid urban expansion of the past two decades, considerable agricultural land (farmland) has been lost, especially vegetation. It can also be seen that a linear correlation is a good estimator for population and EPC, and can be used to compare nighttime light data with other indicators.

However, recent research also recommends that the relationship between urban sprawl and socioeconomic indicators be used to help planners consider available energy resources for each city, according to population density and social needs. Unplanned and unmanaged urban expansion always creates problems that increase shantytowns, environmental pollution, deprivation, and discrimination of resources and budget misallocations in major cities. Uncontrollable urbanization is also effecting temperature changes in Lahore. It is possible that in the future, Lahore will become an urban heat island.

Another factor is that urban area expanded in the horizontal direction in Lahore over the past 40 years. If this had happened in the vertical direction instead, there would be more opportunity to accommodate a greater population and develop a more sustainable city. In the future, Lahore will face more challenges due to continuous urban expansion if there are no new urban towns or vertical development plans, in terms of both EPC and urban population. The annual GDP of Lahore will also be affected, because of high demand of EPC.

## Conclusions

This study found that there was a significant increase in the urban area of Lahore, Pakistan, from 2000 to 2020, which can be seen using both satellite data sets. The results showed a 33% in urban area, using nighttime light data. Data from DMSP/OLS, SNPP-VIIRS, and Landsat were compared for the years 2000 and 2020, and the urban centers were found to increase with the same patterns and tendencies. The urban area extended toward the southeastern parts of the city because of the river on the north side and the Indian border to the east.

NTLD is a good estimator of economic activities—i.e., EPC and population—as analysis shows an overall EPC increase of 21.6% over the past 20 years. Similarly, we also found an overall decrease, of approximately 28.43%, in vegetation land use, which showed a strong positive correlation with EPC ( $R^2 = 0.94$ ) and population density ( $R^2 = 0.97$ ) using total night light area. This study also provided a proposed location for a new urban town which is near to fresh water, highways, and other main cities. This new urban town can be developed in the vertical direction so that it can accommodate more people. As this location is on the Ravi River, it can also provide facilities for hydro-power projects that can be a strong initiative to produce more electricity to support a greater population.

## Acknowledgments

The authors would like to thank the local and provincial governments for providing the statistical data. In addition to NOAA/NGDC and NASA, satellite imagery is freely available for researchers. The authors would like to thank the anonymous reviewers for their constructive comments and suggestions for improving the manuscript.

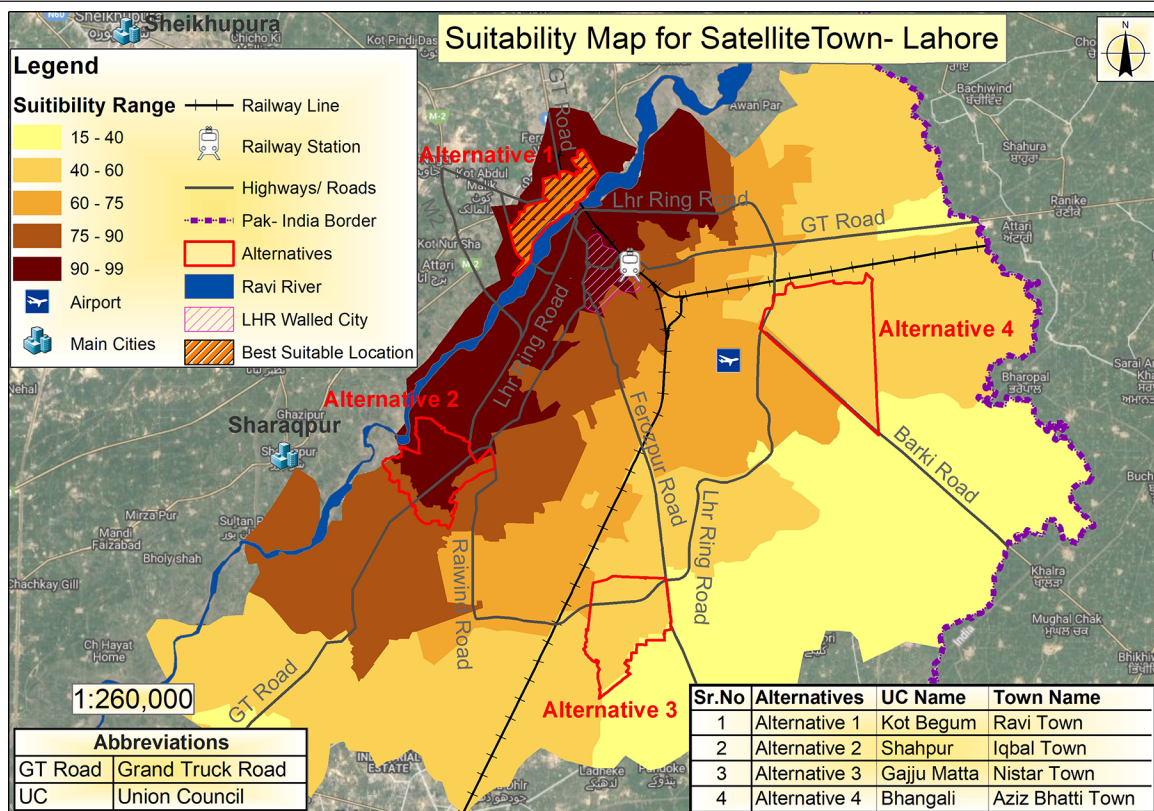


Figure 12. Proposed site for new urban town in Lahore.

## References

- Amaral, S., G. Câmara, A.M.V. Monteiro, J. A. Quintanilha and C. D. Elvidge. 2005. Estimating population and energy consumption in Brazilian Amazonia using DMSP night-time satellite data. *Computers, Environment and Urban Systems* 29(2):179–195.
- Amaral, S., A.M.V. Monteiro, G. Câmara and J. A. Quintanilha. 2006. DMSP/OLS night-time light imagery for urban population estimates in the Brazilian Amazon. *International Journal of Remote Sensing* 27(5):855–870.
- Cao, X., J. Chen, H. Imura and O. Higashi. 2009. A SVM-based method to extract urban areas from DMSP-OLS and SPOT VGT data. *Remote Sensing of Environment* 113(10):2205–2209.
- Deng, C. and C. Wu. 2013. Examining the impacts of urban biophysical compositions on surface urban heat island: A spectral unmixing and thermal mixing approach. *Remote Sensing of Environment* 131:262–274.
- Ding, L., Z. Shao, H. Zhang, C. Xu and D. Wu. 2016. A comprehensive evaluation of urban sustainable development in China based on the TOPSIS-entropy method. *Sustainability* 8(8):746.
- Dowall, D. E. and P. D. Ellis. 2009. Urban land and housing markets in the Punjab, Pakistan. *Urban Studies* 46(11):2277–2300.
- Huang, Q., X. Yang, B. Gao, Y. Yang and Y. Zhao. 2014. Application of DMSP/OLS nighttime light images: A meta-analysis and a systematic literature review. *Remote Sensing* 6(8):6844–6866.
- Imhoff, M. L., W. T. Lawrence, D. C. Stutzer and C. D. Elvidge. 1997. A technique for using composite DMSP/OLS “city lights” satellite data to map urban area. *Remote Sensing of Environment* 61(3):361–370.
- Kiran Chand, T. R., K.V.S. Badarinath, C. D. Elvidge and B. T. Tuttle. 2009. Spatial characterization of electrical power consumption patterns over India using temporal DMSP-OLS night-time satellite data. *International Journal of Remote Sensing* 30(3):647–661.
- Letu, H., M. Hara, H. Yagi, K. Naoki, G. Tana, F. Nishio and O. Shuhei. 2010. Estimating energy consumption from night-time DMSP/OLS imagery after correcting for saturation effects. *International Journal of Remote Sensing* 31(16):4443–4458.
- Liu, Y., Y. Wang, J. Peng, Y. Du, X. Liu, S. Li and D. Zhang. 2015. Correlations between urbanization and vegetation degradation across the world’s metropolises using DMSP/OLS nighttime light data. *Remote Sensing* 7(2):2067–2088.
- Liu, Z., C. He, Q. Zhang, Q. Huang and Y. Yang. 2012. Extracting the dynamics of urban expansion in China using DMSP-OLS nighttime light data from 1992 to 2008. *Landscape and Urban Planning* 106(1):62–72.
- Lo, C. P. 2002. Urban indicators of China from radiance-calibrated digital DMSP-OLS nighttime images. *Annals of the Association of American Geographers* 92(2):225–240.
- Ma, T., Y. Zhou, C. Zhou, S. Haynie, T. Pei and T. Xu. 2015. Night-time light derived estimation of spatio-temporal characteristics of urbanization dynamics using DMSP/OLS satellite data. *Remote Sensing of Environment* 158:453–464.
- Mellander, C., J. Lobo, K. Stolarick and Z. Matheson. 2015. Night-time light data: A good proxy measure for economic activity? *PLoS One* 10(10):e0139779.
- Pandey, B., P. K. Joshi and K. C. Seto. 2013. Monitoring urbanization dynamics in India using DMSP/OLS night time lights and SPOT-VGT data. *International Journal of Applied Earth Observation and Geoinformation* 23:49–61.
- Shi, K., B. Yu, Y. Huang, Y. Hu, B. Yin, Z. Chen, L. Chen and J. Wu. 2014. Evaluating the ability of NPP-VIIRS nighttime light data to estimate the gross domestic product and the electric power consumption of China at multiple scales: A comparison with DMSP-OLS data. *Remote Sensing* 6(2):1705–1724.
- Small, C., F. Pozzi and C. D. Elvidge. 2005. Spatial analysis of global urban extent from DMSP-OLS night lights. *Remote Sensing of Environment* 96(3–4):277–291.
- Sutton, P. 1997. Modeling population density with night-time satellite imagery and GIS. *Computers, Environment and Urban Systems* 21(3–4):227–244.
- Tao, W. 2013. Interdisciplinary urban GIS for smart cities: Advancements and opportunities. *Geo-spatial Information Science* 16(1):25–34.
- Taubenböck, H., T. Esch, A. Felber, M. Wiesner, A. Roth and S. Dech. 2012. Monitoring urbanization in mega cities from space. *Remote Sensing of Environment* 117:162–176.
- Xia, N., L. Cheng and M. Li. 2019. Mapping urban areas using a combination of remote sensing and geolocation data. *Remote Sensing* 11(12):1470.
- Xu, T., G. Coco and J. Gao. 2020. Extraction of urban built-up areas from nighttime lights using artificial neural network. *Geocarto International* 35(10):1049–1066.
- Yi, K., H. Tani, Q. Li, J. Zhang, M. Guo, Y. Bao, X. Wang and J. Li. 2014. Mapping and evaluating the urbanization process in northeast China using DMSP/OLS nighttime light data. *Sensors* 14(2):3207–3226.
- Yin, Z., X. Li, F. Tong, Z. Li and M. Jendryke. 2020. Mapping urban expansion using night-time light images from Luojia1-01 and International Space Station. *International Journal of Remote Sensing* 41(7):2603–2623.
- Zhang, J., P. Li and J. Wang. 2014. Urban built-up area extraction from Landsat TM/ETM+ images using spectral information and multivariate texture. *Remote Sensing* 6(8):7339–7359.
- Zhang, Q. and K. C. Seto. 2011. Mapping urbanization dynamics at regional and global scales using multi-temporal DMSP/OLS nighttime light data. *Remote Sensing of Environment* 115(9):2320–2329.
- Zhao, X., B. Yu, Y. Liu, S. Yao, T. Lian, L. Chen, C. Yang, Z. Chen and J. Wu. 2018. NPP-VIIRS DNB daily data in natural disaster assessment: Evidence from selected case studies. *Remote Sensing* 10(10):1526.
- Zhou, Y., S. J. Smith, C. D. Elvidge, K. Zhao, A. Thomson and M. Imhoff. 2014. A cluster-based method to map urban area from DMSP/OLS nightlights. *Remote Sensing of Environment* 147:173–185.

## Monitoring Earth Hazard with Remote Sensing Techniques

Natural and human disasters are increasingly affecting global communities worldwide in recent decades. With the increasing human population and urbanization, the earth is inevitably more susceptible to manmade hazards. Global warming and its associated environmental instability increase the frequency and severity of the disaster. Rapid Climate change is linked with meteorological events with a high degree of risk probability causing flood disasters. Implementation of proper hazard management such as disaster prevention, disaster preparedness, and adequate disaster relief would reduce the impact of natural disasters. Usage of the convectional earth observation model helps hazard management with a reliable solution but cannot provide early prediction of disaster occurrence, saving people's lives. However, using remote sensing techniques would enable warning systems by building futuristic codes that predict the hazards and warn people on time with greater accuracy. Remote sensing imagery provides a quick method for assessing the variation of hazard impacts, coastal inundation, erosion, and majority affected flood plains using intelligent, visionary technology. The data gathered from sensors provide valuable insights about the spatial phenomena that aid scientists in making accurate decisions about the forecast patterns. Above all satellites, remote sensing is used to detect global environmental problems, explore resources, and monitor disasters by capturing the earth's surface during altered weather conditions. This helps in the early detection of disaster patterns with futuristic mitigation procedures.

The sensors technology captures images of fires, flooding, and volcanic eruption can create a visual impact during the response phase that aids in readiness actions when people are viable to disaster risk. Earth observation systems and GIS helps professionals to make effective project planning with a more accurate analysis. The utilization of various spectral bands such as Visible, infrared, thermal infrared, and synthetic aperture radar provides adequate coverage of environmental patterns and allows technology enhancement to analyze data. Meteorological satellites use High-resolution transmission sensors for cyclone monitoring, intensity assessment, and storm surges. Geo-stationary satellites use global coverage sensors for flood and drought management by collections of multi-date imaginary data for rainfall and river stages. Using its unique spectral signature, it identifies the water standing areas, the sand casting of agricultural lands, and marooned villages to enable hazard recovery plans. SAR sensing system is used to detect forest fires and forest monitoring using microwave techniques to acquire sensory images. There are some challenges about using sensors for hazard prediction where research prospects are needed. As smart sensors use advanced technologies and complex data for prediction, data breaches would lead to misinterpretation of results, increasing the risk to

human lives. An adequate skilled workforce is required to analyze the collected sensor data. In the future, integrating IoT and artificial intelligence would create autonomous drones that aid in inspecting the geographical patterns in multi-dimensional views to accelerate high definitions imagery for efficient prediction of results. This special issue enumerates the role of remote sensors for earth hazard predictions and future advancements. We welcome scholars and practitioners of this platform to emphasize this topic and present submissions that fall within the scope of remote sensing techniques for the accurate prediction of environmental hazards.

The topics of interest include:

- Role of Artificial intelligence in generating patterns in sensor data
- Disaster management cycle and it's important in hazard mitigation
- Advantages of geometrics in disaster risk management
- Usage and applications o GIS in flood forecasting
- Advanced Earth observation system tools for project planning
- RadarSat and use cases in detecting oil seeps
- Big data and its uses for accurate data collection in sensors
- Role of climate change in creating environmental risk
- Advancement in satellite sensors for earth's behavioral prediction
- Role of autonomous drones in capturing multispectral images

**Deadline for Manuscript Submission**  
**June 5, 2022**

**Submit your Manuscript to**  
**<http://asprs-pers.edmgr.com>**

### Guest Editors

**Dr. Priyan Malarvizhi Kumar**, mkprian@khu.ac.kr and p.malarvizhikumar@ieee.org, *Department of Computer Science and Engineering, Kyung Hee University, South Korea.*

**Dr. Fatemeh Afghah**, fatemeh.afghah@nau.edu, *School of Informatics, Computing and Cyber Systems, Northern Arizona University.*

**Dr. Manimuthu Arunmozhi**, arunmozhi.m@ntu.edu.sg, *Cybersecurity Research Center (CYSREN), Nanyang Technological University, Singapore.*



# An Optimal GeoAI Workflow for Pan-Arctic Permafrost Feature Detection from High-Resolution Satellite Imagery

Mahendra R. Udawalpola, Amit Hasan, Anna Liljedahl, Aiman Soliman, Jeffrey Terstriep, and Chandi Witharana

## Abstract

*High-spatial-resolution satellite imagery enables transformational opportunities to observe, map, and document the micro-topographic transitions occurring in Arctic polygonal tundra at multiple spatial and temporal frequencies. Knowledge discovery through artificial intelligence, big imagery, and high-performance computing (HPC) resources is just starting to be realized in Arctic permafrost science. We have developed a novel high-performance image-analysis framework—Mapping Application for Arctic Permafrost Land Environment (MAPLE)—that enables the integration of operational-scale GeoAI capabilities into Arctic permafrost modeling. Interoperability across heterogeneous HPC systems and optimal usage of computational resources are key design goals of MAPLE. We systematically compared the performances of four different MAPLE workflow designs on two HPC systems. Our experimental results on resource utilization, total time to completion, and overhead of the candidate designs suggest that the design of an optimal workflow largely depends on the HPC system architecture and underlying service-unit accounting model.*

## Introduction

Big image-data analysis has become essential in an array of scientific applications, such as computer vision (Kucuk *et al.* 2017), medical imaging (El-Baz and Suri 2020), materials science (Okunev *et al.* 2020), and astronomy (Kremer *et al.* 2017). The advancements of satellite sensor technology, coupled with the ever-increasing spatial resolution and temporal frequency of image acquisitions, ideally position remote sensing applications in the big-data landscape (Wang *et al.* 2015; Liu *et al.* 2018). Satellite imagery archives are being radically transformed from terabytes to petabyte scale (Witharana *et al.* 2021). The sheer volumes of imagery pose new challenges in storage, analysis, and visualization techniques (Liu 2015; Y. Ma *et al.* 2015), and the requirements exceed the capabilities of existing general-purpose computing resources. Therefore, highly efficient workflows with high-performance computing resources are required for implementing big-imagery applications.

High-throughput computing (HTC) and high-performance computing (HPC) are both important in high-resolution imagery analysis on a petabyte scale. HTC is used for workloads that consist of tasks that are independent of each other and can start or complete in any order (e.g., automated feature extraction from thousands of satellite images in repeated mapping applications). Therefore, there is a lot of flexibility in scheduling these HTC jobs in HPC systems. In contrast, an HPC

workload is characterized by its scalability or running time. Typically, an HPC workload consists of a single job that coordinates multiple processes which run at the same time. When running these jobs, input–output requirements are important. Usually, HTC tasks operate on a small volume of data and HPC workloads operate on large volumes of data. But in running many HTC jobs, the limitations of input–output bandwidth become significant. Usually, most supercomputers are designed for HPC workloads. Huerta *et al.* (2019) argue that new applications require a paradigm shift in computing architecture to address large data sets, deep-learning algorithms, and hybrid workloads using both HPC and HTC. It is imperative to find out how applications with hybrid workloads can be run efficiently in existing HPC resources. Remote sensing (RS) big-data applications typically consist of hybrid workloads requiring efficient use of existing HPC systems. Lee *et al.* (2011) reviewed advances in HPC applied to remote sensing problems, and in particular HPC-based platforms, such as multi-processor systems and large-scale and heterogeneous networks of computers.

A seamless application of HPC resources for translating big satellite imagery into science-ready products can enable knowledge discovery at the nexus of the human and natural systems (Chi *et al.* 2016). In recent years, the use of HPC resources has become an inextricable component in big-imagery applications (Wang *et al.* 2018). A plethora of applications can be found in the literature involving big imagery and HPC. Amat *et al.* (2015) developed a workflow for light-sheet microscopy, which involves several tens of terabytes of data. Schmied *et al.* (2016) compared the performance of an automated workflow on a single workstation and an HPC cluster. Liu *et al.* (2016) analyzed a geosciences workflow on multi-core processors and graphical processing units (GPUs), achieving a 5× speedup on a multi-core processor and a 43× speedup for some parts of the workflow on GPU. In a recent study, Al-Saadi *et al.* (2021) compared workflow application designs for high-resolution satellite-imagery analysis. They analyzed three workflow designs using the Extreme Science and Engineering Discovery Environment (XSEDE) HPC system for two use cases, for a total of 4672 high-resolution satellite and aerial images and 8.35 TB of data.

Modern HPC systems consist of many HPC computer nodes. Each node contains multi-core central processing units (CPUs) and multi-GPUs. RS big-data applications need to use both CPUs and GPUs in their workflow, because GPUs are efficient at processing RS images and CPUs are efficient at executing complex algorithms. Several traditional parallel paradigms are widely used in these systems, such as OpenMP and Message Passing Interface. Implementation of parallel RS algorithms using Message Passing Interface is difficult, and HPC systems are not optimized for data-intensive computing (Wang *et al.* 2016). RS workloads involve both HPC and HTC features, so they are considered hybrid HPC/HTC workloads. A single RS workload may not be large enough for use in many multiple nodes. It is therefore critical to examine how to optimize RS hybrid HPC/HTC workloads in a single node with

Mahendra R. Udawalpola, Amit Hasan, and Chandi Witharana are with the Department of Natural Resources and the Environment, University of Connecticut (mahendra.udawalpola@uconn.edu).

Anna Liljedahl is with the Woodwell Climate Research Center, Falmouth, MA.

Aiman Soliman and Jeffrey Terstriep are with the National Center for Supercomputing Applications, University of Illinois Urbana–Champaign.

Contributed by Alper Yilmaz, August 30, 2021 (sent for review September 17, 2021).

Photogrammetric Engineering & Remote Sensing  
Vol. 88, No. 3, March 2022, pp. 181–188.  
0099-1112/22/181–188

© 2022 American Society for Photogrammetry  
and Remote Sensing  
doi: 10.14358/PERS.21-00059R2

multi-CPU and multi-GPU cores. The use of HPC resources is measured using service units (SUs). RS workflows with big-imagery analysis need to be optimized for both SUs and running time. Different HPC systems measure the use of SUs by different accounting models. These different configurations present new challenges in designing efficient workflows for targeted applications which require both CPU and GPU processing.

Traditional remote sensing image-analysis algorithms fail to grapple with the image complexities and high-level semantics arising from sub-meter-resolution satellite imagery (Blaschke 2010; Blaschke *et al.* 2014; Lang *et al.* 2018). Sophisticated algorithms which exploit color, texture, spatial arrangement, and context, and construct high-level abstractions based on low-level motifs, are needed for automated object detection, segmentation, and classification (Ma *et al.* 2019). Deep-learning convolutional neural nets (DLCNNs; LeCun *et al.* 2015) have shown great potential for semantic object-instance segmentation in detecting and delineating each distinct object in an image of common objects from everyday images. The success of DLCNNs in computer-vision applications has received great interest from the remote sensing community (Ma *et al.* 2019). But DLCNN algorithms are computationally intensive and demanding of memory. Thus, it is important to optimize data management, image processing, classification, and visualization techniques, because they serve as key bottlenecks in image-to-assessment pipelines.

Archived observation data was predicted by the Open Geospatial Consortium to exceed an exabyte by 2015 (Karmas *et al.* 2016). But it is estimated that up to 95% of the data present in existing archives have never been accessed (Nikolaou *et al.* 2014). Over the last decade, the entire Arctic has been imaged at 0.5-m resolution several times by commercial satellite sensors of Maxar Technologies (previously known as DigitalGlobe; Witharana *et al.* 2020). The image repository at the Polar Geospatial Center at the University of Minnesota provides transformational opportunities to observe, monitor, and document permafrost thaw occurring across the Arctic tundra, which is a logistically challenging region with an extremely sparse field observation network. Landscapes of Alaska, Canada, and Russia harbor approximately 5 million km<sup>2</sup> of tundra. But imagery is underutilized, and derived science products are rare despite their unprecedented potential for pan-Arctic permafrost monitoring and modeling applications.

Permafrost—unique landscapes comprising Earth materials that remain at or below 0°C for at least two consecutive years—covers approximately 24% of the exposed land surface of the Northern Hemisphere (Brown *et al.* 1997). Ice-rich permafrost can be identified by atypical surface features called ice-wedge polygons (IWP), which are underlain by ice wedges several meters wide and deep that form a connected network across the tundra (Kanevsky *et al.* 2016). Vegetation and geology maps suggest that about two-thirds or more of the Arctic landscape is occupied by polygonal ground (Kokelj *et al.* 2015; Reynolds *et al.* 2019) and therefore ice-rich ground, but the exact extent and the prevailing IWP types (i.e., whether the ice wedges experience melt or not) are largely unknown.

Over recent decades, ice-wedge degradation—the transformation of low-centered polygons into high-centered polygons—has been documented at several locations across the Arctic tundra in the field and through localized remote sensing analyses (Liljedahl *et al.* 2016; Steedman *et al.* 2017). The shift from one IWP type to the other is documented to occur in less than a decade (Liljedahl *et al.* 2016), with unusually warm summers, wildfires, or human activities initiating the onset of ice-wedge degradation (Jorgenson *et al.* 2006; Jones *et al.* 2015; Reynolds *et al.* 2020). Degradation of ice wedges is a quasi-cyclic process, often occurring over a shorter time scale than the formation of new permafrost (aggradation), with the latter controlled by the accumulation of organic and mineral soil above the ice wedge (Kanevskiy *et al.* 2017). Understanding the spatiotemporal dynamics behind the evolution of ice-wedge polygonal tundra demands objective and detailed maps consolidating the extent of ice wedges and their prevailing successional stages (Witharana *et al.* 2021).

Despite the alarming signals, the Arctic science community has a limited understanding of the spatiotemporal continuity of these

otherwise locally observed changes. The lack of knowledge about the larger geographical extent and successional stage of IWPs introduces uncertainties to regional and pan-Arctic estimates of carbon, water, and energy fluxes. Remote sensing provides transformational opportunities to observe, monitor, and measure the Arctic polygonal landscape at multiple spatial scales and in varying temporal windows (Nitze *et al.* 2018; Witharana *et al.* 2019). IWPs are difficult to detect in any remote sensing imagery with a spatial resolution coarser than 4 m (Muster *et al.* 2012). Sub-meter-resolution commercial satellite imagery (e.g., Maxar) demonstrates greater promise for accurate delineation and characterization of ice-wedge polygonal networks. Due to IWPs' varying spectral and morphometric characteristics, visual inspection and manual digitization has so far been the most widely adopted and promising method for delineating polygons from high-resolution remote sensing imagery (Witharana *et al.* 2021). A considerable number of local-scale studies have analyzed ice-wedge degradation processes using satellite imagery, as well as imagery and lidar data from manned and unmanned aerial vehicles (Muster *et al.* 2013). Most studies to date have relied on manual image interpretation or semi-automated approaches (Skurikhin *et al.* 2014) and been confined to site-to-local-scale mapping. Therefore, there is a need and an opportunity to use very-high-spatial-resolution imagery in regional-scale mapping efforts to spatiotemporally document microtopographic changes due to thawing ice-rich permafrost.

Despite the remarkable performance of DLCNNs in everyday image understanding, bottlenecks still exist in the translation to geo-object detection from remote sensing imagery. Image dimensions, multiple spectral channels (more than the standard red, green, and blue channels), spatial reference, seasonality, and most importantly the semantic complexity of geo-objects aggregated into multiple spatial scales impose greater friction on the inferential strength of DLCNN model predictions. The scalability of automated analysis over millions of square kilometers comprising heterogeneous landscapes reinforces the need for efficient workflows. To surmount these challenges, we have developed a novel image-to-assessment pipeline—Mapping Application for Arctic Permafrost Land Environment (MAPLE)—which can be deployed in heterogeneous supercomputing resources. MAPLE is a first-of-its-kind pan-Arctic mapping effort that attempts to characterize microtopography using sub-meter-resolution imagery without compromising geographical extent.

The overarching goal of MAPLE is to produce the first pan-Arctic IWP map using a large volume of commercial satellite imagery available at the Polar Geospatial Center and HPC resources from computing facilities funded by the US National Science Foundation. In the first stage, we will produce a circumpolar IWP map for the regions that have been identified as high-probability ground ice content by Brown *et al.* (2002). Then we will progressively extend the mapping to medium- and low-probability ground ice areas of Brown *et al.* (2002), ultimately covering the entire tundra. The ongoing mapping area (Figure 1) includes around 25 000 satellite images and over 180 TB of data.

The main objective of this article is to analyze the computational efficiency of the MAPLE workflow in heterogeneous HPC environments, which involve both CPUs and GPUs. We further aim to understand how different workflow designs interact with underlying SU accounting models of the HPC systems, which in turn support optimal resource usage to complete image-analysis problems at hand.

## Methods

### Mapping Application for Arctic Permafrost Land Environment (MAPLE)

Figure 2 shows a generalized framework for high-performance image analysis with MAPLE using imagery from the Polar Geospatial Center and computing resources from multiple computing environments, such as Frontera at the Texas Advanced Computing Center and XSEDE, to produce science-ready products. The MAPLE workflow (Figure 3) is threefold: image preprocessing, DLCNN prediction (inferencing), and postprocessing. While the first and last segments involve CPU implementations, prediction can operate on GPUs or CPUs. MAPLE takes

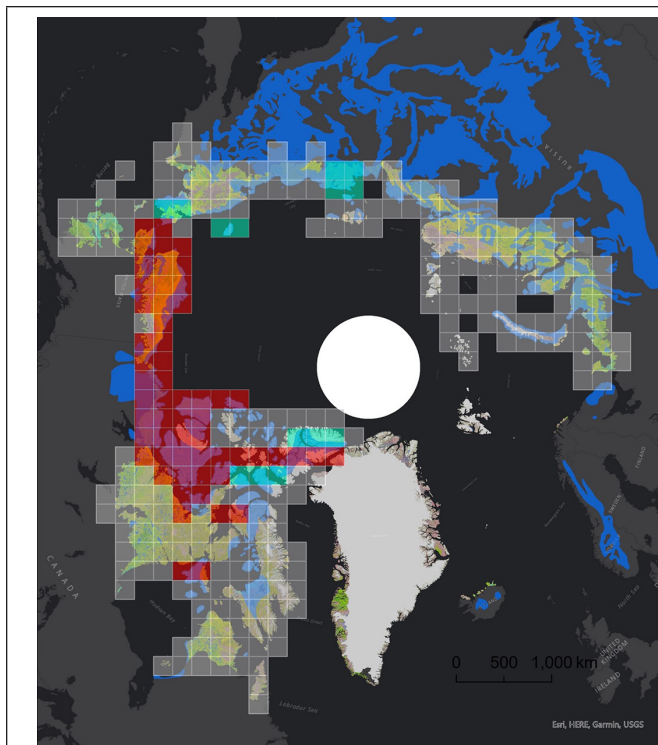


Figure 1. Ongoing deployment of Mapping Application for Arctic Permafrost Land Environment (MAPLE) in Arctic polygonal tundra. The map is overlain by the circumpolar Arctic vegetation map of Reynolds *et al.* (2019) and the high-probability ground ice map of Brown *et al.* (2002). Colored grid cells (200×200 km) represent the progress of the mapping. Red and dark-green squares represent completed areas and areas in progress, respectively. Gray squares represent the area to be mapped. Blue shading represents the Circum-Arctic Map of Permafrost and Ground-Ice Conditions, Version 2 (Brown *et al.* 2002), and light-green shading represents the Circumpolar Arctic Vegetation Map (Reynolds *et al.* 2020), which were used as guides to prioritize mapping areas.

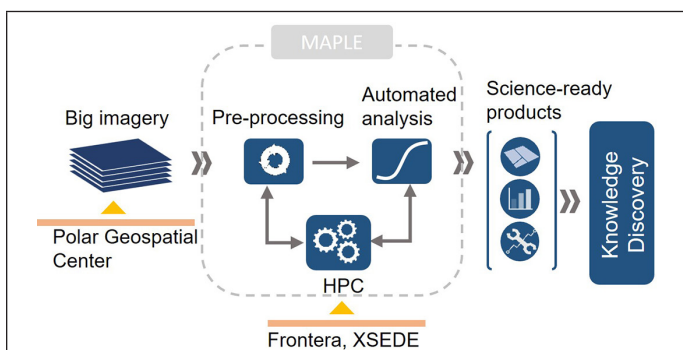


Figure 2. General semantic diagram for high-performance analysis of very-high-spatial-resolution satellite imagery using Mapping Application for Arctic Permafrost Land Environment (MAPLE). The images are obtained from the Polar Geospatial Center at the University of Minnesota, then processed by the MAPLE workflow using high-performance computing (HPC) resources from the Frontera system at the Texas Advance Computing Center and the Bridges system from the Extreme Science and Engineering Discovery Environment (XSEDE). The ice-wedge polygon map and the surface water-body map serve as the two key science-ready products of the workflow.

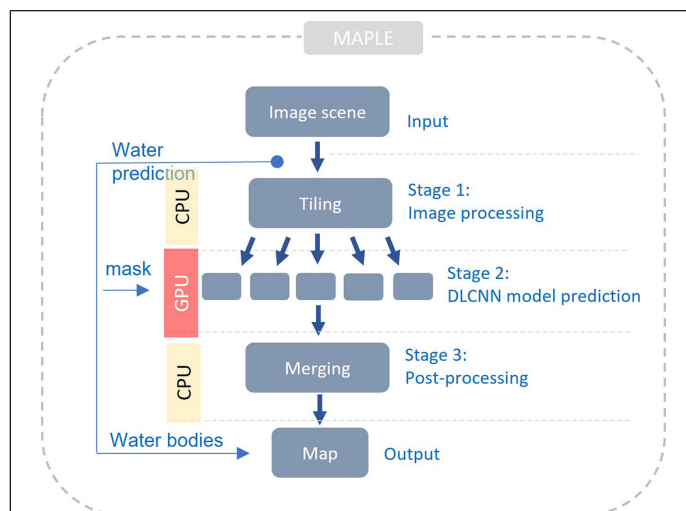


Figure 3. General semantic diagram of the Mapping Application for Arctic Permafrost Land Environment (MAPLE) workflow. MAPLE is a modular workflow consisting of three stages relying on both central processing unit (CPU) and graphical processing unit (GPU) resources. Stage 1 is a CPU-based implementation, which involves two operations: automated extraction of surface water bodies and tiling of the input image scene into small patches for use in later stages. Stage 2 is a GPU-based operation. It implements the deep-learning convolutional neural net (DLCNN) algorithm for predicting ice-wedge polygons. In stage 3, stitching of shape files and removal of duplicates are performed using CPU resources. The final output of the MAPLE workflow are the ice-wedge polygon map and surface water-body map of the input image scene.

high-resolution satellite images as input and outputs two key geospatial layers: ice-wedge polygons and surface water bodies. The spatial resolution of satellite imagery is acquired at 0.5 m, comprising multispectral channels (blue, green, red, near-infrared, or more depending on the sensor) at 16-bit radiometric resolution with a typical footprint of 20×20 km (i.e., 160 million pixels/image). At the initial stage, we process the high-probability region of the IWP map using MAPLE. Figure 1 shows the progress of MAPLE deployment in polygonal tundra.

We use Mask RCNN (He *et al.* 2016) as the key DLCNN model in MAPLE. DLCNN models show better performance in GPUs than in CPUs. Usually, the amount of memory available in GPUs (on average, 16 GB) is much smaller than that in CPUs. Therefore, we cannot perform DLCNN operations for the complete satellite image in GPU memory. Due to this limitation, we need to split the satellite image, which is around 5 GB on disk (40 000×40 000 pixels) into small tiles (200×200 pixels). To alleviate any terminological ambiguities, throughout this article we will use the term *image scene* to refer to an entire satellite image and the term *image tile* to refer to a subsetting array obtained by tiling the *image scene* according to predefined tile dimensions. Due to this splitting, the ice-wedge polygons can be intersected by the boundaries and may be missed in the prediction stage. To alleviate this effect, we keep a 10% overlap between image tiles, resulting in more than 40 000 image tiles per image scene. These image tiles are saved using a compressed HDF5 binary data format, after excluding water bodies and No-data areas. Subsequently, compressed tiles are accessed in parallel within the workflow and output detected ice-wedge polygons. Each parallel process stores predicted ice-wedge polygons as an individual shape file.

In the postprocessing stage (stage 3), the shape files generated by each GPU are stitched into a single shape file. The resulting shape file contains duplicate polygons along the seams of images tiles due to the 10% overlap. We remove those duplicate polygons during this stage. Figure 4 depicts automated mapping results of ice-wedge polygons and water bodies from example locations comprising different tundra types in Alaska and Canada.



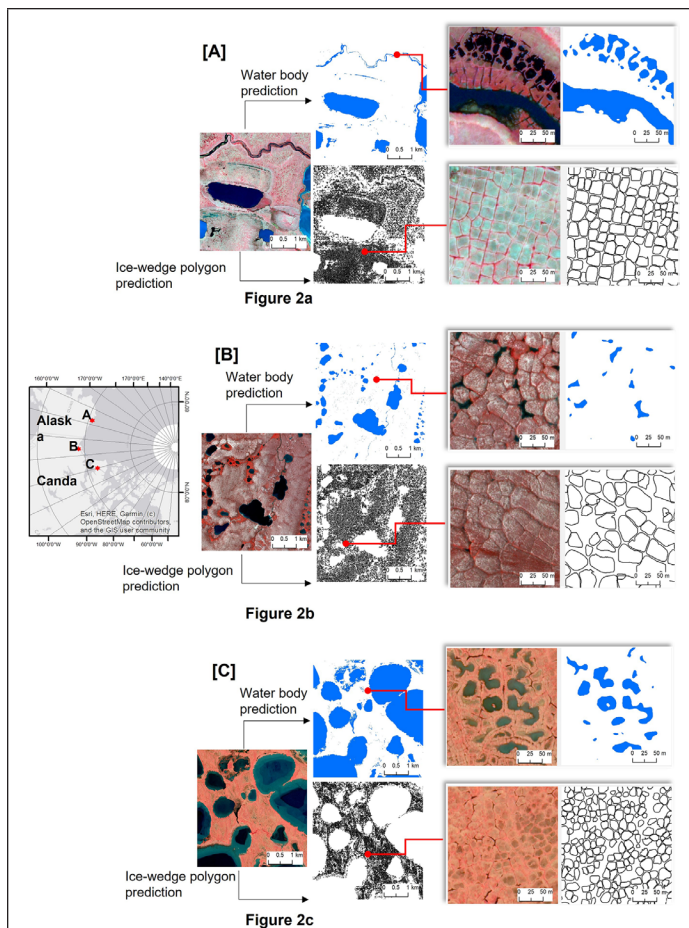


Figure 4. Sample input image and output ice-wedge polygons and water bodies of different scales for the Mapping Application for Arctic Permafrost Land Environment (MAPLE) workflow for (a) the North Slope of Alaska, and (b and c) Canada (see inset map at left). In each subfigure, the leftmost image shows the high-resolution satellite image. The second column shows the water-body map (blue) and ice-wedge polygon map of the corresponding area. The third column shows a zoomed view of two separate areas of the previous image patch. The rightmost column shows the water-body map (blue) and ice-wedge polygon map of the previous images. Imagery © 2016 DigitalGlobe, Inc.

An efficient workflow is required, because we need to process thousands of high-resolution satellite images. We use several techniques to optimize our workflow. The first is to minimize the area of processing by removing large numbers of water bodies. The Arctic region contains many water bodies, on scales from sub-meter to hundreds of meters. The MAPLE workflow first detects these water bodies using techniques developed by Kaiser *et al.* (2021). The predicted water from stage 1 of the workflow is used as a precursor layer for tiling the image. This will avoid unnecessary implementation of the IWP prediction algorithm on water areas in stage 2. Iterative prediction and use of the water mask not only produces a sub-meter-scale map of surface water but also speeds up the IWP prediction. The second optimization strategy is to remove image overlaps. A given satellite footprint has a considerable number of spatial overlaps with its neighbors, due to different imaging times and different sensors. We can significantly reduce the processing volume and computing resources (caused by duplicate application of the DLNN model on the same spatial locales) by removing these image overlaps. We have developed an algorithm that calculates the image overlaps and excludes them from processing in our workflow for a given image footprint.

### Model Training

We used a transfer learning strategy to retrain the Mask RCNN network. Using the online tool VGG Image Annotator, an annotated ice-wedge

polygon data set was created from satellite imagery comprising heterogeneous tundra types. We randomly selected 512 cropped subsets from different tundra types (tussock, non-tussock, and sedge) considering the spectral and spatial variability. The training data set consists of 9200 hand-annotated ice-wedge polygons. We started with pretrained weights generated by the COCO data set and trained only the head layers of the Mask RCNN network. The training was implemented using an NVIDIA GeForce RTX 2080 GPU with 10 GB of memory. We trained the Mask RCNN model with a mini-batch size of two image tiles, 250 steps per epoch, a learning rate of 0.001, a learning momentum of 0.9, a weight decay of 0.0001, and 50 epochs.

### Workflow Designs

Modern HPC resources such as Frontera and XSEDE consist of multiple nodes. Each node contains multiple CPUs and GPUs. Each CPU and GPU contains multiple cores. Programs should be designed to use these resources optimally. Figure 5 shows a semantic diagram of the sequential workflow (design 1) in a single computing node. In this setup, we do not use multiple CPUs and GPUs available in the node. The three stages of preprocessing, inferencing, and postprocessing are executed sequentially.

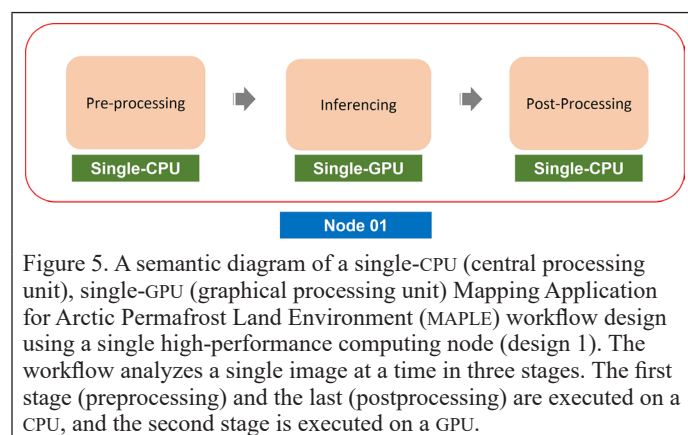


Figure 6 shows a semantic diagram of the design in which multiple GPUs in a single computing node are used in the inferencing stage. Here the image tiles generated in the preprocessing stage are stored in a single multi-threaded queue and processed using multiple GPUs in a single node.

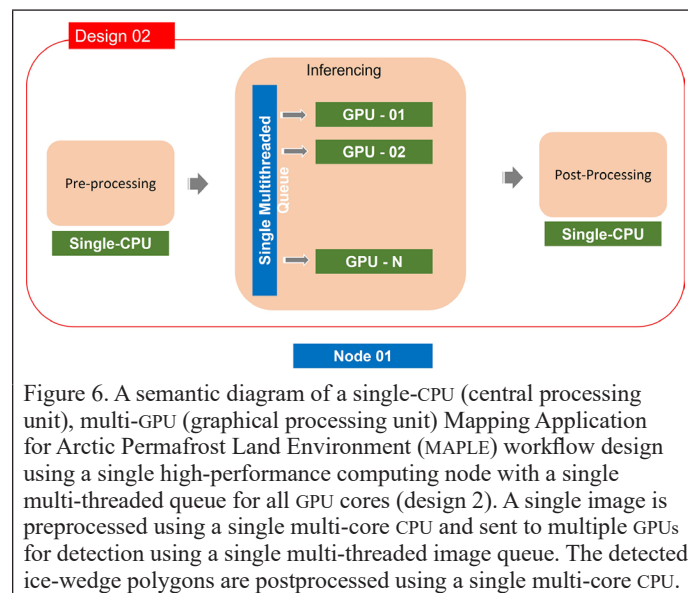


Figure 7 shows a semantic diagram of a design similar to the one in Figure 6. In this workflow, we use a dedicated queue for each GPU core, as illustrated. The image tiles generated in the preprocessing stage are distributed among separate queues and then inferred by a dedicated GPU core. Figure 8 shows a multi-CPU, multi-GPU workflow

design in which we processed multiple images per batch (design 4). In preprocessing, we use multiple CPU cores in a single node. Then tiles from each image are processed in separate nodes for the inferencing stage using the optimum number of GPUs available in that node. The shape files generated in the inferencing stage are processed in a single HPC node using multiple CPU cores in the postprocessing stage.

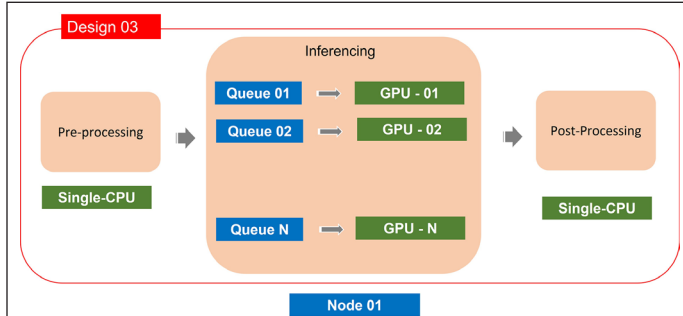


Figure 7. A semantic diagram of a single-CPU (central processing unit), multi-GPU (graphical processing unit) Mapping Application for Arctic Permafrost Land Environment (MAPLE) workflow design using a single high-performance computing node with a dedicated queue for each GPU core (design 3). A single image is preprocessed using a single multi-core CPU and sent to multiple GPUs for detection of ice-wedge polygons using a dedicated image queue for each GPU. The detected ice-wedge polygons are postprocessed using a single multi-core CPU.

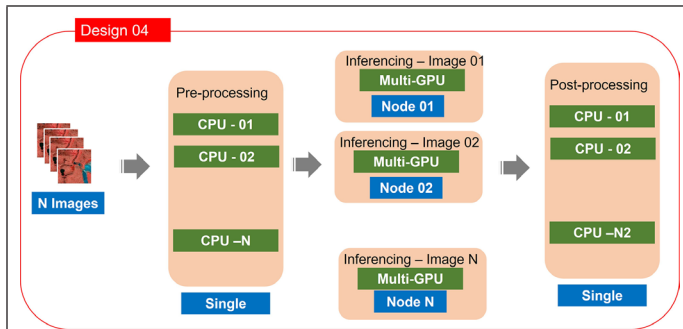


Figure 8. A semantic diagram of a multi-CPU (central processing unit), multi-GPU (graphical processing unit) Mapping Application for Arctic Permafrost Land Environment (MAPLE) workflow design using multiple high-performance computing nodes with a dedicated queue for each GPU core (design 4). A set of images is preprocessed using multiple CPU cores in a single node and sent to multiple GPUs in different nodes for detection of ice-wedge polygons, with a dedicated image queue for each GPU. The detected ice-wedge polygons are postprocessed using a single node with multiple CPU cores.

## Numerical Experiments

The numerical experiments were carried out on the Frontera Longhorn HPC system computing nodes and XSEDE Bridges2 computing nodes. The former consists of 96 computing nodes and the latter of 24 computing nodes. Node specifications are listed in Table 1.

The effective use of HPC resources depends on the underlying resource accounting model, HPC architecture, and workflow design. Project resources are allocated based on SUs. In the Frontera Longhorn system, one SU is calculated by multiplying the job duration in wall-clock hours, the charge rate per node hour, and the number of nodes per job. Therefore, to get maximum resource use we need to use all four GPUs per job. In contrast, on XSEDE Bridges2, one SU is calculated by multiplying the job duration, the number of GPUs per node, the charge rate per hour, and the number of nodes. Here we must calculate the optimum number of GPUs for a single job. We can optimize our workflow based on node time and SUs. In Frontera Longhorn, these two are proportional, but in XSEDE Bridges2, the optimum workflows for time and SUs can be different. We will examine the four different MAPLE workflow designs illustrated in Figures 5 through 8 to find the optimum designs on different HPC systems.

Table 1. Computing node configurations for Frontera Longhorn (Texas Advanced Computing Center) and Extreme Science and Engineering Discovery Environment (XSEDE) Bridges2.

System	Frontera Longhorn	XSEDE Bridges2
Processor	IBM Power 9	Intel Xeon Gold 6248
Total Processors/Node	2	2
Total Cores/Processor	20	20
Total Cores/Node	40	40
Clock Rate (GHz)	2.3	2.5
RAM (GB)	256	512
GPUs/Node	4 × NVIDIA Tesla V100	8 × NVIDIA Tesla V100
GPU RAM/Core (GB)	16	32

GPU = graphical processing unit; RAM = random-access memory.

## Results and Discussion

We evaluated the time taken for three stages of the sequential workflow (design 1) described in Figure 5 for different image dimensions as a base case. Figure 9 shows the computation results for Frontera: preprocessing time, inferencing time, postprocessing time, and total time for images with different sizes on a CPU or a GPU. The gray bars show the time taken for a 400-million-pixel image on a CPU. Orange, green, and brown bars respectively, represent 400-, 1600-, and 3600-million-pixel images on a GPU. The computation time depends on the image size as well as the number of polygons detected. Comparing the first two bars for inferencing, it is evident that using a GPU for inferencing achieves a 9.0× speedup. The reason for this speedup is that DLNN computations can be performed in parallel with many GPU cores. Increasing the size of the image increases the time in all stages. The time taken to process a 3600-million-pixel image on a GPU is on the same order as the time taken to process 400 million pixels using only a CPU.

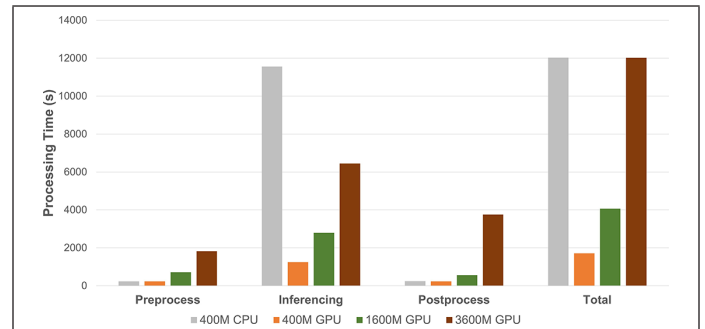
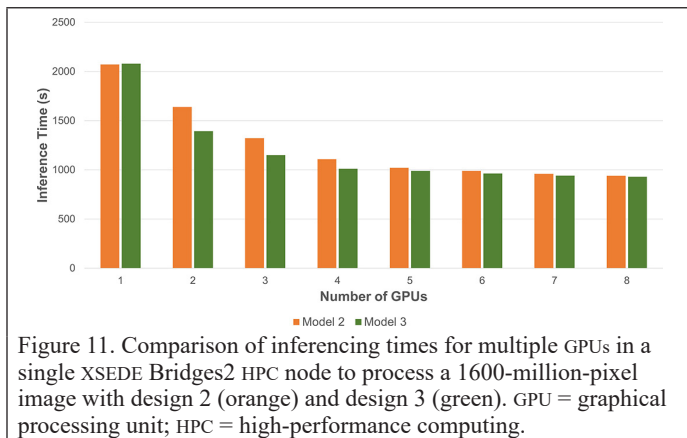
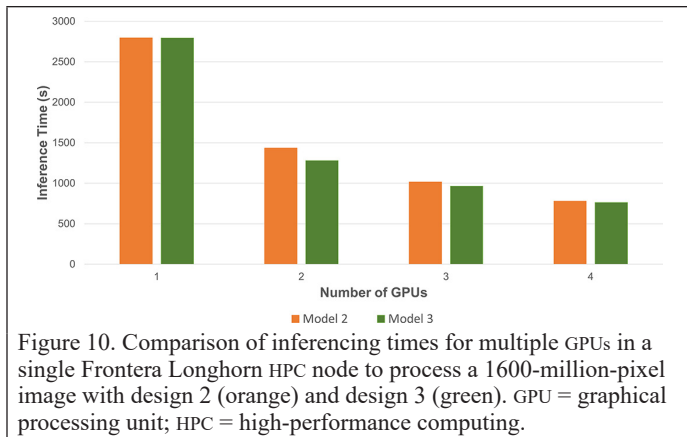


Figure 9. Comparison of time taken for Mapping Application for Arctic Permafrost Land Environment (MAPLE) workflow design 1 on Frontera for different image sizes on CPUs and GPUs. Gray represents the computation times for a 400-million-pixel image on a CPU. Orange, green, and brown represent the computation times for a 400-million-, 1600-million-, and 3600-million-pixel image, respectively, on a GPU. The first three groups of bars show computation times for preprocessing, inferencing, and postprocessing stages, respectively. The last group shows the total time taken to process each image.

Figures 10 (Frontera Longhorn) and 11 (XSEDE Bridges2) show the comparison of inferencing times for designs 2 and 3 with a 160-million-pixel image. The use of a dedicated queue in design 3 improves the running time for all four cases. Using four GPUs, we manage to obtain a 3.6× speed up in Frontera and a 2.0× speedup in XSEDE. The perfect speedup cannot be obtained because of input-output operations and serial sections in the workflow.



Service units are important in processing large numbers of images, because the number of computing resources is limited. In Frontera, running time and service units consumed are proportional because of its accounting model; therefore we will only present results for running time in Frontera. But in XSEDE those two can be different, so we examine both service units and running time in that system.

Figure 12 shows the service units consumed by inferencing a 1600-million-pixel image with up to eight GPUs in XSEDE with designs 2 and 3. The most efficient use of service units can be obtained with a single GPU—that is, design 1. But with the four GPUs, we can achieve a 2× speedup with 2.2 service units.

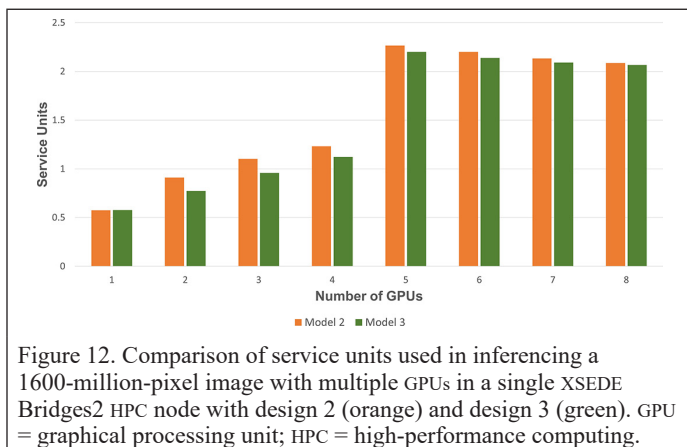


Figure 13 shows the computation times for a full workflow (design 3) for a 1600-million-pixel image with up to four GPUs in Frontera. The speedup achieved for a full workflow using four GPUs is 2.0×. The reason for the lower speedup is the increase in the percentage of serial workload. Figure 14 shows the running times for design 3 in XSEDE, where we can use up to eight GPUs per node. The speedup achieved with multiple GPUs saturates at 1.5× with four GPUs.

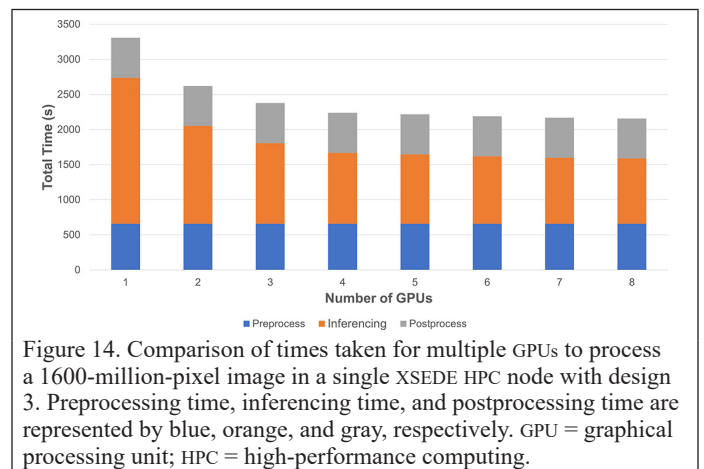
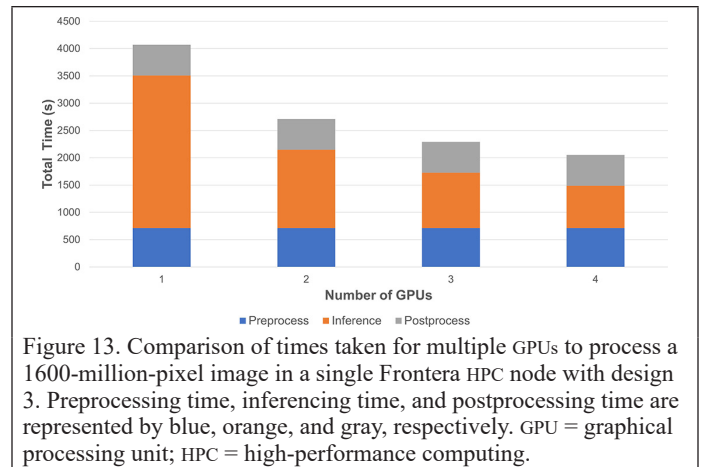


Figure 15 shows the total SUs consumed in XSEDE when using up to eight GPU cores. The most efficient use of SUs occurs when the code is run with one GPU core. But we can get a 1.5× speedup for four GPUs with 1.75× SU use. Figure 16 shows the total amount of time taken to process one 1600-million-pixel image using design 4 with four GPUs in a Frontera HPC node. Preprocessing and postprocessing are done using multiple CPU cores in a GPU node. The speedup using 10 CPU cores in a single computing node for preprocessing is 7.5×, and for postprocessing it is 9.7×, which results in a combined speedup of 8.4×. Preprocessing is a memory-intensive task. It needs four times the memory of the image. With 256 GB RAM available in one node, we can only process up to 10 1600-million-pixel images. The first bar of Figure 16 shows the result we obtain with design 3. A speedup of 2.4× with five CPUs and 2.9× is achieved with design 4 compared to design 3 with a full workflow. Compared with design 1, a speedup of 3.4× with five CPUs and 4.0× with 10 CPUs is achieved. This 4.0× speedup means we can process four times faster than design 1 with the same resources in Frontera.

Figure 17 shows the total time taken with design 4 in XSEDE. Preprocessing and postprocessing are done using up to 10 CPUs cores per image batch and four GPUs per image. The speedup saturates after four CPU cores. Figure 18 shows the SUs consumed to process images with design 4 using up to 10 CPU cores per image batch and a single GPU core per image. The SUs at first decrease slightly with the increase of CPU cores, but increase again after four cores due to the restriction that only four CPUs are allowed for allocation to one unit (GPU) in the shared GPU queue. If we want to allocate more than four CPU cores, we need to allocate two GPUs. This increases the SUs used by the calculations, because SUs are proportional to the number of GPUs. The same happens when we use more than eight CPU cores.

## Conclusion

We developed the Mapping Application for Permafrost Land Environment (MAPLE) by combining deep learning, big imagery, and HPC resources. Our workflow can run on heterogeneous HPC systems,



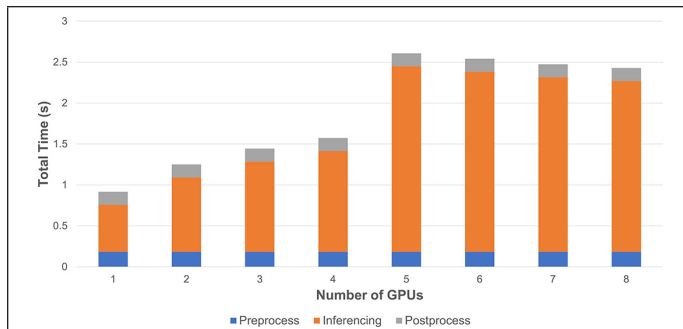


Figure 15. Comparison of service units used for multiple GPUs to process a 1600-million-pixel image in a single XSEDE HPC node with design 3. Preprocessing time, inferencing time, and postprocessing time are represented by blue, orange, and gray, respectively.

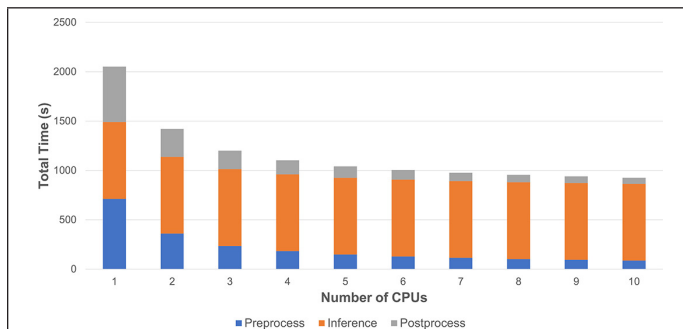


Figure 16. Comparison of times taken to process 1600-million-pixel images in the Frontera HPC system using design 4 with four GPUs per image. A batch of images is sent for preprocessing using a multi-core CPU and then inferencing is done using four GPUs per image. Then postprocessing is performed using a multi-core CPU. Preprocessing time, inferencing time, and postprocessing time are represented by blue, orange, and gray, respectively. CPU = central processing unit; GPU = graphical processing unit; HPC = high-performance computing.

demonstrating its interoperability for large-scale implementation. We tested the workflow with different HPC settings and compared the speedup and resource utilization. Four workflow designs were checked with the Frontera Longhorn and XSEDE Bridges2 HPC systems.

The speedup achieved with design 4 in Frontera is  $3.4\times$  with five CPUs and four GPUs. The number of parallel processes that can be used depends on the amount of main memory in the computing node. The pipeline saturates in Frontera after four GPUs and five CPUs. It is safe and effective to use five images per batch, as the gain in speedup is very small with 10 images (which is the memory limit) per batch. We can process an image with 33% of SUs with five images per batch in design 4 compared to design 1, according to the Frontera accounting design. The speedup achieved in XSEDE design 4 is  $2\times$  for the full workflow, which is obtained with five CPUs and four GPUs. But this will use more SUs per single image, due to the XSEDE accounting model. In XSEDE, design 4 uses the fewest SUs with four images per batch and one GPU per image.

The multi-CPU, multi-GPU design can be used effectively with heterogeneous HPC systems. Design 4 is the fastest of all the designs. But with a different HPC system, the optimum number of images per batch (CPUs) can be different. Design 4 also has the lowest SU usage with different numbers of GPUs per image. The resource usage can be different with different HPC systems due to the accounting design and system architecture. Therefore, we need to test design 4 in different HPC systems to find out optimum CPU and GPU combinations before doing large-scale calculations to optimize our workflow. Design 4 is suitable for big-imagery GeoAI workflows such as MAPLE in existing HPC systems.

## Acknowledgments

This research was supported by the US National Science Foundation grants 1720875, 1722572, 1927872, 1927723, and 1927729.

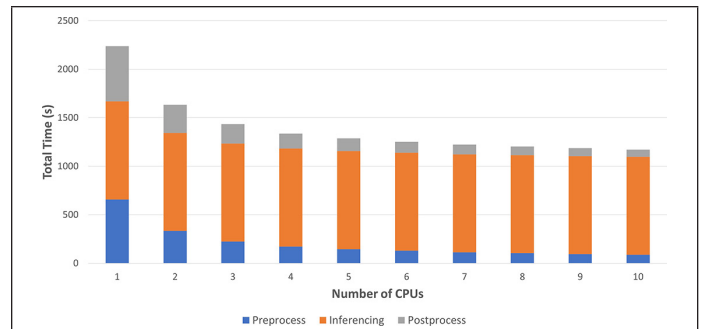


Figure 17. Comparison of times taken to process 1600-million-pixel images in the XSEDE HPC system with different number of CPUs per image batch and four GPUs per image, using design 4. A batch of images is sent for preprocessing using a multi-core CPU, and then inferencing is done using four GPUs per image. Then postprocessing is performed using a multi-core CPU. Preprocessing time, inferencing time, and postprocessing time are represented by blue, orange, and gray, respectively. CPU = central processing unit; GPU = graphical processing unit; HPC = high-performance computing.

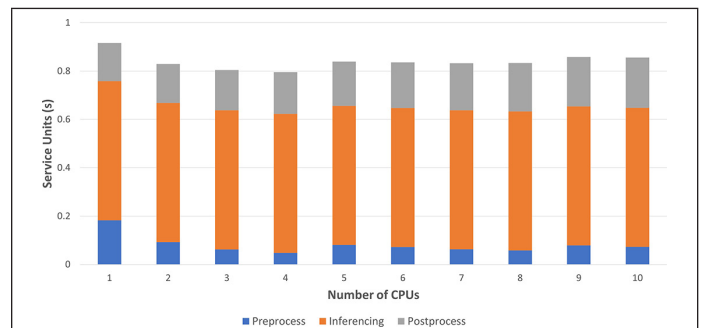


Figure 18. Comparison of service units used to process 1600-million-pixel images in the XSEDE HPC system with different numbers of CPUs per image batch and a single GPU per image, using design 4. A batch of images is sent for preprocessing using a multi-core CPU, and then inferencing is done using one GPU per image. Then postprocessing is performed using a multi-core CPU. Preprocessing time, inferencing time, and postprocessing time are represented by blue, orange, and gray, respectively. CPU = central processing unit; GPU = graphical processing unit; HPC = high-performance computing.

Supercomputing resources were provided by the Extreme Science and Engineering Discovery Environment (award DPP 190001) and Texas Advanced Computing Center (award DPP20001). The authors would like to thank the Polar Geospatial Center at the University of Minnesota for imagery support.

## References

- Al-Saadi, A., I. Paraskevatos, B. C. Gonçalves, H. G. Lynch, S. Jha and M. Turilli. 2021. Comparing workflow application designs for high resolution satellite image analysis. *Future Generation Computer Systems* 124:315–329.
- Amat, F., B. Höckendorf, Y. Wan, W. C. Lemon, K. McDole and P. J. Keller. 2015. Efficient processing and analysis of large-scale light-sheet microscopy data. *Nature Protocols* 10:1679–1696.
- Bhuiyan, M.A.E., C. Witharana and A. K. Liljedahl. 2019. Big imagery as a resource to understand patterns, dynamics, and vulnerability of Arctic polygonal tundra. Page C13E-1374 in *AGU Fall Meeting Abstracts*.
- Blaschke, T. 2010. Object based image analysis for remote sensing. *ISPRS Journal of Photogrammetry and Remote Sensing* 65(1):2–16.
- Blaschke, T., G. J. Hay, M. Kelly, S. Lang, P. Hofmann, E. Addink, R. Q. Feitosa, F. van der Meer, H. van der Werff, F. van Coillie and D. Tiede. 2014. Geographic object-based image analysis—Towards a new paradigm. *ISPRS Journal of Photogrammetry and Remote Sensing* 87:180–191.

- Brown, J., O. J. Ferrians Jr., J. A. Heginbottom and E. S. Melnikov. 1997. *Circum-Arctic Map of Permafrost and Ground-Ice Conditions*. Location: US Geological Survey.
- Brown, J., O. Ferrians, J. A. Heginbottom and E. Melnikov. 2002. *Circum-Arctic Map of Permafrost and Ground-Ice Conditions, Version 2*. Boulder, Colo.: National Snow and Ice Data Center.
- Chi, M., A. Plaza, J. A. Benediktsson, Z. Sun, J. Shen and Y. Zhu. 2016. Big data for remote sensing: Challenges and opportunities. *Proceedings of the IEEE* 104(11):2207–2219. <https://doi.org/10.1109/JPROC.2016.2598228>.
- El-Baz, A. and J. S. Suri, eds. 2020. *Big Data in Multimodal Medical Imaging*. Boca Raton, Fla.: CRC Press.
- He, K., X. Zhang, S. Ren and J. Sun. 2016. Deep residual learning for image recognition. Pages 770–778 in *Proceedings of the IEEE Conference on Computer Vision and Pattern Recognition*, held in Las Vegas, Nev., 27–30 June 2016. Location: IEEE.
- Huerta, E. A., R. Haas, S. Jha, M. Neubauer and D. S. Katz. 2019. Supporting high-performance and high-throughput computing for experimental science. *Computing and Software for Big Science* 3:5.
- Jones, B. M., G. Grosse, C. D. Arp, E. Miller, L. Liu, D. J. Hayes and C. F. Larsen. 2015. Recent Arctic tundra fire initiates widespread thermokarst development. *Scientific Reports* 5:15865.
- Jorgenson, M. T., Y. L. Shur and E. R. Pullman. 2006. Abrupt increase in permafrost degradation in Arctic Alaska. *Geophysical Research Letters* 33(2):L02503.
- Kaiser, S., G. Grosse, J. Boike and M. Langer. 2021. Monitoring the transformation of Arctic landscapes: Automated shoreline change detection of lakes using very high resolution imagery. *Remote Sensing* 13(14):2802.
- Kanevskiy, M., Y. Shur, T. Jorgenson, D.R.N. Brown, N. Moskalenko, J. Brown, D. A. Walker, M. K. Reynolds and M. Buchhorn. 2017. Degradation and stabilization of ice wedges: Implications for assessing risk of thermokarst in northern Alaska. *Geomorphology* 297:20–42.
- Kanevskiy, M., Y. Shur, M. T. Jorgenson, C.-L. Ping, G. J. Michaelson, D. Fortier, E. Stephani, M. Dillon and V. Tumskoy. 2013. Ground ice in the upper permafrost of the Beaufort Sea coast of Alaska. *Cold Regions Science and Technology* 85:56–70.
- Karmas, A., A. Tzotsos and K. Karantzalos. 2016. Geospatial big data for environmental and agricultural application. In *Big Data Concepts, Theories, and Applications*, edited by S. Yu and S. Guo, 353–389. Cham, Switzerland: Springer.
- Kokelj, S. V., J. Tunnicliffe, D. Lacelle, T. C. Lantz, K. S. Chin and R. Fraser. 2015. Increased precipitation drives mega slump development and destabilization of ice-rich permafrost terrain, northwestern Canada. *Global and Planetary Change* 129:56–68.
- Kremer, J., K. Stensbo-Smidt, F. Gieseke, K. S. Pedersen and C. Igel. 2017. Big universe, big data: Machine learning and image analysis for astronomy. *IEEE Intelligent Systems* 32(2):16–22.
- Kucuk, A., J. M. Banda and R. A. Angryk. 2017. A large-scale solar dynamics observatory image dataset for computer vision applications. *Scientific Data* 4:170096.
- Lang, S., A. Baraldi, D. Tiede, G. Hay and T. Blaschke. 2018. Towards a (GE) OBIA 2.0 manifesto—Achievements and open challenges in information & knowledge extraction from big Earth data. Pages 18–22 in *Proceedings of the GEOBIA 2018*, held in Montpellier, France, 18–22 June 2018. Edited by J. Editor. Location: Publisher.
- LeCun, Y., Y. Bengio and G. Hinton. 2015. Deep learning. *Nature* 521:436–444.
- Lee, C. A., S. D. Gasster, A. Plaza, C.-I. Chang and B. Huang. 2011. Recent developments in high performance computing for remote sensing: A review. *IEEE Journal of Selected Topics in Applied Earth Observations and Remote Sensing* 4(3):508–527. <https://doi.org/10.1109/JSTARS.2011.2162643>.
- Liljedahl, A. K., J. Boike, R. P. Daanen, A. N. Fedorov, G. V. Frost, G. Grosse, L. D. Hinzman, Y. Iijima, J. C. Jorgenson, N. Matveyeva, M. Necsoiu, M. K. Reynolds, V. E. Romanovsky, J. Schulla, K. D. Tape, D. A. Walker, C. J. Wilson, H. Yabuki and D. Zona. 2016. Pan-Arctic ice-wedge degradation in warming permafrost and its influence on tundra hydrology. *Nature Geoscience* 9:312–318.
- Liu, J., D. Feld, Y. Xue, J. Garcke, T. Soddemann and P. Pan. 2016. An efficient geosciences workflow on multi-core processors and GPUs: A case study for aerosol optical depth retrieval from MODIS satellite data. *International Journal of Digital Earth* 9:8:748–765.
- Liu, P. 2015. A survey of remote-sensing big data. *Frontiers in Environmental Science* 3:45.
- Liu, P., L. Di, Q. Du and L. Wang. 2018. Remote sensing big data: Theory, methods and applications. *Remote Sensing* 10(5):711.
- Ma, L., Y. Liu, X. Zhang, Y. Ye, G. Yin and B. A. Johnson. 2019. Deep learning in remote sensing applications: A meta-analysis and review. *ISPRS Journal of Photogrammetry and Remote Sensing* 152:166–177.
- Ma, Y., H. Wu, L. Wang, B. Huang, R. Ranjan, A. Zomaya and W. Jie. 2015. Remote sensing big data computing: Challenges and opportunities. *Future Generation Computer Systems* 51:47–60.
- Muster, S., B. Heim, A. Abnizova and J. Boike. 2013. Water body distributions across scales: A remote sensing based comparison of three Arctic tundra wetlands. *Remote Sensing* 5(4):1498–1523.
- Muster, S., M. Langer, B. Heim, S. Westermann and J. Boike. 2012. Land cover classification of Samoylov Island and Landsat subpixel water cover of Lena River Delta, Siberia, with links to ESRI grid files. *Pangaea*, <https://doi.org/10.1594/PANGAEA.786927>.
- Nikolaou, C., K. Kyzirakos, K. Bereta, K. Dogani, S. Giannakopoulou, P. Smeros, G. Garbis, M. Koubarakis, D. E. Molina, O. C. Dumitru, G. Schwarz and M. Datcu. 2014. Big, linked and open data: Applications in the German Aerospace Center. Pages 444–449 in *The Semantic Web: ESWC 2014 Satellite Events*. Edited by V. Presutti, E. Blomqvist, R. Troncy, H. Sack, I. Papadakis and A. Tordai. European Semantic Web Conference 2014, held in Anissaras, Greece, 25–29 May 2014. Lecture Notes in Computer Science vol. 8798. Cham, Switzerland: Springer.
- Nitze, I., G. Grosse, B. M. Jones, V. E. Romanovsky and J. Boike. 2018. Remote sensing quantifies widespread abundance of permafrost region disturbances across the Arctic and Subarctic. *Nature Communications* 9:5423.
- Okunev, A. G., M. Y. Mashukov, A. V. Nartova and A. V. Matveev. 2020. Nanoparticle recognition on scanning probe microscopy images using computer vision and deep learning. *Nanomaterials* 10(7):1285.
- Raynolds, M. K., J. C. Jorgenson, M. T. Jorgenson, M. Kanevskiy, A. K. Liljedahl, M. Nolan, M. Sturm and D. A. Walker. 2020. Landscape impacts of 3D-seismic surveys in the Arctic National Wildlife Refuge, Alaska. *Ecological Applications* 30(7):e02143.
- Raynolds, M. K., D. A. Walker, A. Balser, K. Bay, M. Campbell, M. M. Cherosov, F.J.A. Daniëls, P. B. Eidesen, K. A. Ermokhina, G. V. Frost, B. Jedrzejek, M. T. Jorgenson, B. E. Kennedy, S. S. Kholod, I. A. Lavrinenko, O. V. Lavrinenko, B. Magnússon, N. V. Matveyeva, S. Metúsalemsson, L. Nilsen, I. Olthof, I. N. Pospelov, E. B. Pospelova, D. Pouliot, V. Razzhivin, G. Schaepman-Strub, J. Šibík, M. Y. Telyatnikov and E. Troeva. 2019. A raster version of the Circumpolar Arctic Vegetation Map (CAVM). *Remote Sensing of Environment* 232:111297.
- Schmied, C., P. Steinbach, T. Pietzsch, S. Preibisch and P. Tomancak. 2016. An automated workflow for parallel processing of large multiview SPIM recordings. *Bioinformatics* 32(7):1112–1114.
- Skurikhin, A. N., C. J. Wilson, A. Liljedahl and J. C. Rowland. 2014. Recursive active contours for hierarchical segmentation of wetlands in high-resolution satellite imagery of arctic landscapes. Pages 137–140 in *2014 Southwest Symposium on Image Analysis and Interpretation*, held in San Diego, Calif., 6–8 April 2014. Edited by J. Editor. Location: IEEE.
- Steedman, A. E., T. C. Lantz and S. V. Kokelj. 2017. Spatio-temporal variation in high-centre polygons and ice-wedge melt ponds, Tuktoyaktuk Coastlands, Northwest Territories. *Permafrost and Periglacial Processes* 28(1):66–78.
- Wang, L., Y. Ma, J. Yan, V. Chang and A. Y. Zomaya. 2018. pipsCloud: High performance cloud computing for remote sensing big data management and processing. *Future Generation Computer Systems* 78(1):353–368.
- Wang, L., W. Song and P. Liu. 2016. Link the remote sensing big data to the image features via wavelet transformation. *Cluster Computing* 19:793–810.
- Witharana, C., M.A.E. Bhuiyan and A. K. Liljedahl. 2019. Towards first Pan-Arctic ice-wedge polygon map: Understanding the synergies of data fusion and deep learning in automated ice-wedge polygon detection from high-resolution commercial satellite imagery. Page C22C-07 in *AGU Fall Meeting Extracts*, held in San Francisco, Calif., 9–13 December 2019. Edited by J. Editor. Location: Publisher.
- Witharana, C., M.A.E. Bhuiyan, A. K. Liljedahl, M. Kanevskiy, T. Jorgenson, B. M. Jones, R. Daanen, H. E. Epstein, C. G. Griffin, K. Kent and M. K. Ward Jones. 2021. An object-based approach for mapping tundra ice-wedge polygon troughs from very high spatial resolution optical satellite imagery. *Remote Sensing* 13(4):558.
- Zhang, W., C. Witharana, A. K. Liljedahl and M. Kanevskiy. 2018. Deep convolutional neural networks for automated characterization of Arctic ice-wedge polygons in very high spatial resolution aerial imagery. *Remote Sensing* 10(9):1487.

# Assessing the Impact of Land Use Changes on Net Primary Productivity in Wuhan, China

Yan Gu, Zhenfeng Shao, Xiao Huang, Yuanhao Fu, Jiyuan Gao, and Yewen Fan

## Abstract

Since 2000, major changes have taken place in Wuhan city. Land use and land cover (LULC) has changed significantly, characterized by increased construction land, reducing farmland, grassland, and forest land due to the rapid urbanization process. Taking advantage of LULC data and Moderate Resolution Imaging Spectroradiometer Net Primary Production (MODIS NPP) data from 2000 to 2020, we analyze the impact of LULC type transformation on NPP, reveal the relationship between LULC type and NPP, and quantify the impact of urban expansion on NPP by taking Wuhan, China as a study case. The results showed that: 1) the transformation from farmland and grassland to construction land was a dominant LULC change type in Wuhan during the investigated period; 2) there exists a significant negative correlation between NPP and changes in farmland, woodland, and grassland area; 3) the distance from the city center has a significant positive correlation with NPP, and the dynamics of NPP vary in different regions; 4) there is a significant positive correlation between NPP and night light data. The results of this study provide scientific references for the formation of greening construction and sustainable development strategies in Wuhan.

## Introduction

Net Primary Productivity (NPP) of vegetation refers to the amount of organic matter accumulated by green plants (per unit area and per unit time) through photosynthesis. NPP not only reflects the CO<sub>2</sub> fixation capacity of vegetation under natural environmental conditions, but also represents the quality status and production capacity of ecosystems (Yang *et al.* 2021). As human activities are constantly changing the Earth's ecosystem, NPP is a key ecosystem indicator that measures the influence of human interference with the environment (Zhang *et al.* 2021; Zhuang *et al.* 2022).

Numerous efforts have been made to study NPP based on varying driving factors and regional environments (Su *et al.* 2020; Xu *et al.* 2020; Zhuang *et al.* 2022). Many pieces of evidence have shown that NPP is more closely related to climate factors (Li and Qin 2019; Sun *et al.* 2019; Zahra *et al.* 2020). Based on the Carnegie-Ames-Stanford approach (CASA) model, Lin and Narangarav *et al.* (2015) analyzed the temporal and spatial patterns of NPP derived from Moderate-Resolution Imaging Spectroradiometer (MODIS) Normalized Difference Vegetation Index (NDVI) in Mongolia using factor variance analysis and regression analysis. Zhang *et al.* (2020) studied the ecosystem of two high-yielding grasslands in the Great Plains of Central America in

the 21st century, and the results showed that elevated atmospheric CO<sub>2</sub> has a fertilizing effect on the grassland ecosystem NPP. Li *et al.* (2007) analyzed the spatiotemporal dynamic changes of landscape pattern in Jilin Province by using landscape index models such as landscape diversity, fragmentation degree, and average patch fractal dimension. Shao and Zhang (2016) proposed a new optical and microwave integrated vegetation index (VI) to estimate forest aboveground biomass using Landsat 8 Operational Land Imager (OLI) and RadarSAT-2 satellite data. Based on Landsat thematic mapper (TM) and field survey data, Zhou *et al.* (2011) discussed the applications of the K-nearest neighbor (KNN) technique in estimating terrestrial carbon. Mustafa *et al.* (2012) combined the output of the Physiological Growth Principle model with leaf area index (LAI) from advanced Spaceborne Heat and Reflection Radiometer satellite images to improve their estimated LAI. Qiu *et al.* (2014) studied the seasonal and interannual spatial and temporal dynamic patterns and complex relationships of vegetation and climate factors in China during 1982–1998 based on Global Inventory Modeling and Mapping Studies (GIMMS) data set and using wavelet transform method. Stohr *et al.* (2010) used thermal infrared images to identify the effectiveness of plants affected by high CO<sub>2</sub> concentrations under soybean canapes in east-central Illinois. Bayarsaikhan *et al.* (2020) estimated the NPP of Mongolia during 1982–2015 using the third-generation GIMMS NDVI data and CASA model. Xiong *et al.* (2004) estimated NPP of the Mongolian Plateau by using a vegetation index based on pattern decomposition. Handcock and Csillag (2004) predict NPP at monthly temporal resolution for 16 years (1981–1996) at an 8-km spatial resolution for the approximately 106 km<sup>2</sup> area of Ontario, Canada.

Urbanization is one of the most important social and economic phenomena. The rapid expansion of urban fabrics has become an alarming issue (Hadeel *et al.* 2009; Shao *et al.* 2021; Xiao *et al.* 2019). Efforts have been made to investigate the effect of climate factors He *et al.* 2021; Berauer *et al.* 2021), as well as the effect of land use and land cover (LULC) dynamics on NPP (Zhang *et al.* 2020; Xing *et al.* 2021). Ma (2020) studied the impact of the spatiotemporal distribution of LULC on total primary production and net primary production in Schleswig-Holstein, northern Germany. Ge *et al.* (2021) analyzed the relative contribution of human activities and climate change on China's NPP using residual trend analysis. Pan *et al.* (2021) assessed the impact of individual farmland displacement on NPP in a data-driven manner using the mean difference method, the newly introduced ridge regression method, and the method based on actual change excluding climate impacts. Zhang *et al.* (2020) took Zhengzhou, China, as the study area and explored the urban expansion pattern and its relationship with NPP and climate change. Yan *et al.* (2008) used National Oceanic and Atmospheric Administration/Advanced Very High Resolution Radiometer (NOAA/AVHRR) remote sensing data and NPP model, combined with China's LULC data from 1990 to 2000, to evaluate the impact of farmland conversion on agricultural productivity. Yang *et al.* (2021) used NDVI from MODIS and meteorological data to estimate the regional NPP in the Yangtze River Basin from 2001 to 2018 and

Yan Gu, Zhenfeng Shao, and Yewen Fan are with State Key Laboratory of Information Engineering in Surveying, Mapping and Remote Sensing, Wuhan University, Wuhan 430072, China (shaozhenfeng@whu.edu.cn).

Xiao Huang is with the Department of Geosciences, University of Arkansas, Fayetteville, AR 72701, USA.

Yuanhao Fu is with the School of Geography and Information Engineering, China University of Geosciences, Wuhan 430074, China.

Jiyuan Gao is with the School of Resource and Environmental Sciences, Wuhan University, Wuhan 430072, China.

Contributed by Alper Yilmaz, September 9, 2021 (sent for review October 25, 2021; reviewed by Cheng Zhong, Alper Yilmaz, Cheng Zhong).

Photogrammetric Engineering & Remote Sensing  
Vol. 88, No. 3, March 2022, pp. 189–197.  
0099-1112/22/189–197

© 2022 American Society for Photogrammetry  
and Remote Sensing  
doi: 10.14358/PERS.21-00065R3



analyzed the influence of LULC on the NPP. Taking Jiangyin County in the Yangtze River Delta region as a study case, Xu *et al.* (2006) estimated LULC dynamics in the Yangtze River Delta region using Landsat TM and ETM+ images and evaluated the impact of urbanization on regional NPP and annual NPP in 1991 and 2002. Li *et al.* (2020) quantified the impact of LULC change on China's terrestrial ecosystem NPP from 2001 to 2012. Guan *et al.* (2019) established and analyzed the long-term direct and indirect effects of urbanization on NPP by taking Kunming City, China, as an example.

Analyzing the spatiotemporal characteristics of urban expansion is of great significance for guiding urban planning and protecting the priority farmland resources and ecological environment in a scientific and reasonable manner. So far, existing efforts have mainly focused on the impact of climate and LULC changes on NPP, with few quantitative analyses. In this study, we aim to analyze the impact of LULC type transformation on NPP, reveal the relationship between LULC type and NPP, and quantify the impact of urban expansion on NPP by taking Wuhan, China, as a study case. This study provides scientific support and evidence for the formulation of Wuhan's green development route.

## Materials and Methods

### Study Area

Wuhan, also referred to as “Han” and known as “Jiangcheng”, is the capital city of Hubei Province, China. Wuhan is located in the eastern Jiangnan Plain with high terrain in the north and low terrain in the south. Wuhan is the largest metropolis and the only subprovincial city in central China. The Yangtze River (the third-longest river in the world) and its largest tributary, the Hanshui River, run through the center of the city. Thanks to its superior geographical condition, Wuhan has been given the name of the “thoroughfares of nine provinces”. The climate of Wuhan belongs to the north subtropical monsoon humid climate. Entering the new century, Wuhan has seen rapid development in its economy. In October 2016, Wuhan was listed as a megacity by the Outline of the Development Plan for the Yangtze River Economic Belt. Among the top 100 cities in Asia released by the World Trade Organization, Wuhan ranked 15th. However, the acceleration of urbanization in Wuhan leads to sharp changes in LULC, posing threats to the ecological environment (Wan *et al.* 2019; Wang *et al.* 2021; Zhou

*et al.* 2021). On 18 June 2021, the Regulations for Urban Physical Examination and Evaluation of Territorial Spatial Planning issued by the Ministry of Natural Resources was officially implemented. These regulations are expected to benefit high-quality urban development and improve urban planning in China. Therefore, quantitative evaluation of the impact of climate change and land use change caused by human activities on regional NPP in the process of urbanization (Qin *et al.* 2016; Zhou *et al.* 2013) plays an essential role in the sustainable development of Wuhan.

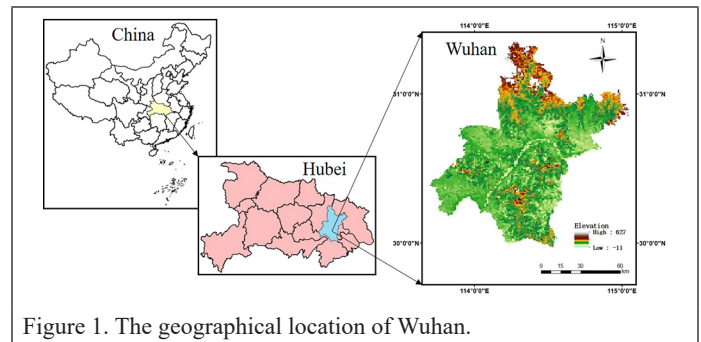


Figure 1. The geographical location of Wuhan.

### Data Sets and Preprocessing

The major data sets used in this study include MODIS NPP data and LULC data. In this section, we detailed the preprocessing steps of MODIS data, the LULC data, and other data sets.

#### MODIS Data and Preprocessing

In this study, we used the MODIS-NPP product (MOD17A3) with a spatial resolution of 1 km, obtained from NASA's website (<https://modis.gsfc.nasa.gov/>). A total of 68 images from 2000 to 2020 were included in this study. We used the MODIS Reprojection Tool for format conversion, projection conversion, and resampling of the retrieved MODIS images.

#### LULC Data and Preprocessing

The LULC data used in this study were retrieved from the Data Center for Resources and Environmental Sciences of the Chinese Academy of Sciences (<http://www.resdc.cn>), including five periods of data in

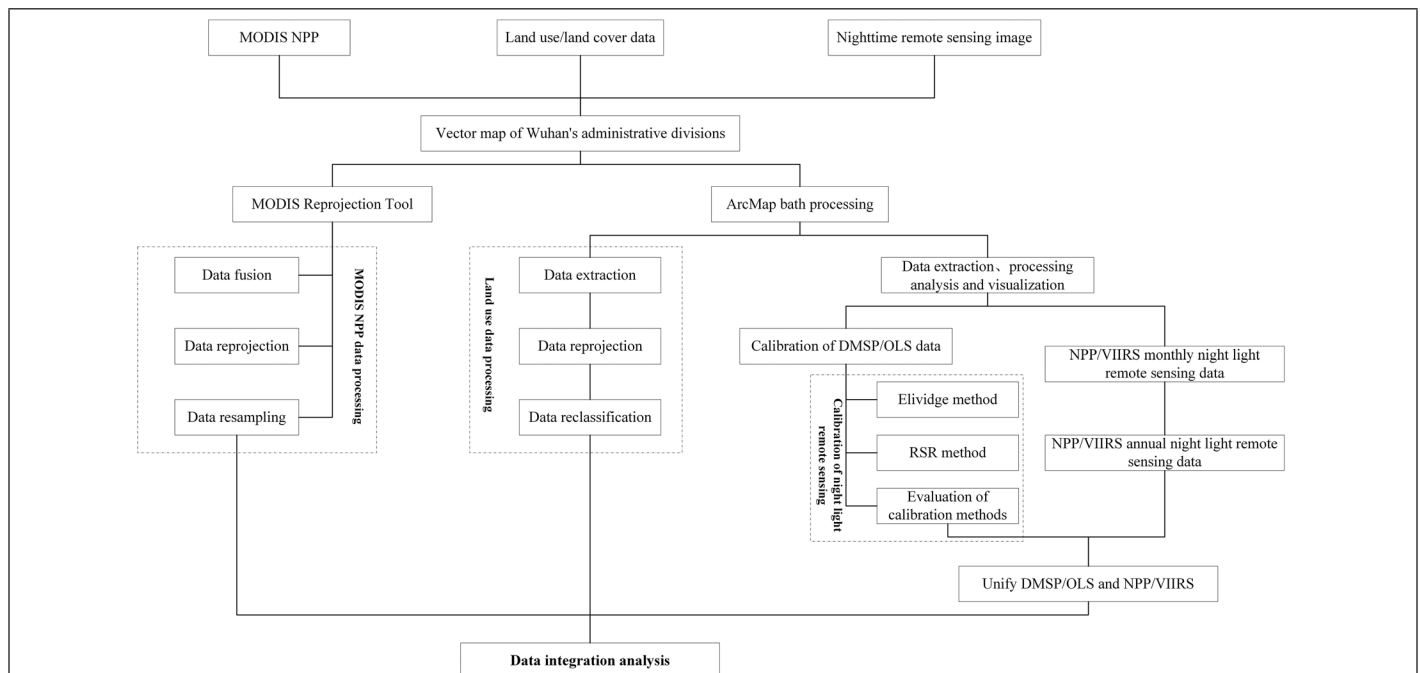


Figure 2. The flowchart of our study workflow. MODIS NPP = Moderate Resolution Imaging Spectroradiometer Net Primary Production; DMSP/OLS = Defense Meteorological Satellite Program/Operational Linescan System; RSR = ridgeline sampling regression; NPP/VIIRS = National Polar-Orbiting Partnership/Visible Infrared Imaging Radiometer Suite.

years 2000, 2005, 2010, 2015, and 2020, with a spatial resolution of 1 km. According to the “Classification System of Land Use/Land Cover Remote Sensing Monitoring Data” of the Chinese Academy of Sciences, LULC types were classified as shown in Table 1.

Table 1. Land use and land cover (LULC) types in Wuhan.

LULC Codes	LULC Types	Meanings
1	Farmland	Paddy field and dry land
2	Forestland	Forestland, shrubbery, dredge forestland, immature forestland, mirage, nursery, and all kinds of garden
3	Grassland	Grassland
4	Waters	Drainage channels, lakes, reservoirs and ponds, and beaches
5	Constructive land	Urban land, rural residential land, and other construction land
6	Unused land	Swamp, bare land, and sand

#### Other Data Sets and Preprocessing

The administrative boundaries of Wuhan used in this study were downloaded from the Data Center for Resources and Environmental Sciences, Chinese Academy of Sciences (<http://www.resdc.cn>) and were processed in ArcGIS 10.2. The nighttime light remote sensing data were derived from two products, i.e., nighttime imagery from the *Defense Meteorological Satellite Program/Operational Linescan System (DMSP/OLS)* satellites with a time span from 1992 to 2013 and nighttime imagery from *Suomi National Polar-Orbiting Partnership/Visible Infrared Imaging Radiometer Suite (NPP/VIIRS)* satellite with a time span from April 2012 to December 2020, retrieved from national environmental information (<https://www.ngdc.noaa.gov>). Note that *NPP/VIIRS* nighttime light product is on a monthly basis and was processed to obtain the annual lumination. We followed Elvidge *et al.* (2019) and the ridge line sampling regression (RSR) method (Zhang *et al.* 2016) to calibrate these two products, leading to a continuous nighttime light remote sensing imagery of Wuhan city from 2000 to 2020.

#### Data Analysis

##### Variation Rate of Pixel-Level NPP

We used a nonparametric trend degree (SEN) method to simulate the changing trend of NPP at the pixel level in Wuhan from 2000 to 2020 and implemented a nonparametric test method, i.e., Mann-Kendall, to test the significance of the changing trend:

$$\beta = \text{mean} \left( \frac{x_j - x_i}{j - i} \right) \quad \forall j > i, i = 1, 2, 3 \dots n \quad (1)$$

where  $x_i$  and  $x_j$  are the values of NPP in Wuhan in the  $i$ th year, and the research time span is 21 years.  $\beta > 0$  indicates that NPP shows an upward trend with time increasing.  $\beta < 0$  indicates that NPP decreases with time.

Standardized test statistic  $Z$  was defined:

$$S = \sum_{i=1}^{n-1} \sum_{j=i+1}^n \text{sign}(x_j - x_i) \quad (2)$$

$$\text{sign} = \begin{cases} 1 & (\theta > 0) \\ 0 & (\theta = 0) \\ -1 & (\theta < 0) \end{cases} \quad (3)$$

$$Z = \begin{cases} \frac{S}{\sqrt{\text{Var}(S)}} & (S > 0) \\ 0 & (S = 0) \\ \frac{S+1}{\sqrt{\text{Var}(S)}} & (S < 0) \end{cases} \quad (4)$$

where the test statistic  $S$  follows an approximately normal distribution and  $\text{Var}(S)$  is variance. A significance test can be obtained given different significance levels of  $\alpha$ .

#### Correlation Analysis

Correlation measures the degree of the mutual relationship between the two variables. Partial correlation analysis, also known as net correlation analysis, investigates the linear correlation between two variables while controlling for the linear influence of other variables. The correlation coefficient, based on Wuhan pixel NPP and its influence factors function can be expressed as Equation 5 and the partial correlation coefficient function can be expressed as Equation 6,

$$R_{xy} = \frac{\sum_{i=1}^n [(x_i - \bar{x})(y_i - \bar{y})]}{\sqrt{\sum_{i=1}^n (x_i - \bar{x})^2 \sum_{i=1}^n (y_i - \bar{y})^2}} \quad (5)$$

where  $n$  is the year,  $x_i$  is the impact factor,  $y_i$  represents the NPP value of Wuhan in the  $i$ th year,  $\bar{x}$  and  $\bar{y}$  are the mean values of  $x$  and  $y$ , respectively.

$$R_{xy,z} = \frac{R_{xy} - R_{xz}R_{yz}}{\sqrt{(1 - R_{xz}^2)(1 - R_{yz}^2)}} \quad (6)$$

where  $R_{xy,z}$  is the partial correlation coefficient of  $x$  and  $y$  after controlling variable  $z$ .  $R_{xy}$ ,  $R_{xz}$ , and  $R_{yz}$  are the correlation coefficients of  $x$  and  $y$ ,  $x$  and  $z$ ,  $y$  and  $z$ , respectively.

#### Dynamics of LULC

LULC dynamics can be used to compare the strength and speed of urban expansion in different periods and provide a great reference for urban planning (Samie *et al.* 2017). The calculation that quantifies the dynamics of LULC function can be expressed as Equation 7,

$$K = \frac{U_b - U_a}{U_a} \times \frac{1}{T} \times 100\% \quad (7)$$

where  $K$  is the annual change rate of certain a LULC type.  $U_a$  and  $U_b$  are the area of a certain LULC type at the beginning and end of the investigated period, respectively.  $T$  denotes the changing time period of a certain LULC type.

#### Results

We first summarize major results and then detail specific findings. The major results are as follows: 1) the LULC of Wuhan city has changed greatly since 2000; 2) the spatial and temporal variation of NPP in Wuhan is notable; 3) the NPP trends of Wuhan city greatly differ at different scales; 4) urbanization has an impact on the NPP change in Wuhan, and the NPP increases significantly with the increase of buffer distance.

##### LULC Changes in Wuhan from 2000–2020

After interpreting five remote sensing images in Wuhan from 2000 to 2020, we performed the dynamic monitoring of land changes. The results show that the major LULC types in Wuhan are farmland and water bodies. The rapid development of Wuhan's economy since 2000 leads to its rapid expansion, with patterns of LULC undergoing significant changes. For instance, the area of construction land increased from 635 km<sup>2</sup> in 2000 to 1142 km<sup>2</sup> in 2020, responsible for the decrease in farmland, grassland, and forestland. The grassland area decreased from

73 km<sup>2</sup> in 2000 to 55 km<sup>2</sup> in 2020, the farmland decreased from 5255 km<sup>2</sup> in 2000 to 4800 km<sup>2</sup> in 2020, and the forestland decreased from 802 km<sup>2</sup> in 2000 to 32 km<sup>2</sup> in 2020. In comparison, water bodies and the unused land area remained relatively unchanged. The water area slightly decreased from 1754 km<sup>2</sup> in 2000 to 1743 km<sup>2</sup> in 2020, and the

unused land slightly increased from 62 km<sup>2</sup> in 2000 to 71 km<sup>2</sup> in 2020. From 2010 to 2015, the farmland in Wuhan decreased by 194 km<sup>2</sup>, while the construction land area increased by 507 km<sup>2</sup>.

### Spatiotemporal Variation of Annual

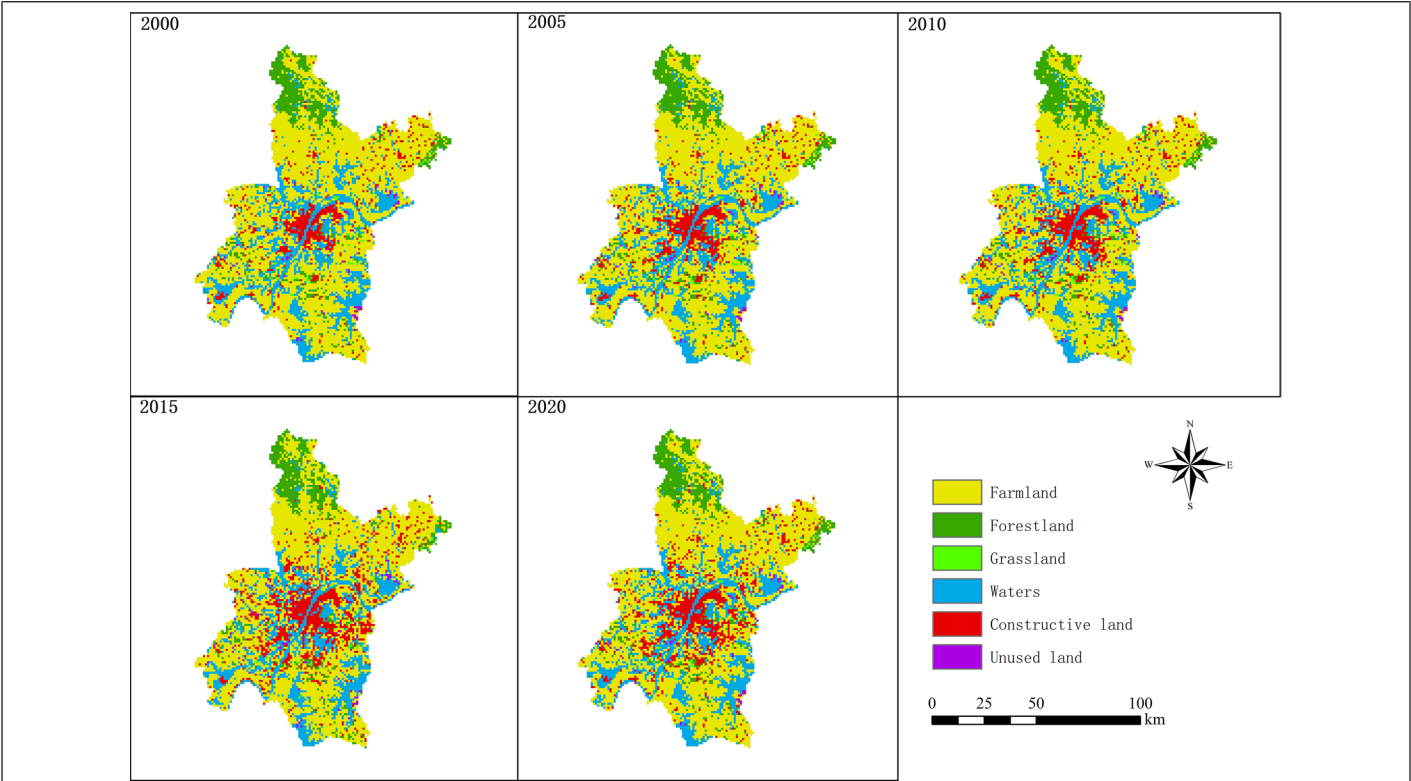


Figure 3. Changes of LULC types in Wuhan from 2000 to 2020.

Table 2. Coverages of different LULC categories and their changing dynamics in China from 2001 to 2012 (unit: km<sup>2</sup>).

Periods	Constructive			Forestland	Waters	Unused Land
	Grassland	Land	Farmland			
2000–2005	–6	134	–129	–10	16	–5
K(%)	–1.644%	4.22%	–0.491%	–0.249%	0.1824%	–1.613%
2005–2010	–2	65	–61	–3	1	0
K(%)	–5.97%	1.691%	–0.238%	–0.076%	0.011%	0
2010–2015	–2	209	–194	–10	–3	0
K(%)	–0.615%	5.012%	–0.766%	–0.253%	–0.034%	0
2015–2020	–8	99	–71	–9	–25	14
K(%)	–2.54%	1.898%	–0.292%	–0.231%	–0.283%	4.912%

Table 3. 2000–2020 land transfer matrix (unit: km<sup>2</sup>).

	2020						SUM
	Grassland	Constructive Land	Farmland	Forest	Waters	Unused Land	
Grassland	21	7	15	10	19	1	73
Constructive land	2	349	229	18	36	1	635
Farmland	15	622	4024	189	377	28	5255
Forest	9	39	177	527	49	1	802
Waters	8	123	336	26	1241	20	1754
Unused land	0	2	19	0	21	20	62
SUM	55	1142	4800	770	1743	71	8581

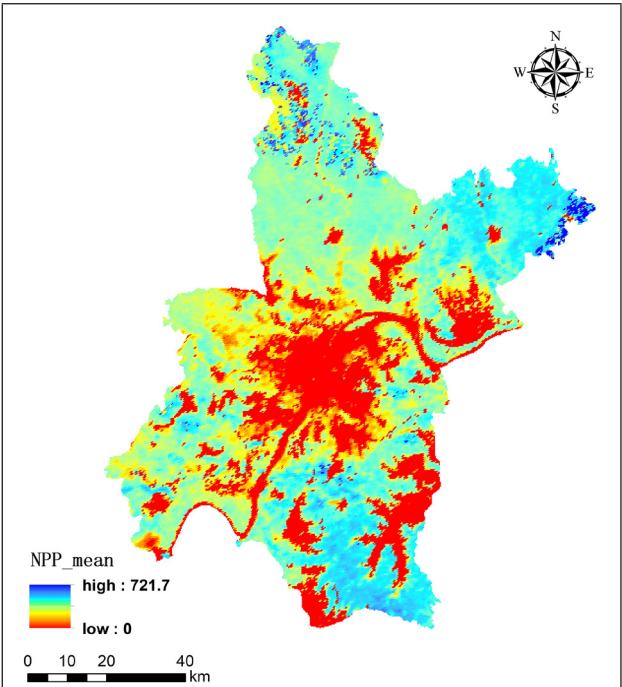


Figure 4. Average net primary production (NPP) distribution in Wuhan from 2000 to 2020.



## NPP in Wuhan from 2000 to 2020

### Spatial Variation

Based on the statistical analysis of the MODIS MOD17A3 data in Wuhan, the annual average NPP of the investigated 21 years was  $342.41 \text{ g C/m}^2$ . Areas with NPP of  $0\text{--}200 \text{ g C/m}^2$  account for 21.36% of the total area, while  $200\text{--}400 \text{ g C/m}^2$  accounting for 19.67%,  $400\text{--}600 \text{ g C/m}^2$  accounting for 58.08%, and  $>600 \text{ g C/m}^2$  accounting for 0.87%. The spatial distribution of the NPP in Wuhan suggests that NPP is low in the central Wuhan and high in its periphery, which corresponds to the fact that the central Wuhan is featured by a commercial activity center with high intensity of human activity.

### Temporal Variation

From a temporal perspective, NPP in Wuhan changed greatly from 2005 to 2010. In comparison, changes were relatively slight from 2015 to 2020. The annual mean value of NPP in Wuhan ranges from  $283.59\text{--}389.39 \text{ g C/m}^2$ , and the annual total value ranges from  $37\,014\,214.58\text{--}53\,408\,758.32 \text{ g C}$ . The minimum NPP occurred in 2001, and the interannual variation of NPP was notable. During the time period of 2000–2006, the NPP of Wuhan fluctuated with no significant change. After 2006, the NPP of Wuhan showed a significant upward trend. In general, from 2000 to 2020, the overall NPP of Wuhan showed a significant upward trend, with an annual change of  $+3.77 \text{ NPP g C/m}^2$ . During the investigated 21-year period, NPP in Wuhan increased by

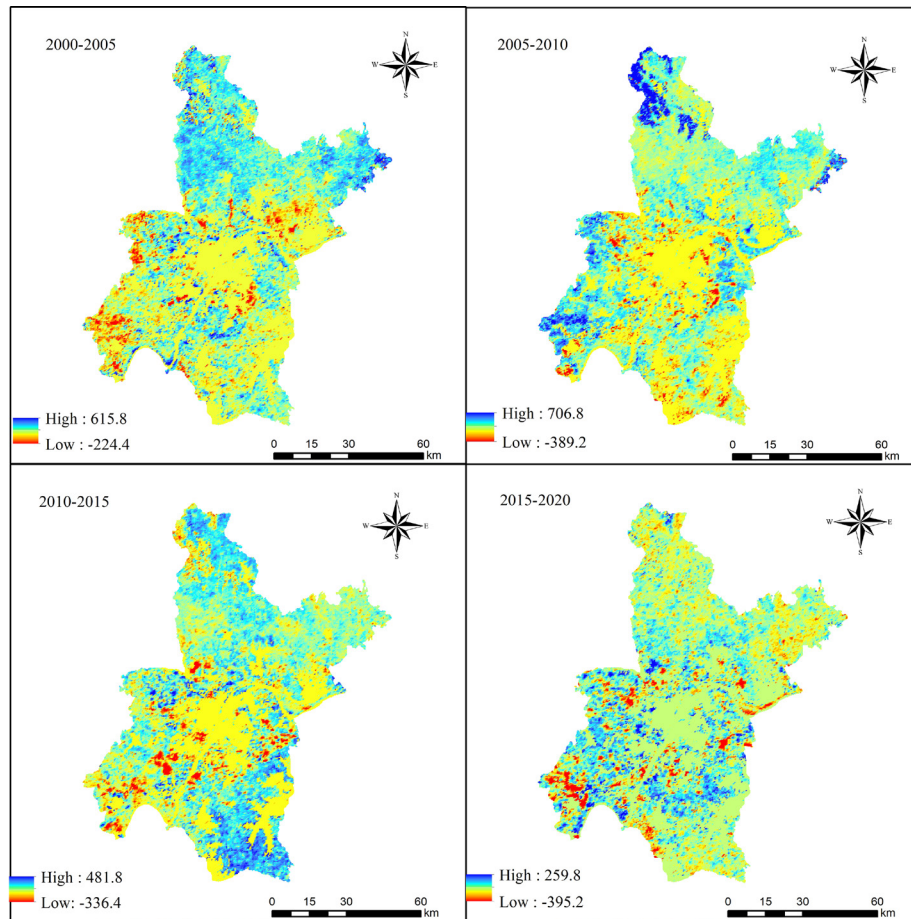


Figure 5. Net primary production (NPP) dynamics in Wuhan from 2000 to 2020.

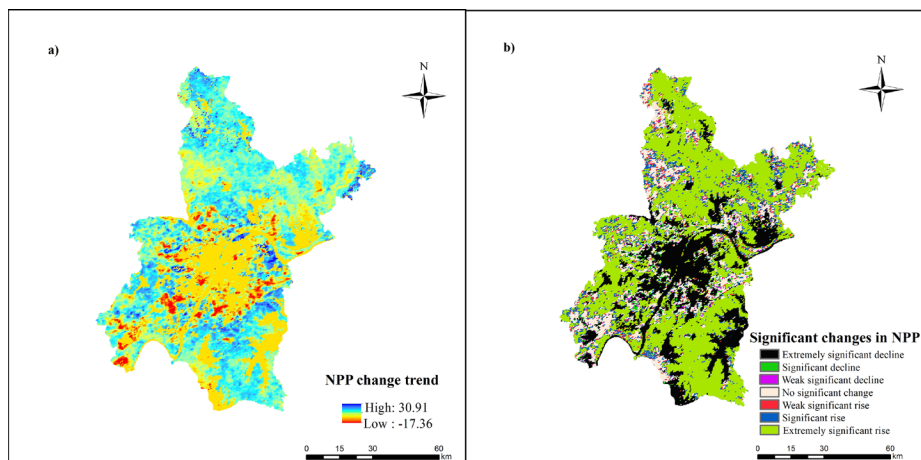


Figure 6. The changing trend (a) and significance (b) of net primary production (NPP) in Wuhan from 2000 to 2020.

16 394 543.74 g C. Given the results from the SEN trend analysis and Mann-Kendall test, our study area was divided into three categories: 1) no significant increase/decline region and weak significant increase/decline region ( $0.05 < P < 0.1$ ); 2) significant increase/decrease zone ( $0.01 < P < 0.05$ ); 3) very significant increase/decrease region ( $0 < P < 0.01$ ). Areas with a very significant increase, significant increase, and weak significant increase of NPP accounted for 62.29% of the study area, suggesting that Wuhan's NPP was on the rise. Moreover, NPP in Wuhan changed significantly, accounting for 72.81% of the total area studied. The results suggested that the NPP in central Wuhan notably decreased,

indicating that human activities had an impact on NPP, and the significant increase of NPP in the surrounding area could be attributed to the establishment of ecological protection areas (Istvan *et al.* 2020).

### NPP Changes of Different LULC Types

Wuhan can be divided into five regions, i.e., the eastern region, western region, southern region, northern region, and central region. Due to the difference in vegetation cover intensity and human activity intensity, the annual mean value of NPP varies greatly across these regions. From the LULC type map of Wuhan, it can be seen that the central region of Wuhan contains mainly construction land, with a low vegetation coverage rate and high intensity of human activities. Therefore, the annual average value of NPP is the smallest in the central region. In comparison, the eastern region contains mainly farmland, leading to the largest NPP value. However, for Wuhan as a whole or in five different regions, we observed that the average annual NPP presented an overall upward trend, suggesting that the urban ecological environment of Wuhan had been further improved during the investigated period under the general requirements of ecological priority, green development, and intensive economy.

Our results suggest that patterns of LULC in Wuhan have changed significantly. Therefore, we quantified the relationship between the annual mean value of NPP in Wuhan and the dynamics of different LULC areas from 2000 to 2020. In general, the average NPP and total NPP of different LULC types showed an increasing trend. The increasing trend of forest land was the most obvious, with the annual average increase rate of NPP of 8.82 g C/m<sup>2</sup>. In comparison, the annual average change rate of NPP of the construction land was the least obvious and showed a decreasing trend from 2000 to 2005. The average annual increase rate of NPP was 3.08 g C/m<sup>2</sup>, and the average annual increase rate was 3.08 g C/m<sup>2</sup>.

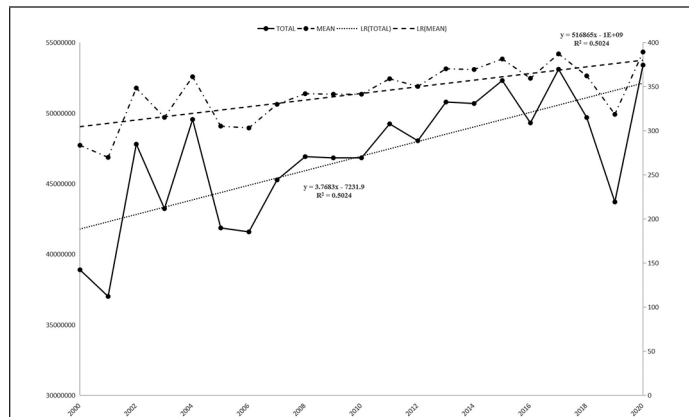


Figure 7. Changes in net primary production (NPP) in Wuhan from 2000 to 2020.

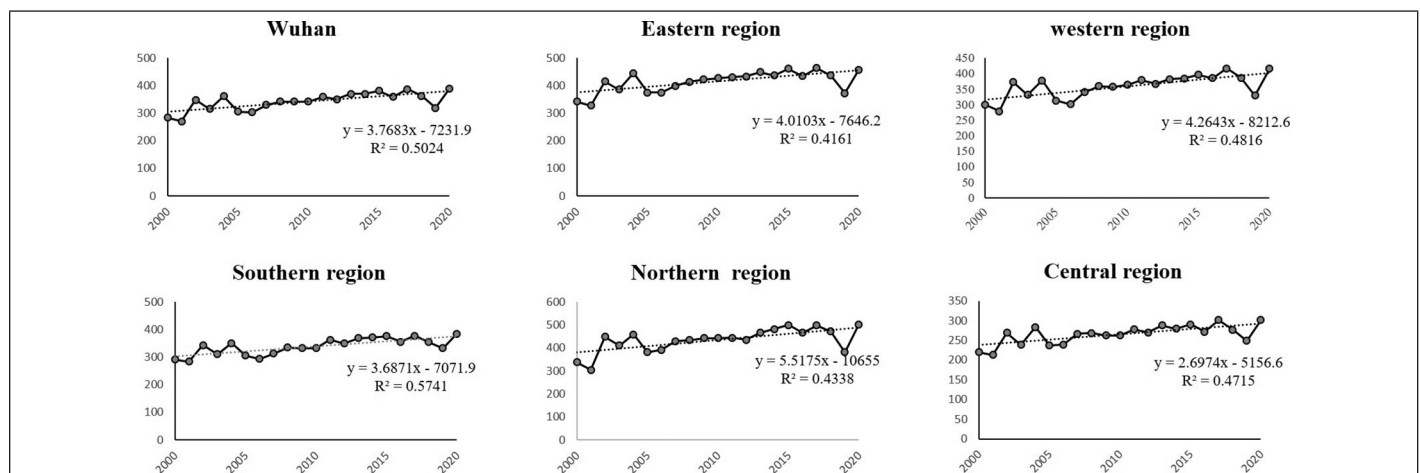


Figure 8. Net primary production (NPP) trends of Wuhan as a whole and Wuhan in five different regions from 2000 to 2020.

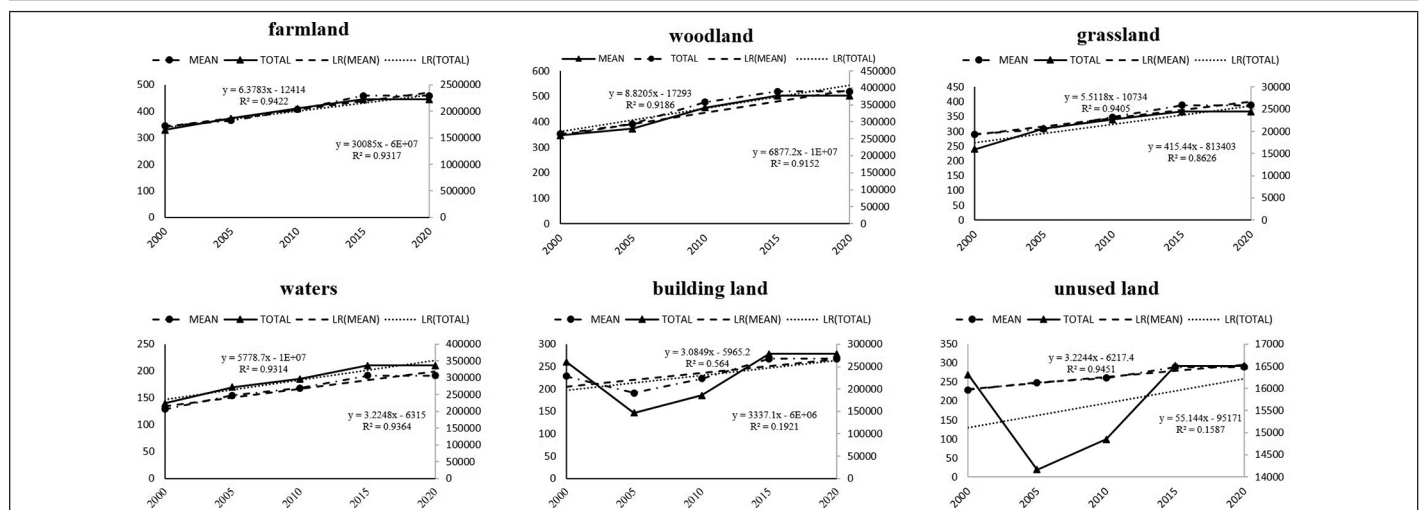


Figure 9. Net primary production (NPP) changes of different land use and land cover (LULC) types.

In this study, we statistically analyzed the annual change area of LULC types in Wuhan from 2000 to 2020 and explored the relationship between LULC types and the average annual NPP. The results are shown in Table 4. Among all the LULC types, the farmland has the highest

Table 4. Relationship between area changes in different land use and land cover (LULC) types and annual average net primary production (NPP) in Wuhan from 2000 to 2020.

LULC Codes	LULC Types	Correlation	
		R <sup>2</sup>	Formula
1	Farmland	0.9555	$y = -0.2724x + 1774.7$
2	Forestland	0.8387	$y = -5.4138x + 4693.2$
3	Grassland	0.767	$y = -6.0147x + 733.15$
4	Waters	0.0063	$y = -0.1698x + 465.98$
5	Constructive land	0.6039	$y = 0.1226x + 127.05$
6	Unused land	0.0939	$y = 1.3177x + 183.48$

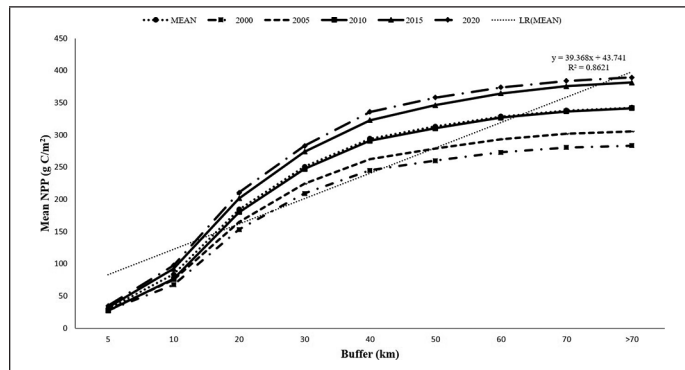


Figure 10. Changes of annual average net primary production (NPP) in different buffer zones in Wuhan from 2000 to 2020.

correlation with the average annual NPP. The areas of farmland, forestland, grassland, and water area were found negatively correlated with the average annual NPP, with R<sup>2</sup> values of 0.96, 0.84, 0.77, and 0.01, respectively. Construction land was positively correlated with average annual NPP (R<sup>2</sup> = 0.60). As for water and unused land, we found no significant correlation between them and the annual NPP.

### The Impact of Urban Sprawl on NPP

#### NPP Dynamics in Different Buffer Zones in Wuhan

In this session, we quantitatively analyzed the NPP changes caused by the urbanization process by establishing buffers with varying distances towards the city center. The results were shown in Figure 10. We noticed that the mean values of NPP were significantly correlated with the buffer distances, with an R<sup>2</sup> of 0.86 (the relationship could be summarized as  $Y = 39.36x + 43.74$ ). With the increase of distance from the city center, the mean NPP in different buffers increased. We also noticed that the mean NPP in the five years of 2000, 2005, 2010, 2015, and 2020 all increased with the increase of buffer distances. Such patterns can be explained by the distribution of land use types. Within 5 km of the buffer zone, the LULC type is mainly construction land with a low average NPP. The farther the distance from the city center, the more forestland and farmland area, the less disturbed by human activities, leading to increased average NPP.

#### The Relationship Between Nightlight Intensity and NPP

In this study, we calibrated different products of nighttime light intensity, an indicator that has been increasingly used by economists as a proxy for measuring economic activity (Juan *et al.* 2020; Shao *et al.* 2021), to reveal the development of urban areas in Wuhan city from 2000–2020. In general, Wuhan's urban sprawl is obvious. The statistical analysis of nightlight intensity and its relation with NPP is presented in Figure 12. The results showed that the correlation between nighttime light intensity and NPP values were strong, with an R<sup>2</sup> of 0.61 between nighttime light mean and NPP annual mean and an R<sup>2</sup> of 0.36 between total nighttime light and total NPP annual.

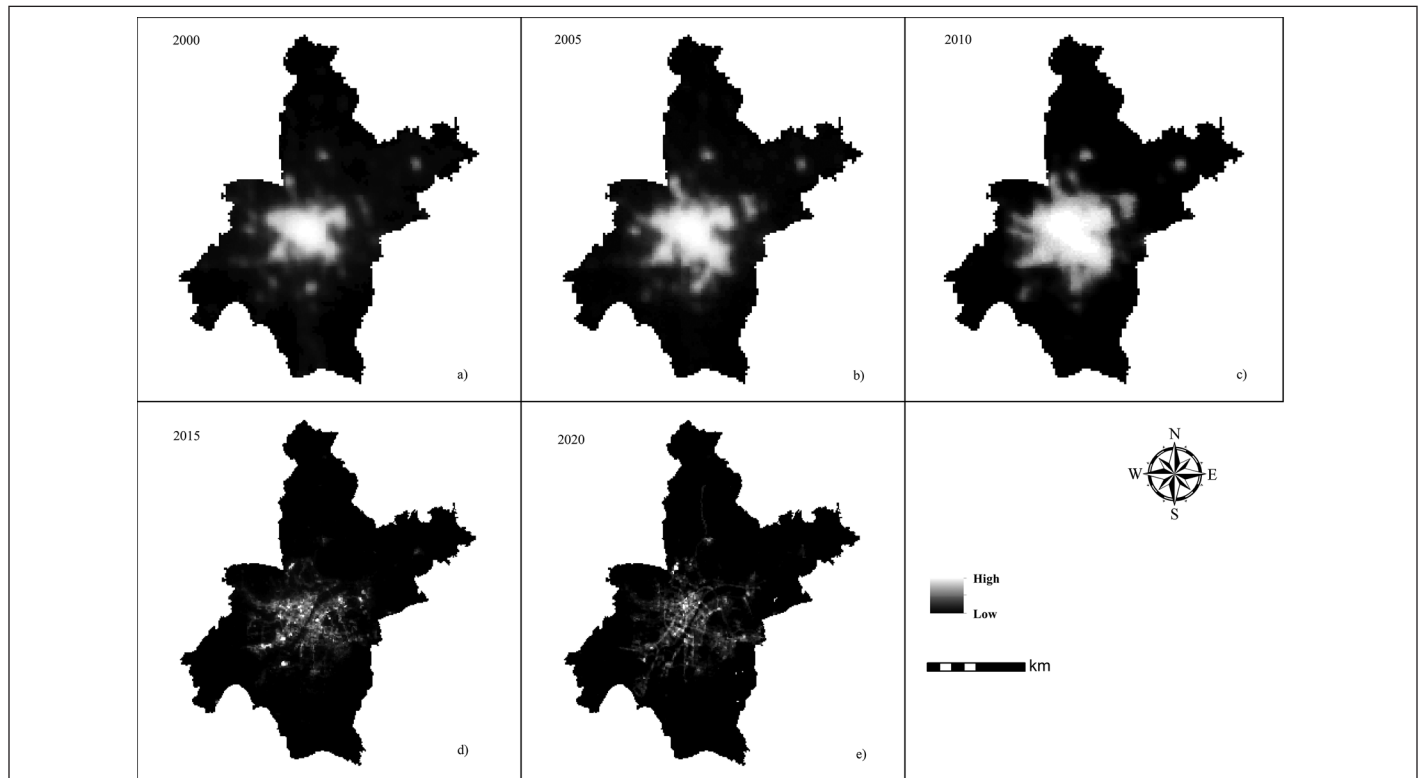


Figure 11. Changes of nighttime light in Wuhan from 2000 to 2020 ((a), (b), (c) Defense Meteorological Satellite Program/Operational Linescan System (DMSP/OLS); (d), (e) National Polar-Orbiting Partnership/Visible Infrared Imaging Radiometer Suite (NPP/VIIRS)).



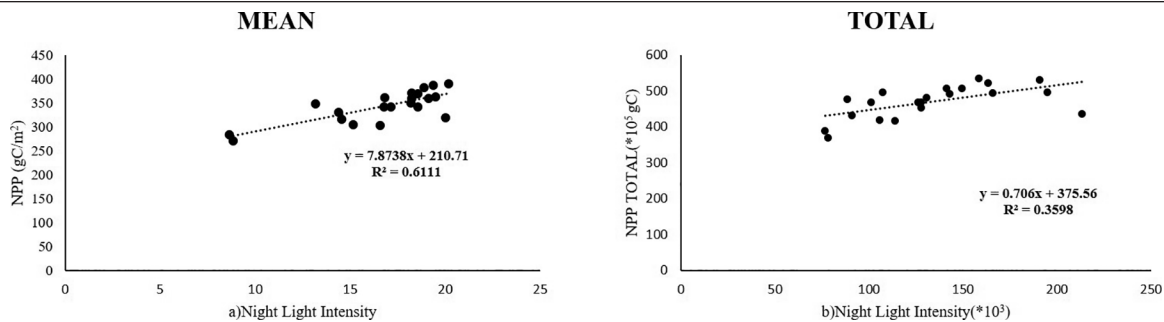


Figure 12. Relationship between nighttime light intensity and NPP in Wuhan from 2000 to 2020: (a) nighttime light intensity mean value and NPP mean value; (b) total nighttime light intensity and total NPP.

## Discussion

Urban expansion has been a notable trend in many global cities, and cities greatly differ in their urbanization patterns. Under the context of urbanization, NPP serves as an important indicator to monitor the quality status and production capacity of ecosystems. The rapid development of remote sensing techniques and the ubiquitous of remote sensing data benefit the monitoring NPP with finer spatiotemporal granularity.

### The Patterns of Urban Expansion

The rapid expansion of urban land has become an important feature of the accelerated development of cities and the social economy (Hadeel *et al.* 2009; Li *et al.* 2020). From 2000 to 2020, the urban expansion of Wuhan has similarities and uniqueness compared with other cities in China. Relying on “Wuhan Urban Green Space System Planning (2003–2020)”, the urban greening construction is well defined to promote an urban living environment with the ecological greening landscape. Wuhan is being developed towards a “green river city” with a living environment featured by “crossed by two rivers and covered with green mountains”, and strives to become a world city with a more competitive and sustainable environment. It can be seen from the trend of NPP that Wuhan is making steady progress towards this goal.

### NPP Changes

Taking advantage of remote sensing products at varying scales, our results show that there exist notable differences in the spatial distribution of NPP in Wuhan, characterized by a concentration of low NPP values in the middle and high NPP values in the periphery, which corresponds to the industrial spatial structure, referred to as “2 axes + 2 centers + 3 rings + 4 pieces + 5 plates”. Moreover, there exist significant interannual differences, and NPP trends vary in different regions, presumably due to the distribution of LULC in Wuhan. Investigation on the relationship between the spatiotemporal variation of NPP and urban expansion provides guidance on urban planning in a more scientific and reasonable manner. We encourage more studies to be conducted to explore the relationship between urban industrial spatial structure and NPP.

### Limitations

The LULC data used in this study involve five images from Resources and Environmental Sciences and Data Center of the Chinese Academy of Sciences in the years 2000, 2005, 2010, 2015, and 2020. We acknowledge that the temporal coverage is relatively short with relatively simple classification schemes of LULC types. For further studies, we plan to use more detailed classification schemes and expand our investigated period. In addition to the impact of LULC change on NPP, we believe the intensity of human activities also has a certain impact on NPP, which is not covered by this study. Therefore, we encourage further efforts to be made to investigate the quantitative relationship between the intensity of human activities and NPP.

## Conclusions

Analyzing the spatiotemporal characteristics of urban expansion is of great significance for guiding urban planning and protecting the priority farmland resources and ecological environment in a scientific

and reasonable manner. Since 2000, major changes have taken place in Wuhan city. LULC has changed dramatically in a short time, characterized by increased construction land, reducing farmland, grassland, and forest land due to the rapid urbanization process. In this study, we aim to analyze the impact of LULC-type transformation on NPP, reveal the relationship between LULC type and NPP, and quantify the impact of urban expansion on NPP in Wuhan, China. The results suggest that the urbanization process has a significant impact on NPP. The LULC of Wuhan city has changed greatly since 2000, and the spatial and temporal variation of NPP in Wuhan is notable. The further away from the city center, the higher the NPP value. However, the urban expansion in Wuhan does not lead to decreased NPP. On the contrary, the NPP in Wuhan has been steadily increasing since 2006, presumably due to the fact that the forest land in Wuhan has remained unchanged since 2006 and also due to the more rational use of land in Wuhan. In 2006, Wuhan issued the General Plan for Land Use (2006–2020), aiming to establish arrangements for and promote the optimization of LULC. Such a plan is also related to the concept of overall planning, coordination, innovation, and green in Wuhan’s urban construction and development. According to the NPP dynamics, we can conclude that the urban ecological environment of Wuhan has been improved during the investigated period.

## Acknowledgments

This work is supported by the National Key Research and Development Program of China with grant number 2018YFB2100501, and the National Natural Science Foundation of China with grant numbers 42090012, in part by 03 special research and 5G project of Jiangxi Province in China (20212ABC03A09); Zhuhai industry university research cooperation project of China (ZH22017001210098PWC).

## References

- Bayarsaikhan, S., U. Mandakh, A. Dorjsuren, B. Batsaikhan, Y. Bao, Z. Adiya and P. Myagmartseren. 2020. Variations of vegetation net primary productivity and its responses to climate change from 1982 to 2015 in Mongolia. *ISPRS Annals of the Photogrammetry, Remote Sensing and Spatial Information Sciences* v-3-2020:347–353.
- Berauer, J., A. Wilfahrt, A. Schuchardt, M. Schlingmann, A. Schucknecht and A. Jentsch. 2021. High land-use intensity diminishes stability of forage provision of mountain pastures under future climate variability. *Agronomy* 11(5):910–910.
- Ding, L., Z. Shao, H. Zhang, X. Cong and D. Wu. 2016. A comprehensive evaluation of urban sustainable development in China based on the TOPSIS-entropy method. *Sustainability* 8(8):746. <https://doi.org/10.3390/su8080746>.
- Elvidge, C., F. Hsu, K. Baugh, T. Ghosh and Q. Weng. 2014. National trends in satellite-observed lighting: 1992–2012. *Remote Sensing Applications Series* 23:97–118.
- Ge, W., L. Deng, F. Wang and J. Han. 2021. Quantifying the contributions of human activities and climate change to vegetation net primary productivity dynamics in China from 2001 to 2016. *Science of the Total Environment* 773:145648–145648.

- Guan, X., H. Shen, X. Li, W. Gan and L. Zhang. 2019. A long-term and comprehensive assessment of the urbanization-induced impacts on vegetation net primary productivity. *Science of the Total Environment* 669:342–352.
- Hadeel, A., M. Jabbar and X. Chen. 2009. Application of remote sensing and GIS to the study of land use/cover change and urbanization expansion in Basrah province, southern Iraq. *Geo-Spatial Information Science* 12(2):135–141.
- Handcock, R. and F. Csillag. 2004. Spatio-temporal analysis using a multiscale hierarchical ecoregionalization. *Photogrammetric Engineering and Remote Sensing* 70(1):101–110.
- He, Y., W. Yan, F. Deng and X. Qu. 2021. Spatio-temporal variation of net primary productivity of farmland ecosystem in central Yunnan Plateau. *IOP Conference Series: Earth and Environmental Science* 697(1):012024.
- Istvan, G., H. Adam, B. Jacob and R. Scott. 2020. Local color and morphological image feature based vegetation identification and its application to human environment street view vegetation mapping, or how green is our county? *Geo-Spatial Information Science* 23(3):222–236.
- Juan, L., L. Juan, X. Liu, Q. Wang and D. Niu. 2020. Temporal and spatial pattern changes of regional economic development based on night-time light data. *Journal of Physics: Conference Series* 1646:012083. <https://doi.org/10.1088/1742-6596/1646/1/012083>.
- Li, H., J. Ding, J. Zhang, Z. Yang, B. Yang, Q. Zhu and C. Peng. 2020. Effects of land cover changes on net primary productivity in the terrestrial ecosystems of China from 2001 to 2012. *Land* 12:480–480.
- Li, J., F. Gao and B. Zhang. 2007. Dynamic change of landscape pattern at Jilin Province from 1980 to 2000. *Geo-Spatial Information Science* 10(2):128–132.
- Li, Y. and Y. Qin. 2019. The response of net primary production to climate change: A case study in the 400 mm annual precipitation fluctuation zone in China. *International Journal of Environmental Research and Public Health* 16(9). <https://doi.org/10.3390/ijerph16091497>.
- Li, Z., W. Luan, Z. Zhang and M. Su. 2020. Relationship between urban construction land expansion and population/economic growth in Liaoning Province, China. *Land Use Policy* 99:105022.
- Lin, C. and D. Narangarav. 2015. Deriving the spatiotemporal NPP pattern in terrestrial ecosystems of Mongolia using MODIS imagery. *Photogrammetric Engineering and Remote Sensing* 81(7):587–598.
- Ma, L. 2020. Effects of spatial–temporal land cover distribution on gross primary production and net primary production in Schleswig-Holstein, northern Germany. *Carbon Balance and Management* 15(1). <https://doi.org/10.1186/s13021-020-00138-3>.
- Mustafa, Y., A. Stein, V. Tolpekin and P. Van Laake. 2012. Improving forest growth estimates using a Bayesian network approach. *Photogrammetric Engineering and Remote Sensing* 78(1):45–51.
- Pan, N., S. Wang, Y. Liu, T. Hua, J. Zhang, F. Xue and B. Fu. 2021. Quantifying responses of net primary productivity to agricultural expansion in drylands. *Land Degradation and Development* 32(5):2050–2060.
- Qin, X., J. Sun, M. Liu and X. Lu. 2016. The impact of climate change and human activity on net primary production in Tibet. *Polosh Journal of Environmental Studies* 25(5):2113–2120.
- Qiu, B., W. Li, M. Zhong, Z. Tang and C. Chen. 2014. Spatiotemporal analysis of vegetation variability and its relationship with climate change in China. *Geo-Spatial Information Science* 17(3):170–180.
- Samie, A., X. Deng, S. Jia and D. Chen. 2017. Scenario-based simulation on dynamics of land-use-land-cover change in Punjab Province, Pakistan. *Sustainability* 9(8). <https://doi.org/10.3390/su9081285>.
- Shao, Z., N. Sumari, A. Portnov, F. Ujoh, W. Musakwa and P. Mandela. 2021. Urban sprawl and its impact on sustainable urban development: A combination of remote sensing and social media data. *Geo-Spatial Information Science* 24(2):241–255.
- Shao, Z., Y. Tang, X. Huang and D. Li. 2021. Monitoring work resumption of Wuhan in the COVID-19 epidemic using daily nighttime light. *Photogrammetric Engineering and Remote Sensing* 87(3):197–206.
- Shao, Z. and L. Zhang. 2016. Estimating forest aboveground biomass by combining optical and SAR data: A case study in Genhe, Inner Mongolia, China. *Sensors* 16(6):834.
- Stohr, C., R. Darmody, B. Wimmer, I. Krapac, K. Hackley, A. Iranmanesh and A. Leakey. 2010. Detecting carbon dioxide emissions in soybeans by aerial thermal infrared imagery. *Photogrammetric Engineering and Remote Sensing* 76(6):735–741.
- Su, C., M. Dong, B. Fu and G. Liu. 2020. Scale effects of sediment retention, water yield, and net primary production: A case-study of the Chinese Loess Plateau. *Land Degradation and Development* 31(11):1408–1421.
- Sun, J., T. Zhou, W. Du and Y. Wei. 2019. Precipitation mediates the temporal dynamics of net primary productivity and precipitation use efficiency in China's northern and southern forests. *Annals of Forest Science* 76(3):1–12.
- Wan, H., Y. Shao, J. Campbell and X. Deng. 2019. Mapping annual urban change using time series Landsat and NLCD. *Photogrammetric Engineering and Remote Sensing* 85(10):715–724.
- Wang, Z., L. Xu, Y. Shi, Q. Ma, Y. Wu, Z. Lu, L. Mao, E. Pang and Q. Zhang. 2021. Impact of land use change on vegetation carbon storage during rapid urbanization: A case study of Hangzhou, China. *Chinese Geographical Science* 1–14. <https://doi.org/10.1007/S11769-021-1183-Y>.
- Xiao, R., X. Huang, W. Yu, M. Lin and Z. Zhang. 2019. Interaction relationship between built-up land expansion and demographic-social-economic urbanization in Shanghai-Hangzhou Bay metropolitan region of Eastern China. *Photogrammetric Engineering and Remote Sensing* 85(3):231–240.
- Xing, W., Y. Chi, X. Ma and D. Liu. 2021. Spatiotemporal characteristics of vegetation net primary productivity on an intensively-used estuarine Alluvial Island. *Land* 10(2):130–130.
- Xiong, Y., M. Kanako, H. Masahiro, O. Kazato, K. Ichirou, T. Tamio, F. Shinobu and F. Noboru. 2004. Verification of net primary production estimation method in the Mongolian Plateau using Landsat ETM+data. *Geo-Spatial Information Science* 7(2):117–122.
- Xu, C., M. Liu, S. An, J. Chen and P. Yan. 2006. Assessing the impact of urbanization on regional net primary productivity in Jiangyin County, China. *Journal of Environmental Management* 85(3):597–606.
- Xu, H., C. Zhao, X. Wang. 2020. Elevational differences in the net primary productivity response to climate constraints in a dryland mountain ecosystem of northwestern China. *Land Degradation and Development* 31(15):2087–2103.
- Yan, H., J. Liu, H. Huang, B. Tao and M. Cao. 2008. Assessing the consequence of land use change on agricultural productivity in China. *Global and Planetary Change* 67(1):13–19.
- Yang, H., X. Zhong, S. Deng and H. Xu. 2021. Assessment of the impact of LUCC on NPP and its influencing factors in the Yangtze River basin, China. *CATENA* 206. <https://doi.org/10.1016/J.CATENA.2021.105542>.
- Zahra, A., R. Elham, B. Ommolbanin, H. Zamani, P. Vijay, M. Mohsen, R. Mohamadreza. 2020. Impact of climate change on net primary production (NPP) in south Iran. *Environmental Monitoring and Assessment* 192(6):344–351.
- Zhang, J., B. Felzer and T. Troy. 2020. Projected changes of carbon balance in mesic grassland ecosystems in response to warming and elevated CO2 using CMIP5 GCM results in the Central Great Plains, USA. *Ecological Modelling* 434(C). <https://doi.org/10.1016/J.ECOLMODEL.2020.109247>.
- Zhang, P., Y. Li, W. Jing, D. Yang, Y. Zhang, Y. Liu, W. Geng, T. Rong, J. Shao, J. Yang, M. Qin and J. Yang. 2020. Comprehensive assessment of the effect of urban built-up land expansion and climate change on net primary productivity. *Complexity*. <https://doi.org/10.1155/2020/8489025>.
- Zhang, Q., B. Pandey and K. Seto. 2016. A robust method to generate a consistent time series from DMSP/OLS nighttime light data. *IEEE Transactions on Geoscience and Remote Sensing* 54(10):5821–5831.
- Zhang, Y., Y. Pan, M. Li, Z. Wang, J. Wu, X. Zhang and Y. Cao. 2021. Impacts of human appropriation of net primary production on ecosystem regulating services in Tibet. *Ecosystem Services* 47(4):101231. <https://doi.org/10.1016/J.ECOSER.2020.101231>.
- Zhou, G., X. Xu, H. Du, H. Ge, Y. Shi and Y. Zhou. 2011. Estimating aboveground carbon of Moso bamboo forests using the K-nearest neighbor technique and satellite imagery. *Photogrammetric Engineering and Remote Sensing* 77(11):1123–1131.
- Zhou, W., Z. Sun, J. Li, C. Gang and C. Zhang. 2013. Desertification dynamic and the relative roles of climate change and human activities in desertification in the Heihe River Basin based on NPP. *Journal of Arid Land* 5(4):465–479.
- Zhou, Y., M. Chen, Z. Tang and M. Ziao. 2021. Urbanization, land use change, and carbon emissions: Quantitative assessments for city-level carbon emissions in Beijing-Tianjin-Hebei region. *Sustainable Cities and Society* 66. <https://doi.org/10.1016/J.SCS.2020.102701>.
- Zhuang Q., Shao Z., Li D., Huang X., Cai B., Altan O., Wu S. 2022. Unequal weakening of urbanization and soil salinization on vegetation production capacity. *GEODERMA* 411:115712.
- Zhuang Q., Shao Z., Huang X., Zhang Y., Wu W., Feng X., Lv X., Ding Q., Cai B. and Altan O. 2021. Evolution of soil salinization under the background of landscape patterns in the irrigated northern slopes of Tianshan Mountains, Xinjiang, China. *CATENA* 206:105561.

# Call for Submissions

## AI-Based Environmental Monitoring with UAV Systems

*Photogrammetric Engineering and Remote Sensing (PE&RS)* is seeking submissions for a special issue on AI-Based Environmental Monitoring with UAV Systems.

Global warming and climate change have become the most important factor threatening the world. Climate change results in dramatical environmental hazards and threatens the planet and human life. A wide variety of policies have been proposed to decrease the effects of global warming and climate change. The most important one is the Paris Agreement which aims to limit global warming to well below two degrees Celcius. Many countries have formulated long term low greenhouse gas emission development strategies related to the Paris Agreement which aimed to meet the essential strategies addressing issues with climate change, environmental protection and low carbon.

The astonishing developments on unmanned aerial vehicle (UAV) systems and artificial intelligence (AI) technologies enables a great opportunity to monitor the environment and propose reliable solutions to restore and preserve the planet and human health.

Data acquisition and processing paradigm has been changed as a result of technological developments. It is obvious that new solutions, innovative approaches will make significant contributions to solve the problems which our planet is facing. UAV data can be collected by various platforms (planes or helicopters, fixed wing systems, drones) and sensors for earth observation and sustainable environmental monitoring which are also utilized by the United Nations to support the delivery of its mandates, resolutions, and activities.

UAV based earth observation data and AI techniques have a wide range of applications such as risk management, disaster monitoring and assessment, environmental impact evaluation and restoration, monitoring agriculture and food cycles, urban analysis, digital twin and smart city applications and providing increased situation awareness. This growth of widely available UAV data associated with the exponential increase in digital computing power, machine learning and artificial intelligence plays a key role in the environmental monitoring and solution generation of geospatial information for the benefit of humans and the planet.

The proposed special issue aims to contributes ASPRS's key mission on 'Simplify and promote the use of image-based geospatial technologies for the end-user', 'Promote collaboration between end users and geospatial experts to match data and technology to applications and solutions' and 'promote the transfer of geospatial data and information technology to developing nations' by

serving as an innovative knowledge exchange platform for authors from the globe to deliberate on the latest advancements, state-of-the-art developments and solutions that can help the community to solve many real-world challenges on the topic of "*AI-Based Environmental Monitoring with UAV Systems*."

This special issue aims to bring researchers to share knowledge and their expertise about state-of-art developments and contribute to the goal of a livable world by integrating human creativity with UAV and AI technologies for environmental monitoring to combat global threats on ecosystems. We wish to discuss the latest developments, opportunities and challenges that can solve many real-world challenges in environmental monitoring including but not limited to:

- AI-Based UAV and GIS Applications
- AI-Based Object Detection and Recognition from UAV Imagery
- AI-Based Digital Twin Applications
- AI-Based Smart City Applications

Papers must be original contributions, not previously published or submitted to other journals. Submissions based on previous published or submitted conference papers may be considered provided they are considerably improved and extended. Papers must follow the instructions for authors at <http://asprs-pers.edmgr.com/>.

**Deadline for Manuscript Submission**  
**May 1, 2022**

**Submit your Manuscript to**  
**<http://asprs-pers.edmgr.com>**

### Guest Editor

**Tolga Bakirman, PhD, Yildiz Technical University, Turkey**

Dr. Tolga Bakirman. [bakirman@yildiz.edu.tr](mailto:bakirman@yildiz.edu.tr) is an assistant professor at Yildiz Technical University in the Department of Geomatic Engineering.



# Information Extraction from High-Resolution Remote Sensing Images Based on Multi-Scale Segmentation and Case-Based Reasoning

Jun Xu, Jiansong Li, Hao Peng, Yanjun He, and Bin Wu

## Abstract

*In object-oriented information extraction from high-resolution remote sensing images, the segmentation and classification of images involves considerable manual participation, which limits the development of automation and intelligence for these purposes. Based on the multi-scale segmentation strategy and case-based reasoning, a new method for extracting high-resolution remote sensing image information by fully using the image and nonimage features of the case object is proposed. Feature selection and weight learning are used to construct a multi-level and multi-layer case library model of surface cover classification reasoning. Combined with image mask technology, this method is applied to extract surface cover classification information from remote sensing images using different sensors, time, and regions. Finally, through evaluation of the extraction and recognition rates, the accuracy and effectiveness of this method was verified.*

## Introduction

With the rapid advancement of remote sensing technology and the popularization of high-resolution remote sensing images, in order to accurately extract information from high-resolution remote sensing images, experts focus on remote sensing information to extract the ecological environment (Shao *et al.* 2014; Cao *et al.* 2015), sustainable development (Shao *et al.* 2020; Shao *et al.* 2020), protection of cultivated land (Shao *et al.* 2020), and other issues that have been under in-depth and extensive research.

The accuracy of large-scale information extraction from high-resolution remote sensing images, the degree of complexity, and universality of the method are still big challenges (Wang *et al.* 2013). The existing methods of extraction of surface cover classification information fail to meet practical application requirements (Zhang *et al.* 2013). The reasons for this are:

1. The decision tree has poor antinoise abilities (Shao *et al.* 2016); obtaining clustering results using the fuzzy clustering method when the sample size is too large is difficult (Shao *et al.* 2018); geographic information systems (GIS)-aided classification methods are limited by the present status and accuracy of GIS data; the support vector machine (SVM) algorithm has difficulties solving the problem of multi-classification (Zhang *et al.* 2018).
2. Artificial neural networks are prone to local minimization problems, the relationship between knowledge rules is not transparent, and expert systems do not have sufficient learning ability (Du *et*

*al.* 2002); convolutional neural networks have a huge demand for samples (Shao *et al.* 2020).

The idea of case-based reasoning was first described by Schank of Yale University in the United States. Its principle is to use the original case to explain or solve a new problem. It is mainly to solve the problem through the method of analogy, to integrate problem solving and learning, and to use case to express knowledge, emphasizing the use of past experience accumulation and appropriate modifications to solve new problems; many scholars have also tried to apply this method to the fields of geography and remote sensing. The case-based approach has played an important role in the classification of and information extraction from radar images (Li *et al.* 2004; Li *et al.* 2009), synthetic-aperture radar (SAR) images (Chen *et al.* 2008), SPOT-5 images (Liu *et al.* 2014), and hyperspectral images (Tang 2010). But it does not form a unified model.

As of yet, there has been no in-depth study of the case-based and case-based management methodologies of information extraction from high-resolution remote sensing images.

Currently, the following three problems commonly exist in object-oriented image classification methods for information extraction (Miao *et al.* 2010):

1. First, the optimal segmentation scale problem: The spectral characteristics of high-resolution remote sensing images are less stable, and the texture features are more variable, resulting in different optimal segmentation scales for each type of surface cover (Wang *et al.* 2009). Common methods for determining the optimal image segmentation scale include the trial and error method, maximum area method, object function method, local variance method, and area ratio method. However, the calculations involved are cumbersome and the result obtained cannot be used as a fixed value (Li, 2013).
2. Second, the optimal combination of features: The feature information from high-resolution remote sensing images is rich, and in order to get the best combination of features for each type of surface cover the redundant features need to be removed (Shao *et al.* 2020). Due to the characteristics of object-oriented classification with small samples and high-dimensional features, the quality of feature selection may be affected due to a limitation in the number of samples.
3. Finally, the applicability of classifiers: There are various classifiers, such as artificial neural networks (Pacifi *et al.* 2009), expert systems (Sun *et al.* 2007), fuzzy clustering (Li *et al.* 2011), support vector machine (Chang *et al.* 2012), and decision tree (Yan 2011; Chen *et al.* 2013). However, each classifier has its own limitations, creating a need to further amend and improve the classification strategy and enhance the applicability of the classifier for high-resolution images of the different types of surface cover.

This paper proposes a new method of high-resolution remote sensing information extraction. This method constructs multi-scale cases of different land cover classification types and uses case-based reasoning to predict the land cover type of the target case.

Jun Xu, Yanjun He, and Bin Wu are with the School of Natural Resources and Surveying, Nanning Normal University, Nanning 530001, China (Corresponding author, Yanjun He: heyanjun@nnnu.edu.cn).

Jun Xu and Hao Peng are with the State Key Laboratory of Information Engineering in Surveying, Mapping and Remote Sensing, Wuhan University, Wuhan 430079, China. Jiansong Li is with the School of Remote Sensing and Information Engineering, Wuhan University, Wuhan 430079, China..

Contributed by Zhenfeng Shao, October 27, 2020 (sent for review March 9, 2021; reviewed by Nana Yaw Danquah Twumasi, Nan Yang, Bin Hu).

Photogrammetric Engineering & Remote Sensing  
Vol. 88, No. 3, March 2022, pp. 199–205.  
0099-1112/22/199–205

© 2022 American Society for Photogrammetry  
and Remote Sensing  
doi: 10.14358/PERS.20-00104R3

## Methodology

In view of the rich image features of high-resolution remote sensing images, a method using multi-scale segmentation combined with case-based reasoning for information extraction from high-resolution remote sensing images was designed. The first step in the method is to use a multi-level and multi-layer, multi-scale segmentation strategy to segment the target image in multi-scale. Then, feature selection and weight calculation are done, and a multi-level and multi-layer case base is constructed. After that, the Kullback-Leibler divergence similarity model and K-nearest neighbor search strategy are used to construct the case reasoning classifier, combined with image mask and feature fusion, which is driven by the case study to achieve the intelligent extraction of information from remote sensing images.

The flowchart of the method technology is shown in Figure 1.

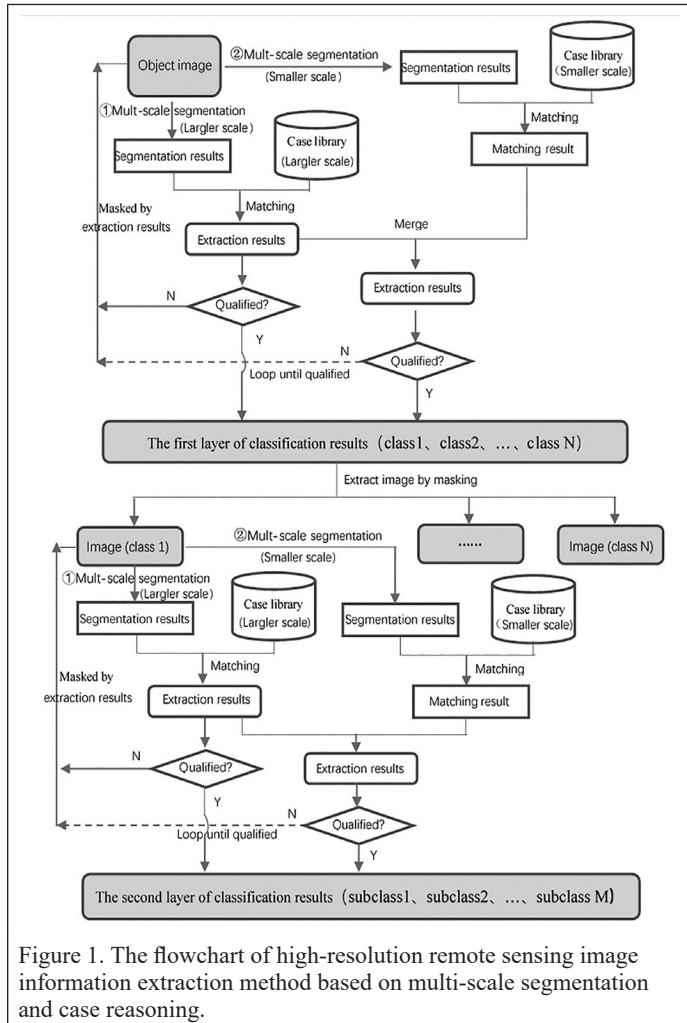


Figure 1. The flowchart of high-resolution remote sensing image information extraction method based on multi-scale segmentation and case reasoning.

## Multi-Scale Segmentation

### Multi-Level and Multi-Layer Image Segmentation

Multi-layer classification of the surface cover is a multi-level classification system, with the first layer containing several parent classes; the second layer is a number of subclasses corresponding to each parent class; and the third layer is a number of subcategories corresponding to each subclass. To extract the surface cover classification type, a layer-by-layer classification system is used starting at the highest level, which is the first layer, and continuing to the end of the lowest level (Shao *et al.* 2019; Zhou *et al.* 2014).

With the multi-level image segmentation, the first step uses a large scale segmentation to extract larger area land patches (Cao *et al.* 2015). These extracted larger areas are then masked to separate them out from the remaining undivided portions with smaller segmentation scales.

After this, the land patches with smaller area are extracted. The above steps are repeated until the completion of the extraction of the target of this layer (Xu *et al.* 2017).

### Determination of Optimal Segmentation Parameters

The multi-level and multi-layer segmentation strategy is adopted so the optimal segmentation parameter becomes an optimal “less-segmentation” parameter. Multi-scale segmentation mainly involves band weight, scale, shape factor, compactness, and four other parameters (Xu *et al.* 2017). The area, brightness mean value, and standard deviation eigenvalue of each band under different segmentation parameters were calculated; the weighted mean selection method was combined with the maximum area for optimal segmentation parameter selection (Gu *et al.* 2009).

## Case Library Construction

### Case Expression

The traditional object-oriented model is used to represent the case; that is, case characteristics and case type are used to describe the case (Du *et al.* 2002). The case features include basic, matching, and auxiliary features. The basic and auxiliary features are used to describe nonimage features of the case, correspondingly record case metadata information and statistical information, and participate in retrieval and matching (Shao *et al.* 2014). Matching features are used to describe image features that play an important role in the process of reasoning and have a causal relationship with the inference results; these features also record case characteristics such as spectral, geometric, and texture information.

Accordingly, a case can be expressed as Equation 1:

$$s = (f_1, f_2, \dots, f_n; \sigma_s) \quad (1)$$

Here,  $f_n$  is the eigenvalue of the  $n$ th attribute of case  $s$ ,  $n$  is the number of attribute features, and  $\sigma_s$  is the surface cover classification type (Zhou *et al.* 2017).

### Case Library Structure

The case library consists of cases and weights. Each type of feature corresponds to a group of cases, each case constitutes a property table, and each property table corresponds to a set of weights. Each layer corresponds to a plurality of surface cover objects and a plurality of segmentation scales, and each scale corresponds to a set of attribute tables, that is, a case database (Xu *et al.* 2018).

The case is organized hierarchically according to the classification level and scale level of the case to form a multi-layer and multi-scale case library. The structure of a case library is shown in Figure 2.

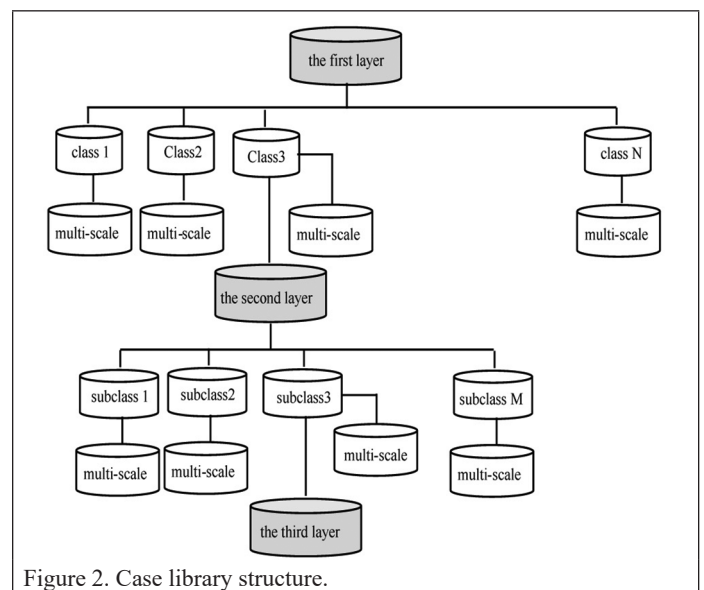


Figure 2. Case library structure.

### Feature Selection and Weight Calculation

The improved relief algorithm is used to calculate the matching feature weight of a case. Then, features whose weights are greater than the

threshold are selected as the final matching feature of the case. The basic idea is based on feature weights calculated from all the training samples and the total number of samples is set as the number of iterations. First, the sums of the feature weights in a class are averaged, then the averages of the features obtained for each class are summed to give the summed average. This is done to achieve the weight of matching features (Li 2004; Yang 2011).

After feature selection, the weight values of the retained features are normalized to obtain the final weight value of the case matching feature.

### Case Match

#### Similarity Measurement Model

Using Kullback-Leibler divergence as a measure of similarity between cases, Equation 2 is:

$$\text{Sim} = \exp\left(-\sqrt{\sum_{i=1}^n \left(\frac{w_i(a_i - b_i)}{\sigma_i}\right)^2}\right) \quad (2)$$

where Sim is the case similarity value;  $D$  is the Kullback-Leibler divergence;  $w_i$  is the weight of the  $i$ th attribute of the case;  $a_i$  is the  $i$ th attribute of Case A; and,  $b_i$  is the  $i$ th attribute of Case B.

#### Case Retrieval Strategy

A staged neighbor search strategy is adopted to improve retrieval efficiency. The strategy organizes the case structure into two levels: a representative case library and subcase library. These levels are divided into two stages for case retrieval. In the first procedure, the nearest neighbor retrieval method is used to set the similarity threshold  $\theta_1$  ( $0 < \theta_1 < 1$ ) and the representative case with the highest similarity with the new case is found in the representative case library. The second procedure sets the similarity threshold  $\theta_2$  ( $0 < \theta_2 < 1$ ) in the K-nearest neighbor method for further searching to find the  $k$  most similar cases.

### Matching Postprocessing

#### Image Mask

When the split layer and the case base complete the first case match, a part of the split layer map is extracted to identify the first information extraction results and the remaining part of the split layer, that is not identified from the map, is masked. Only the remaining part of the masked image, which has not been extracted is obtained. Then the masked image for the second image segmentation and information is extracted, and so on until the land cover classification objects in the original remote sensing image have been extracted and identified to the maximum extent.

#### Feature Fusion

After multiple image masking and case matching, the surface cover classification results are obtained multiple times, and then the merger and element fusion processing are performed to obtain the final result of surface cover classification information extracted from the original image.

### Experiment

To verify this method, two *WorldView-2* satellite remote sensing images of the Qinzhou City of Guangxi Province and one Siwei Digital Camera (SWDC)-4 aerial image of the Guigang City of Guangxi Province were used. The *WorldView-2* image sizes (of both) were 6564×4219 (pixels). The acquisition times were April 2015 and January 2013. Both images had a spatial resolution of 0.5 meters and were acquired with the China Geodetic Coordinate System 2000. The SWDC-4 aerial image size was 6394×3872 (pixels) with 0.2 meters spatial resolution. The geographical location diagram is shown in Figure 3.

This method was used to completely extract information on surface cover from the experimental image, and the same case library was used to extract information from the *WorldView-2* images acquired from different regions and at different times.

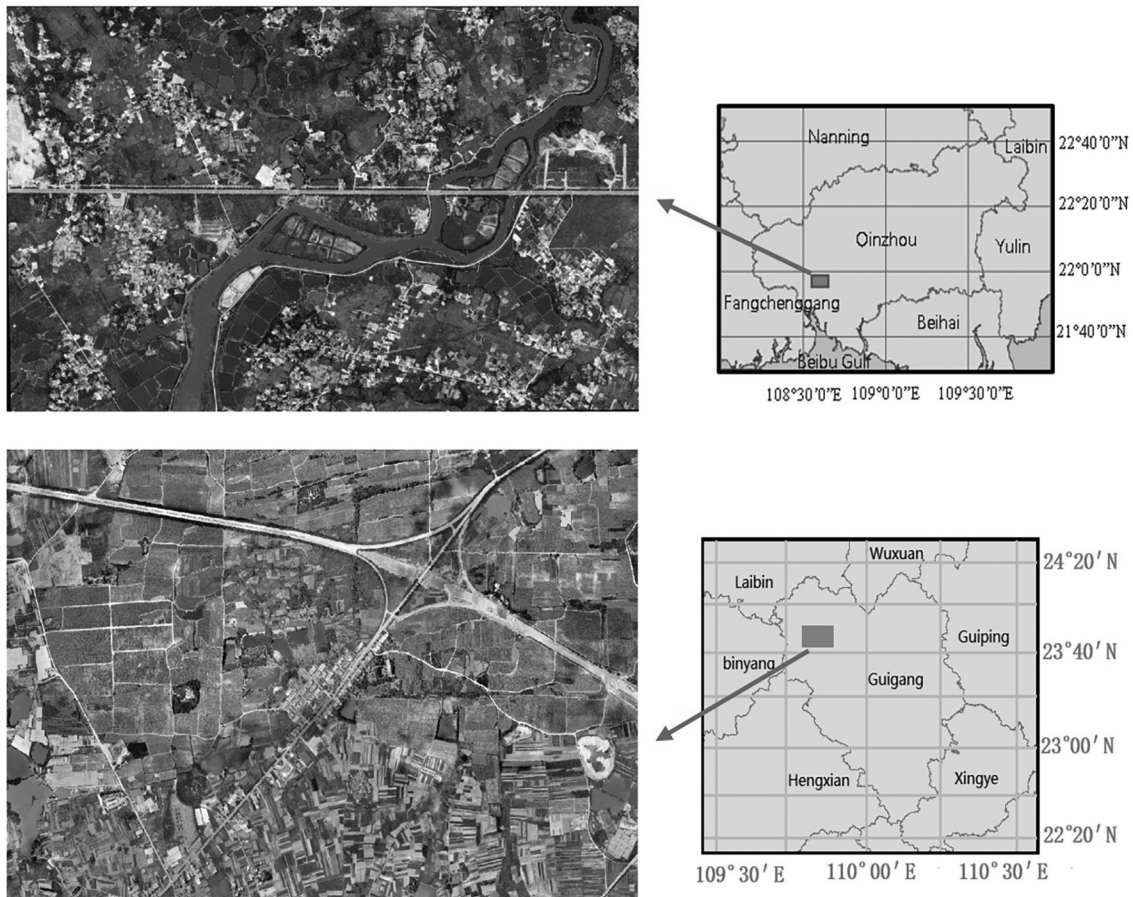


Figure 3. Experimental image geographic location diagram.



## Information Extraction Experiment

### WorldView-2 Satellite Image Experiment

This method was used to extract classification information from *WorldView-2* images taken in April 2015, including those of cultivated lands, forest lands, buildings, roads, and water bodies. The results are shown in Figure 4 as:

1. a multi-scale segmentation result image;
2. a first extraction result image;
3. a nonextracted image;
4. a re-extraction result;
5. and a final result extracted from the first extraction result and the re-extraction result.

### SWDC-4 Aerial Images Experiment

This method was used to extract classification information from the SWDC-4 aerial images taken in May 2013, including those of cultivated lands, forest lands, buildings, roads, and water bodies. The results are shown in Figure 5.

## Accuracy Evaluation

In order to verify the accuracy of this method, the extraction results of the five major land cover classifications were referenced with the land cover analysis (LCA) layer of the National Geoinformation Survey in order to determine if the correct objects were extracted from the high-resolution remote sensing images.

The extraction rate and the recognition rate are taken as the accuracy evaluation indexes for extracted surface cover classification information by this method, wherein extraction rate = total amount extracted/total number of plaques  $\times 100\%$ ; recognition rate = number of correct extractions/total number of extractions  $\times 100\%$ ; total number of extractions = number of correct extractions + number of incorrect extractions. The evaluation accuracy of information extraction from the experimental image is presented in Table 1 and Table 2.

The “total number of spots” refers to that on the LCA layer. In Table 1, the extraction rate of the five types of surface covered objects is above 60% and the recognition rate is above 90%, which shows good accuracy. Among them, the building extraction rate was the highest, reaching 89.07%, followed by that of water bodies, which indicates that most of the target images with building and water body information could be identified and extracted. In Table 2, although the experimental data comes from different sensors, the image resolution is high, and the method used in this paper still has good results and high accuracy (Shao *et al.* 2020).

## Case Reuse Experiment

To test the reusability of the case and further verify the effectiveness of the proposed method, we used the case library constructed in the section “Case Library Construction.” Experimental images were used to extract information from different regions and times. The experimental results are shown in Figure 6.

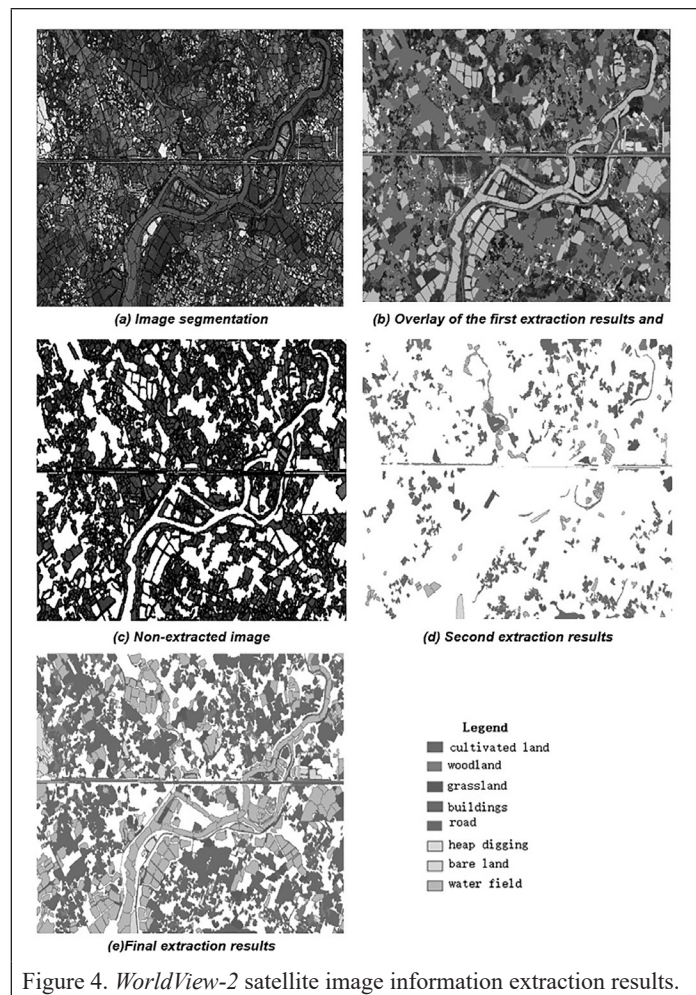


Figure 4. *WorldView-2* satellite image information extraction results.



Figure 5. Siwei Digital Camera-4 aerial image information extraction results.

Table 1. Evaluation of the accuracy of information extraction from the experimental image (*WorldView-2* satellite image).

Code	Total Number of Spots	Number of Correct Extractions	Number of Incorrect Extractions	Total Number of Extractions	Extraction Rate (%)	Recognition Rate (%)
0100	815	549	13	562	68.98	97.69
0300	352	256	8	264	75.00	96.97
0500	750	652	16	668	89.07	97.60
0600	42	27	0	27	64.29	100
1000	424	339	0	339	79.95	100

Table 2. Evaluation of the accuracy of information extraction from the experimental image (*Siwei Digital Camera-4* aerial image).

Code	Total Number of Spots	Number of Correct Extractions	Number of Incorrect Extractions	Total Number of Extractions	Extraction Rate (%)	Recognition Rate (%)
0100	2514	1574	14	1588	63.17	99.12
0300	90	79	6	85	94.44	92.94
0500	165	135	5	140	84.85	96.43
0600	168	136	3	139	82.74	97.84
1000	28	18	0	18	64.29	100

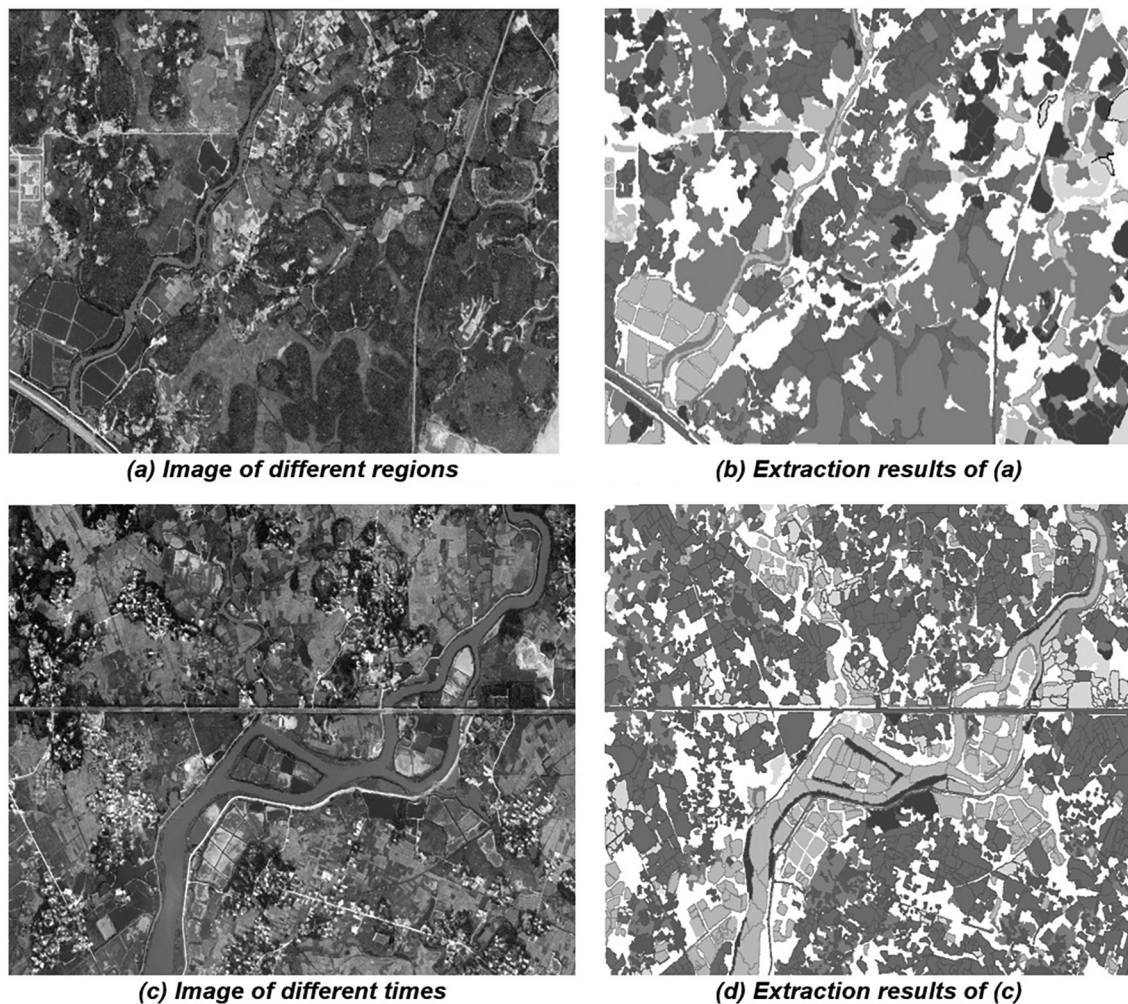


Figure 6. Case reusability experiment results.

Figure 6a is an image showing different regions at the same time as that in the section “Case Library Construction,” and Figure 6c is an image taken in January 2013 in the same region as that in section “Information Extraction Experiment.” The surface cover classification results obtained by this method are shown in Figure 6b and 6d, respectively. For Figure 6b, most of the information on cultivated land, forest land, building construction, and water bodies can be correctly identified and extracted because the image acquisition time is consistent with

that in the case library. As for Figure 6d, part of the cultivated land information was not identified and extracted due to the seasonality of vegetation and crop cultivation. In addition, due to the dry season in winter, the area of the water bodies extracted is also reduced. However, this extraction result can also reflect realistic surface cover. Through this experiment, we tested the reusability of a case and further verified the correctness of the proposed method.



### Comparison with SVM Method

In order to verify the superiority of the proposed method, the SVM method was also used to extract the surface information in the *WorldView-2* image obtained in April 2015. The comparison of the extraction results of the SVM method and the proposed method is shown in Figure 7.

By comparing the results of extracting the surface coverage information from the SVM method and the proposed method, it is found that the results extracted by the SVM method are rich in information and have good visual effects, but there are also many incorrectly extracted surface coverage objects, which require a large amount of manual removal later. The amount of information extracted by the proposed method is relatively small, and there are relatively few erroneously extracted surface coverage objects, and the workload of later manual removal is small.

### Discussion

Case-based reasoning is based on the high-resolution, remote sensing image surface cover classification information extraction system, and the prerequisite is the sufficient case library. The case library should not only cover different regions, different seasons, different sensors, and different resolutions, but also ensure that each type of case has a considerable number. The main reason is that the accuracy of the information extraction experiment in this paper is affected by the lack of a sufficient case library.

In the experiment, five types of land cover were extracted and the classification information, such as whether it was cultivated lands, woodlands, grasslands, house buildings, roads, or water bodies, was determined. According to the extraction results in each experiment, the spectral characteristics of a single forest, building, road, and water body were better, particularly of a water body and road. This was followed by woodlands and housing construction. The worst was for the cultivated land because of the different crop types due to seasonal changes and tillage. This caused the spectral and texture features of arable land to vary greatly in different seasons and different periods. To accurately extract cultivated land information the cropland needs to be further subdivided according to crop type, season, and farming cycle, and then corresponded to a large number of cultivated land acquisition samples to build a more extensive case library to meet the case-based reasoning method's requirements. If a certain kind of crop can be identified, such as sugar cane, then a case library image of sugar cane could be built and subsequently used by this method to extract sugarcane ground information.

Generally, the merits of the proposed method are the high accuracy of information extraction and the small amount of follow-up manual intervention. In the case that the case library is sufficiently rich, the extraction accuracy and the number of extractions will be continuously improved with the operation of the case reasoning system. Compared

with the classic object-oriented information extraction method like the SVM method, the drawbacks of this method are that it is difficult to obtain all the information of the entire remote sensing image, and it depends on a suitable segmentation scale and a rich case library.

Due to the limited number of experimental cases, the effect of case learning was not significant; this paper does not present the experimental results for case learning. However, with the continual expansion and enrichment of the case library, the effect of case learning will become more and more obvious.

### Conclusion

Due to the similar imaging mechanisms of high resolution remote sensing images, in the same region the surface cover characteristics will have certain similarities and stability in terms of geographical features. For example, crop planting type, planting distribution, and plant characteristics will be similar, and topographical features will be relatively stable (Zhang et al. 2020). At the same time, the spectral and textural features of vegetation cover change with seasonal changes and different growth periods have different characteristics. In view of the above characteristics of high-resolution remote sensing images, it can be concluded that they are very suitable for use with the case-based reasoning method to extract land cover classification information from high-resolution remote sensing images (Xu 2017).

The objective of this paper is to integrate multi-scale segmentation and case-based reasoning, and based on the proposed integration method to realize the automatic extraction of land cover classification information from high-resolution remote sensing images, and verify the effectiveness and accuracy of the method through integrated experiments. Since the surface vegetation will show different characteristics according to the geographical area and growing season, it is particularly important to obtain high-resolution remote sensing image data sources with a wide coverage area and long time series and to establish a corresponding case database. The method proposed in this paper makes full use of the nonimage features and multi-scale characteristics of the surface cover classification object. With the operation mechanism of the case reasoning system and case self-learning, the accuracy of surface cover classification information extraction will be increased. In addition, there are some other issues worthy of consideration. For example, how to further optimize case feature combinations of different case libraries or case matching similarity models. These will be our future studies.

### Acknowledgments

Author contributions are: conceptualization, Jiansong Li and Jun Xu; methodology, Hao Peng and Jun Xu; validation, Jun Xu, Yanjun He, Hao Peng; formal analysis, Jiansong Li and Jun Xu; data curation, Jun Xu, Yanjun He; writing—original draft preparation, Jun Xu

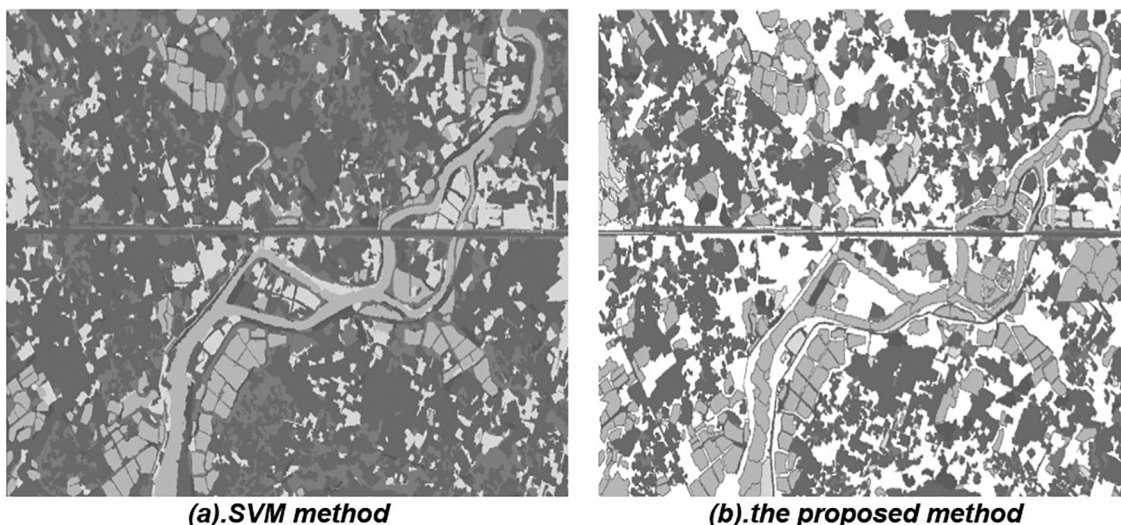


Figure 7. The experiment results of the support vector machine method and the proposed method.



and Jiansong Li; writing–review and editing, Jun Xu, Jiansong Li, Hao Peng; supervision, Jun Xu; funding acquisition, Jun Xu and Bin Wu. All authors have read and agreed to the published version of the manuscript. This work is supported by the National Key Research and Development Program of China (2018YFB0505401), the Key Research and Development Program of Yunnan province in China (2018IB023), the Research Project from the Ministry of Natural Resources of China under Grant 4201-240100123, the National Natural Science Foundation of China under Grants 41771452, 41771454, 41890820, and 41901340, the National Science Fund of Hubei Province in China under Grant 2018CFA007, the Project to Improve the Basic Research Ability of Young and Middle-Aged Teachers in Guangxi Universities under Grant 2019KY0426, and the Guangxi Science and Technology Plan Project (AD19245041). The authors are sincerely grateful to the editors as well as the anonymous reviewers for their valuable suggestions and comments that helped us improve this paper significantly.

## References

- Cao, J. N., Z. F. Shao and J. Guo. 2015a. A multi-scale method for urban tree canopy clustering recognition using high-resolution image. *Optik—International Journal for Light and Electron Optics* 126(13):1269–1276.
- Cao, J. N., Z. F. Shao, J. Guo, Y. W. Dong and P. L. Wang. 2015b. A multi-scale method for urban tree canopy clustering recognition using high-resolution image. *Optik* 126(13):1269–1276. <https://doi.org/10.1016/j.ijleo.2015.02.094>.
- Chang, C. Y., G. X. Zhao, L. Wang, X. C. Zhu and Z. Gao. 2012. Land use classification based on RS object-oriented method in coastal spectral confusion region. *Transactions of the Chinese Society of Agricultural Engineering* 28(5):226–231.
- Chen, F. L., C. Wang, H. Zhang and F. Wu. 2008. Multi-temporal SAR images classification using case-based reasoning. *Geomatics and Information Science of Wuhan University* 33(11):1154–1157.
- Chen, L. P. and W. B. Wu. 2013. Remote sensing image classification based on object-oriented technique and C4.5 algorithm. *Remote Sensing Information* 28(2):116–120.
- Du, Y. Y., C. H. Zhou, G. G. Shao and F. Z. Su. 2002a. The application of geo-case based reasoning. *Geo-Information Science* 7(1):98–103.
- Du, Y. Y., C. H. Zhou, Q. Q. Shao, F. Z. Su, Z. Z. Shi and S. E. Ye. 2002b. Theoretic and application research of geo-case based reasoning. *Acta Geographica Sinica* 57(2):151–158.
- Gu, D. X., X. G. Li, C. Y. Liang and F. G. Li. 2009. Research on case retrieval with weight optimizing and its application. *Journal of Systems Engineering* 24(6):764–768.
- Li, C. F., J. Y. Yin and J. J. Zhao. 2011. An extraction algorithm of urban vegetation from remote sensing image based on object-oriented approach. *Science of Surveying and Mapping* 36(5):112–114, 120.
- Li, G. H. 2013. *Surface Coverage Extraction and Change Analysis in Ningwu Coalfield Areas*. Shanxi Taiyuan: Taiyuan University of Technology.
- Li, X., A. G. O. Yeh, and Q. F. Liao. 2004. Case-based reasoning (CBR) for land use classification using radar images. *Journal of Remote Sensing* 8(3):246–253.
- Li, X., A. G. O. Yeh, J. Qian, B. Ai and Z. X. Qi. 2009. A matching algorithm for detecting land use changes using case-based reasoning. *Photogrammetric Engineering and Remote Sensing* 75(11):1319–1332.
- Li, X. Z. 2004. *Study on Feature Selection and Ensemble Learning Based on Feature Selection for High-Dimensional Datasets*. Beijing: Tsinghua University.
- Liu, Y. and X. Li. 2014. Domain adaptation for land use classification: A spatio-temporal knowledge reusing method. *ISPRS Journal of Photogrammetry and Remote Sensing* 98:133–144.
- Miao, Y. P., R. H. Zhang and B. G. Zhao. 2010. Research on methods of information extraction from high resolution remote sensing images. *Geomatics and Spatial Information Technology* 33(4):150–152.
- Pacifici, F., F. D. Frate, C. Solimini and W. Emery. 2009. An innovative neural-net method to detect temporal changes in high-resolution optical satellite imagery. *IEEE Transactions on Geoscience and Remote Sensing* 45(9):2940–2952.
- Shao, Z. F. and J. J. Cai. 2018. Remote sensing image fusion with deep convolutional neural network. *IEEE Journal of Selected Topics in Applied Earth Observations and Remote Sensing* 11(5):1656–1669. <https://doi.org/10.1109/JSTARS.2018.2805923>.
- Shao, Z. F., L. Ding, D. R. Li, O. Altan, Md. Enamul Huq, C. M. Li. 2020a. Exploring the relationship between urbanization and ecological environment using remote sensing images and statistical data: A case study in the Yangtze River Delta, China. *Sustainability, MDPI, Open Access Journal* 12(14):1–28.
- Shao, Z. F., H. Y. Fu, P. Fu and L. Yin. 2016. Mapping urban impervious surface by fusing optical and SAR data at the decision level. *Remote Sensing* 8(11):945. <https://doi.org/10.3390/rs8110945>.
- Shao, Z. F., C. Li, D. Li and L. Ding. 2020b. An accurate matching method for projecting vector data into surveillance video to monitor and protect cultivated land. *International Journal of Geo-Information* 9(7):1–17.
- Shao, Z. F., C. M. Li, D. R. Li, O. Altan, L. Zhang and L. Ding. 2020c. An accurate matching method for projecting vector data into surveillance video to monitor and protect cultivated land. *ISPRS International Journal of Geo-Information* 9:448. <https://doi.org/10.3390/ijgi9070448>.
- Shao, Z. F., Y. Pan, C. Y. Diao and J. J. Cai. 2019. Cloud detection in remote sensing images based on multiscale features-convolutional neural network. *IEEE Transactions on Geoscience and Remote Sensing* 57(6):4062–4076. <https://doi.org/10.1109/TGRS.2018.2889677>.
- Shao, Z. F., N. S. Sumari and A. Portnov. 2020d. Urban sprawl and its impact on sustainable urban development: A combination of remote sensing and social media data. *Geo-spatial Information Science* 2020(3):1–15.
- Shao, Z. F., P. H. Tang, Z. Y. Wang., N. Saleem, S. Yam and C. Sommai. 2020e. BRRNet: A fully convolutional neural network for automatic building extraction from high-resolution remote sensing images. *Remote Sensing* 12(6):1050. <https://doi.org/10.3390/rs12061050>.
- Shao, Z. F., Y. J., Tian and X. L. Shen. 2014a. BASI: A new index to extract built-up areas from high-resolution remote sensing images by visual attention model. *Remote Sensing Letters* 5(4):305–314.
- Shao, Z. F., W. X. Zhou and L. Zhang. 2014b. Improved color texture descriptors for remote sensing image retrieval. *Journal of Applied Remote Sensing* 8:083584.
- Sun, X. B., W. Fan, P. Yan, Y. Huang and Y. H. Ma. 2007. A brief review on classification methods of land cover based on remote sensing image. *Chinese Agricultural Science Bulletin* 23(9):607–610.
- Tang, X. F. 2010. *Research on Classification Techniques of the Hyperspectral Images Based on Case-Based Reasoning*. Harbin, China: Harbin Institute of Technology.
- Wang, H. Y., W. Su and J. Q. Zhou. 2009. Object-oriented information extraction method of remote sensing image based on multi-classifier mixed. *Engineering of Surveying and Mapping* 18(5):23–26.
- Wang, W. C. and W. B. Zou. 2013. Methods of extraction in high resolution remote sensing image information. *Beijing Surveying and Mapping* 27(4):1–5.
- Xu, J. 2017. *High Resolution Remote Sensing Image Information Extraction Method for Multi-Scale Segmentation and Case-Based Reasoning*. Hubei, China: Wuhan University.
- Xu, J. and J. S. Li. 2018. Case library construction method using high-resolution remote sensing land cover classification information. *Journal of Spatial Science* 63(2):1–11. <https://doi.org/10.1080/14498596.2018.1499560>.
- Xu, J., X. Li and J. S. Li. 2017a. Method of extracting of remote sensing images water information based on case-based reasoning. *Journal of Guangxi University (Natural Science Edition)* 42(3):1078–1085.
- Xu, J., X. M. Zhang and J. S. Li. 2017b. Road information extraction method of high resolution remote sensing image based on bi-level case reasoning model. *Journal of Dalian Maritime University* 43(4):104–111. <https://doi.org/10.1641/j.cnki.issn1006-7736.2017.04.015>.
- Yan, E. P. 2011. *Medium and High-Resolution Remote Sensing Image Broadleaf Forest Information Extraction*. Hunan Changsha: Central South University of Forestry and Technology.
- Yang, N. 2011. *Feature Selection for Object-Oriented Classification of High-Resolution Remote Sensing Images*. Shanxi Xi'an, China: Xi'an University of Science and Technology.
- Zhang, H. C., X. G. Ning, Z. F. Shao and H. Wang. 2019. Spatiotemporal pattern analysis of China's cities based on high-resolution imagery from 2000 to 2015. *ISPRS International Journal of Geo-Information* 8(5):241. <https://doi.org/10.3390/ijgi8050241>.
- Zhang, R., Z. F. Shao and X. Huang. 2020a. Object detection in UAV images via global density fused convolutional network. *Remote Sensing* 12(3140):1–17.
- Zhang, R. Q., Z. F. Shao, X. Huang, J. M. Wang and D. R. Li. 2020b. Object detection in UAV images via global density fused convolutional network. *Remote Sensing* 12(19):3140. <https://doi.org/10.3390/rs12193140>.
- Zhou, X. R., Z. F. Shao, W. Zeng and J. Liu. 2014. Semantic graph construction for 3D geospatial data of multi-versions. *Optik: Zeitschrift für Licht-und Elektronenoptik* 2014:1730–1734.
- Zhou, W. X., N. Shawn, C. M. Li and Z. F. Shao. 2017. Learning low dimensional convolutional neural networks for high-resolution remote sensing image retrieval. *Remote Sensing* 9(5):489. <https://doi.org/10.3390/rs9050489>.

---

## IN-PRESS ARTICLES

- Xuzhe Duan, Qingwu Hu, Pengcheng Zhao, and Shaohua Wang. A low-cost and portable indoor 3D mapping approach using biaxial line laser scanners and a one-dimension laser rangefinder integrated with MEMS.
- Jun Chen, Cunjian Yang, Zhengyang Yu. Research on Machine Intelligent Perception of Urban Geographic Location Based on High Resolution Remote Sensing Images.
- Lihua Wang, lifeng Liang, Benhua Tan, Sicheng Li, Zhiming Kang, Xiujuan Liu. Identifying the driving factors of urban land surface temperature.
- Clement Akumu, Sam Dennis. Urban Land Cover/Use Mapping and Change Detection Analysis Using Multi-Temporal Landsat OLI with Lidar-DEM and Derived TPI.
- Amit Hasan, Mahendra Udawalpola, Anna Liljedahl, Chandi Witharana. Use of Commercial Satellite Imagery to Monitor Changing Arctic Polygonal Tundra.
- Lei Zhang, Bowen Wen, Ming Zhang, Qiongqiong Lan, and Qian Wang. An Evaluation of Pan-Sharpening Methods for SuperView-1 Satellite Imagery.
- Bo Yingjie, Li Guoqing, Zeng Yelong, and Liu Zhe. Floating Solar Park Impacts Urban Land Surface Temperature Distribution Pattern.
- He Yanjun, Xu Jun, Li Jiansong, Peng Hao, Wu Bin. Information Extraction from High-resolution Remote Sensing Images Based on Multi-scale Segmentation and Case-based Reasoning.
- Gaofei Yin. Smartphone Digital Photography for Fractional Vegetation Cover Estimation.
- Toshihiro Sakamoto, Daisuke Ogawa, Satoko Hiura, Nobusuke Iwasaki. Alternative procedure to improve the positioning accuracy of orthomosaic images acquired with Agisoft Metashape and DJI P4 Multispectral for crop growth observation
- Guangyun Li, Senzhen Sun, Yangjun Gao, Li Wang. Robust Dynamic Indoor Visible Light Positioning Method Based on CMOS Image Sensor.
- Zhenfeng Shao, Hongping Zhang, Wenfu Wu, Xiao Huang, Jisong Sun, Jinqi Zhao, Yewen Fan. Comparing the sensitivity of pixel-based and sub-watershed-based AHP to weighting criteria for flood hazard estimation.
- Gang Qiao, Hongwei Li. Lake Water Footprint Determination Using Linear Clustering-based Algorithm and Lake Water Changes in the Tibetan Plateau from 2002 to 2020.
- Jason Parent, Chandi Witharana, Michael Bradley. Classifying and georeferencing indoor point clouds with ARCGIS.
- Paul Pope, Brandon Crawford, Anita Lavadie-Bulnes, Emily Schultz-Fellenz, Damien Milazzo, Kurt Solander, Carl Talsma. Towards Automated/Semi-Automated Extraction of Faults from Lidar Data
- Li Tan, Guoming Li, Xin Liu, Aike Kan. Feature-based convolutional neural network for very-high-resolution urban imagery classification
- Ravi Dwivedi, Syed Azeemuddin. Conjunctive use of Landsat-8 OLI and MODIS Data for Delineation of Burned Areas
- Chih-Hung Hsu, Che-Hao Chang, Chih-Tsung Hsu, Shiang-Jen Wu, Po-Hsien Chung. Hydrological Topography Dataset (HTD) - the Dataset for High Resolution 2D Urban Flood Modeling.
- Xiaojun Yang, Feilin Lai. Improving land cover classification over a large coastal city through stacked generalization with filtered training samples.
- Xiaoyue Wang, Hongxin Zhang, Dailiang Peng. Evaluation of urban vegetation phenology using 250 m MODIS vegetation indices.
- Zhihua Xu, Xingzheng Lu, Wenliang Wang, Ershuai Xu, Rongjun Qin, Yiru Niu, Xu Qiao, Feng Yang, Rui Yan. Monocular Video Frame Optimization through Feature-based Parallax Analysis for 3D Pipe Reconstruction.

# WHO'S WHO IN ASPRS

Founded in 1934, the American Society for Photogrammetry and Remote Sensing (ASPRS) is a scientific association serving thousands of professional members around the world. Our mission is to advance knowledge and improve understanding of mapping sciences to promote the responsible applications of photogrammetry, remote sensing, geographic information systems (GIS) and supporting technologies.

## BOARD OF DIRECTORS

### BOARD OFFICERS

**President**

Christopher Parrish, Ph.D.  
Oregon State University

**President-Elect**

Lorraine B. Amenda, PLS, CP  
Towill, Inc.

**Vice President**

Bandana Kar  
Oak Ridge National Lab

**Past President**

Jason M. Stoker, Ph.D.,  
U.S. Geological Survey

**Treasurer**

Stewart Walker, Ph.D.  
photogrammetry4u

**Secretary**

Harold Rempel  
ESP Associates, Inc.

---

## COUNCIL OFFICERS

ASPRS has six councils. To learn more, visit <https://www.asprs.org/Councils.html>.

**Sustaining Members Council**

Chair: Ryan Bowe  
Deputy Chair: Melissa Martin

**Technical Division Directors Council**

Chair: Bill Swope  
Deputy Chair: Hope Morgan

**Standing Committee Chairs Council**

Chair: David Stolarz  
Deputy Chair: TBA

**Early-Career Professionals Council**

Chair: Madeline Stewart  
Deputy Chair: Kyle Knapp

**Region Officers Council**

Chair: Demetrio Zourarakis  
Deputy Chair: Jason Krueger

**Student Advisory Council**

Chair: Lauren McKinney-Wise  
Deputy Chair: Oscar Duran

---

## TECHNICAL DIVISION OFFICERS

ASPRS has seven professional divisions. To learn more, visit <https://www.asprs.org/Divisions.html>.

**Geographic Information Systems Division**

Director: Denise Theunissen  
Assistant Director: Jin Lee

**Lidar Division**

Director: Ajit Sampath  
Assistant Director: Mat Bethel

**Photogrammetric Applications Division**

Director: Ben Wilkinson  
Assistant Director: Hank Theiss

**Primary Data Acquisition Division**

Director: Greg Stensaas  
Assistant Director: Srinu Dharmapuri

**Professional Practice Division**

Director: Bill Swope  
Assistant Director: Hope Morgan

**Remote Sensing Applications Division**

Director: Amr Abd-Ehrahman  
Assistant Director: Tao Liu

**Unmanned Autonomous Systems (UAS)**

Director: Jacob Lopez  
Assistant Director: Bahram Salehi

---

## REGION PRESIDENTS

ASPRS has 13 regions to serve the United States. To learn more, visit <https://www.asprs.org/regions.html>.

**Alaska Region****Cascadia Region**

Robert Hariston-Porter

**Eastern Great Lakes Region**

Michael Joos, CP, GISP

**Florida Region**

Xan Fredericks

**Heartland Region**

Whit Lynn

**Intermountain Region**

Robert T. Pack

**Mid-South Region**

David Hughes

**Northeast Region****North Atlantic Region****Pacific Southwest Region**

John Erickson, PLS, CP

**Potomac Region**

Dave Lasko

**Rocky Mountain Region****Western Great Lakes Region**

Adam Smith



# SUSTAININGMEMBERS

## ACI USA Inc.

Weston, Florida  
<https://acicorporation.com/>  
 Member Since: 2/2018

## Aerial Services, Inc.

Cedar Falls, Iowa  
[www.AerialServicesInc.com](http://www.AerialServicesInc.com)  
 Member Since: 5/2001

## Applanix

Richmond Hill, Ontario, Canada  
<http://www.applanix.com>  
 Member Since: 7/1997

## Ayres Associates

Madison, Wisconsin  
[www.AyresAssociates.com](http://www.AyresAssociates.com)  
 Member Since: 1/1953

## Dewberry

Fairfax, Virginia  
[www.dewberry.com](http://www.dewberry.com)  
 Member Since: 1/1985

## Environmental Research Incorporated

Linden, Virginia  
[www.eri.us.com](http://www.eri.us.com)  
 Member Since: 8/2008

## Esri

Redlands, California  
[www.esri.com](http://www.esri.com)  
 Member Since: 1/1987

## GeoCue Group

Madison, Alabama  
<http://www.geocue.com>  
 Member Since: 10/2003

## GeoWing Mapping, Inc.

Richmond, California  
[www.geowingmapping.com](http://www.geowingmapping.com)  
 Member Since: 12/2016

## GPI Geospatial Inc.

formerly Aerial Cartographics of America, Inc. (ACA)  
 Orlando, Florida  
[www.aca-net.com](http://www.aca-net.com)  
 Member Since: 10/1994

## Green Grid Inc.

San Ramon, California  
[www.greengridinc.com](http://www.greengridinc.com)  
 Member Since: 1/2020

## Halff Associates, Inc.

Richardson, Texas  
[www.halff.com](http://www.halff.com)  
 Member Since: 8/2021

## Keystone Aerial Surveys, Inc.

Philadelphia, Pennsylvania  
[www.kasurveys.com](http://www.kasurveys.com)  
 Member Since: 1/1985

## Kucera International

Willoughby, Ohio  
[www.kucerainternational.com](http://www.kucerainternational.com)  
 Member Since: 1/1992

## L3Harris Technologies

Broomfield, Colorado  
[www.l3harris.com](http://www.l3harris.com)  
 Member Since: 6/2008

## Merrick & Company

Greenwood Village, Colorado  
[www.merrick.com/gis](http://www.merrick.com/gis)  
 Member Since: 4/1995

## NV5 Geospatial

Sheboygan Falls, Wisconsin  
[www.quantumspatial.com](http://www.quantumspatial.com)  
 Member Since: 1/1974

## Pickett and Associates, Inc.

Bartow, Florida  
[www.pickettusa.com](http://www.pickettusa.com)  
 Member Since: 4/2007

## Riegl USA, Inc.

Orlando, Florida  
[www.rieglusa.com](http://www.rieglusa.com)  
 Member Since: 11/2004

## Robinson Aerial Surveys, Inc.(RAS)

Hackettstown, New Jersey  
[www.robinsonaerial.com](http://www.robinsonaerial.com)  
 Member Since: 1/1954

## Sanborn Map Company

Colorado Springs, Colorado  
[www.sanborn.com](http://www.sanborn.com)  
 Member Since: 10/1984

## Scorpius Imagery Inc.

Newark, Delaware  
[aerial@scorpiusimagery.com](mailto:aerial@scorpiusimagery.com)  
 Member Since: 6/2021

## Surdex Corporation

Chesterfield, Missouri  
[www.surdex.com](http://www.surdex.com)  
 Member Since: 12/2011

## Surveying And Mapping, LLC (SAM)

Austin, Texas  
[www.sam.biz](http://www.sam.biz)  
 Member Since: 12/2005

## T3 Global Strategies, Inc.

Bridgeville, Pennsylvania  
<https://t3gs.com/>  
 Member Since: 6/2020

## Terra Remote Sensing (USA) Inc.

Bellevue, Washington  
[www.terrareremote.com](http://www.terrareremote.com)  
 Member Since: 11/2016

## Towill, Inc.

San Francisco, California  
[www.towill.com](http://www.towill.com)  
 Member Since: 1/1952

## Woolpert LLP

Dayton, Ohio  
[www.woolpert.com](http://www.woolpert.com)  
 Member Since: 1/1985

# SUSTAININGMEMBERBENEFITS

## Membership

- ✓ Provides a means for dissemination of new information
- ✓ Encourages an exchange of ideas and communication
- ✓ Offers prime exposure for companies

## Benefits of an ASPRS Membership

- Complimentary and discounted Employee Membership\*
- E-mail blast to full ASPRS membership\*
- Professional Certification Application fee discount for any employee
- Member price for ASPRS publications
- Discount on group registration to ASPRS virtual conferences
- Sustaining Member company listing in ASPRS directory/website
- Hot link to company website from Sustaining Member company listing page on ASPRS website
- Press Release Priority Listing in PE&RS Industry News
- Priority publishing of Highlight Articles in PE&RS plus, 20% discount off cover fee
- Discount on PE&RS advertising
- Exhibit discounts at ASPRS sponsored conferences (exception ASPRS/ILMF)
- Free training webinar registrations per year\*
- Discount on additional training webinar registrations for employees
- Discount for each new SMC member brought on board (Discount for first year only)

\*quantity depends on membership level



WHITTLES  
PUBLISHING

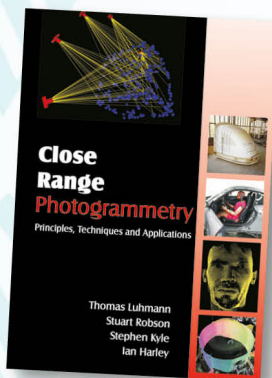
SIMPLY BRILLIANT BOOKS

**ASPRS**  
MEMBER EXCLUSIVE

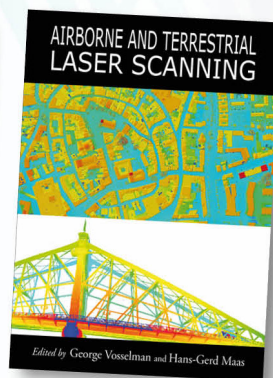
**20%**  
DISCOUNT

ON ALL WHITTLES  
PUBLISHING BOOKS  
USING CODE WPASPRS2

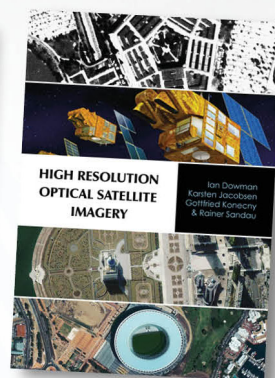
WHITTLES PUBLISHING'S  
STABLE OF CLASSIC  
GEOMATICS BOOKS  
INCLUDES THE THREE  
WINNERS OF THE  
PRESTIGIOUS KARL KRAUS  
MEDAL AWARDED BY ISPRS



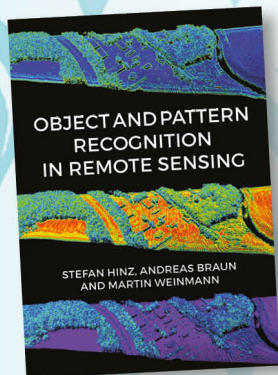
978-1870325-73-8  
(Available as a CD)



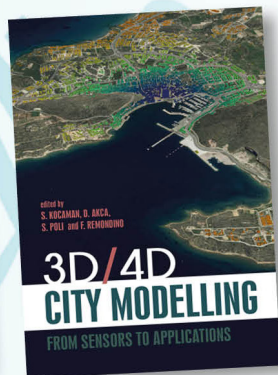
978-1904445-87-6



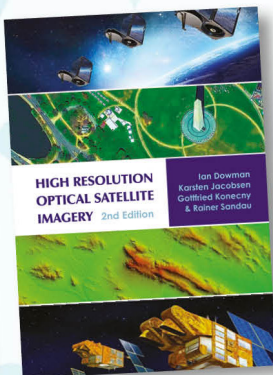
ISBN? Website only has 2nd edition



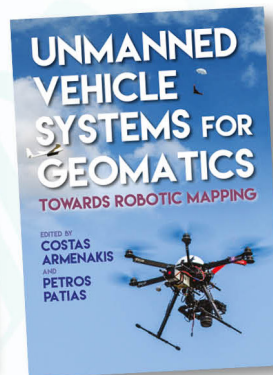
978-184995-128-9



978-184995-475-4



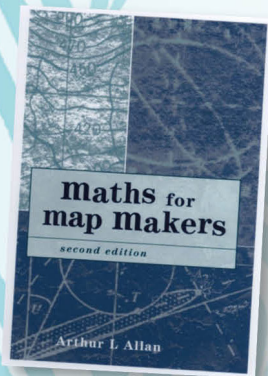
978-184995-390-0



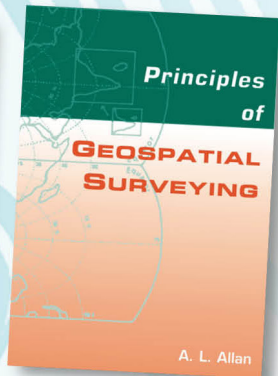
978-184995-127-2

OUR LIST  
CONTINUES  
TO EXPAND  
WITH THESE  
NEW TITLES

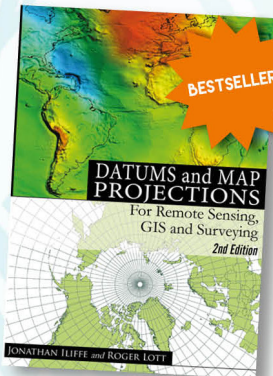
BROWSE OUR WEBSITE TO SEE OUR FULL RANGE  
OF ACCLAIMED GEOMATICS BOOKS



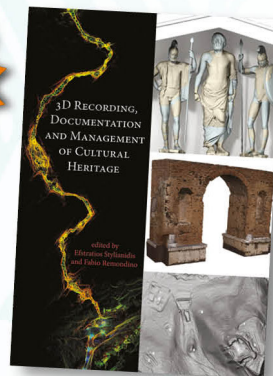
978-1870325-99-8



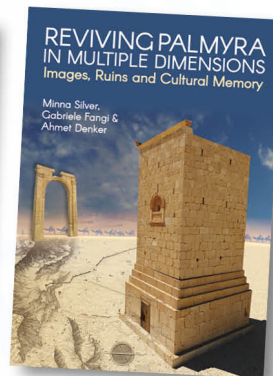
978-1904445-21-0



978-1904445-47-0



978-184995-168-5



978-184995-296-5

WWW.WHITTLESUBLISHING.COM



LEARN  
DO  
GIVE  
BELONG

**ASPRS Offers**

- » Cutting-edge conference programs
- » Professional development workshops
- » Accredited professional certifications
- » Scholarships and awards
- » Career advancing mentoring programs
- » *PE&RS*, the scientific journal of ASPRS

[asprs.org](http://asprs.org)

ASPRS